TECHNOLOGY • RESEARCH HIGHLIGHTS • VISIONS • SCIENCE •
175

Structural integrity of Ni-base alloy welds

Hannu Hänninen | Anssi Brederholm | Teemu Sarikka |
Roman Mouginot | Petra Holmström | Tapio Saukkonen |
Aki Toivonen | Päivi Karjalainen-Roikonen |
Pekka Nevasmaa | Heikki Keinänen | Esa Leskelä |
Matias Ahonen | Ulla Ehrnstén | Pertti Aaltonen

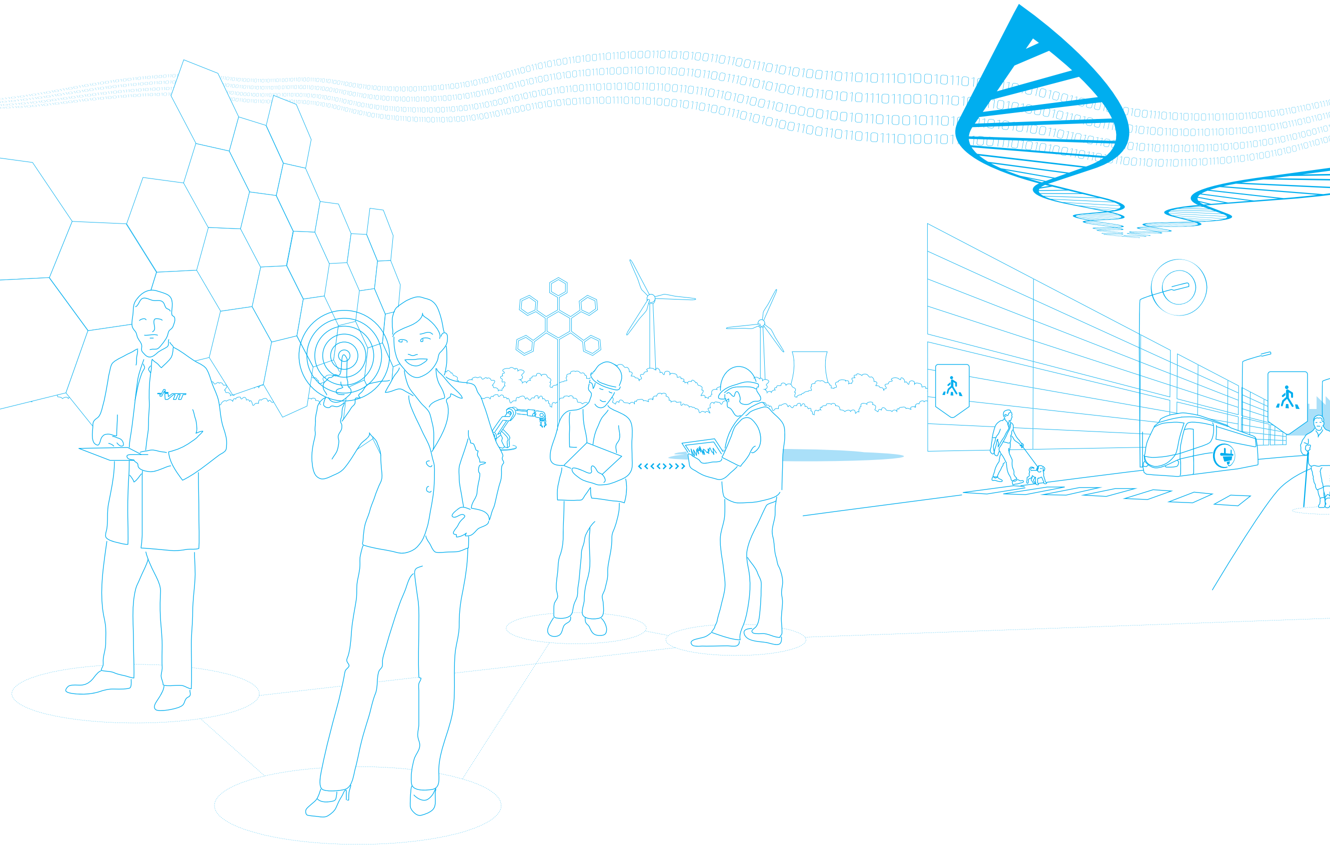

VTT

VTT TECHNOLOGY 175

Structural integrity of Ni-base alloy welds

Hannu Hänninen, Anssi Brederholm, Teemu Sarikka,
Roman Mouginot, Petra Holmström & Tapio Saukkonen
Aalto University School of Engineering

Aki Toivonen, Päivi Karjalainen-Roikonen, Pekka Nevasmaa,
Heikki Keinänen, Esa Leskelä, Matias Ahonen, Ulla Ehrnstén
& Pertti Aaltonen
VTT Technical Research Centre of Finland

ISBN 978-951-38-8259-4 (Soft back ed.)
ISBN 978-951-38-8260-0 (URL: http://www.vtt.fi/publications/index.jsp)

VTT Technology 175

ISSN-L 2242-1211
ISSN 2242-1211 (Print)
ISSN 2242-122X (Online)

JULKAISIJA – UTGIVARE – PUBLISHER

VTT
PL 1000 (Tekniikantie 4 A, Espoo)
02044 VTT
Puh. 020 722 111, faksi 020 722 7001

VTT
PB 1000 (Teknikvägen 4 A, Esbo)
FI-02044 VTT
Tfn +358 20 722 111, telefax +358 20 722 7001

VTT Technical Research Centre of Finland
P.O. Box 1000 (Tekniikantie 4 A, Espoo)
FI-02044 VTT, Finland
Tel. +358 20 722 111, fax +358 20 722 7001

Grano Oy, Kuopio 2014

Structural integrity of Ni-base alloy welds

Ni-seosten hitsausliitosten rakenteellinen turvallisuus.
Hannu Hänninen, Anssi Brederholm, Teemu Sarikka, Roman Mouginot, Petra Holmström, Tapio Saukkonen, Aki Toivonen, Päivi Karjalainen-Roikonen, Pekka Nevasmaa, Heikki Keinänen, Esa Leskelä, Matias Ahonen, Ulla Ehrnstén & Pertti Aaltonen.
Espoo 2014. VTT Technology 175. 257 p.

Abstract

The Tekes project Structural integrity of Ni-base alloy welds (SINI) was carried out at Aalto University and VTT during the period from 2010 to 2014. In nuclear industry applications, the degradation of Ni-base alloy dissimilar metal welds (DMWs), both in pressurised water reactor (PWR) and in boiling water reactor (BWR) plants, is an extensive international problem. The project participates with ongoing international cooperation in USA (Electric Power Research Institute EPRI, Alloy 690/52/152 PWSCC Research Collaboration) and in Japan (Tohoku University) for the conduction of new Ni-base alloy research. The research need is actual, especially because indications have been found in the DMWs in the reactor pressure vessel nozzle of BWRs similar to Finnish BWR designs and European pressurised water reactor (EPR PWR) -plant under construction contains a large number of varying and new types of dissimilar metal welds of which no previous experience is available.

The main focus of the project was to investigate the weldability of Alloy 690 base metal corresponding filler metal Alloy 52 and the properties of the welded joint. Comparable reactor pressure vessel (RPV) safe-end weld joint was made by narrow-gap tungsten inert gas (TIG) welding with Alloy 52 filler metal for research purposes. Also prototypical BWR reactor pressure vessel (RPV) safe-end weld joint was made with Alloy 82/182 filler metals. Determination of the mechanical properties and characterization of the microstructures of the welded joints were conducted. Crack initiation tests in autoclave were made in different environments. After PINC (Program for the Inspection of Nickel Alloy Components) round-robin program new PARENT (Program to Assess Reliability of Emerging Non-destructive Techniques for Dissimilar Metal Welds) round-robin program was started where VTT participated. Based on the PINC results, new non-destructive testing methods were developed to enhance the reliability of detection and accuracy of sizing of flaws in nickel-based alloy dissimilar metal welds.

Separate reports:

1. Holmström, P. (2012), The effect of mismatch on the mechanical properties of a dissimilar metal weld. M.Sc. Thesis, Aalto University, Espoo, Finland, 162 p. + app. 4 p.

2. Mouginot, R. and Hänninen, H. (2013), Microstructures of nickel-base alloy dissimilar metal welds. Aalto University publication series SCIENCE + TECHNOLOGY, 5/2013, https://aaltodoc.aalto.fi/handle/123456789/9006, Aalto University, Espoo, Finland, 178 p.

3. Keinänen, H. (2013), Computational estimation of the risk of hot cracking in narrow gap welding. Research report VTT-R-08369-13, VTT Technical Research Centre of Finland, Espoo, Finland, 27 p. + app. 10 p.

Keywords Nickel-base alloys, welding, weld metal, dissimilar metal welds, nuclear power plant, environment-assisted cracking, fracture toughness, scanning electron microscopy, NDT

Ni-seosten hitsausliitosten rakenteellinen turvallisuus

Structural integrity of Ni-base alloy welds.
Hannu Hänninen, Anssi Brederholm, Teemu Sarikka, Roman Mouginot, Petra Holmström, Tapio Saukkonen, Aki Toivonen, Päivi Karjalainen-Roikonen, Pekka Nevasmaa, Heikki Keinänen, Esa Leskelä, Matias Ahonen, Ulla Ehrnstén & Pertti Aaltonen.
Espoo 2014. VTT Technology 175. 257 s.

Tiivistelmä

Tekes-projektissa Structural Integrity of Ni-base Alloy Welds (SINI) vuosina 2010–2014 Aalto-yliopistossa ja VTT:llä suoritettu tutkimus kohdistui ydinvoimalaitoksissa käytettäviin uusiin materiaaleihin ja hitsausmenetelmiin. Ydinvoimalaitosten Ni-seosten ja niiden hitsausliitosten vaurioituminen sekä painevesireaktori (PWR)- että kiehutusvesireaktori (BWR) -olosuhteissa on laaja kansainvälinen käytettävyys- ja tutkimusongelma. SINI-projekti osallistui useaan kansainväliseen yhteishankkeeseen USA:ssa (Electric Power Research Institute EPRI, Alloy 690/52/152 PWSCC Research Collaboration) ja Japanissa (Tohokun yliopisto). Myös Suomessa tutkimustarve on suuri: BWR-laitosten kriittisissä paineastian/putkiston eriparihitsausliitoksissa on havaittu indikaatioita, ja eurooppalainen painevesireaktorilaitos (EPR-PWR) sisältää kaikissa tärkeimmissä komponenteissa runsaasti uusia Ni-seoksia ja niiden eriparihitsausliitoksia, joista ei ole aiempaa käyttökokemusta.

Projekti keskittyi erityisesti Alloy 690 -seosta vastaavan hitsauslisäaineen Alloy 52 hitsattavuuden ja hitsausliitoksen ominaisuuksien tutkimiseen. Tutkimuksia varten hitsattiin kapearailo-TIG-menetelmällä reaktoripaineastian safe-end-hitsausliitosta vastaavat koehitsit Alloy 52 -lisäaineella. Lisäksi hitsattiin perinteisen BWR-reaktoripaineastian safe-end-hitsausliitosta vastaava koehitsi Alloy 82/182 -lisäaineella. Hitsausliitoksista määritettiin niiden mekaaniset ominaisuudet sekä karakterisoitiin syntyvät mikrorakenteet. Autoklaavikokeilla tutkittiin särön ydintymistä eri ympäristöissä. PINC (Program for the Inspection of Nickel Alloy Components) –monilaboratoriotestauksen jatkona käynnistyi PARENT-ohjelma (Program to Assess Reliability of Emerging Non-destructive Techniques for Dissimilar Metal Welds), johon VTT osallistui. Ohjelmassa jatkettiin PINCin tulosten pohjalta uusien rikkomattomien tarkastusmenetelmien kehittämistä sekä parannettiin vikojen havaitsemistarkkuutta ja koon määrittämistä nikkelipohjaisissa eriparihitsausliitoksissa.

Erilliset raportit:

1. Holmström, P. (2012), The effect of mismatch on the mechanical properties of a dissimilar metal weld. M.Sc. Thesis, Aalto University, Espoo, Finland, 162 p. + app. 4 p.

2. Mouginot, R. and Hänninen, H. (2013), Microstructures of nickel-base alloy dissimilar metal welds. Aalto University publication series SCIENCE + TECHNOLOGY, 5/2013, https://aaltodoc.aalto.fi/handle/123456789/9006, Aalto University, Espoo, Finland, 178 p.

3. Keinänen, H. (2013), Computational estimation of the risk of hot cracking in narrow gap welding. Research report VTT-R-08369-13, VTT Technical Research Centre of Finland, Espoo, Finland, 27 p. + app. 10 p.

Avainsanat Nikkelipohjaiset hitsauslisäaineet, hitsaus, eriparihitsi, ydinvoimalaitos, ympäristön aiheuttama murtuminen, murtumissitkeys, pyyhkäisyelektronimikroskopia, NDT

Preface

This research is primarily addressed to the needs of the nuclear power plant (NPP) industry. The SINI project is based on the earlier ERIPARI and PERDI projects, in which the background research and test method development were carried out. The degradation of dissimilar metal welds in both BWR- and PWR-plants is currently an area of widespread international interest. The SINI research project was conducted in cooperation with a number of different on-going and international cooperative research projects. The research is particularly relevant because indications have been found in the reactor pressure vessel nozzle dissimilar metal welds of BWRs similar to Finnish BWR designs. In nuclear power industry, dissimilar metal welding is widely used in many constructions and systems. The operating experience of major nuclear power plant pressure boundary components has recently shown that dissimilar metal weld joints can jeopardize the plant availability and safety because of increased incidences of environment-assisted cracking (EAC, PWSCC) of Alloy 600 and corresponding weld metals (Alloys 182/82). Alloy 690 and associated weld metals (Alloys 152/52) are widely used for repair and replacement of the affected thick-section components. In the new reactors such as EPR these are the main construction materials. The selection of new materials relies mainly on laboratory results and short-term service experience. The long-term behavior of these materials and their performance in the plant has still to be demonstrated.

The main aims of the research are to develop reliable research methods for the measurement, evaluation and design of dissimilar metal joints for new materials. In practice, using microstructural characterization, mechanical testing and fracture mechanical testing, the properties of new materials and their dissimilar metal joints at elevated temperatures and real process environments are obtained. The ageing of nuclear materials, their degradation mechanisms and the development of the NDE techniques for dissimilar metal joints are the main deliverables of the project. The fabrication methods of the studied joints and some of the important features of their behavior based on the mock-up samples are also developed in the project. Also the purpose of the study was to transfer the high level knowledge from the nuclear industry to conventional industries in the field of dissimilar metal welds and their long-term behavior in operation.

Contents

List of symbols

AES	Auger Electron Spectroscopy
BTR	Brittle Temperature Range
BWR	Boiling Water Reactor
°C	Degree Celsius
cc	Cubic Centimetre
CGZ	Coarse Grained Zone
cm	Centimetre
CMTR	Certified Material Test Report
DMW	Dissimilar Metal Weld
EAC	Environment Assisted Cracking
EBSD	Electron Backscattering Diffraction
EDS	Energy Dispersive X-ray Spectrometer
EFPHs	Effective Full-Power Hours
EPRI	Electric Power Research Institute
ESCA	Electron Spectroscopy for Chemical Analysis
GTAW	Gas Tungsten Arc Welding
HAZ	Heat-Affected Zone
HPLC	High-Performance Liquid Chromatography
HT	Heat Treatment
IPF	Inverse Pole Figure
LAS	Low-alloy Steel
LVDT	Linear Variable Displacement Transducer

LPSCC	Low-Potential Stress Corrosion Cracking
LWR	Light Water Reactor
NDE	Non-Destructive Examination
NPP	Nuclear Power Plant
p	Pressure
ppb	Parts Per Billion
ppm	Parts Per Million
PWHT	Post-Weld Heat Treatment
PWR	Pressurised Water Reactor
PWSCC	Primary Water Stress Corrosion Cracking
Q	Activation Energy
RPV	Reactor Pressure Vessel
SCC	Stress Corrosion Cracking
SEM	Scanning Electron Microscope
SMAW	Shielded Metal Arc Welding
T	Temperature
t	Time
Tekes	the Finnish Funding Agency for Innovation
TEM	Transmission Electron Microscope
TIG	Tungsten Inert Gas (Welding)
TVO	Teollisuuden Voima Oy
VTT	VTT Technical Research Centre of Finland
WEDM	Wire Electric Discharge Machining
XPS	X-ray Photoelectron Spectroscopy
σ	Stress
$\varnothing$	Diameter

1. Introduction

Dissimilar metal welds (DMWs) are widely used in high-temperature operating components, especially nuclear power plants (NPPs) to join the ferritic steel nozzles of reactor pressure vessels, steam generators and pressurizers to the austenitic stainless steel pipes using a safe-end. DMWs have been found susceptible to environment-assisted cracking (EAC) in boiling water reactor (BWR) conditions where their microstructures and prevailing residual stresses/strains affect the EAC susceptibility [Holmström et al. 2013]. DMWs are also used in primary water systems of pressurised water reactors (PWRs) [Wang et al. 2013] where nickel-base filler metal DMWs have been found to suffer from the stress corrosion cracking susceptibility in primary water conditions (PWSCC) [Hänninen et al. 2007a, 2007b, Karlsen & Pakarinen 2009, Hänninen et al. 2009, 2011]. The operating experience of major NPP pressure boundary components has recently shown [Hänninen et al. 2007a, 2007b, 2011] that DMW joints can markedly affect the plant availability and safety because of increased incidences of EAC and PWSCC of Alloy 600 and corresponding nickel-base weld metals, such as Alloys 182/82. All-weld metals of Alloy 182 and 82 have been found clearly more susceptible to EAC than all-weld metals of Alloy 152 and 52 which hardly show any crack initiation susceptibility in e.g. doped steam conditions [Karlsen & Pakarinen 2009, Hänninen et al. 2009, 2011]. The selection of new welding methods and materials relies mainly on laboratory results and short-term service experience. Their long-term behaviour and performance in the plant has still to be demonstrated [Hänninen et al. 2011].

In modern PWR, the transition from filler metals Alloys 82 and 182 to Alloys 52 and 152 with higher Cr contents and the new weld design using narrow-gap welding (NGW) technique are made to ensure the structural integrity of the welds. However, metallurgical changes still occur at the interface and transition region, especially due to post-weld heat treatment (PWHT), leading to concerns about the long-time behavior of the welds. Long-term mechanical behavior of NGWs and their susceptibility to ageing mechanisms have not been fully characterized yet. Changes in the weld microstructure may cause non-uniform mechanical properties through the thickness direction, depending on both dendrite alignment and residual stress distribution in the weld [Jang et al. 2010].

Alloy 52 weld metal has an FCC austenitic solid solution structure. It is designed to take into solution Ni, Cu, Cr, and Fe upon dilution from base metals, hence keeping a normal single-phase dendritic structure. Typically, a planar growth zone without precipitates appears at the weld interface, followed by a cellular dendritic zone with precipitates in the interdendritic regions. Further in the weld metal, a columnar dendritic zone results from solidification along preferential growth directions and temperature gradients [Alexandrov et al. 2013]. Compared to Alloy 82, it contains less niobium and more titanium, and it has a smaller solidification temperature range [Naffakh et al. 2009]. The main consequence is a coarser dendritic structure with less Nb-riched precipitates. The precipitates are mostly TiN and TiC, distributed in the interdendritic regions and at the GBs. Their number is lower than in the Alloy 82 weld metal, although the precipitation is increased with PWHT [Soares et al. 2007]. Alloy 52 hardness is therefore in average lower than that of the Alloy 82 welds [Kuo & Lee 2002]. In addition, it has a lower tensile strength [Lee & Jeng 2001]. Due to its higher Cr content, Alloy 52 exhibits superior corrosion resistance than Alloy 82. However, it can contain dynamically recrystallized zones which may decrease SCC resistance [Morra et al. 2011].

Dissimilar metal welds (DMWs) are usually divided into two types: (i) joining of two different metals, usually with the addition of a different filler metal, and (ii) joining matching composition metals (i.e. similar metals) with different filler metal [Karlsson 1995]. The structure of a typical type (i) DMW can be divided into the following regions shown in Figure 1: (1) the heat-affected zones (HAZ) of the base metals A and B, (2) the fusion boundary area and the fusion line between the weld metal and base metals A and B, and (3) the weld metal. The composition of the weld metal is affected by the base metals, the filler metal, and the welding procedure and, thus, can have a highly varying composition. The chemical composition of the weld metal, and the chemistry and microstructural features of the near interface areas are the most important parts of a successful DMW. Therefore, the selection of the filler metal and control of the dilution are the two most important factors to take into account when manufacturing a DMW [Lippold & Kotecki 2005].

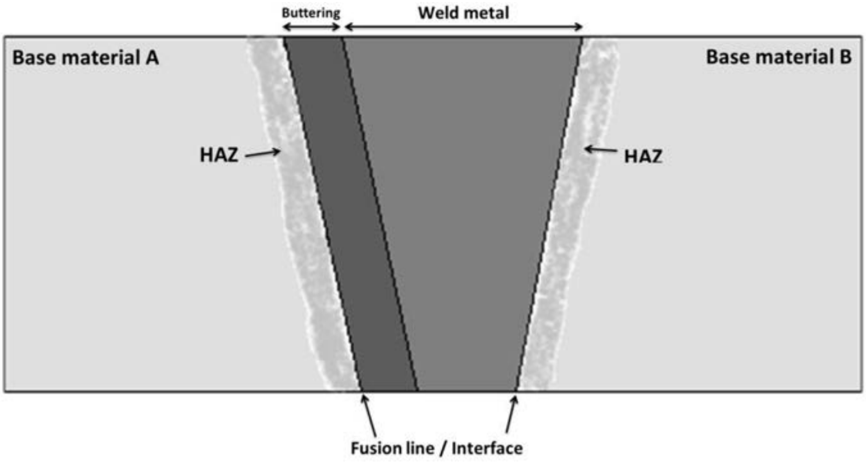

Figure 1. Different structural regions of type (i) DMW.

Narrow-gap welding (NGW) technique is used to join together thick plate materials separated by a very narrow groove. NGW is more economical than the conventional V-grooved weld as it requires less welding consumable, shorter welding times, and reduces the volume of inspection (shown in Figure 2). In addition, the reduced amount of weld metal and lower heat input leads to less shrinkage, distortion and smaller residual stresses/strains. NG-GTAW can be used in special applications with stainless steels and Ni-base alloys for critical structures, such as the DMWs between the RPV LAS and its stainless steel safe-end in new PWR designs in which the quality and the performance of the welded joint are key factors.

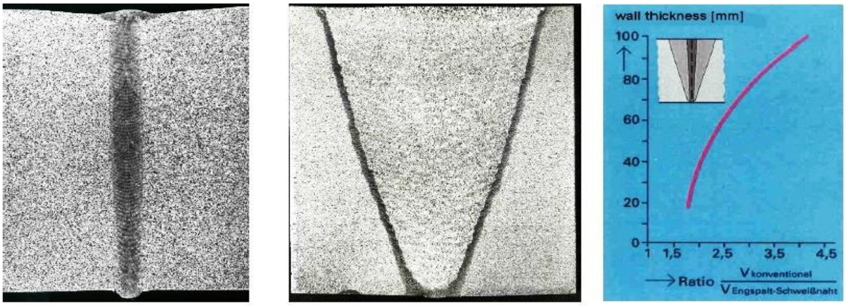

Narrow Gap Welding
material: stainless steel
thickness: 90mm

Conventional Weld
material: carbon steel
thickness: 90mm

Reduction of weld volume using GTA Narrow Gap Welding

Figure 2. Reduction of the weld volume using GTA-NGW technique compared to a conventional V-grooved weld. The reduction of weld volume e.g. for 90 mm wall thickness is factor of ~4. [Engelhard et al. 2000.]

The microstructure of a DMW has some unique characteristics. Firstly, the composition varies from the composition of the base material to the composition of the weld metal across the fusion line. This leads to abrupt changes in the microstructure, mechanical properties and corrosion resistance across the fusion area. Secondly, in DMWs, there is a possibility for a change in crystal structure within the weld's microstructure. This change exists, for example, in the dissimilar metal joints between ferritic steel and austenitic stainless steel. Ferritic and austenitic steels have different crystal structures and this metallurgical mismatch affects the mechanical properties across the fusion line. The metallurgical mismatch can result in the formation of Type II boundary within the weld metal that parallels to the fusion boundary typically less than 100 µm in the weld metal. The third characteristic of DMWs is the formation of residual stresses caused by, in addition to the weld shrinkage, the unequal values of thermal expansion coefficients. These characteristics result in a steep gradient of microstructural features and mechanical properties across the fusion line [Hou et al. 2010]. An example image of typical microstructural characteristics of a fusion boundary area of a DMW is presented in Figure 3 [Sireesha et al. 2001].

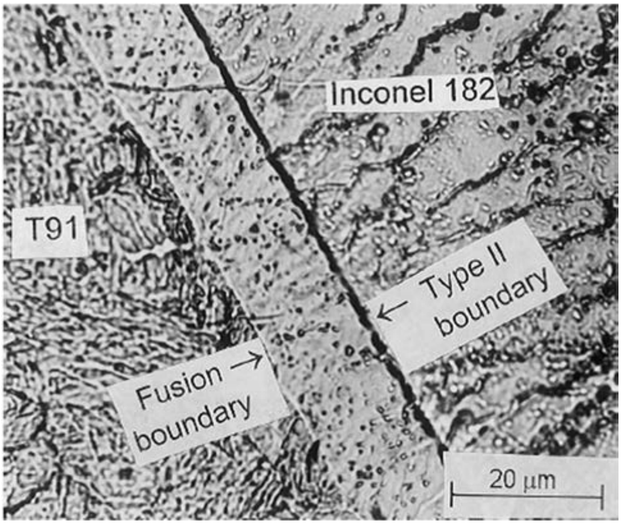

Figure 3. Microstructure of Inconel 182/T91 interface [Sireesha et al. 2001].

Cracking associated with DMWs has been a constant problem and may occur near the fusion boundary either along the martensitic boundary adjacent to the fusion boundary or along the Type II boundary [Nelson et al. 1999]. One of the driving forces of the current mismatch research has been the insight that the fracture toughness and the strength properties of the different zones interact with each other during the progress of the final failure in the case of external loading. This means that measuring the toughness properties alone is not enough to describe the entire failure behavior of a heterogeneous system, e.g., DMW, if the mechanical properties of the different zones are not known. The traditional concept of strength mismatch research in welds focuses on the different strength levels of the weld metal and the base metal. Over- and/or undermatching zones can also form in a weld as a result of hardening of the coarse-grained zone of the HAZ, softening of the HAZ, and as a result of welding a strain or a precipitation hardening material [Nevasmaa & Laukkanen 2005].

The strength mismatch factor M is defined in the Brite Euram structural integrity assessment procedure for European industry (SINTAP) as the ratio of the yield strength of the weld metal σ_{WM} to that of the base metal σ_{BM}:

$$M = \frac{\sigma_{WM}}{\sigma_{BM}} \tag{1}$$

The strength mismatch is considered minimal if the value of M is between 0.9 and 1.1 [Kim et al. 2000]. Traditionally, overmatching the weld metal has been used as a way to secure the weld metal against plastic strains and existing flaws. As a result of overmatching, it is less likely that the defects and cracks within the weld metal will develop into fractures, since overmatching the weld improves the tensile properties and the stress-strain behavior of the weld metal compared to the base metal [Moran & Shih 1998]. Overmatching weld metal with a mismatch factor (M) of 1.2 to 1.3 and with sufficient fracture toughness, benefits many low- and medium-strength steel welds [Bauschke & Koçak 1997]. Another research approach concerning strength mismatching in welds has been high-strength steel applications. It is a common custom to use a weld metal with a global yield strength overmatch of about 1.1. Stronger weld metal tends to direct eventual yielding to the base metal where the toughness is usually better. The problem is, however, that as the base metal strength levels have continuously increased, it will be more and more difficult to obtain the required combination of high tensile properties and sufficiently high toughness for the weld metal [Thaulow et al. 1999b].

If the mismatched situation is considered from a fracture mechanical point of view, undermatching weld can be considered beneficial for high-strength steels due to the smaller probability of cleavage fracture in undermatching welds compared to overmatching ones [Moran & Shih 1998]. This recommendation, however, is mainly theoretical. It has been shown in both experimental and numerical studies that the apparent fracture behavior and toughness of the weld metal or the HAZ can change significantly via the change of the strength of the adjacent material or zone [Nevasmaa & Laukkanen 2005, Thaulow et al. 1999a].

From a fracture mechanical point of view, at least three different directions can be identified within the research of mismatched welds. The first direction aims to clarify the effect of strength mismatch on the present fracture mechanics testing standards. The aim has been to define geometrical limitations with respect to the ligament size and the width of the weld with the focus of the research being on the exact crack location. It has been shown that the mismatch effect is negligible if some restrictions are fulfilled, e.g. an under-matched zone width compared to the thickness of the plate. The second direction of research focuses on a brittle fracture that initiates from cracks at the fusion line. This special case of cracking takes place at the interface of bi-metallic welds that are under external stress. This direction of research has concentrated on determining relevant experimental characterization procedures with appropriate post-test metallography, as well as in numerical solutions for the crack tip constraint. The third direction of research concentrates on ductile fracture behavior by applying limit load analysis and by evaluating the applicability of existing failure assessment diagrams (FADs) to mismatching welds [Nevasmaa & Laukkanen 2005, Thaulow et al. 1999a].

The determination of relevant fracture toughness properties for the various microstructural zones of DMW requires accurate positioning of the pre-fatigued crack in order to sample and hit the desired microstructure. This can be very difficult because of the curvature of the fusion boundary, as well as of the tendency for sudden crack path deflection towards another microstructural region after an inherently ductile initiation event. Obtaining relevant zone-specific strength and toughness based metal properties experimentally hence requires the use of miniature or small-size specimen techniques. Earlier work have shown [Nevasmaa et al. 1999a, 2000, Faidy et al. 2004, Keinänen et al. 2003, Laukkanen et al. 2001] that even in the case of essentially ductile fracture behaviour, the recorded fracture resistance curve can vary a lot depending on the true position of the pre-fatigued crack and the subsequent crack growth path within the DMW. Among the different weld regions, the fusion boundary/near interface zone (NIZ) tends to exhibit the lowest toughness in terms of ductile initiation and tearing resistance. Careful and detailed post-test sectioning metallography and specimen fractography are hence an absolute necessity to identify the actual crack initiation site and propagation path in order to relate the obtained fracture toughness value to the correct weld microstructural zone.

For the moment, no standards are available to assess the structural integrity of DMW components. Moreover, there are no standards for materials testing of DMWs either. Ensuring safe service of a DMW component therefore requires complete strength and fracture toughness based information from all microstructural zones of a DMW. Their true stress-strain behaviour and local fracture resistance and crack growth behaviour should be experimentally investigated and underlying characteristics understood.

1.1 Materials used in dissimilar metal mock-up welds

Base and filler metals used in dissimilar metal mock-up welds and their chemical compositions according to certified material test report (CMTR) analyses are presented in Table 1.

Table 1. Base and filler metals and their chemical compositions used in dissimilar metal mock-up welds according to CMTR analyses.

Base metals	**C**	**Si**	**Mn**	**P**	**S**	**Cr**	**Ni**	**Mo**	**Nb**	**N**	**Ti**	**Fe**	**Al**	**Co**	**Cu**
SA508 (Grade 2)	0.21	0.17	0.78	0.002	0.009	0.45	0.85	0.62		0.014	0.002		0.016	<0.003	0.06
AISI 304	0.019	0.4	1.77	0.03	0.001	18.16	8.07			0.05					
AISI 316L	0.023	0.53	1.29	0.031	0.002	17	10.1	2.04		0.04					
Filer metals															
E 309Mo-17 (electrode OK 67.70)	0.01	0.76	0.6	0.017	0.013	22.6	13	2.7							0.06
E 308L-17 (electrode OK 61.30)	0.03	0.75	0.7	0.019	0.01	19.3	10	0.12							0.08
AISI 309L (OK Band 11.65)	0.012	0.33	1.8	0.014	0.001	23.8	13.2	0.1		0.06					0.05
AISI 308L (OK Band 11.61)	0.007	0.37	1.9	0.013	0.001	20.3	10.3	0.1		0.04					0.05
Alloy 82 (OK Tigrod 19.85)	0.039	0.03	2.98	0.001	0.004	19.94	72.6		Nb+Ta 2.47		0.34			0.01	0.01
Alloy 182 (electrode OK 92.26)	0.03	0.7	5.9	0.01	0.006	16	69		1.7		0.1	5.6			< 0.01
Alloy 52 (Special Metals Inconel 52 welding wire)	0.03	0.13	0.24	<0.001	<0.001	29.2	59.28	0.03	Nb+Ta <0.02		0.51	9.8	0.72	0.009	0.04

Three different base metals were used in weld mock-ups: SA508 (Grade 2) heat-treated reactor pressure vessel steel provided by Uddcomb and AISI 304 and AISI 316L stainless steel plates provided by Outokumpu Oyj.

Different filler metals were used for welding the cladding, the buttering and the joint between pressure vessel steel and stainless steel.

- E 309Mo-17 (electrode OK 67.70) and E 308L-17 (electrode OK 61.30) welding electrodes provided by ESAB company were used for shielded metal arc welded (SMAW) cladding of BWR mock-up.
    - OK 67.70 is an over-alloyed stainless-steel electrode for use as a buttering layer when welding acid resistant clad steels and stainless steels to other types of steel.
    - OK 61.30 is an extra-low carbon electrode for welding stabilised stainless steels of similar composition, except when the full creep resistance of the base metal is to be met.
- AISI 309L (OK Band 11.65) and AISI 308L (OK Band 11.61) welding strips provided by ESAB company were used for submerged arc welded (SAW) claddings of BWR and Alloy 52 NG mock-ups.

  - OK Band 11.65 is a stainless welding strip designed for surfacing using the submerged arc welding process. Together with OK Flux 10.05 it produces a 309L type of weld deposit.
  - OK Band 11.61 is a stainless welding strip designed for surfacing using the submerged arc welding process. Together with OK Flux 10.05 it produces a 308L type of weld deposit.
- Alloy 82 (OK Tigrod 19.85) provided by ESAB company was used for for gas tungsten arc welded (GTAW) root passes of BWR mock-up.
  - OK Tigrod 19.85 is nickel-based, corrosion- and heat-resistant, 20% Cr, 3% Mo, 2.5% Nb electrode for the GTAW welding of high-alloyed steel, heat-resistant steel, corrosion-resistant steel, 9% Ni and similar steels with high notch toughness at low temperatures. It is also suitable for joining dissimilar metals of the type mentioned above.
- Alloy 182 (electrode OK 92.26) was used for for SMAW welded buttering and filling passes of BWR mock-up.
  - OK 92.26 A nickel-based electrode for welding nickel alloys such as Inconel 600 and similar Inconel alloys, cryogenic steels, martensitic to austenitic steels, dissimilar steels, heat-resistant steels and castings with limited weldability.
- Alloy 52 (Inconel 52 welding wire) provided by Special Metals Welding Products Company was used for GTAW welding of Alloy 52 narrow-gap mock-up joint.

2. Boiling water reactor (BWR) safe-end mock-up

A characteristic feature of dissimilar metal weld (DMW) is the metallurgical and material property mismatch resulting from a steep gradient of microstructures with significantly different strength and toughness properties. This mismatch inevitably affects the entire failure behaviour of DMWs under external operational loads, not only from crack initiation standpoint, but especially regarding the development of crack driving force accentuating crack path deviation and subsequent crack growth. The determination of relevant fracture toughness properties for all the different microstructural regions of the DMW is of utmost importance for successful structural integrity and lifetime analyses. Dissimilar metal welds (DMW) can be found in joints where two different structural materials meet, e.g., the joint between the pressure vessel made of ferritic steel and the austenitic stainless steel piping in BWR nuclear power plant. DMWs have been found to be susceptible to premature failures; the environment and the mismatch in material properties between the two joined materials are two of the main reasons for this.

2.1 Manufacturing of the BWR mock-up

A weld mock-up representing the DMW in the safe-end of boiling water reactor (BWR) was manufactured. The weld consists of SA 508 and AISI 304 base metals, an Alloy 182 buttering layer, and Alloy 82 and 182 weld metals. The dimensions and materials of the weld can be seen in Figure 4.

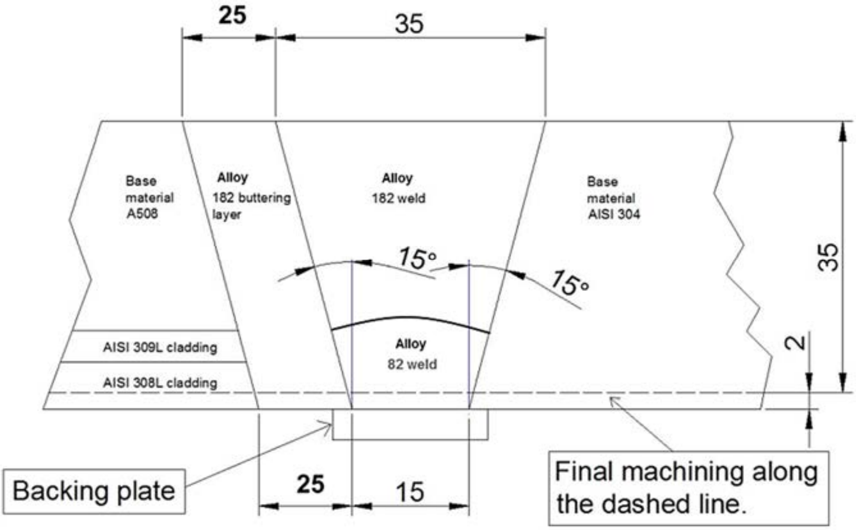

Figure 4. Schematic drawing of the BWR weld mock-up.

The manufacturing of the BWR mock-up was begun by submerged arc welding (SAW) the AISI 309L and 308L strip cladding layers onto a block of SA 508 steel. Beside the SAW cladding the last 50 mm of the cladding next to the groove was shielded metal arc welded (SMAW) (Figure 5). Pre-heat temperature was 150 °C and inter-pass temperature was max. 250 °C.

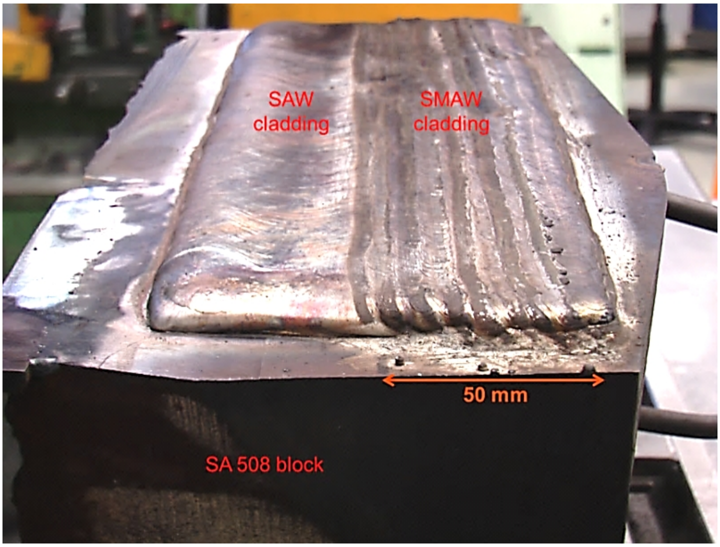

Figure 5. SAW and SMAW cladding of the SA 508 block.

The cladding surface was machined smooth and 45 mm thick slice including the cladding was cut from the SA 508 block. The cladding was post-weld heat treated at temperature of 605 ± 15 °C for 2 h. The cooling and heating rate during the heat treatment was max. 55 °C/h.

After this, the SA 508 base metal was prepared for the buttering weld; the edge of the groove was machined and a support plate was attached (Figure 6). The buttering was SMA welded in several layers using Alloy 182 filler metal up to the final thickness of 25 mm. The welding was made with the electrode perpendicular to (i.e. against) the groove face. Figure 7 displays the buttering layer being welded. The buttering was next machined to the angle of 15° and post-weld heat treated for 1 h at 575 °C. The cooling and heating rate was 30 °C/h. The SA 508 side and the AISI 304 plate were then welded together with Alloy 82 and 182 filler metals (Figure 8). The first 13 passes of the root were gas-tungsten arc welded (GTAW) with Alloy 82 and the rest was filled with SMAW using Alloy 182.

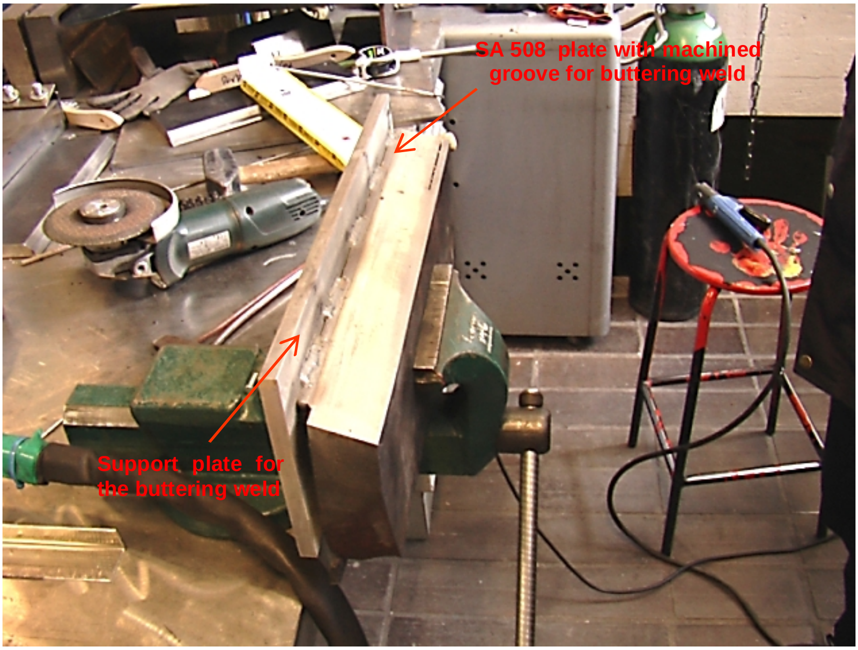

Figure 6. SA 508 plate prepared for the buttering weld.

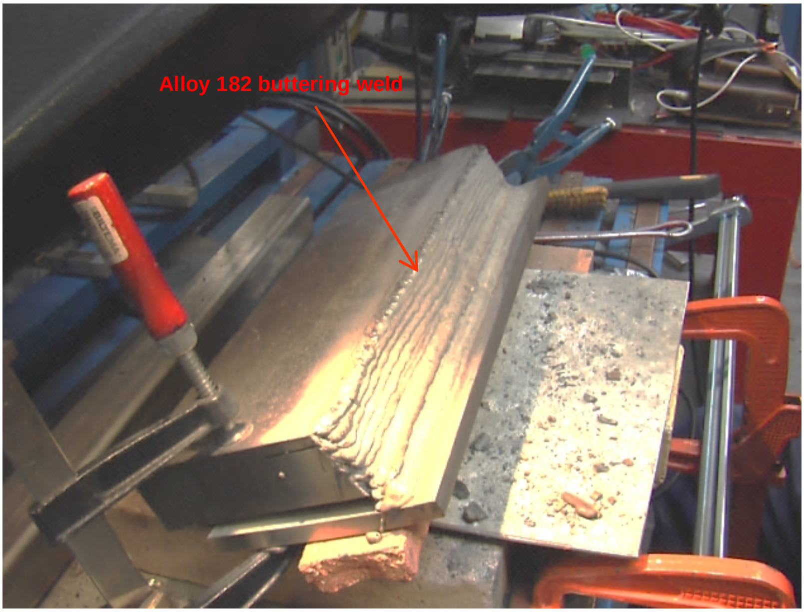

Figure 7. Welding of the buttering layer.

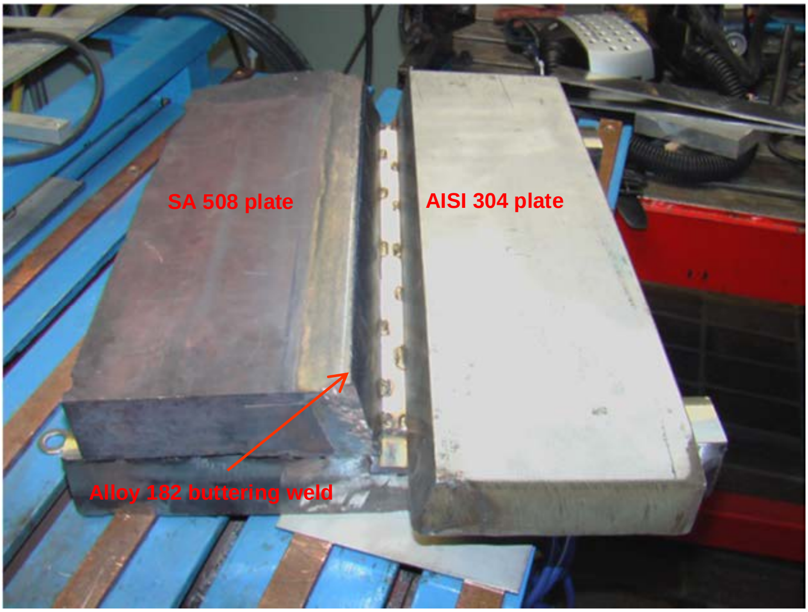

Figure 8. BWR safe end mock-up ready for the joint welding.

The welding parameters are shown in Table 2. The welding conditions and the build up are fully relevant to the actual component. Schematic drawing of the weld pass sequence is shown in Figure 9 and a cross-section micrograph of the completed weldment can be seen in Figure 10. Finally, both the upper and the bottom surface were machined smooth; consequently, the final thickness of the weld was 35 mm.

Table 2. BWR safe end mock-up welding parameters.

Submerged arc welding, strip cladding		**Shielded metal arc welding (SMAW), cladding**		
			Electrode diameter [mm]	Current [A]
Current [A]	630	1. Layer (309)	4	145
Voltage [V]	280	2. Layer (308)	3,2	115
Welding speed [cm/min]	14	3. Layer (308)	4	140
		4. Layer (308)	5	200

SMAW, buttering			**GTAW and SMAW, joint welding**		
	Electrode diameter [mm]	Current [A]		Wire / electrode diameter [mm]	Current [A]
1. Layer OK 92.26 (182)	4	120	Passes 1-13 OK Tigrod (82)	1,6	95
2. Layer OK 92.26 (182)	3,2	95	Passes 14-16 OK 92.26 (182)	2,5	55
3. Layer OK 92.26 (182)	4	125	Passes 17-19 OK 92.26 (182)	3,2	95
Filling layers OK 92.26 (182)	5	150	Passes 20-22 OK 92.26 (182)	4	125
			Passes 23-52 OK 92.26 (182)	5	150

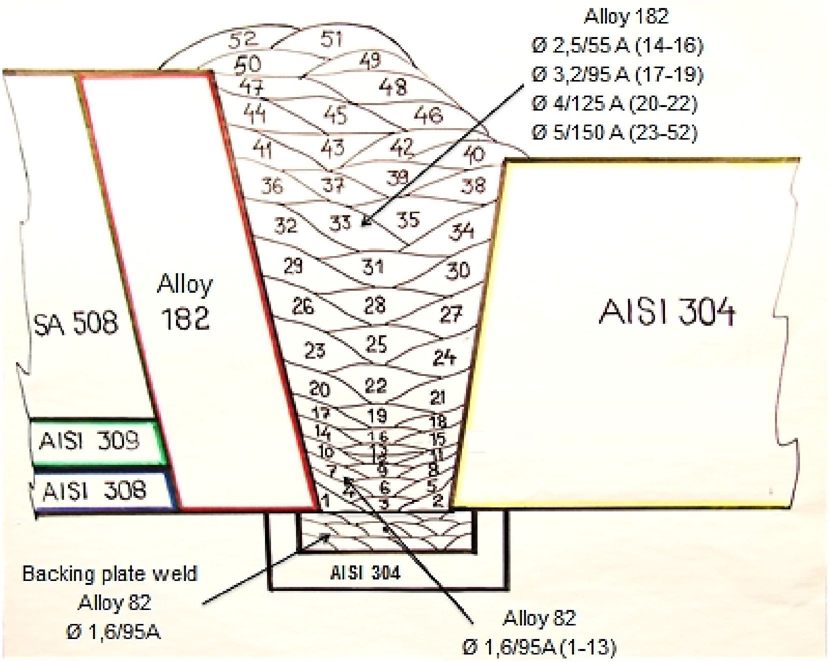

Figure 9. Schematic drawing of the weld pass sequence.

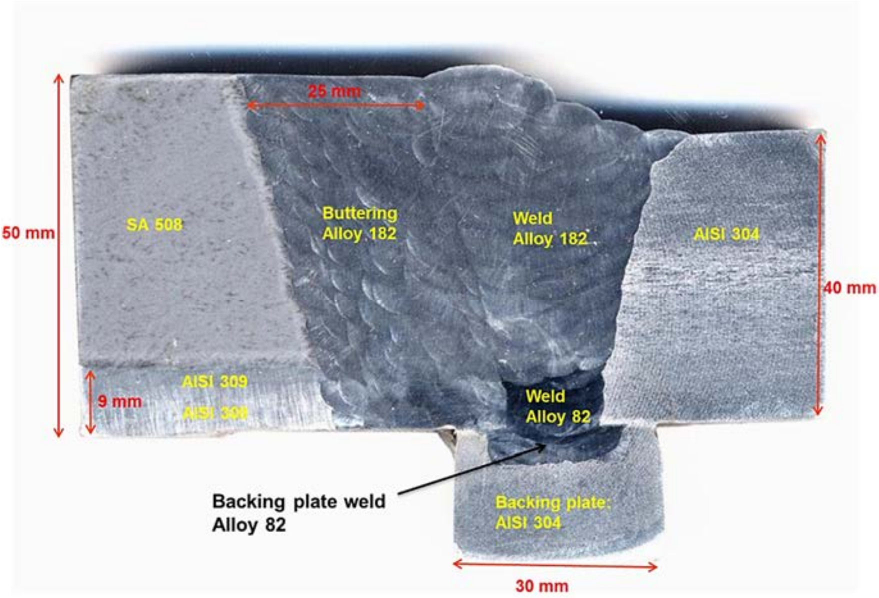

Figure 10. Cross-section macrograph of the BWR safe end mock-up DMW.

2.2 Microscopy

The microstructure of the weld mock-up was examined by optical and electron microscopy. Special attention was paid to the fusion line between SA 508 base metal and Alloy 182 buttering.

2.2.1 Optical microscopy

Figure 11 shows the different structural zones of the SA 508 HAZ. The HAZ consists of structural zones typical to low-alloy steel: grain coarsening, grain refining, and partial grain refining zone. The microstructure of the base metal is bainitic. Different magnification micrographs of the fusion line area between the SA 508 base metal and Alloy 182 buttering are shown in Figure 12. The base metal is over-etched due to the strong etching effect of Aqua Regia. The Type II boundary, marked with a black arrow in the images, was found at a distance of approximately 30 to 50 µm (depending on the location) from the fusion line in the buttering side. The Type II boundary was not completely continuous along the whole weld. The presence of a martensitic zone between the fusion line and the Type II boundary can be observed in Figure 13 (marked with a red arrow). This martensitic zone was not continuous along the fusion line and its thickness varied. The microstructure of the Alloy 182 buttering was dendritic, as can be seen in Figure 14.

Figures 13 and 14 show the fusion line area of the samples post-weld heat treated at 605 °C for 6 h and 24 h, respectively. No carbon-depleted zone on the SA 508 HAZ side of the fusion line was detected in either sample. The thickness of the precipitate-rich zone at the interface was not observed to be affected by the increase in the heat treatment time. The Type II boundary is marked with a black arrow and the precipitate-rich band with a red arrow in Figures 13 and 14.

Figure 11. Microstructure of the SA 508 HAZ.

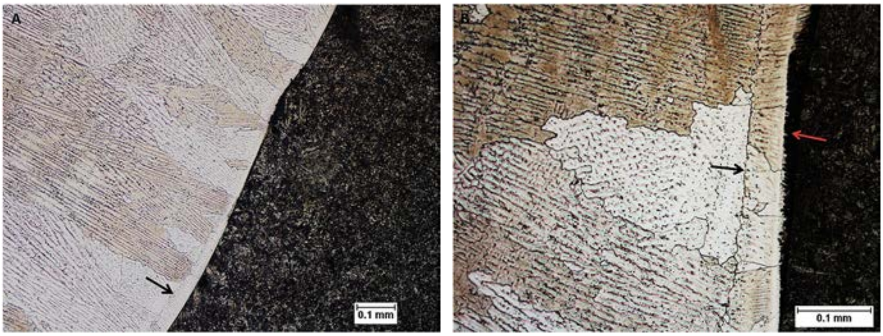

Figure 12. Micrographs of the fusion line area between the SA 508 base metal and Alloy 182 buttering. The Type II boundary is marked with an arrow in both pictures and the martensitic zone is marked with a red arrow in Figure B. The base metal is over-etched due to the strong etching effect of Aqua Regia.

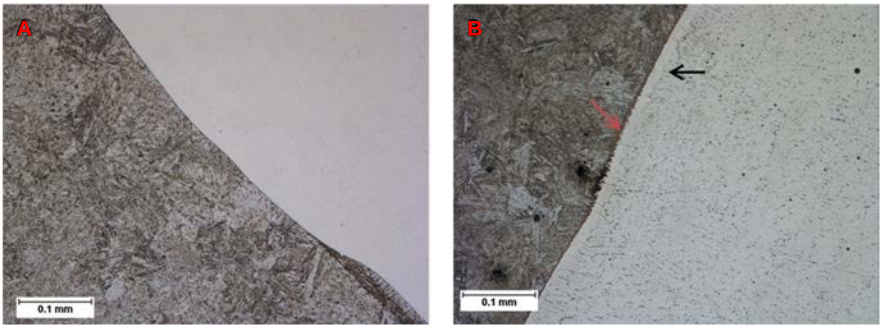

Figure 13. Micrographs of the fusion line (6 h, 605 °C). A) etched with Nital and B) with Aqua Regia.

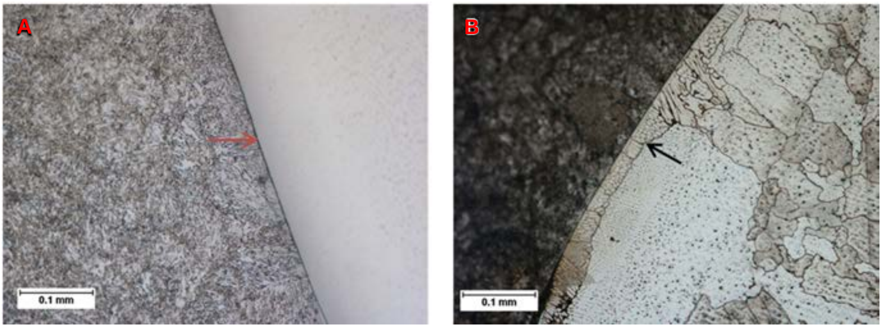

Figure 14. Micrographs of the fusion line (24 h, 605 °C). A) etched with Nital and B) with Aqua Regia.

2.2.2 Scanning electron microscopy (SEM)

Figure 15 shows SEM image of the fusion line between the SA 508 base metal and the Alloy 182 buttering layer. The black arrow in the image shows a continuous Type II boundary present in the SA 508 – Alloy 182 interface. The Type II boundary follows the fusion line in the weld metal side through the interface. The red arrow in the image presents a martensitic zone, which was found between the Type II boundary and the SA 508 – Alloy 182 interface. Higher magnification images of the fusion line are presented in Figure 16. The structure of the martensite band is marked with a red arrow and the Type II boundary can also be seen clearly and is marked with a black arrow in the picture. The fusion line area was found to be heterogeneous, in terms of the shape and geometry, existence of the Type II boundary, and martensite layer. The images presented here are examples of typically found structures in the fusion line.

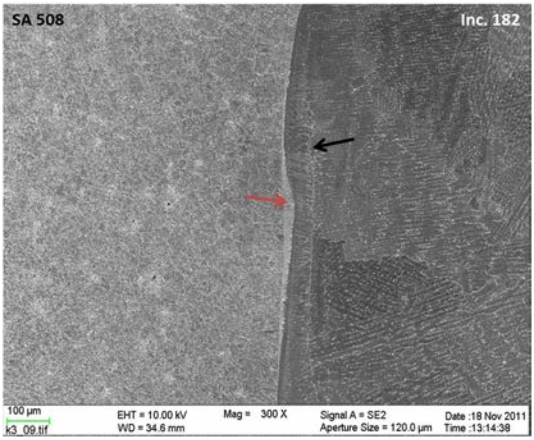

Figure 15. SEM image of SA 508 – Alloy 182 fusion line. The black arrow points at the Type II boundary and the red one at the martensitic layer.

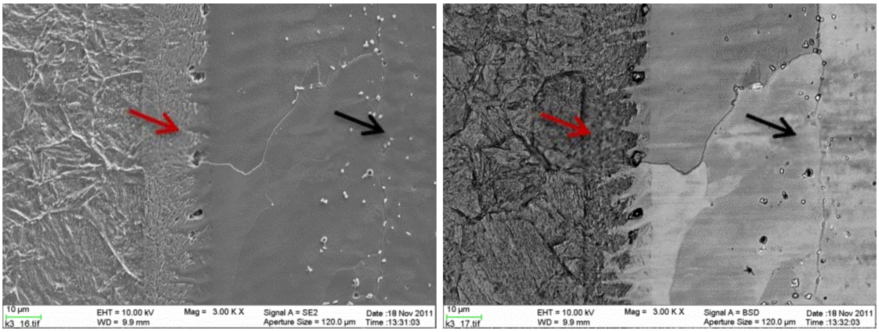

Figure 16. SEM images of SA 508 – Alloy 182 fusion line.

SEM images of the interface of the sample with PWHT of 24 h at 605 °C are presented in Figure 17. The magnification of the area between the fusion line and the Type II boundary shows the existence of titanium and niobium carbides, and manganese sulfides. The martensite layer and the Type II boundary can also be clearly identified from the images.

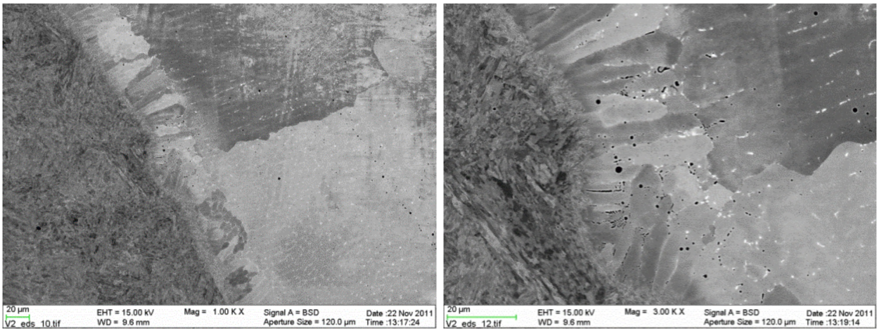

Figure 17. SEM images of fusion line of PWHT sample.

2.2.3 Electron backscattering diffraction (EBSD)

The microstructures of the SA 508 base metal and HAZ were studied with EBSD. EBSD maps in Figure 18 are taken from the corresponding places at the fusion line, at distances of 1.5 mm, 3.5 mm, and 4.5 mm from the fusion line. At the distance of 4.5 mm the material is not heat affected. The coarse-grained structure can be seen in the fusion line (FL) picture, the grain-refined structure in the picture taken from the distance of 1.5 mm from the fusion line, and the partial grain-refined area in the picture taken at the distance of 3.5 mm from the fusion line. The coloring of the inverse pole figure (IPF) maps is almost random. This indicates that there is no texture present. The green color in the local mis-orientation maps indicates local concentration of higher strain.

EBSD maps of a section of the fusion line, where both the martensitic layer (black arrow) and the Type II boundary (red arrow) are marked, are shown in Figure 19. Figure 19a is a pattern contrast map where the grain boundaries are black, Figure 19b shows a phase map where the fcc crystal structure is red and the bcc crystal structure is blue, and Figures 19c and d show the IPF map of the fusion line section. The prior austenite grains can be observed from the IPF map and the fusion line between the martensitic layer and the base metal can be detected from Figure 19b as a difference in orientation.

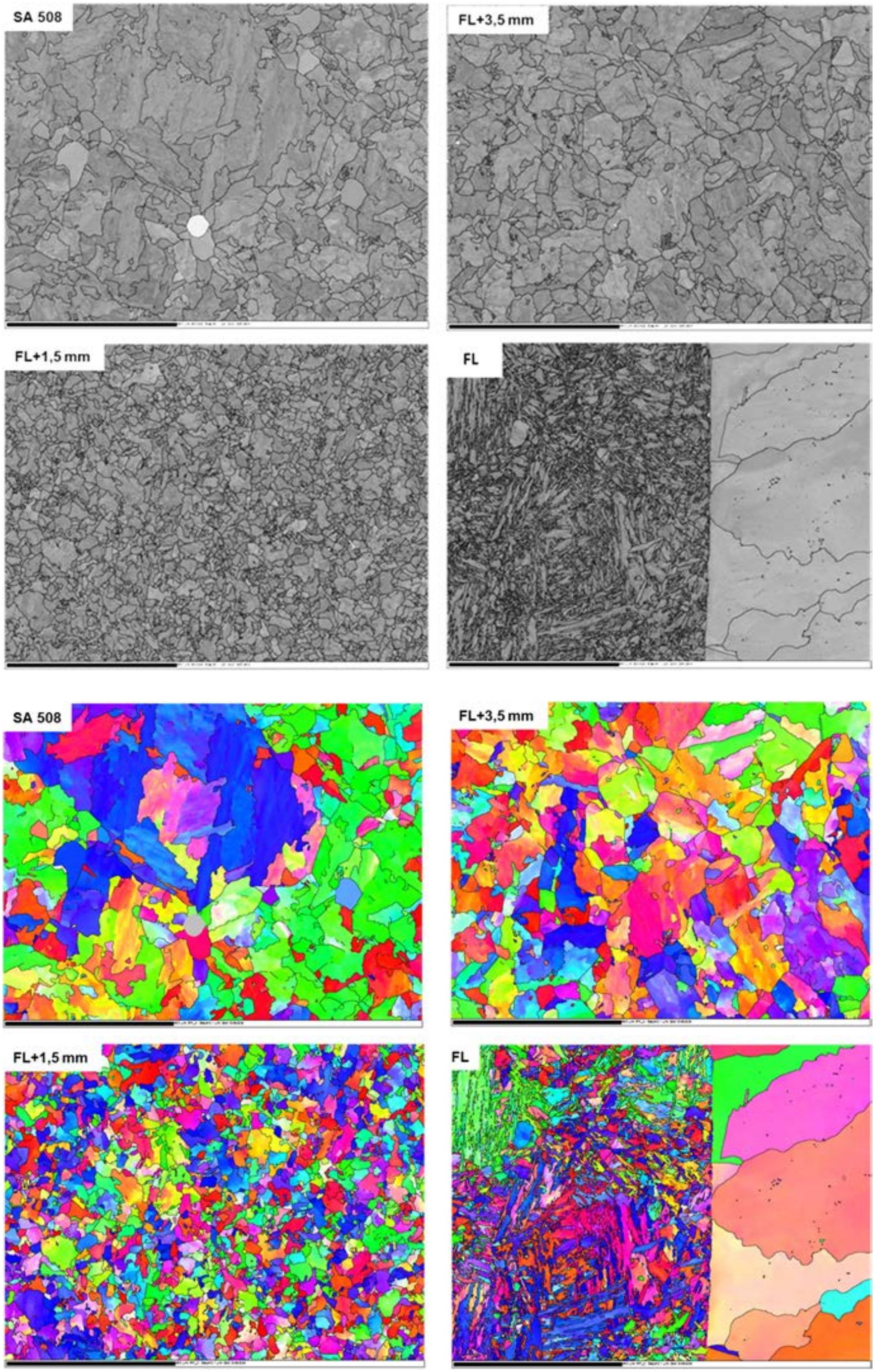
SA 508
FL+3,5 mm
FL+1,5 mm
FL
SA 508
FL+3,5 mm
FL+1,5 mm
FL

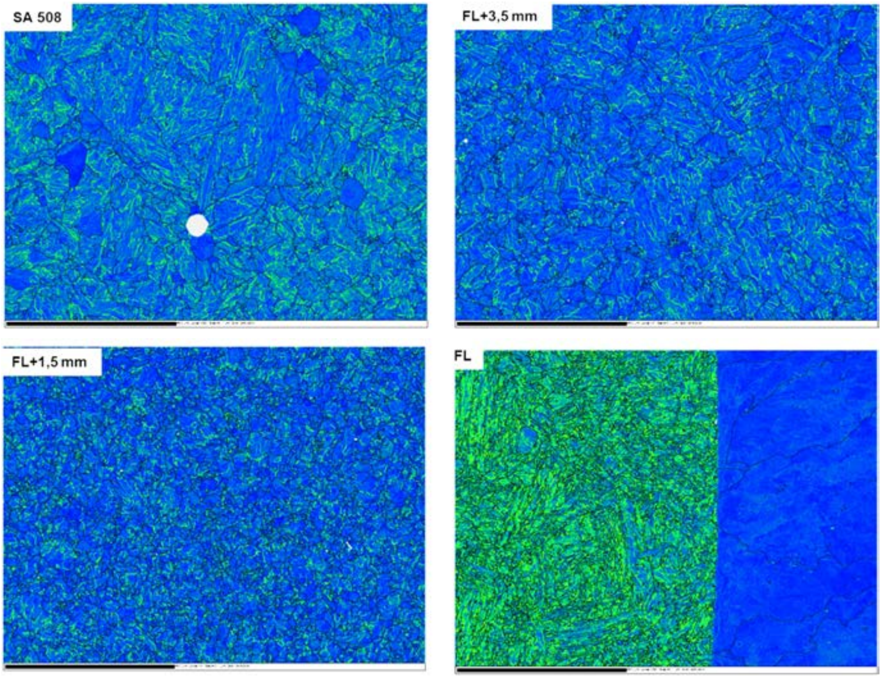

Figure 18. EBSD pattern contrast maps with grain boundaries marked with black lines, EBSD inverse pole figure (IPF) maps, and EBSD local mis-orientation maps of the SA 508 HAZ.

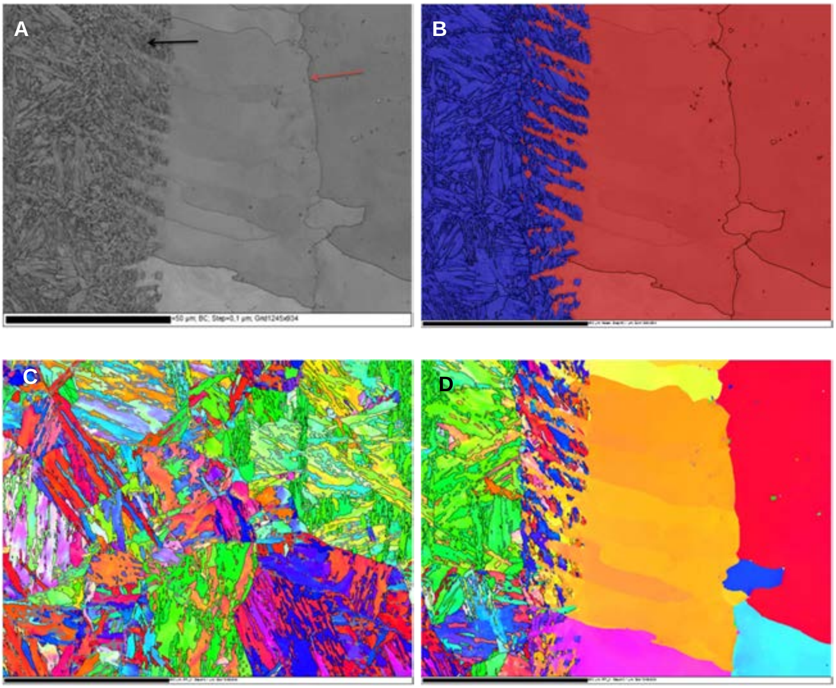

Figure 19. EBSD maps of a section of the fusion line.

2.2.4 Energy-dispersive X-ray spectroscopy (EDS)

EDS analyses were performed on the interface areas of as-welded sample and sample with PWHT at 605 °C for 24 h. Figure 20 shows EDS line scan across the fusion line of as-welded state DMW sample. The Fe content of the base metal is about 95 wt. %. The existence of the martensitic zone can be seen in the figure as an Fe concentration drop to about 85 wt. % and an increase in Ni concentration to about 10 wt. %. The dilution of the elements results in an increased amount of Fe and decreased amounts of Ni and Cr in the solidified weld metal next to the fusion line, compared to the nominal composition of the weld filler metal. At the Type II boundary, a decrease in the Fe concentration can be detected. After the Type II boundary, increasing Fe concentration can be observed.

Figure 21 shows the EDS map of the fusion line area of the as-welded state DMW sample. The composition change in the martensitic zone, compared to the base metal, can clearly be seen in the EDS maps of Fe and Ni. The higher C concentration of the SA 508 base metal reaches to the edge of the martensite zone. The Type II boundary seems to push some elements in front of it when it moves into the weld metal during solidification. This can be seen as a band of Nb carbides and a higher concentration of Si at the Type II boundary.

EDS line scans and maps corresponding to the ones of the as-welded state DMW sample were measured from the sample post-weld heat treated at 605 °C for 24 h. EDS line scans across the fusion line of the PWHT sample are presented in Figure 22. There were no clear differences in the distribution of the elements between the post-weld heat treated sample and the as-welded sample and the same phenomena can be observed from the results. A high concentration of sulfides and carbides can be seen in the EDS map of a section of the fusion line presented in Figure 23. As can be seen, black round Ti carbide precipitates are present in the fusion line of the PWHT sample. White Nb carbides and black Mn sulfides can also be seen on the dendrite boundaries of the PWHT DMW sample.

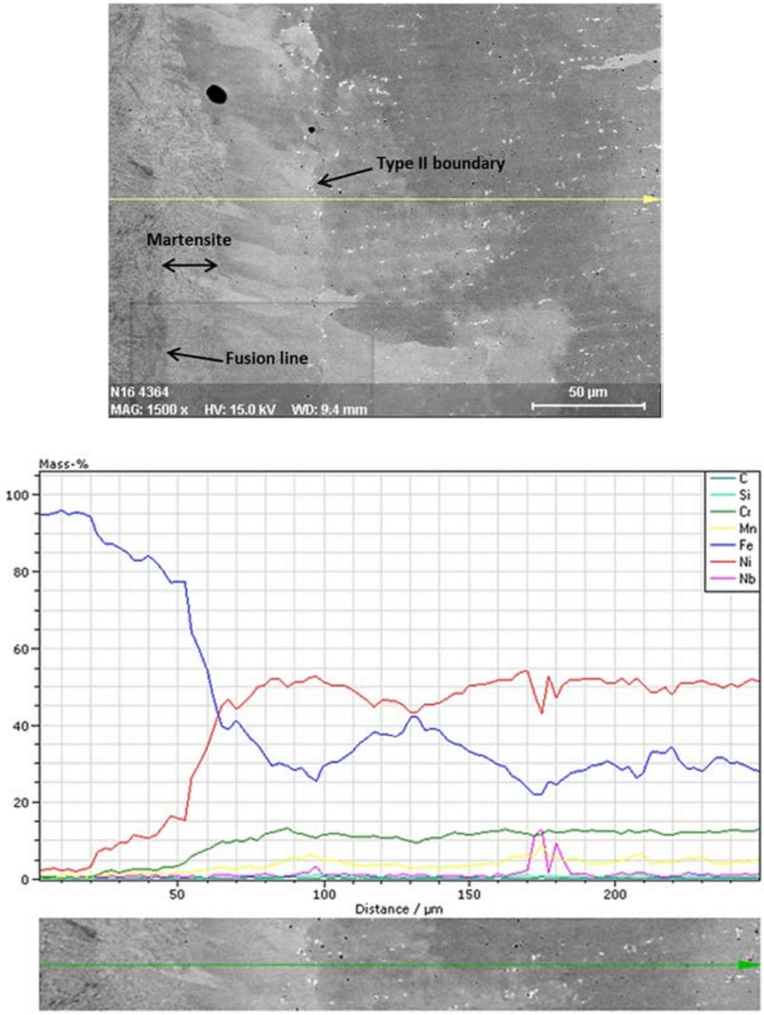

Figure 20. EDS line scan across the fusion line of the as-welded state DMW sample.

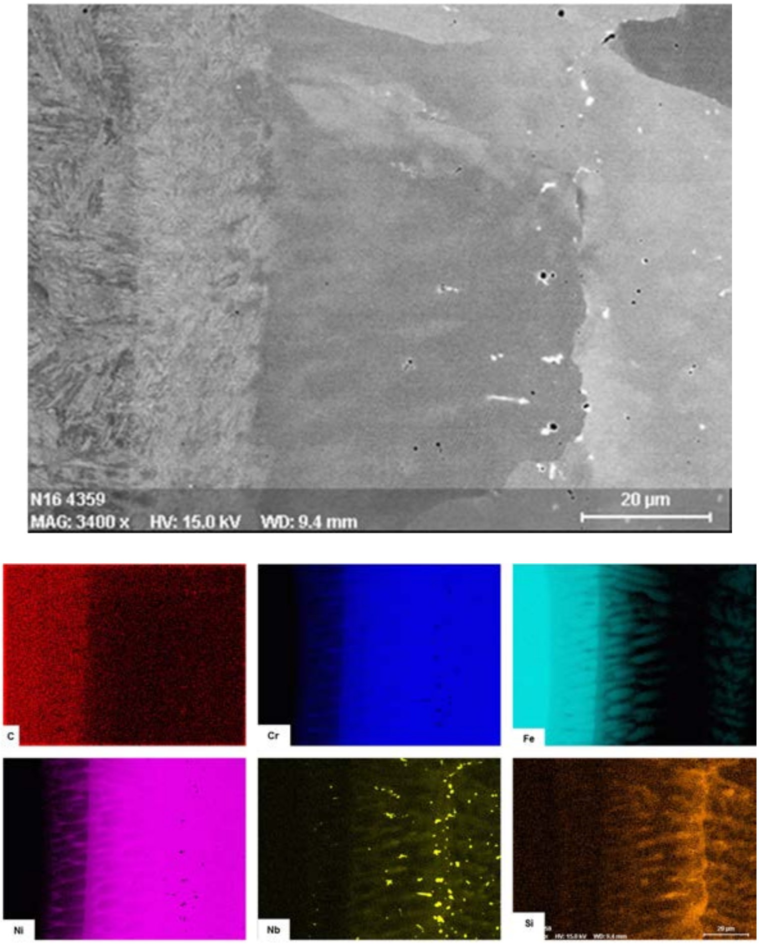

Figure 21. EDS map of the fusion line area of the as-welded state DMW sample.

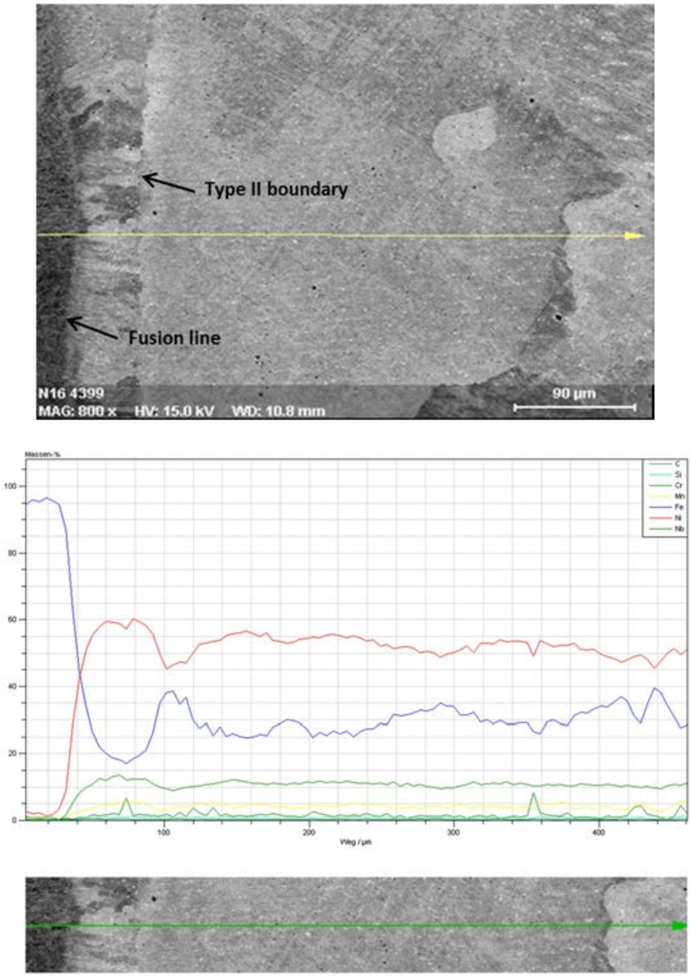

Figure 22. EDS line scans across the fusion line of the PWHT DMW sample.

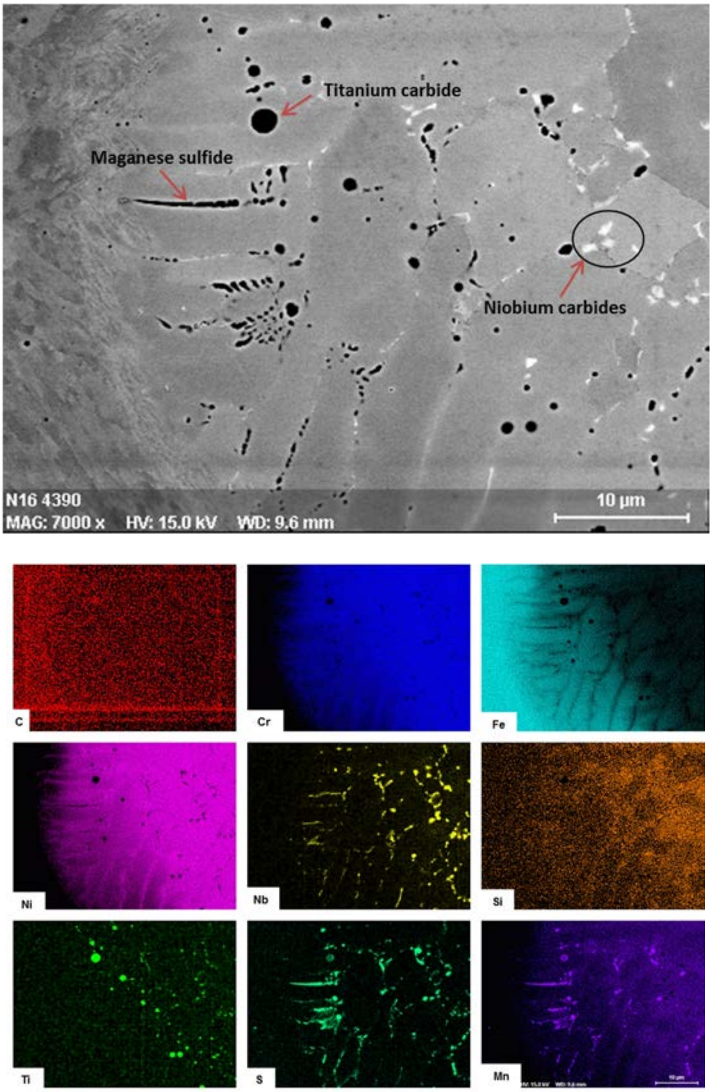

Figure 23. EDS maps of the fusion line area of the PWHT DMW sample.

2.3 Hardness measurements

The microhardness measurements focused on the SA 508 – Alloy 182 buttering interface area. All the results are presented so that the buttering layer is on the left hand side and the base metal on the right hand side of the figure. The fusion line is marked with a red line. The microhardness profiles of as-welded state DMW, measured in three lines from the buttering across the fusion line and the HAZ into the ferritic base metal, are presented in Figure 24. The distance between the indentations was 0.5 mm and the indentation weight was 300 g. The results show a steep increase in hardness with a maximum value of 381 $HV_{0.3}$ at the base metal side of the fusion line (i.e., the grain-coarsened HAZ). After about a 1.5 mm wide hard zone, the hardness decreases and evens out at a hardness value of 212 ± 12 $HV_{0.3}$ (average hardness of the indentations at the distance of 1.5–7 mm). The average hardness of the buttering layer at the distance of -6 mm to -1 mm was 226 ± 13 $HV_{0.3}$.

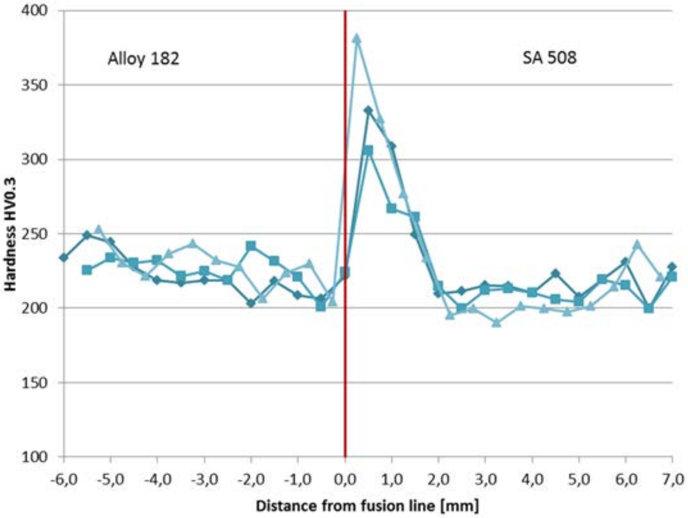

Figure 24. Microhardness profiles across the SA 508 – Alloy 182 fusion line of as-welded BWR-DMW sample.

The hardness profiles measured across the SA 508 – Alloy 182 buttering fusion line of the sample post-weld heat treated at 605 °C for 6 h are presented in Figure 25. The microhardness profile in the left picture extends from the weld metal across the HAZ into the base metal and the distance between the indentations was 0.2 mm, which is well over three times the diameter of the indentation mark. The indentation line in the right picture covers a shorter distance (0.45 mm) of the HAZ and the indentation marks are located closer to each other and the indentation load is smaller. Indentation lines with the corresponding parameters were also performed on a sample post-weld heat treated at 605 °C for 24 h and the results are presented in Figure 26. The heat treatment has decreased the highest hardness value measured from the HAZ by about 120 HV and, as can be seen, there is no detectable difference in the peak hardness values between the two different heat treatment times. The hardness profiles of the heat-treated samples are less sharp compared to those of the as-welded sample, which implies that the strength variation across the fusion line is more moderate after PWHT. The sharpness of the hardness profile of the sample with PWHT of 24 h is slightly milder compared to that of the sample with PWHT of 6 h, however, no significant difference in the shapes of the profiles can be attributed to the longer heat treatment time. The average hardnesses of the HAZ of the post-weld heat treated samples were approximately 250 $HV_{0.5}$, which is lower than the average hardness of the as-welded sample, which was around 350 $HV_{0.5}$. The peak hardness of 350 $HV_{0.1}$ in the lower picture of Figure 26 is significantly higher compared to peak hardness values of the other PWHT samples. That is likely due to the exact location of the indentation. The indentation mark was located exactly in the fusion line and, thus, is located partly in the narrow martensitic zone.

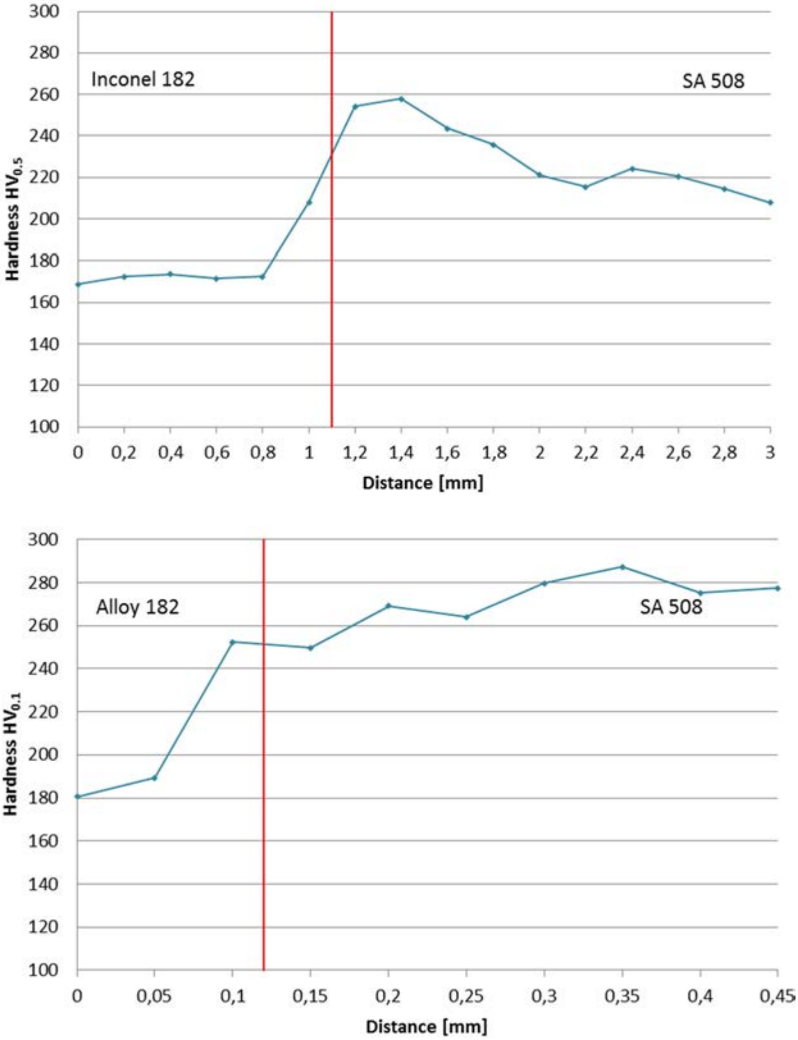

Figure 25. Microhardness profiles across the SA 508 – Alloy 182 fusion line of a sample with PWHT at 605 °C for 6 h.

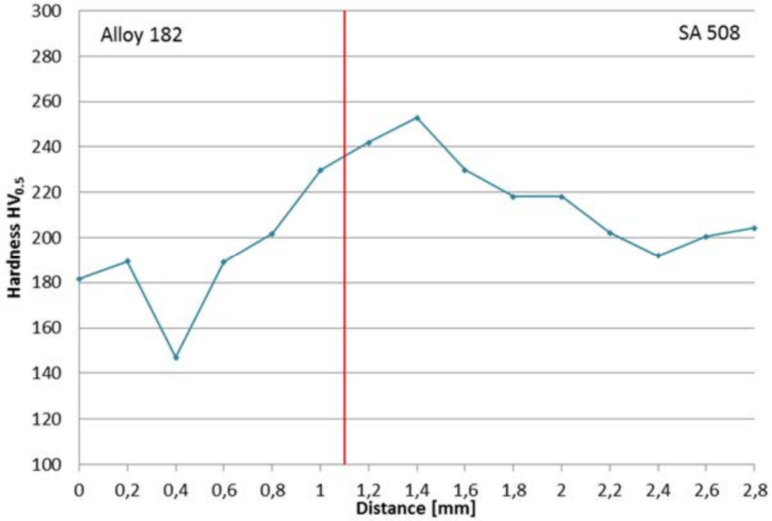

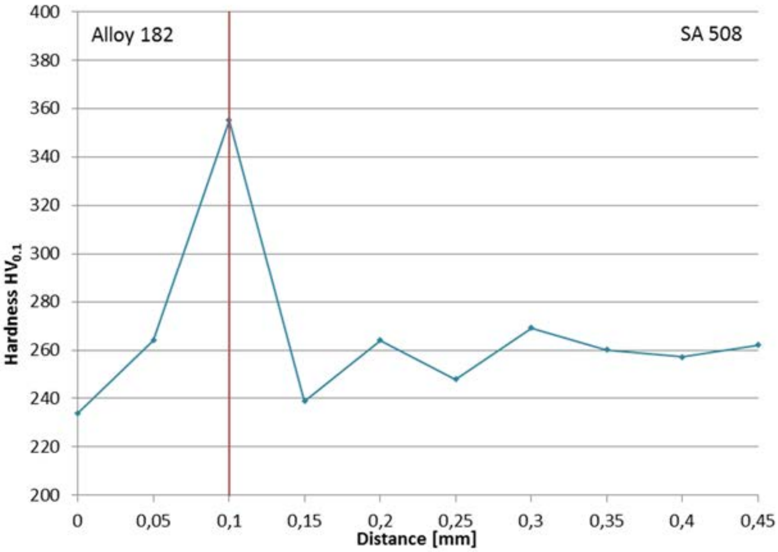

Figure 26. Microhardness profiles across the SA 508 – Alloy 182 fusion line of a sample with PWHT at 605 °C for 24 h.

The results of the nano-indentations from as-welded state sample, sample with PWHT at 605 °C for 6 h, and at 605 °C for 24 h are presented in Figures 27–29, respectively. The measurements were performed across a distance of 0.35 mm. The as-welded state sample shows a significant increase in the fusion line hardness of about 200 units from that of the buttering and SA 508 base metal. The highest individual hardness value was 440. The hardness peak at the SA 508 side of the fusion line is lower in the case of the sample heat treated for 6 h. The peak hardness of the 6 h sample is 373. No noticeable peak in the hardness can be detected in the sample with PWHT of 24 h. The average hardness of the Alloy 182 weld metal was slightly higher in the post-weld heat treated samples compared to the as-welded sample; as-welded: 271 ± 18, PWHT of 6 h: 291 ± 25, and PWHT of 24 h: 289 ± 19.

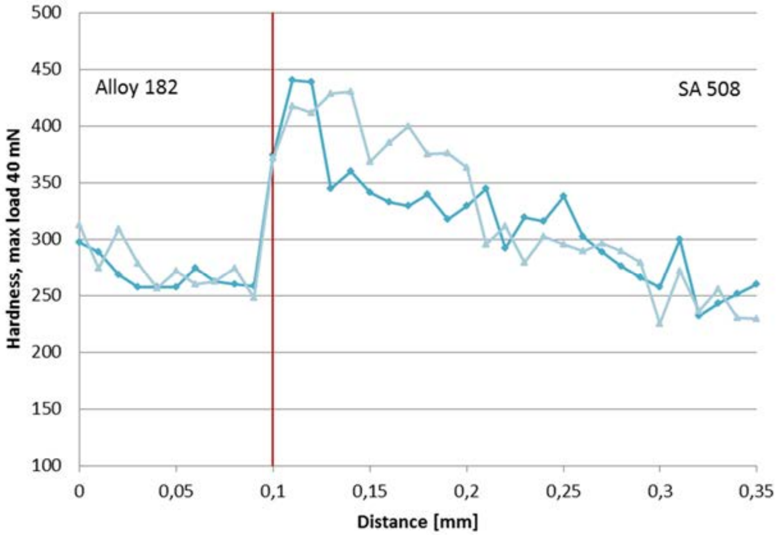

Figure 27. Nano-indentation profiles across the fusion line of as-welded BWR-DMW sample.

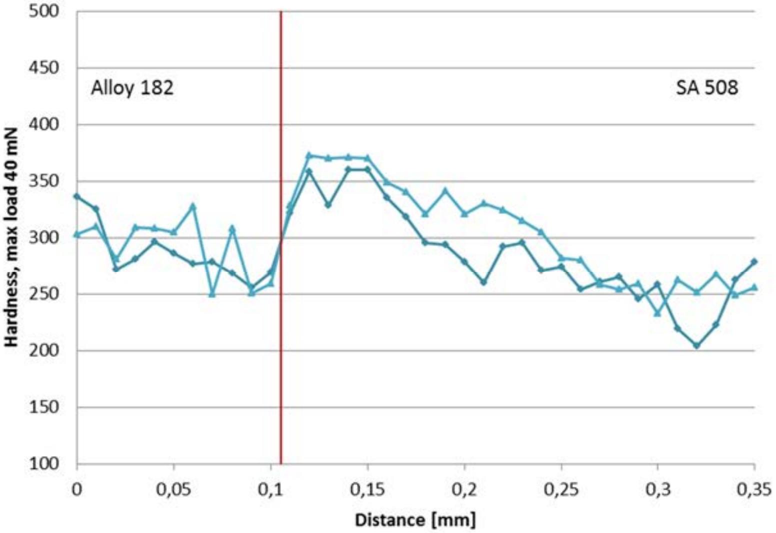

Figure 28. Nano-indentation profiles across the fusion line of a BWR-DMW sample with PWHT at 605 °C for 6 h.

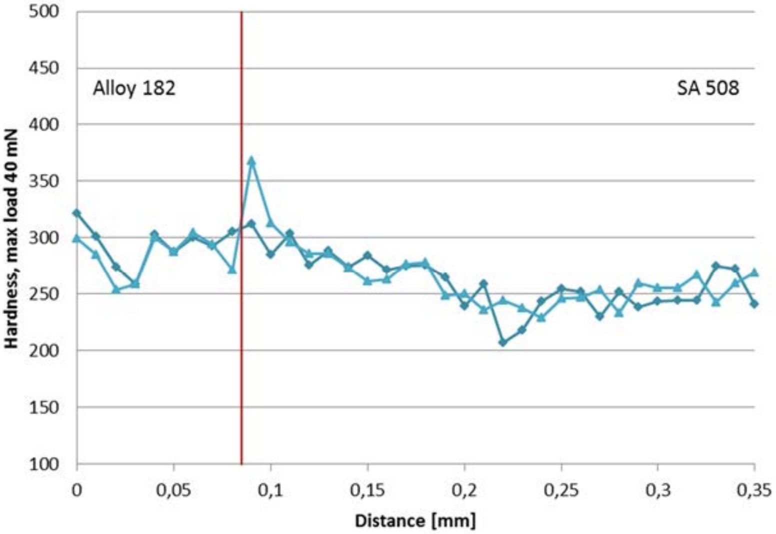

Figure 29. Nano-indentation profiles across the fusion line of a BWR-DMW sample with PWHT at 605 °C for 24 h.

2.4 Tensile testing

The tensile tests were performed using standard round-bar specimens with dimensions of ⌀8 x 105 mm, and in addition miniature-sized flat-bar specimens with dimensions of 1x2x20 mm. The direction of the testing specimens was parallel to the weld direction. The miniature specimens were used to examine the local mechanical properties from the narrow weld zones. The round-bar specimens were used to examine the tensile properties of the weld and base metals, and to validate the results of the miniature specimens. The mismatch state of the DMW was determined from the tensile test results.

Tensile tests on miniature-sized specimens are performed the same way as standard-sized specimens and they provide the same material characteristics. A disadvantage for the miniature specimens is that the small size restricts the sampled area and may not therefore represent the whole material; this may lead to case-dependent results. As a rule of thumb, the specimen thickness should be more than 4–6 times the grain size of the material in order to obtain reliable results on the tensile properties [Kim et al. 2009]. Small-sized tensile specimens have been employed in several studies that concern the mismatch state of DMW but there is no standard for the dimensions of these specimens; the employed dimensions vary from study to study. Most of the employed miniature specimen geometries have turned out to provide reliable results, while some results have been case dependent. According to previous studies, the smallest round bar specimens with a diameter of 1.5 mm and 2 mm have been found to be insufficient and hence unreliable for the determination of the local mechanical properties in a dissimilar metal weld. The thinnest flat-bar specimens (thickness 0.28 mm) have been found to underestimate the tensile test results of the weld metal. Flat-bar specimens with a thickness of 0.5 and 1.0 mm have been found to provide reliable results and hence proven appropriate to characterize the strength mismatch in the dissimilar metal welds [Hou et al. 2010, Nevasmaa & Laukkanen 2005, Kim et al. 2009, Nevasmaa et al. 1999b, Jang et al. 2008, Sireesha et al. 2000].

Standard-sized round bar tensile specimens were extracted with electric discharge machining (EDM) from the SA 508 base metal, buttering layer and the weld metal. The dimensions of the round bar specimens are in accordance to ASTM E 8/E 8M-08 and can be seen in Figure 30. Extraction locations of the round bar specimens can be seen in Figure 31.

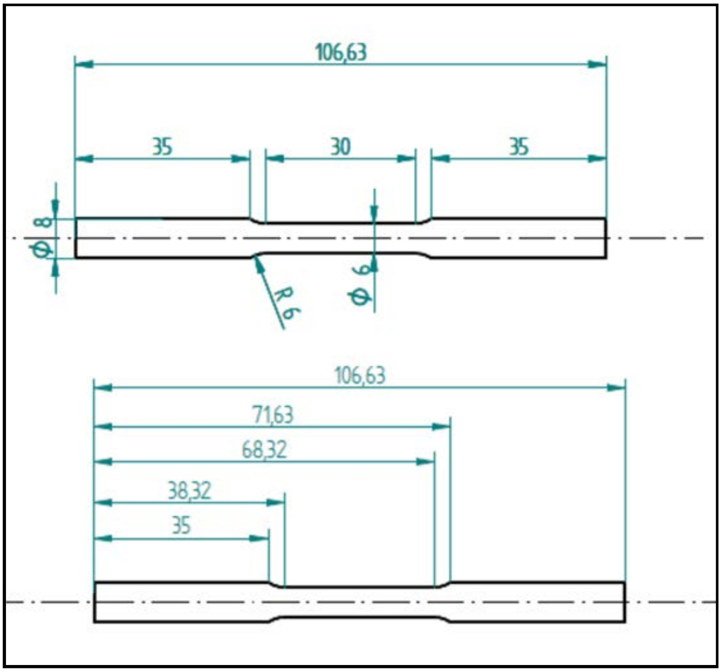

Figure 30. Dimensions of the round bar tensile testing specimens.

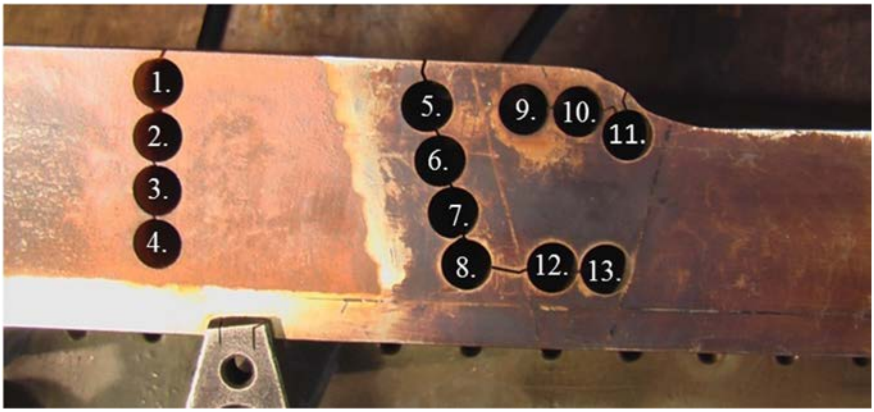

Figure 31. Extraction locations of the round bar specimens.

Miniature flat bar specimens were cut with electrical discharge machining (EDM) from five different locations of the weld; the SA 508 base metal, the fusion line, the fusion line + 1 mm into SA 508, the buttering, and the weld metal. The cross-section of the flat-bar specimens was 1 mm x 2 mm and the total length was 20 mm. The exact dimensions and illustration of the specimens can be seen in Figure 32.

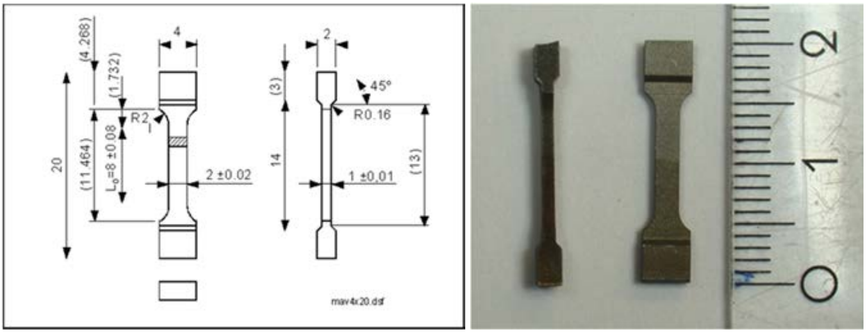

Figure 32. Technical drawing and picture of the miniature flat-bar specimens.

The tensile test results of the round-bar specimens are presented in Table 3 (average is calculated from four/five tested specimens on each location, see Figure 31) and the results of the miniature flat-bar specimens are presented in Table 4 (average is calculated from eight tested specimens on each location). The yield and ultimate tensile strengths of the fusion line and HAZ area are notably higher than those of the base metal. The deviation of the results of these areas is also much larger than that of the base metal. This can be explained by the narrow structural zones of the HAZ. The samples taken from the HAZ, for example, had clearly higher deviation in the ultimate tensile strength and the samples with higher ultimate tensile strength probably consisted of larger portion of the HAZ coarse-grained zone than the samples with lower ultimate tensile strength.

The post-weld heat treated samples had lower yield and ultimate tensile strength compared to the as-welded samples. This correlates well with the hardness measurements performed for the samples of corresponding states. The results of the transverse specimens, which consisted of the buttering layer and the HAZ, are also presented in Table 4. The results showed a small deviation and were around the same magnitude as the tensile test results of the buttering layer. This is because the specimens fractured in the buttering layer.

Table 3. Tensile test results of round-bar specimens.

Specimen		σ_y (MPa)	σ_U (MPa)	El (mm/mm)	E (GPa)
SA 508 base metal	Average	426	603	0.286	210
	STD	13	6	0.043	6
Alloy 182 buttering	Average	381	648	0.461	168
	STD	36	5	0.006	9
Alloy 182 weld metal	Average	366	628	0.467	163
	STD	27	14	0.024	5

Table 4. Tensile test results of miniature-sized flat-bar specimens.

Specimen		$\boldsymbol{\sigma}_y$ (MPa)	$\boldsymbol{\sigma}_U$ (MPa)	Ag (%)	A (%)
SA 508 base metal	Average	417	591	11.3	23.4
	STD	4	7	0.6	1.1
Alloy 182 buttering	Average	347	603	38.7	44.1
	STD	15	17	3.1	3.5
Alloy 182 weld metal	Average	375	605	34.7	41.1
	STD	7	10	3.8	4.0
FL, as-welded	Average	545	722	8.6	14.7
	STD	157	100	4.1	4.0
FL, PWHT	Average	514	688	11.0	16.4
	STD	116	77	4.7	4.6
HAZ, as-welded	Average	560	695	8.2	18.7
	STD	68	49	1.2	2.0
HAZ, PWHT	Average	492	631	9.8	21.2
	STD	52	36	1.3	1.8
Transverse, PWHT	Average	384	597	13.7	22.1
	STD	17	8	2.5	2.1

Table 5 shows comparison between the tensile test results of the different size specimens and, as can be seen, the results of the miniature-sized specimens are in general accordance with the results from the standard-sized round-bar specimens. Only the ultimate tensile strength of the miniature flat-bar specimens was outside the standard deviation of the round-bar specimens.

Table 5. Comparison between the tensile test results of the different specimen dimensions.

Specimen	Yield strength [MPa]		Ultimate tensile strength [MPa]	
	⌀8 x 105 mm round-bar specimens	1 x 2 x 20 mm flat-bar specimens	⌀8 x 105 mm round-bar specimens	1 x 2 x 20 mm flat-bar specimens
SA 508 base metal (BWR-DMW)	426 ± 13	417 ± 4	603 ± 6	590 ± 7
Alloy 182 weld metal	381 ± 36	375 ± 6	628 ± 14	603 ± 11
Alloy 182 buttering	366 ± 27	347 ± 15	648 ± 5	603 ± 17

The strength mismatch factors of the different BWR-DMW weld zones have been calculated using Equation (1) defined by the Brite Euram structural integrity assessment procedure for European industry (SINTAP) and are presented in Table 6. The weld metal and buttering are under-matched in comparison to the SA 508 base metal by 10% and 17%, respectively. The as-welded HAZ is over-matched compared to the base metal. The over-matching of the HAZ in the as-welded sample is greater than the over-matching of the HAZ in the PWHT samples. The largest mismatch factor is 1.61, which is located at the fusion line of the HAZ and the buttering layer. The heat treatment lowered the yield strength of the HAZ and therefore also lowered the mismatch factor in each case.

Table 6. Strength mismatch factors of the different BWR-DMW zones.

Location	M ($\boldsymbol{\sigma}_{WM}/\boldsymbol{\sigma}_{BM}$)
Alloy 182 weld metal / SA 508	0.90
Alloy 182 buttering / SA 508	0.83
Fusion line (as-welded) / SA 508	1.31
Fusion line (605 °C / 6 h) / SA 508	1.23
HAZ (as-welded) / SA 508	1.34
HAZ (605 °C / 6 h) / SA 508	1.18
Fusion line (as-welded) / Alloy 182 buttering	1.57
Fusion line (605 °C / 6 h) / Alloy 182 buttering	1.48
HAZ (as-welded) / Alloy 182 buttering	1.61
HAZ (605 °C / 6 h) / Alloy 182 buttering	1.42

2.5 Fracture mechanical testing

Fracture mechanical characterization of the BWR safe-end mock-up consists of determination of tearing resistance curves, fracture surface characterization and crack path determination. Fracture mechanical testing was performed according to ASTM E1820-99a standard at room temperature using the elastic-compliance method. Both welds were characterized using single-edge bend (SE(B)) specimens of two different sizes (shown in Figure 33): larger sized 10x20x100 mm and sub-sized 5x10x55 mm specimens. All the specimens were side-grooved prior to the fracture mechanical testing (after pre-fatigue). The BWR-DMW fracture mechanical specimens were extracted from the following locations of the weld: notch in the buttering layer, notch at the fusion line, notch at 1 mm from the fusion line into the HAZ of LAS (5x10x55 mm specimens), and notch at 2 mm from the fusion line into the HAZ of LAS (10x20x100 mm specimens). The fusion line and the HAZ specimens were extracted in a tilted position with respect to the weld in order for the fusion line to be parallel to the crack growth direction. The extraction locations of the fracture mechanical specimens are shown in Figure 33 and a list of the BWR-DMW fracture mechanical test specimens is presented Table 7.

Table 7. BWR-DMW fracture mechanical specimens.

Weld Zone	10x20x100 mm SE(B)		5x10x55 mm SE(B)	
	n	Specimen notations	n	Specimen notations
Buttering	4	PU1 – PU4	-	-
Fusion line	3	FL1A, FL2B, and FL3C	3	FLMA – FLMC
Fusion line + 1 mm	-	-	4	FLM1 – FLM4
Fusion line + 2 mm	3	FL+2A – FL+2C	-	-

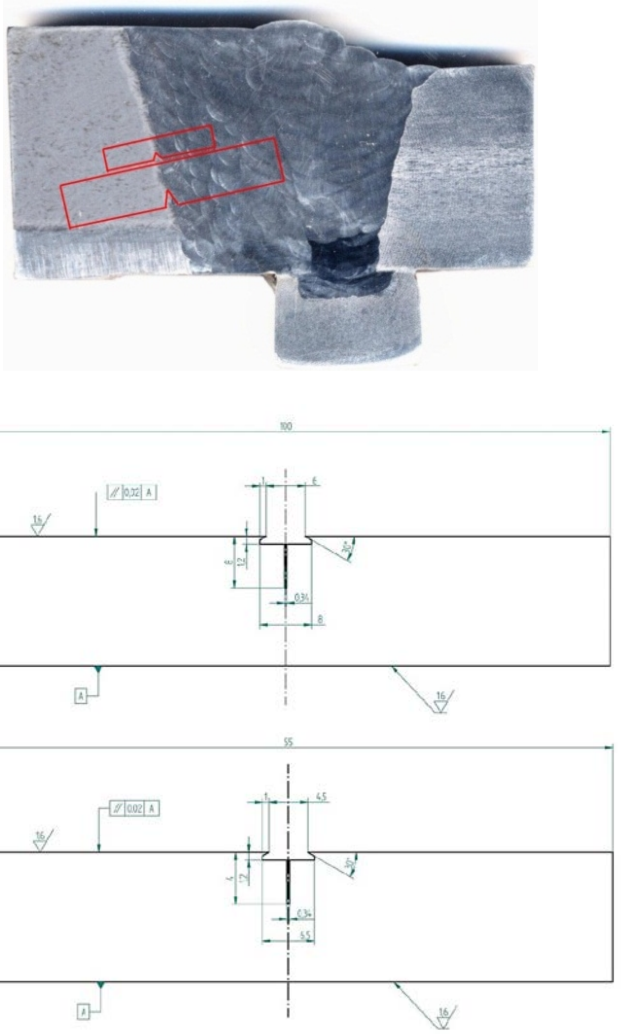

Figure 33. Extraction locations and technical drawings of the 10x20x100 mm and 5x10x55 mm SE(B) specimens used in fracture mechanical testing.

2.5.1 Fracture resistance curves

Fracture resistance curves of BWR-DMW fracture mechanical specimens are shown in Figures 35–38. The fracture resistance was high in all the zones of the weld, especially high in the buttering layer. Some variability can be seen in the fracture resistance, in particular in the specimens with the initial crack at the fusion line. This is, at least partially, due to the variation in the exact location of the pre-fatigue crack tip. The exact location of the pre-fatigue crack tip was estimated to be within ± 0.5 mm from the fusion line. Thus, the exact location of the crack tip can either be in the HAZ side of the fusion line or in the buttering side of the fusion line and the fracture mechanical behavior is dependent of the microstructure ahead of the crack tip.

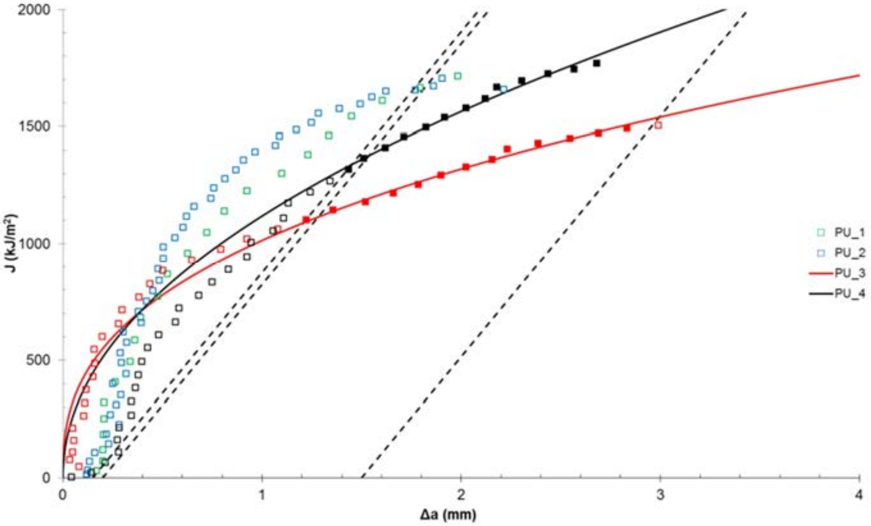

Figure 34. Fracture resistance curves of buttering layer BWR-DMW specimens.

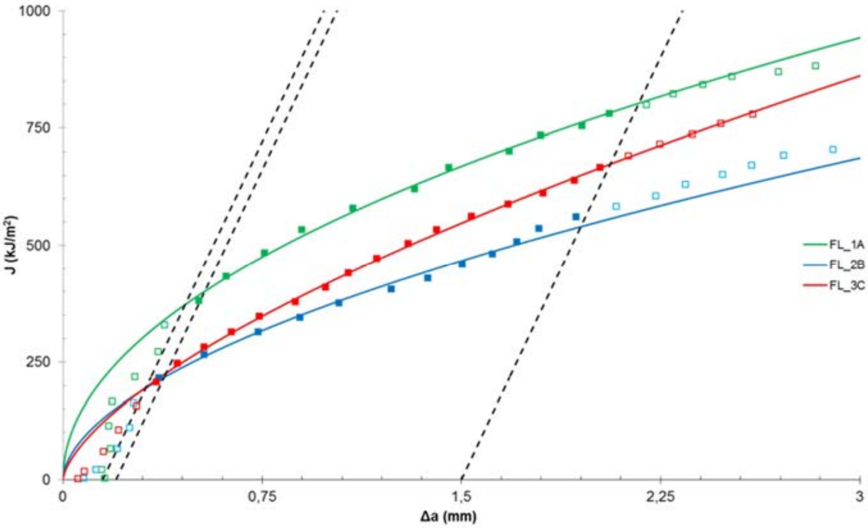

Figure 35. Fracture resistance curves of fusion line BWR-DMW specimens.

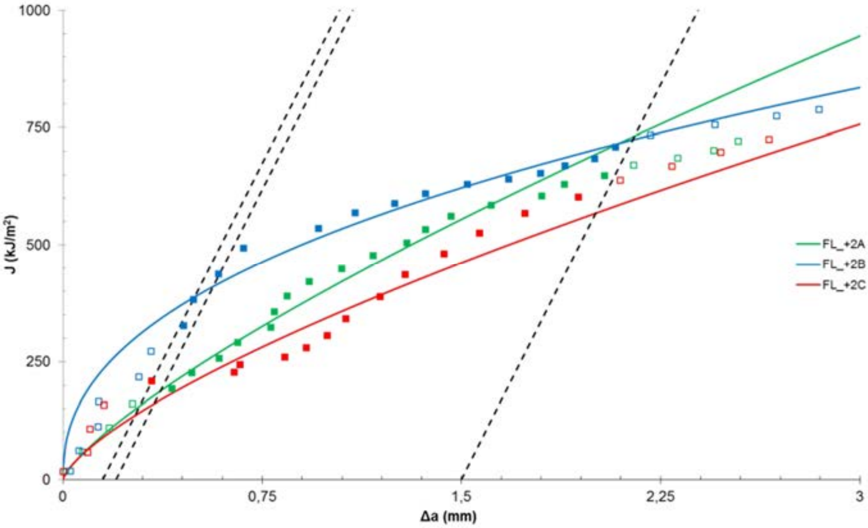

Figure 36. Fracture resistance curves of HAZ BWR-DMW specimens.

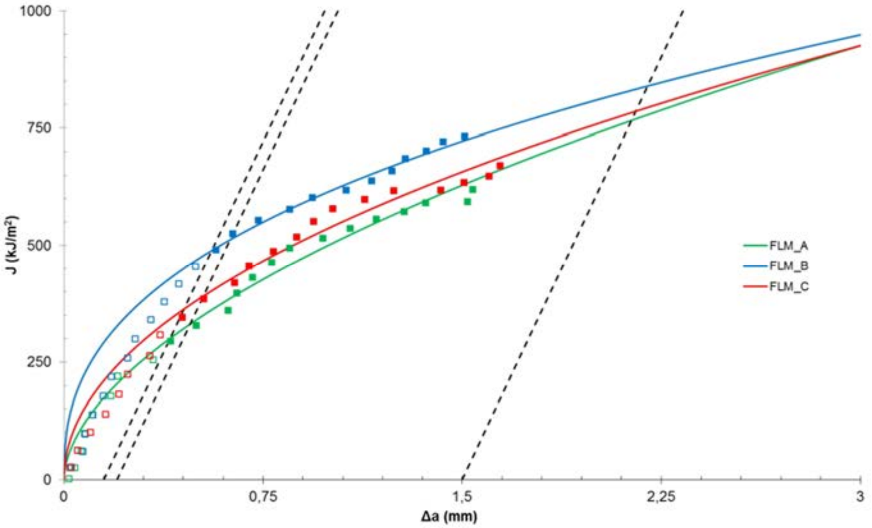

Figure 37. Fracture resistance curves of miniature fusion line BWR-DMW specimens.

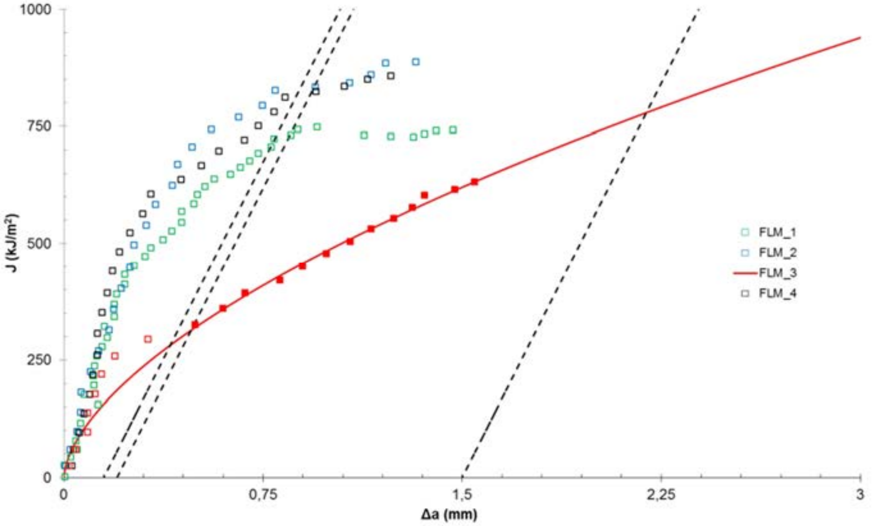

Figure 38. Fracture resistance curves of miniature HAZ BWR-DMW specimens.

2.5.2 Fracture surface characterization

Fracture surfaces of all the studied BWR-DMW fracture mechanical specimens consisted of ductile fracture. There were, however, differences between the fracture surfaces of the specimens from different zones of the weld. An example image of a fracture surface of a buttering layer specimen is shown in Figure 39. The buttering layer specimens had visibly deformed more during the fracture mechanical testing than the specimens from the other zones. The tip of the pre-fatigue crack was more uneven than in the specimens from the other zones and the pre-fatigue crack had propagated in an angle of about 45 degrees to the notch orientation. In the other specimens, the pre-fatigue crack had propagated close to the orientation of the notch. The fracture surfaces of the buttering layer specimens consisted of finely dimpled ductile fracture including a small and fine distribution of MnS particles on the fracture surface, see example images in Figure 40.

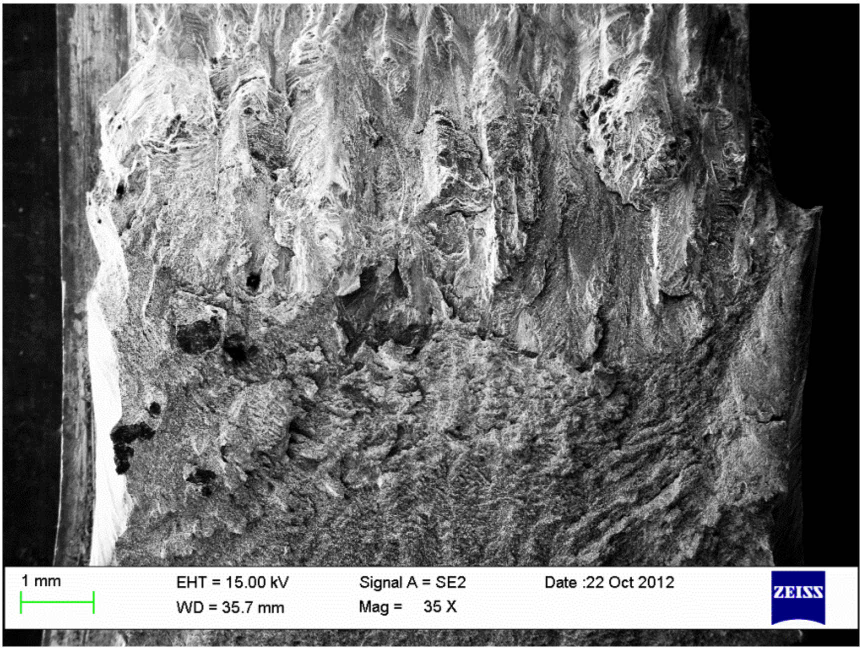

Figure 39. Fracture surface of PU2 buttering layer specimen.

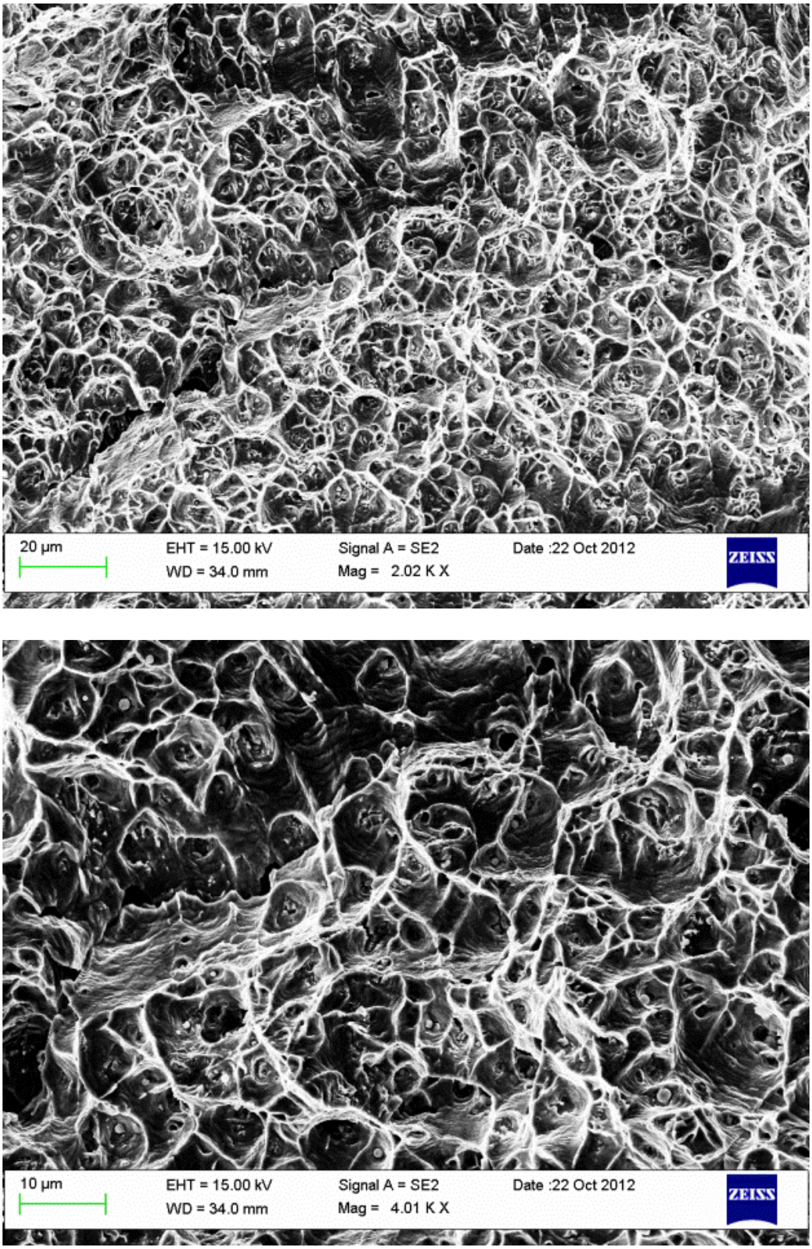

Figure 40. Ductile fracture surface of PU2 buttering layer specimen.

Figure 41 shows fracture surfaces of two different fusion line specimens. The fracture surfaces are from the weld metal side of the specimen and, as can be seen, the crack has propagated inward, which means that the crack has propagated towards the weld metal during the testing. Specimens have deformed clearly less during the testing compared to the buttering layer specimens, which is reasonable since the tearing resistance values were substantially lower. The fracture surfaces of the fusion line specimens were partly similar to the fracture surfaces on the buttering layer specimens. However, in addition to the fine distribution of small MnS particles, there were also clusters of larger MnS particles present on the fracture surface. Figures 41 and 42 show fracture surface microstructures found from the fusion line specimens and Figure 43 and 44 in the HAZ, respectively.

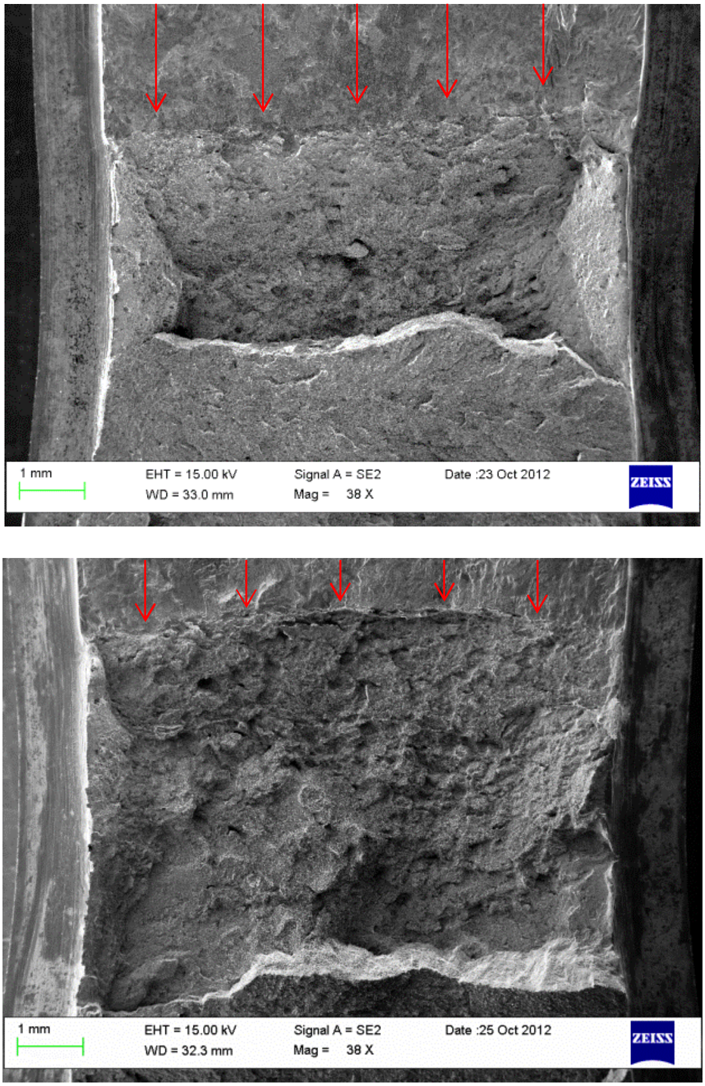

Figure 41. Fracture surfaces of FL1A and FL2B fusion line specimens.

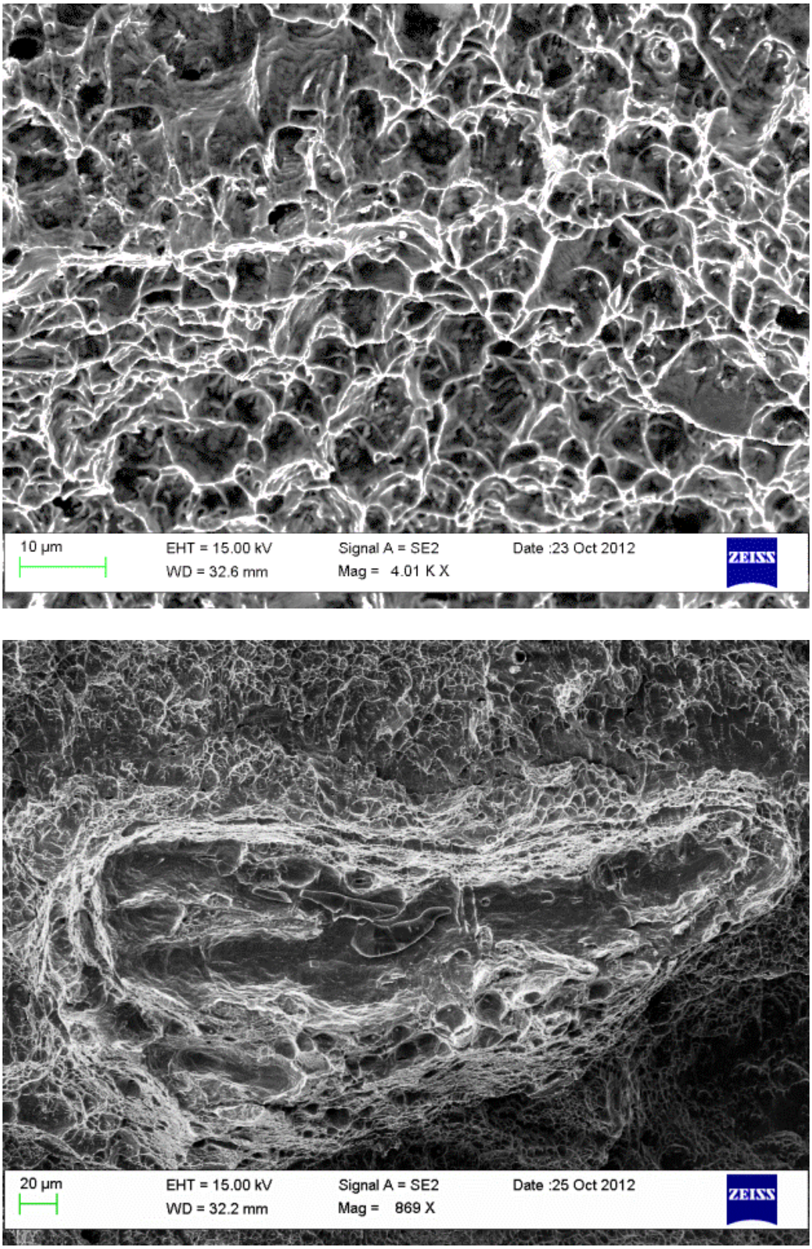

Figure 42. Ductile fracture surfaces on FL1A and FL2B fusion line specimens.

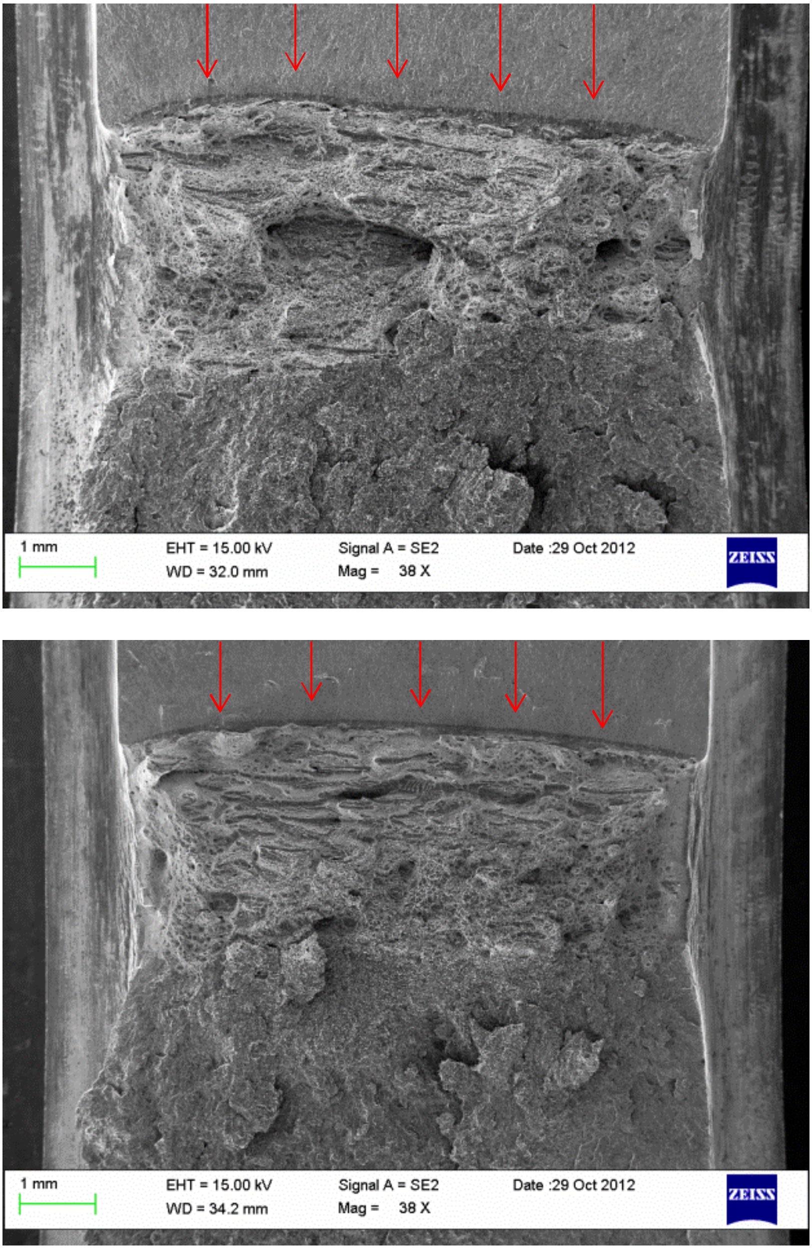

Figure 43. Fracture surfaces of FL2+B and FL+2C HAZ specimens.

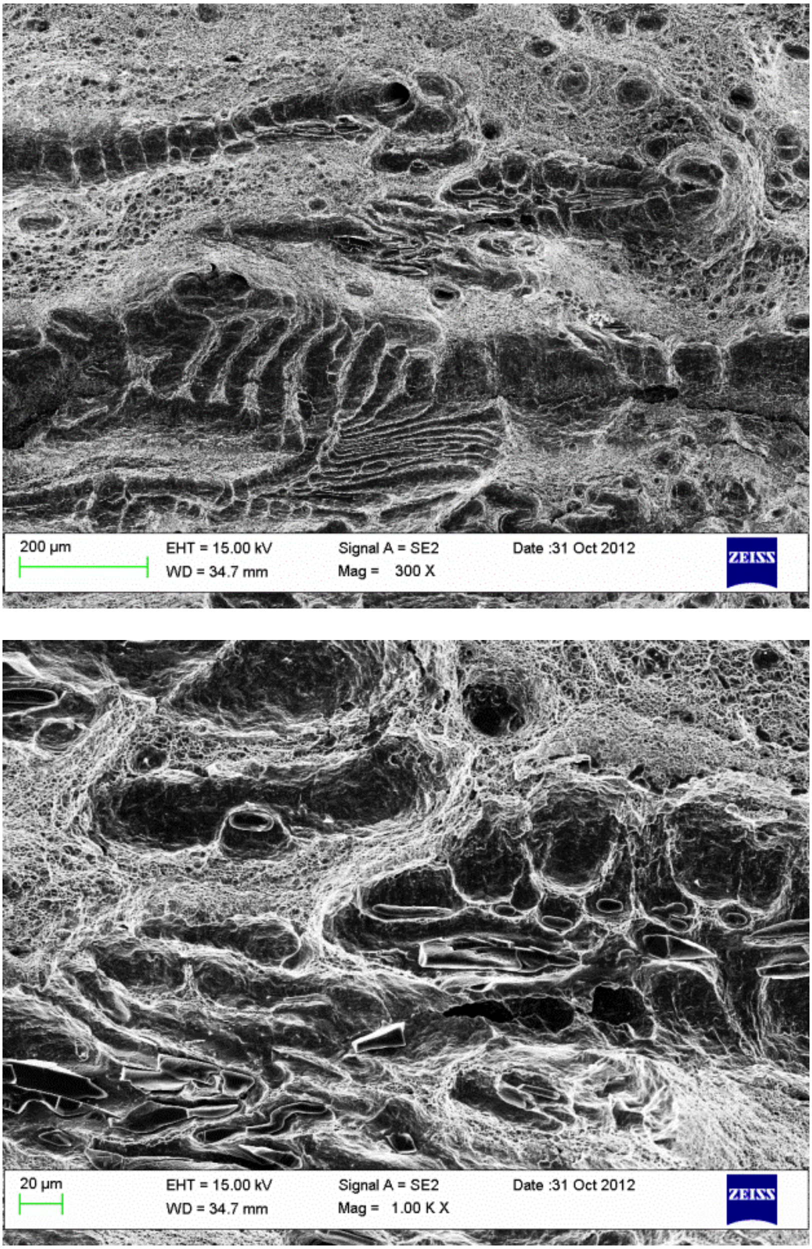

Figure 44. Ductile fracture surface on FL+2C HAZ specimen.

The differences in fracture resistance of the different zones are partly related to the size and distribution of the MnS particles within the microstructure. The buttering layer has high fracture resistance and small and finely distributed MnS particles. The fusion line and the HAZ specimens, on the other hand, have quite similar fracture resistance and their fracture surfaces contain large MnS particles and their clusters. The HAZ specimens contained higher amount of MnS clusters with larger size than the fusion line specimens, but some of them were found also from the fusion line specimens. In the fusion line specimens, the final cleavage crack (crack opening in liquid nitrogen) propagated on a different plane. This suggests that during the testing, the crack propagated into the weld metal and when the fracture resistance of the HAZ (BCC microstructure) is decreased at low temperatures, the crack occurred by cleavage in the HAZ.

2.5.3 3D profilometry and crack path examination

Fracture surfaces of the J-R tested SE(B) fracture toughness specimens were analysed using 3D profilometry. The measurements were performed for the low-alloy steel side halves of the fractured specimens for BWR mock-up. The attained results from the 3D profilometry measurements were a 3D topography map of the fracture surface and a line profile, which was measured in crack growth direction at mid-thickness of the fracture surfaces. The 3D maps for BWR Alloy 182 mock-up specimen fracture surfaces start from the pre-crack region and covers about half of the fracture surface breadth. The differences in altitude of a fracture surface are illustrated with a colour scale from blue to red, where the blue tones correspond to the lowest points of a fracture surface and the red to the highest. It must be pointed out that the colours of the 3D maps are scaled separately for each specimen and therefore the colours of the different fracture surface maps are not directly comparable in absolute units.

Sensofar Plµ 2300 is a non-contact optical imaging profiler. Both confocal and interferometry techniques can be used to illuminate the surface and create a 3D topography by detecting the reflection. Measurement of larger areas (i.e. extended topography) is also possible by using a X-Y motor stage. The objective used in this study was 20x which has an optical resolution of 64 µm. The maximum inclination of the studied surface that the equipment can measure is 42°. The fracture surfaces were mainly measurable with the equipment except for a few specimens where the crack grows in the weld and the cracks have locally steeper inclinations than 42°. In addition, side-grooved areas could not be included in the map because of their inclination, which is 45°, related to the fracture surface.

The studied BWR mock-up SE(B) specimens are presented in Table 8. Representative examples of each specimen series are presented in this chapter. The fracture surfaces studied in this chapter are from the low-alloy steel side halves of the SE(B) specimens.

Table 8. Studied BWR mock-up SE(B) specimens.

Pre-crack tip location	Full-sized SE(B)	Miniature SE(B)
	Sample	Sample
Buttering	PU1	
	PU2	
	PU3	
	PU4	
Fusion line	FL 1A	FLM A
	FL 2B	FLM B
	FL 3C	FLM C
Fusion line + 1 mm		FLM 1
		FLM 2
		FLM 3
		FLM 4
Fusion line + 2 mm	FL +2A	
	FL +2B	
	FL +2C	

In the 10x20x100 mm SE(B) BWR fusion line specimens, the cracks grow towards the buttering during J-R testing and return close to the fusion line in final fatigue. The cracks deviate about 0.8–1.5 mm from the pre-crack tip level during J-R testing according to the line profiles. An example of the profilometry results for full-sized SE(B) specimens are presented in Figures 45 and 46 (specimen FLM 2B). In the case of miniature SE(B) specimens (5x10x55 mm), however, the cracks grow towards the low-alloy steel and do not return to the fusion line region in final fatigue. The cracks deviate about 0.4–0.9 mm from the pre-crack level during J-R testing. Examples of the profilometry results for miniature SE(B) specimens are presented in Figures 47 and 48 (specimen FLM B).

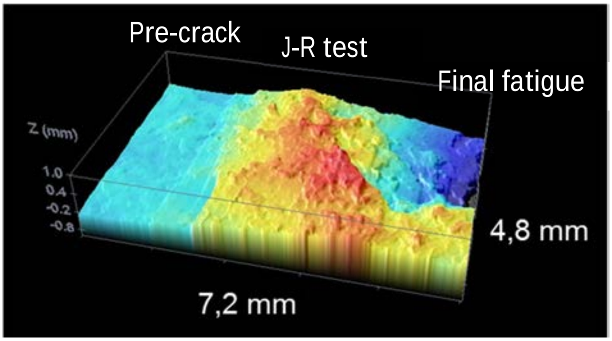

Figure 45. 3D topography map of full-sized (10x20x100 mm) SE(B) specimen FLM 2B fracture surface. Pre-crack, J-R test and start of the final fatigue can approximately be distinguished from the image. The map covers a 4.8 mm wide area from the middle of the specimen fracture surface.

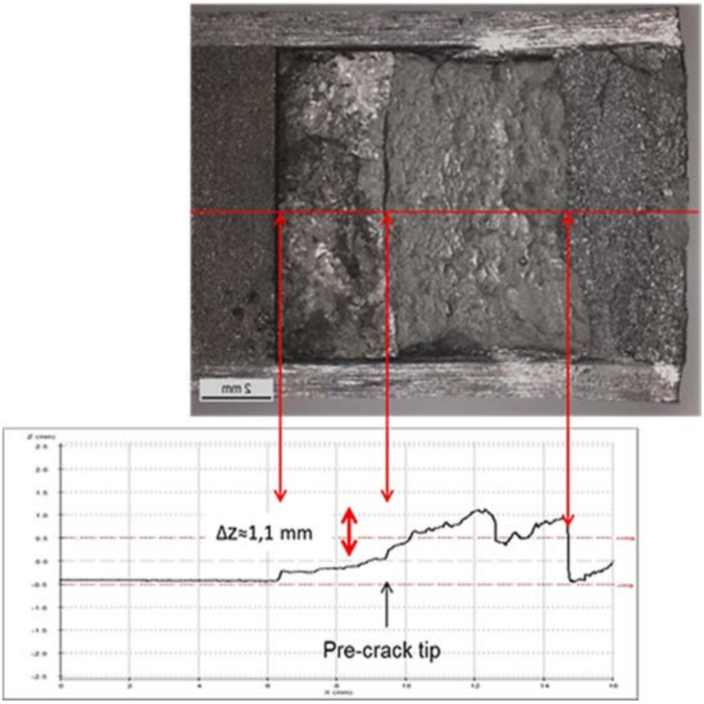

Figure 46. Line profile and fracture surface photograph of full-sized (10x20x100 mm) SE(B) specimen FLM 2B. The starting points of the pre-crack, J-R test and final fatigue are respectively indicated with arrows in the fracture surface photograph. The line profile has been measured from the middle of the fracture surface.

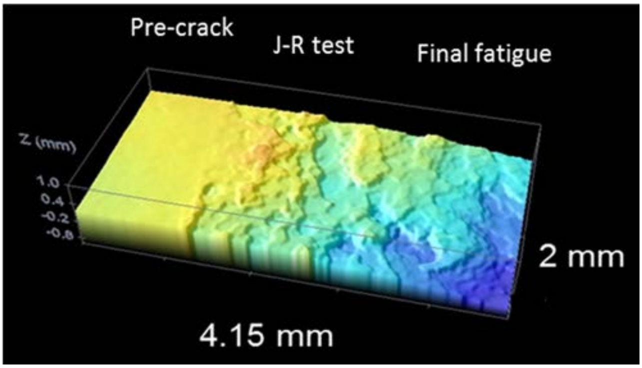

Figure 47. 3D topography map of miniature sized (5x10x55 mm) SE(B) specimen FLM B fracture surface. Pre-crack, J-R test and start of the final fatigue can approximately be distinguished from the image. The map covers a 2 mm wide area from the middle of the specimen fracture surface.

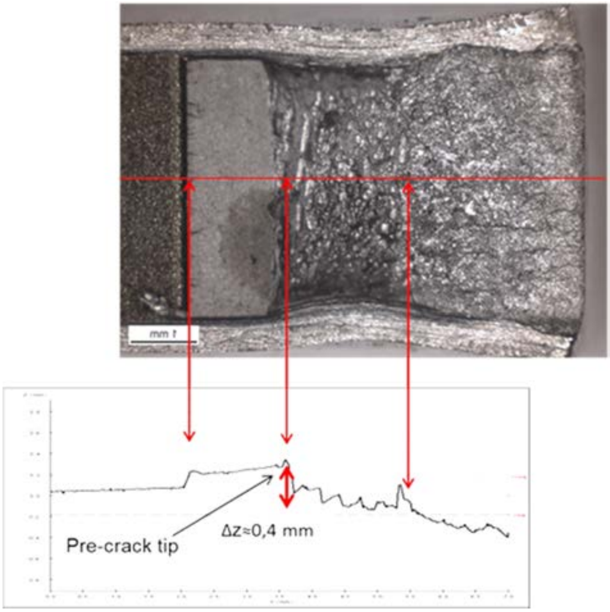

Figure 48. Line profile and fracture surface photograph of miniature sized (5x10x55 mm) SE(B) specimen FLM B. The starting points of the pre-crack, J-R test and final fatigue are respectively indicated with arrows in the fracture surface photograph. The line profile has been measured from the middle of the fracture surface.

Only miniature sized (5x10x55 mm) specimens were tested with the nominal pre-crack tip location of +1 mm (1 mm from the fusion line towards the low-alloy steel). The profilometry results for one of those specimens (FLM 2) are presented in

Figures 49 and 50. The cracks grow towards the pressure vessel steel (0.4–0.8 mm) during J-R testing according to the line profiles.

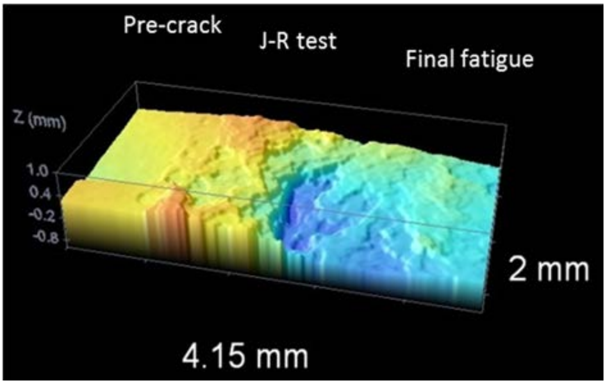

Figure 49. 3D topography map of miniature sized (5x10x55 mm) SE(B) specimen FLM 2 fracture surface. Pre-crack, J-R test and start of the final fatigue can approximately be distinguished from the image. The map covers a 2 mm wide area from the middle of the specimen fracture surface.

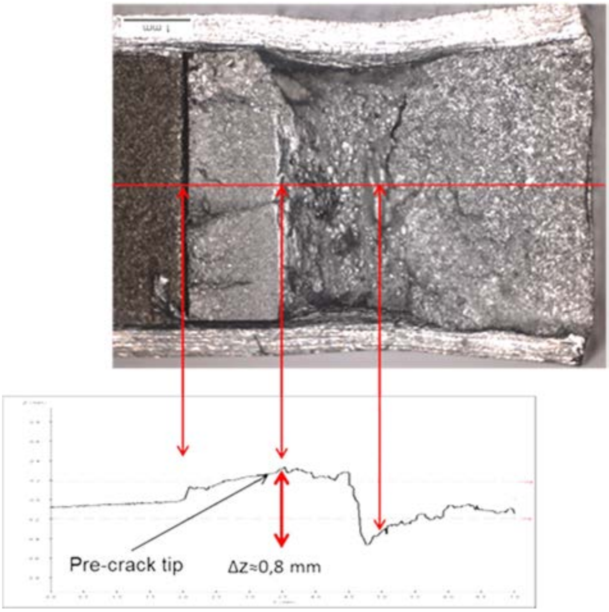

Figure 50. Line profile and fracture surface photograph of miniature sized (5x10x55 mm) SE(B) specimen FLM 2. The starting points of the pre-crack, J-R test and final fatigue are respectively indicated with arrows in the fracture surface photograph. The line profile has been measured from the middle of the fracture surface.

Only full-sized (10x20x100 mm) specimens were tested with the nominal pre-crack tip location of +2 mm (2 mm from the fusion line towards the low alloy steel). The profilometry results for one of those specimens are presented in Figures 51 and 52.

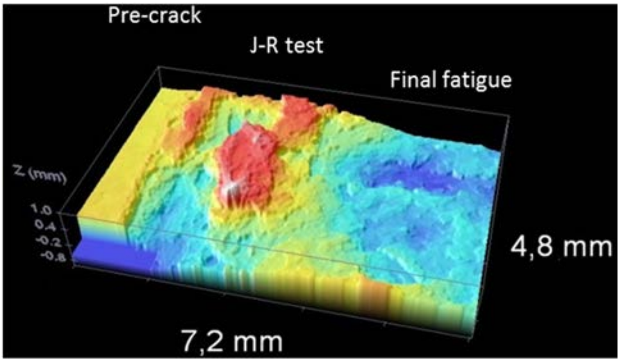

Figure 51. 3D topography map of full-sized (10x20x100 mm) SE(B) specimen (FL +2) fracture surface. Pre-crack, J-R test and start of the final fatigue can approximately be distinguished from the image. The map covers a 4.8 mm wide area from the middle of the specimen fracture surface.

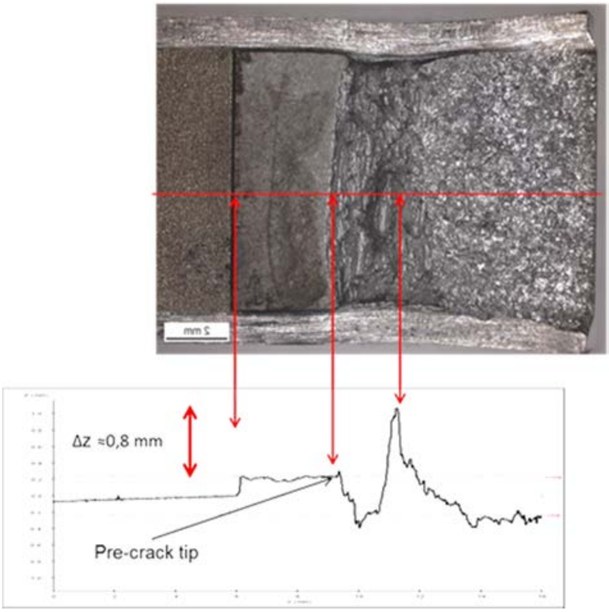

Figure 52. Line profile and fracture surface photograph of full-sized (10x20x100 mm) SE(B) specimen (FL +2). The starting points of the pre-crack, J-R test and final fatigue are respectively indicated with arrows in the fracture surface photograph. The line profile has been measured from the middle of the fracture surface.

In buttering specimens the pre-crack was nominally 1 mm towards the buttering from the fusion line. Profiles for these specimens could not be measured because of their rough topography that includes steep inclinations.

2.6 Conclusions

The microstructural examination of the fusion line region of the as-welded specimens revealed the following characteristics:

1. Type II boundary located in the buttering weld about 30 to 60 μm from the fusion line,
2. a martensitic zone located between the Type II boundary and the fusion line,
3. no traces of a carbon-depleted zone next to the fusion line were detected,
4. and HAZ with microstructural zones typical of low-alloy steel (LAS) was detected.

The fusion line area displayed a heterogeneous microstructure, i.e., the fusion line consisted of:

1. both the martensitic zone and the Type II boundary,
2. only the martensitic zone but no Type II boundary, or
3. was a single fusion line.

The Type II boundary and the martensitic zone were not continuous along the whole fusion line and the distance of the Type II boundary from the fusion line varied. The martensitic zone existed both alone and next to the Type II boundary at the fusion line and its width varied.

The EDS results showed an increase in Ni composition, from about 1 to 10 wt. %, and a decrease in Fe composition, from around 95 to 85 wt. %, in the martensitic zone compared to that of the base metal. The martensitic zone has formed as a result of the transition in composition between the LAS and Ni-base filler metal. The EDS maps also showed a decrease in Fe composition at the Type II boundary. The Type II boundary has pushed segregating elements in front of it while moving into the weld metal during solidification. This can be seen as a band of Nb and Ti carbides and a higher concentration of Si at the Type II boundary in the EDS maps. No carbon-depleted zone was found in the HAZ at the SA 508 side of the fusion line. The high nickel concentration of Alloy 182 lowers the activity of carbon which reduces the diffusion rate and thereby reduces carbon migration. Carbon-depleted zones usually form at the immediate vicinity of the fusion line of ferritic steel and a stainless steel weld as a result of PWHT. The two different PWHTs were not found to cause a carbon-depleted zone at the fusion line of the studied samples.

A hardness peak was observed at the SA 508 HAZ of the as-welded state DMW sample. The peak is caused by the coarse-grained microstructure that has formed next to the fusion line as a result of the rapid cooling from high peak temperatures above A_{c3} during the welding process. The hardness and the microstructure of this area suggest that the coarse-grained structure consists likely of bainitic microstructure. The PWHT samples showed hardness peak in the SA 508 HAZ of about 120 $HV_{0.3}$ lower than that of the as-welded samples. This decrease in hardness is the result of the tempering of the microstructure. The two different PWHT hold times do not seem to have significant effect on the peak hardness values in the HAZ, although the sample with longer heat treatment time displayed a less sharp hardness profile.

The miniature size flat-bar tensile test specimens were found to provide valid results. The highest tensile strength values were measured on the specimens extracted from the ferritic steel HAZ of the as-welded sample. As expected, the tensile strength values for the PWHT samples were lower compared with those of the as-welded samples. The tensile test results are in compliance with the hardness profiles.

The weld metal and the buttering layer were found to be under-matching in comparison to the SA 508 base metal by 10% and 17%, respectively. According to the SINTAP procedure, over-/under-matching can be considered minimal if it is less than 10% and needs to be taken into consideration only when it exceeds this value. The highest mismatch, 161%, was found at the weld fusion line between the HAZ and the buttering layer in the as-welded samples. Heat treatment lowered the mismatch to a range of 142–148%.

The fracture mechanism of the fracture mechanical test specimens was ductile and no brittle behavior was found in the studied zones. Some variability was observed in the fracture resistance of the specimens with the initial pre-crack at the fusion line. This is, at least partially, due to the variation in exact location of the pre-fatigue crack tip in the specimen. In the fusion line samples, the pre-fatigue crack may have grown into the HAZ side or into the buttering side of the fusion line. If the pre-fatigue crack has grown into the buttering side of the fusion line, the fracture resistance of the sample is closer to that of the buttering layer and if the pre-fatigue crack has grown into the HAZ side of the fusion line, the fracture resistance is closer to that of the HAZ. The distribution of the MnS particles in the microstructure is very different in the buttering layer and in the HAZ of LAS. Buttering layer has small and finely distributed MnS particles in its microstructure while in LAS the MnS inclusions are large and form elongated clusters. This is the main reason for the much higher fracture resistance of the buttering layer than that of HAZ.

3. Alloy 52 narrow-gap and EAC weld mock-ups

Regarding metallurgical design and fabrication welding, there are recent development trends that need to be taken into account in view of structural design and integrity assessment of NPP multi-metal components. New high-chromium (~ 30%) nickel-base filler metals such as Alloys 52, 152 and 52M with high PWSCC resistance are extensively used to replace former Alloy 82 and 182 in fabrication of new PWRs, as well as for repair and replacement of the affected thick-section components in existing NPPs [Wang et al. 2013]. Simultaneously, advanced welding processes such as narrow-gap (narrow groove) methods (NGW) have been introduced as gas-tungsten arc welding (GTAW) of thick section components including DMWs for safe-ends made without any buttering layer. All these changes inevitably require mastery of the existing correlations and known relationships between the mixing (dilution) of the base metal, the compositional gradients of alloying elements, the resulting microstructures and damage and failure phenomena in DMWs. The distribution of alloying elements, characteristics and widths of microstructural zones and the gradient of mechanical properties in the near interface zone (NIZ) of a narrow-gap Alloy 52/152 weld without any buttering can therefore be expected to differ to some extent from a conventional V-groove Alloy 82/182 weld with a buttering layer [Nevasmaa et al. 2013].

3.1 Manufacturing of the Alloy 52 narrow-gap and EAC weld mock-ups

A dissimilar metal narrow-gap weld mock-up, composed of SA 508 and AISI 304 base metals and Alloy 52 filler metal, was manufactured. This mock-up was manufactured to resemble the dissimilar metal safe-end nozzle weld of nuclear reactor pressure vessel. The pressure vessel is made of ferritic SA 508 low-alloy steel and the inner surface of the vessel is cladded with AISI 309L and 308L stainless steels in order to protect it from corrosion. The dimensions and materials of the weld can be seen in Figure 53.

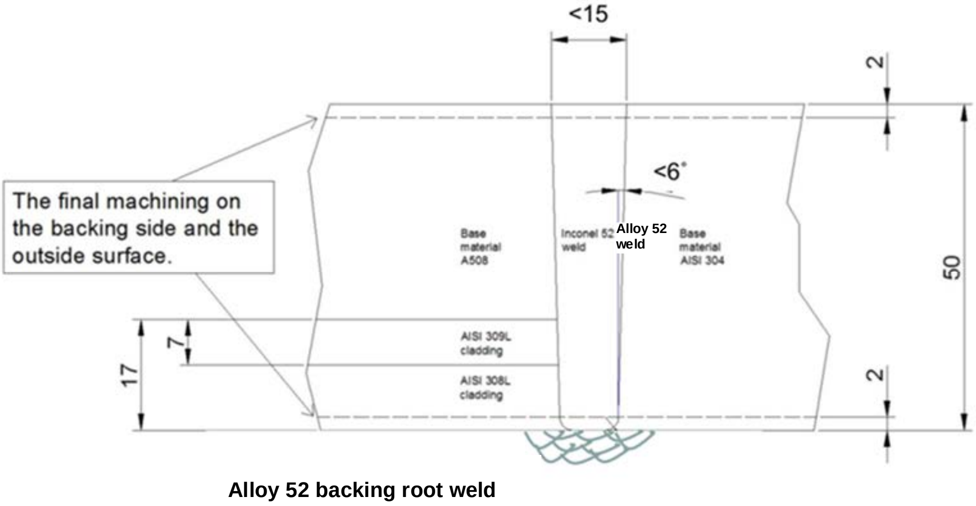

Figure 53. Schematic drawing of the Alloy 52 narrow-gap weld mock-up.

The manufacturing of the mock-up was begun by submerged arc welding (SAW) of the AISI 309L and 308L cladding layers onto a block of pressure vessel steel SA 508, Figure 54. Preheat temperature was 150 °C and interpass temperature was max. 250 °C.

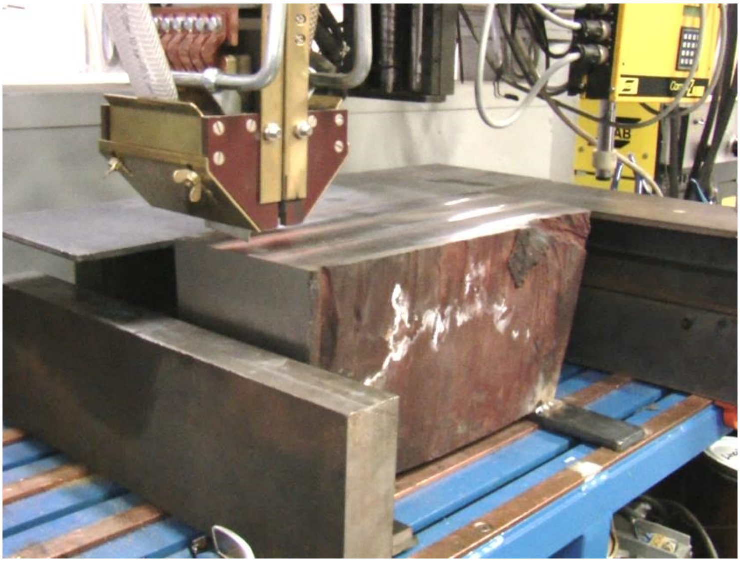

Figure 54. Submerged arc welding (SAW) of the AISI 309L and 308L cladding layers onto a block of pressure vessel steel SA 508.

The cladding surface was machined smooth and an about 50 mm thick slice including the cladding was cut from the SA 508 steel block, Figures 55 and 56.

Figure 55. Machining of the cladding.

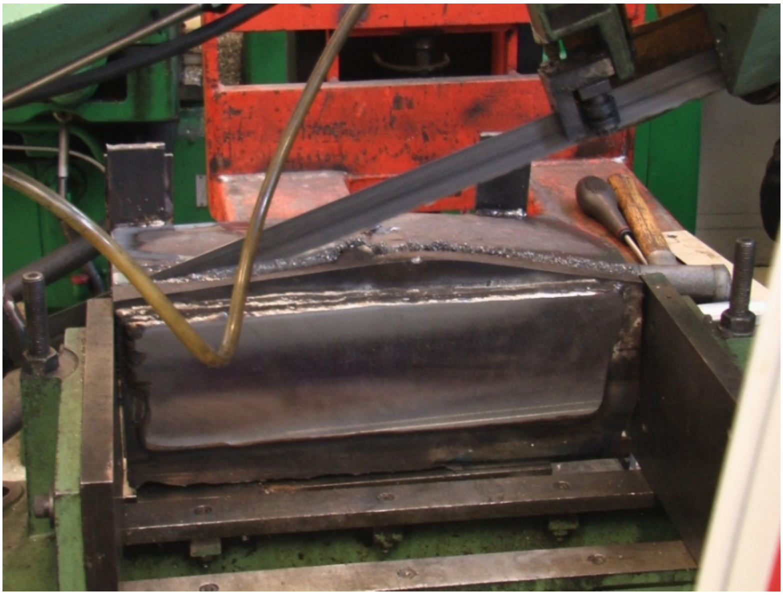

Figure 56. Cutting of 50 mm thick slice with the cladding from the SA 508 steel block.

The cladding was post-weld heat treated at the temperature of 605 ± 15 °C for 2 h. The cooling and heating rate during the heat treatment was max. 55 °C/h.

Before actual mock-up welding pre-mock-ups were manufactured to find applicable welding parameters. In pre-mock-ups materials used were carbon steel S 355 (without stainless steel cladding) and AISI 304. In Figure 57 is presented a pre-mock-up before welding and in Figure 58 the stiffener plates welded under the mock-up.

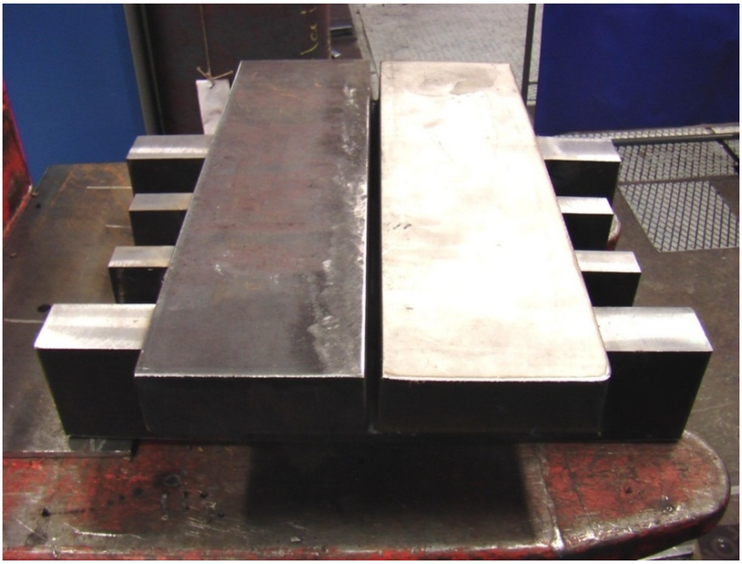

Figure 57. Pre-mock-up of S 355 carbon steel and AISI 304 stainless steel before welding.

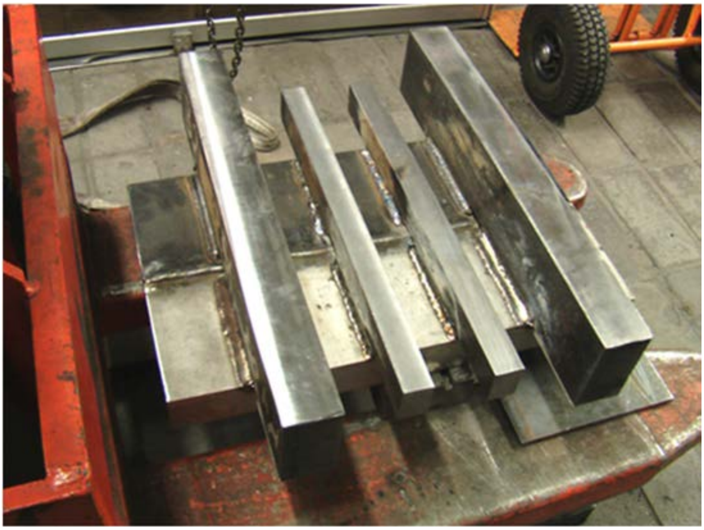

Figure 58. Stiffener plates welded under the pre-mock-up.

In Figure 59 is presented fixture of the pre-mock-up for welding. Pre-heat temperature was 220 °C (min. 175 °C) and interpass temperature max. 250 °C. In front of the weld the camera is monitoring the welding process in order to see the shape of the weld pool and the position of the welding electrode and wire in the narrow-gap groove. In Figure 60 actual welding is in progress and the arc in the groove can be seen via the monitor.

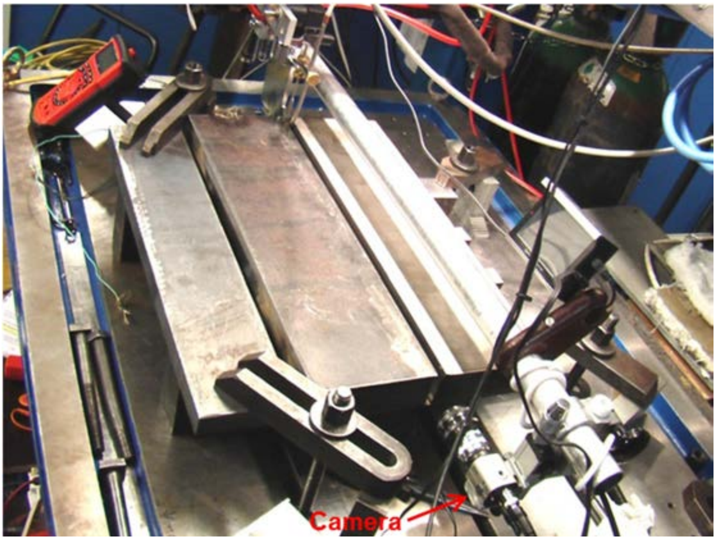

Figure 59. Fixture of the pre-mock-up for welding.

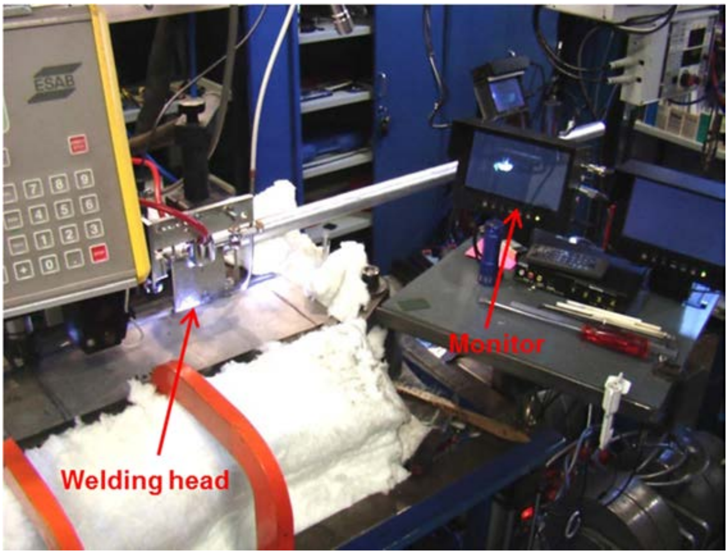

Figure 60. Welding in progress and the arc can be seen via the monitor.

While approaching the surface and finishing the weld with the narrow-gap torch, an additional gas shield was needed, Figure 61. In figure camera is also seen which monitors the weld surface right after welding. Thermocouple measures the pre-heat and inter-pass temperatures during the welding.

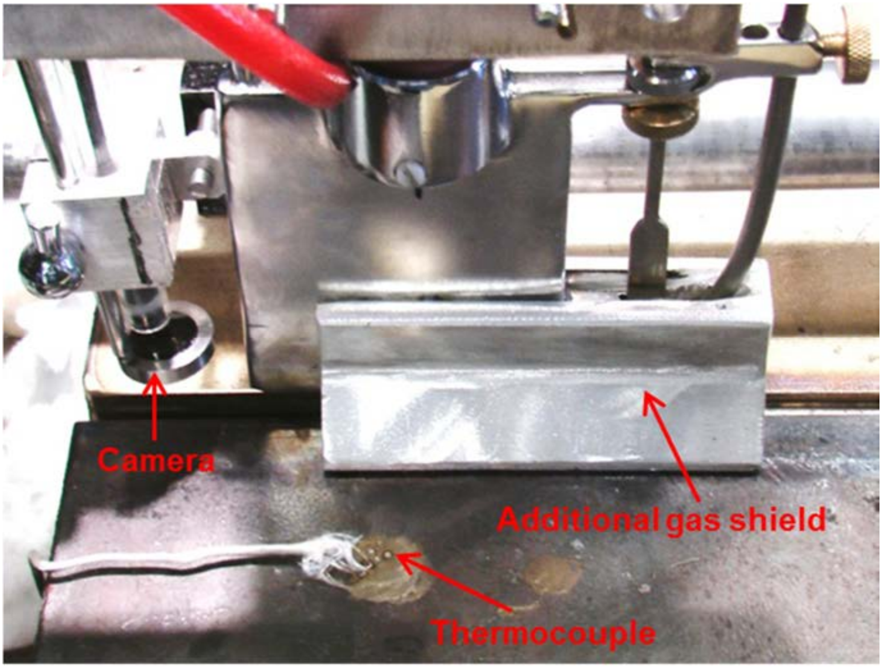

Figure 61. Use of the additional gas shield when approaching the surface.

In Figure 62 is presented a completed pre-mock-up and in Figure 63 a cross-section of a NG weld.

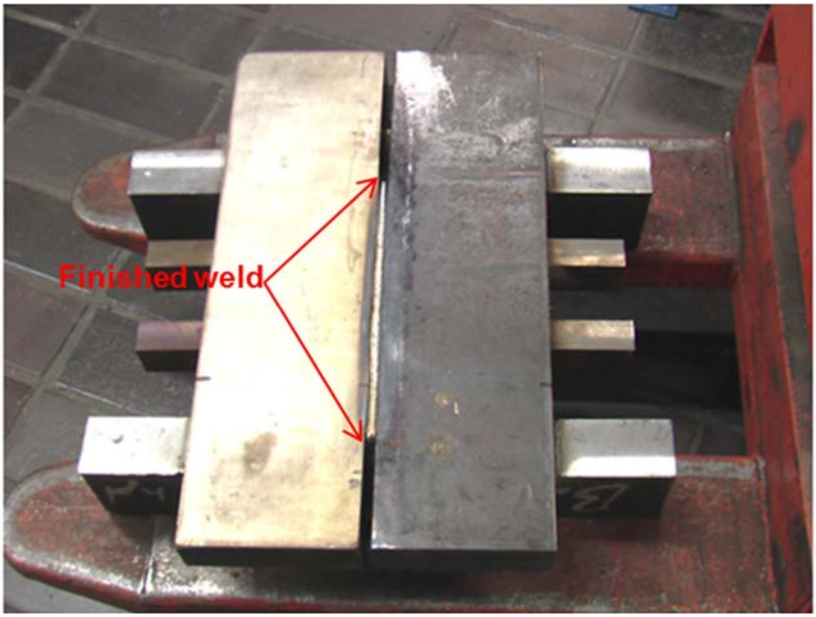

Figure 62. Completed pre-mock-up.

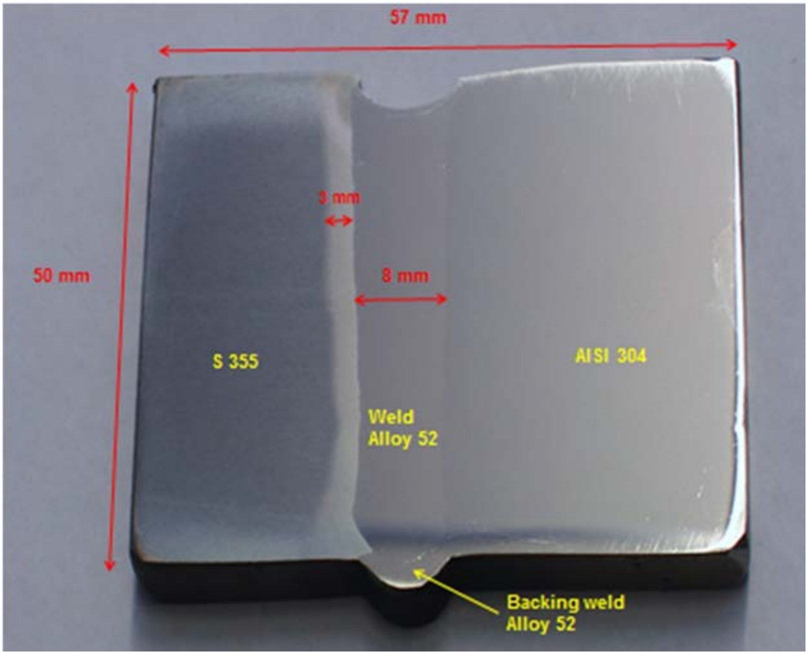

Figure 63. Cross-section of the pre-mock-up weld.

After pre-mock-up welding actual NG mock-up was prepared for welding, Figure 64. Procedure was similar to the pre-mock-up manufacturing regarding welding of the cladding, heat-treatment of the cladding, machining of the groove and the backing weld of the root. Weld starting and ending plates were welded into the SA 508 and AISI 304 plates to obtain maximum length of the NG weld.

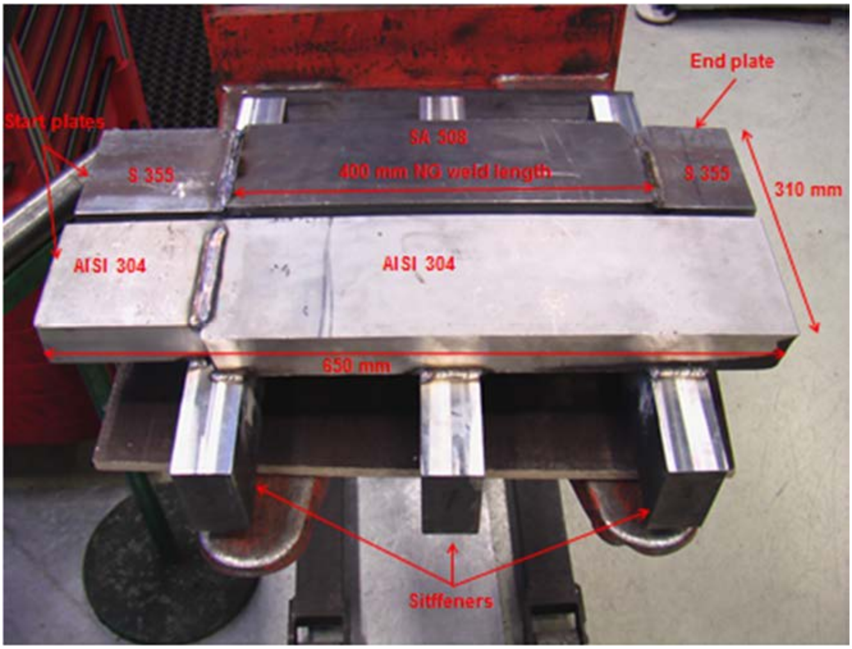

Figure 64. Alloy 52 narrow-gap mock-up ready for connection welding.

During the welding of the first seven passes, hot cracking type weld defects were observed on the weld surface, Figure 65. The cracking stopped to occur when welding reached the interface of the cladding and the SA 508 pressure vessel steel.

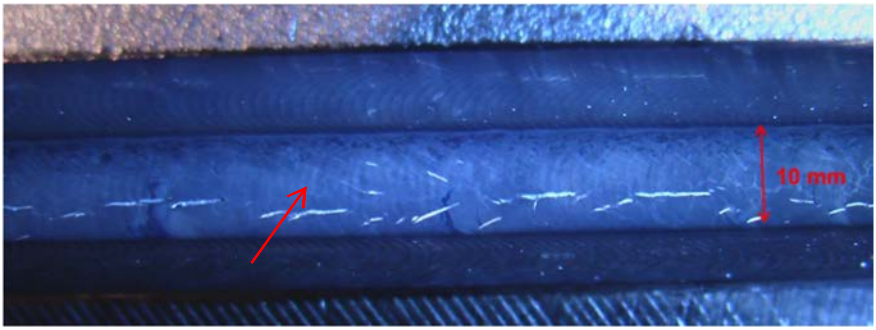

Figure 65. Hot cracking type weld defects in the surface of the first weld passes.

Two similar mock-ups were welded and one of them was post-weld heat-treated as shown in the time-temperature diagram in Figure 66, and the other one was left to as-welded condition. In Figure 67 is presented cross-section of the completed weld mock-up.

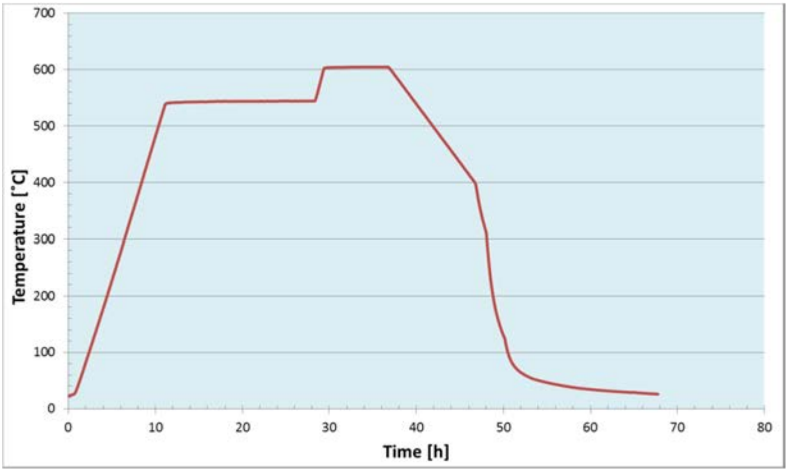

Figure 66. Post-weld heat treatment of Alloy 52 NG mock-up.

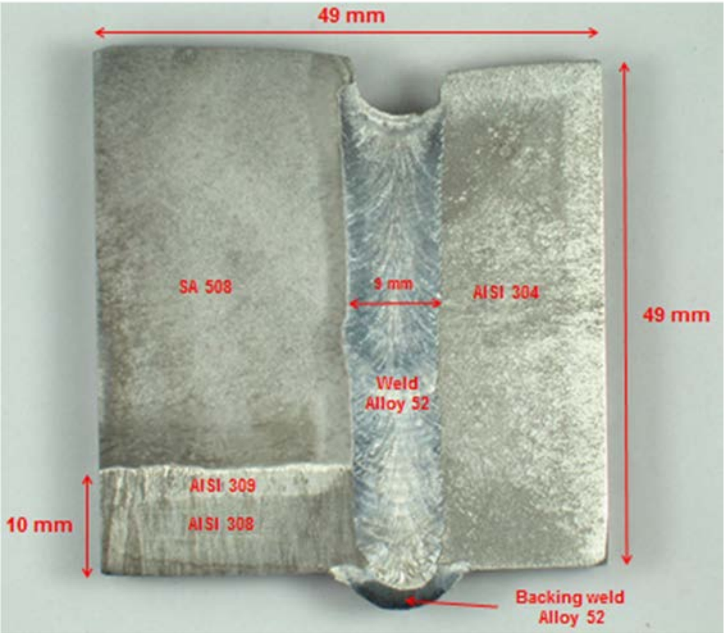

Figure 67. Completed Alloy 52 NG weld mock-up.

Because of the cracking in the first weld passes, an other mock-up was made, called EAC mock-up. In Figure 68 is presented the schematic drawing of the mock-up.

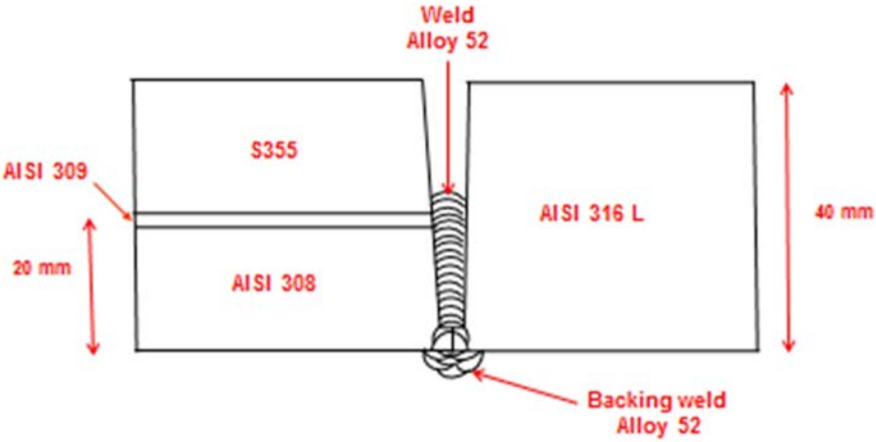

Figure 68. Schematic drawing of Alloy 52 narrow-gap weld mock-up.

In this weld mock-up thick AISI 309 and 308 submerged arc strip cladding was welded on carbon steel (Figure 69) and then Alloy 52 narrow gap connection weld was made to stainless steel plate in the same way as in Alloy 52 mock-up. The aim was to get rid of the hot cracking, when the rigidity of the mock-up increases during welding. Another objective was to have more Alloy 52 samples for EAC crack initiation testing program.

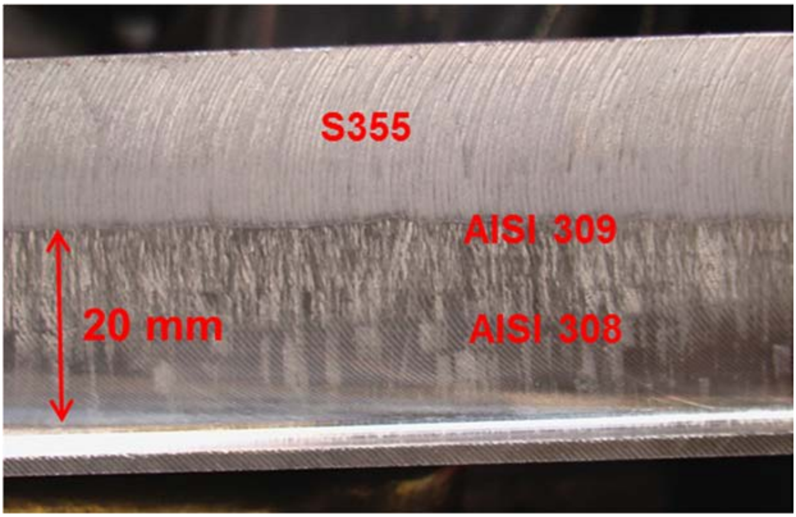

Figure 69. Thick AISI 309 and 308 submerged arc strip cladding welded on S 355 carbon steel plate and machined NG groove.

During welding similar hot cracks as in Alloy 52 mock-up occurred in the whole weld pass sequence up to cladding and carbon steel interface where the hot cracking stopped. In Figure 70 hot cracks are present in the surface of the weld. In Figure 71 is a cross-section image of the completed EAC mock-up where in yellow is marked cracked and non-cracked regions.

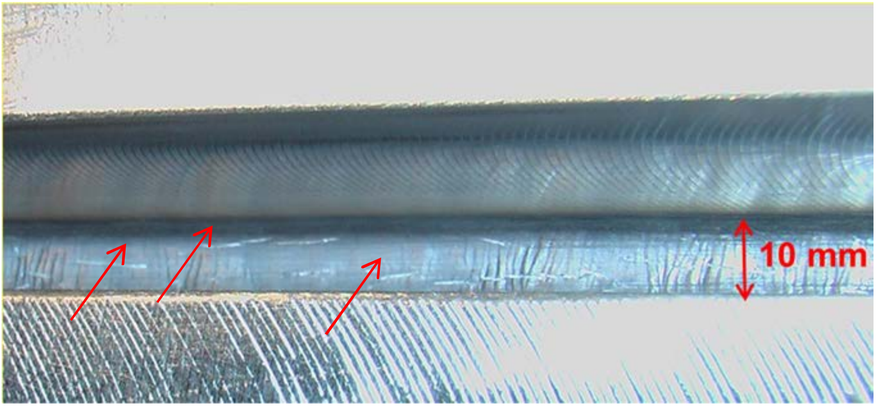

Figure 70. Hot cracks on the weld surface.

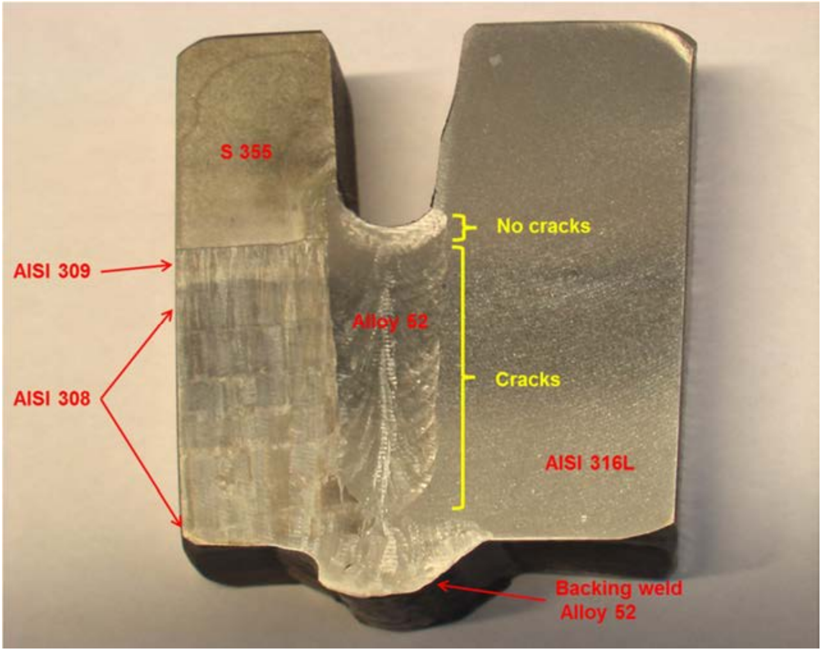

Figure 71. Cross-section image of the completed EAC mock-up, where in yellow is marked cracked and non-cracked weld regions.

3.2 Microscopy

The microstructures of Alloy 52 NG weld mock-up were examined by optical and electron microscopy. Special attention was paid to the fusion line between SA 508 base metal and Alloy 52 weld metal.

3.2.1 Optical microscopy

Figure 72 shows the microstructure of SA 508 HAZ of the NG-DMW in as-welded condition. The typical HAZ regions of low-alloy steel are observable. The microstructure of the base metal is bainitic. When going closer to the fusion line, the material experiences higher temperatures during welding. Thus, a higher fraction of austenite forms. After cooling, the austenite transforms into a fine distribution of ferrite grains and bainite. Along the fusion line, the temperature is at its highest. It triggers the growth of austenite grains and forms the grain coarsening zone.

Figure 73a shows the fusion line between SA 508 and Alloy 52 etched with 2% Nital. A carbon-depleted zone (CDZ) with a width of around 0.01–0.02 mm can be observed. The CDZ has formed as a result of carbon migration at high temperature from the base metal to the weld metal due to the composition gradients. Figure 73b shows the Alloy 52 side of the fusion line. The grain boundaries seem to be mainly Type I boundaries and a zone with a width of about 0.05 mm is free of precipitates along the fusion line. The columnar dendritic structure starts after this zone. Figure 73c shows what seems to be a Type II boundary along the fusion line. It is, however, closer to the interface (about 0.01 mm) than usual Type II boundaries (0.1 mm). It is rather difficult to say if the grains are continuous across the interface since the two materials react differently to the etchants. Since the interface is ferritic/austenitic, discontinuity is to be expected. Figure 74 shows a global view of the Alloy 52 weld metal and the weld passes. Figure 75 shows the microstructure of the Alloy 52 weld metal consisting of columnar dendrites.

Figure 72. Microstructure of the SA 508 – Alloy 52 interface of the as-welded state NG-DMW.

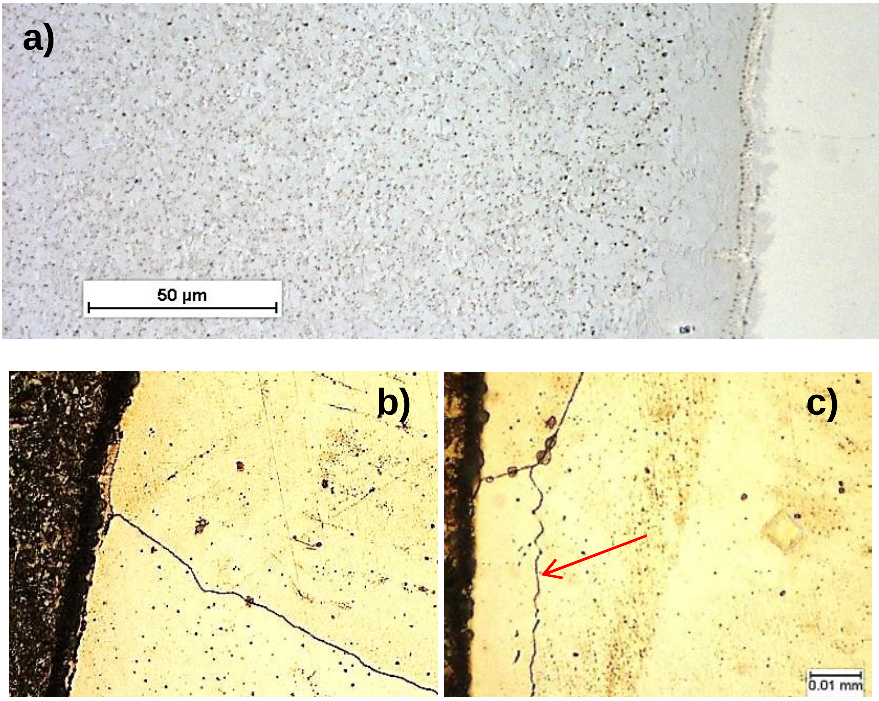

Figure 73. Microstructure of the AW SA 508 – Alloy 52 fusion line with: a) CDZ in the LAS side, b) a layer free of precipitates on the weld metal side along the fusion line, and c) Type II boundary (red arrow).

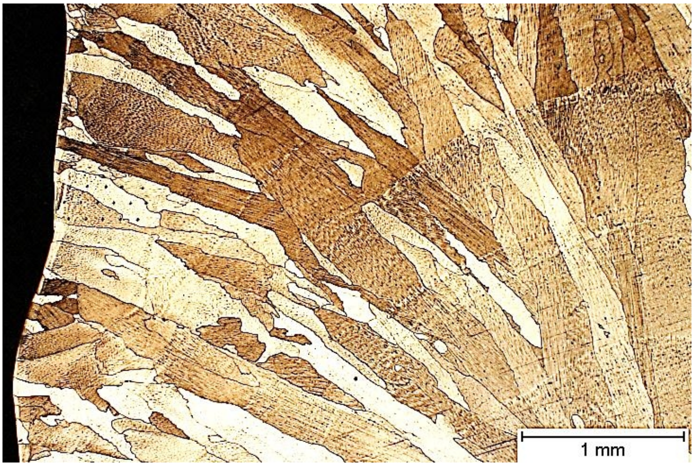

Figure 74. Microstructure of the AW Alloy 52 weld metal. The grains start to grow perpendicular to the interface and then their orientation follows the heat gradient in the weld passes.

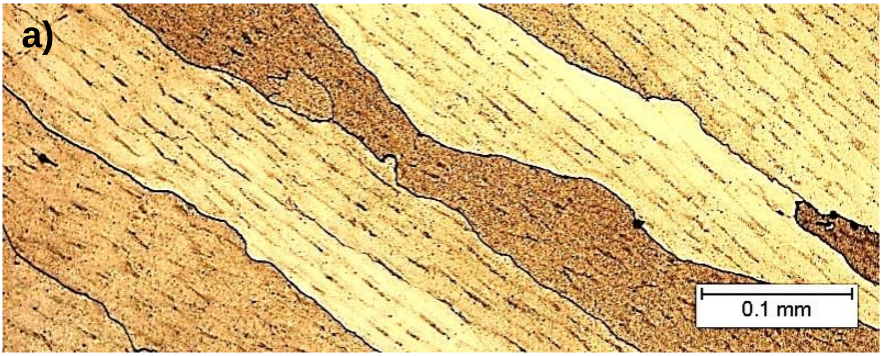

Figure 75. Microstructure of the AW Alloy 52 weld metal with columnar dendrite grains.

The microstructure of SA 508 HAZ of the NG-DMW in a PWHT condition is shown in Figure 76. The HAZ consists of the same distinct zones typical to the HAZ of SA 508 as in the as-welded DMW and, thus, the PWHT does not seem to have an effect on the microstructural properties of the HAZ. PWHT affects, however, on the microstructure of the interface, as shown in Figure 77. Figure 77a shows the interface etched with 2% Nital. A CDZ is clearly wider than that of the as-welded condition, with a width of about 0.1 mm. In addition, the fusion line itself is much darker etched than in the as-welded sample which suggests a higher carbon content at the fusion line. Figures 77b and c show formation of multiple precipitates in the weld metal side of the fusion line at approximately 50 µm from the interface. Figure 77d shows what looks like a Type II boundary. It is, however, much closer to the interface (about 10 µm) than what is reported in the literature (about 100 µm).

Figure 78 shows a global view of the Alloy 52 weld metal after PWHT. The direction of the grains does not change. Figure 79 shows closer views of the microstructure of the Alloy 52 weld metal. The previous columnar dendrites seem to have evolved in a cellular structure during the heat treatment.

Figure 76. Microstructure of the SA 508 – Alloy 52 interface of the PWHT state NG-DMW.

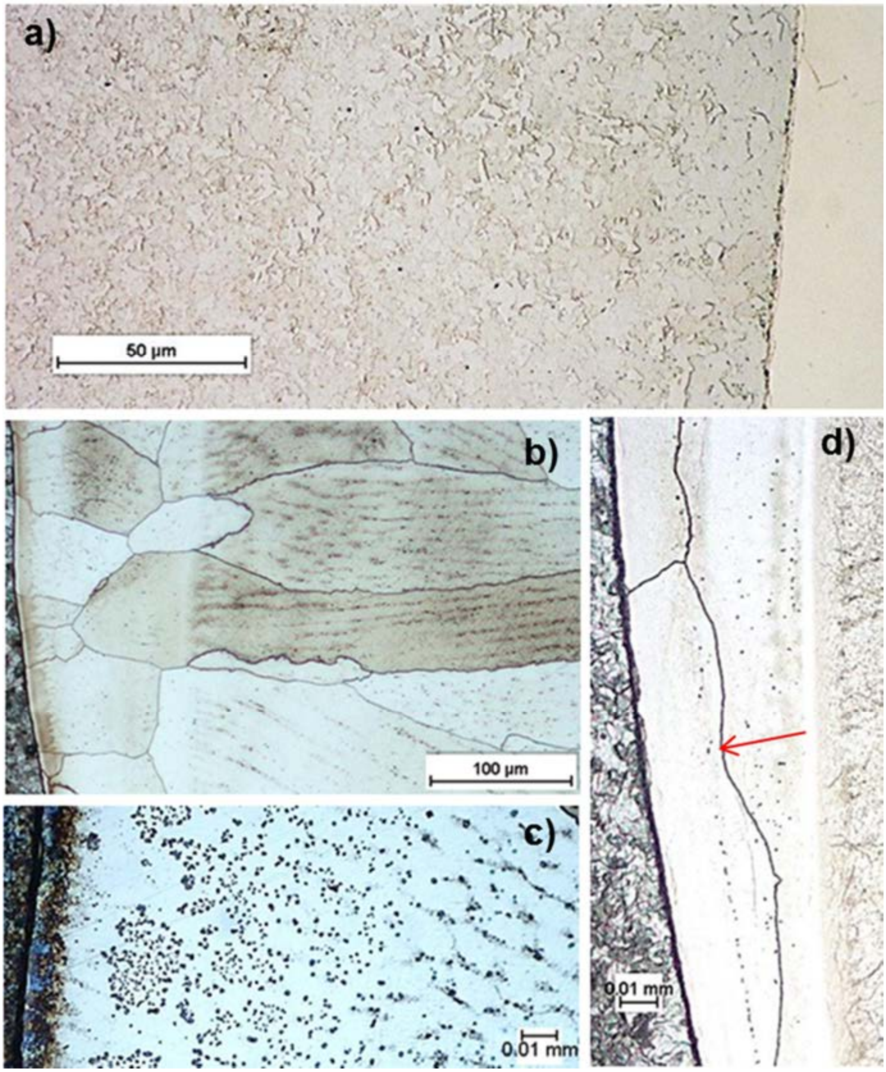

Figure 77. Microstructure of the PWHT SA 508 – Alloy 52 interface: a) CDZ on the SA 508 side and the dark etched fusion line, b) Alloy 52 weld metal along the fusion line, c) extensive precipitation in the weld metal close to the fusion line, and d) a Type II boundary (red arrow).

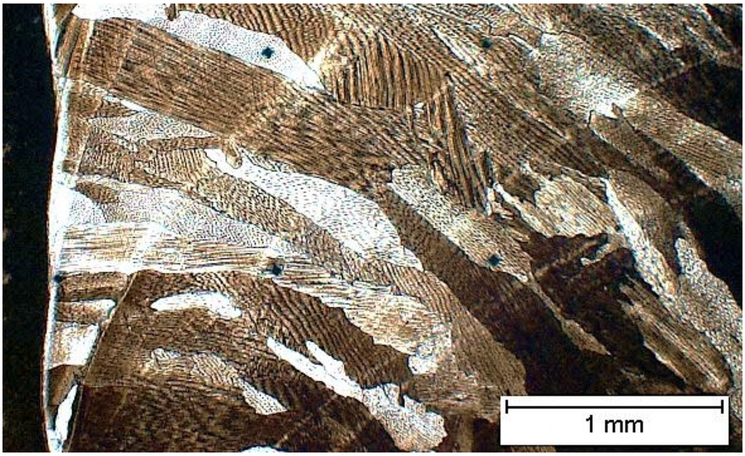

Figure 78. Alloy 52 weld metal after PWHT.

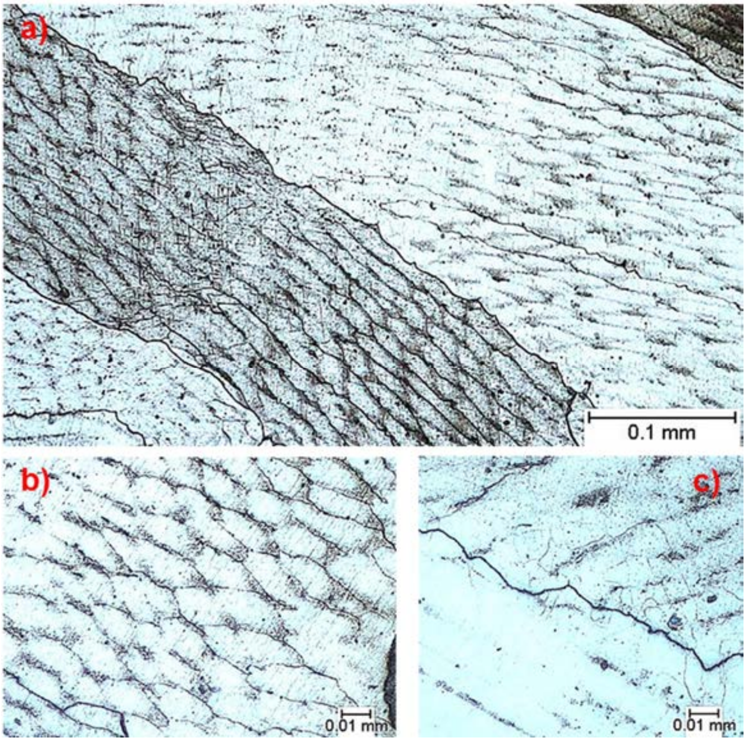

Figure 79. Microstructures of Alloy 52 weld metal after PWHT: a) several grains, b) close view of the cellular structure, and c) close view of a solidification grain boundary.

3.2.2 Scanning electron microscopy (SEM)

SEM pictures of the as-welded and PWHT conditions of the Alloy 52 NG DMW are shown in Figures 80 and 81, respectively. Emphasis is put on the differences caused by the PWHT in the SA 508 HAZ: the carbon-depleted zone is increased after PWHT (from about 30 to 80 µm) and carbides are dissolved to a great extent, Figure 80 and 81.

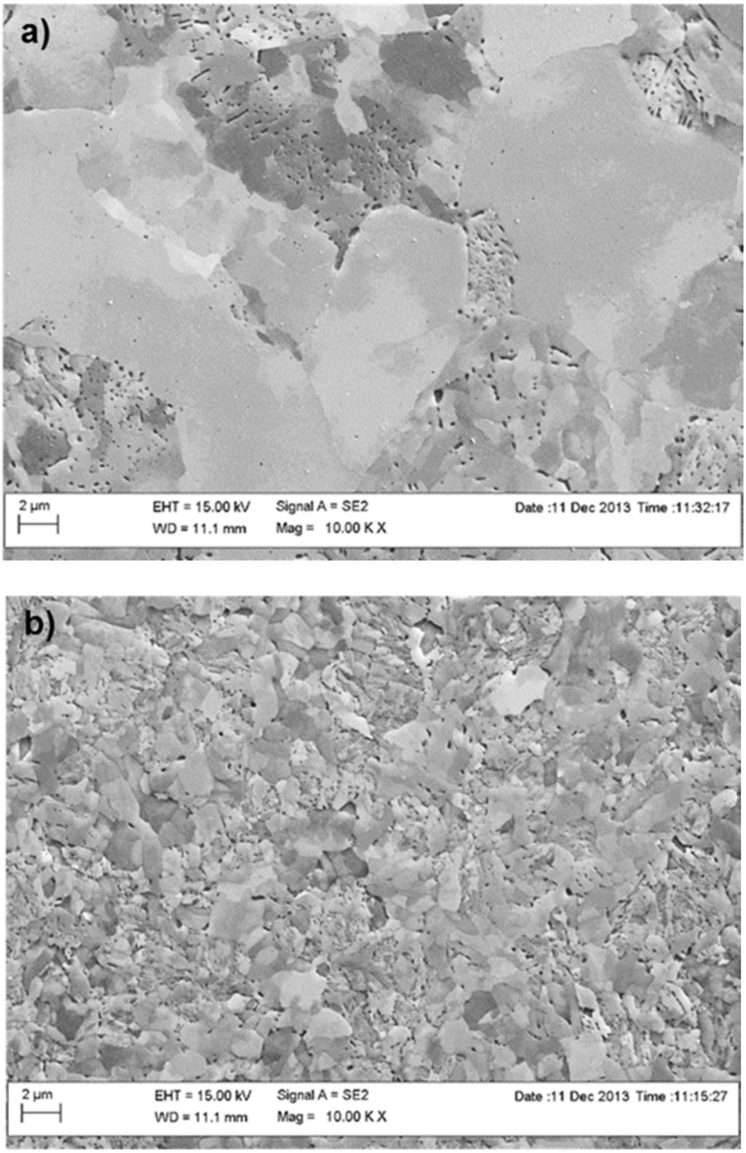

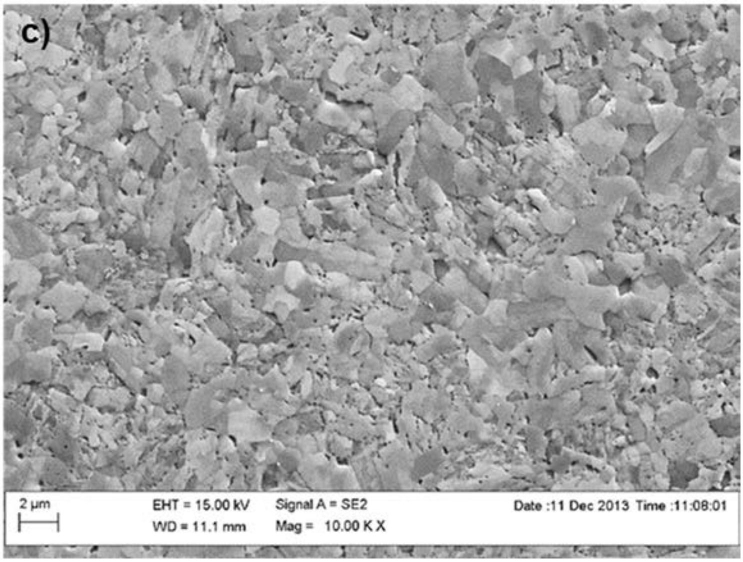
c)
2 µm
EHT = 15.00 kV
WD = 11.1 mm
Signal A = SE2
Mag = 10.00 K X
Date :11 Dec 2013 Time :11:08:01

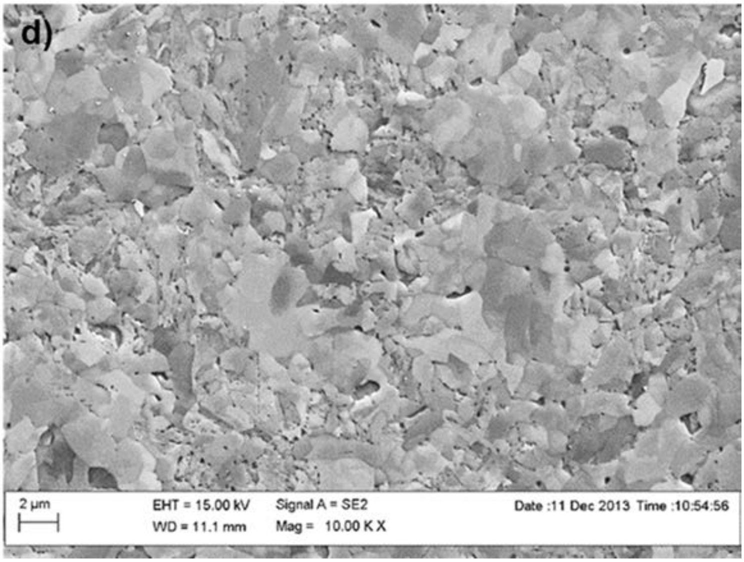
d)
2 µm
EHT = 15.00 kV
WD = 11.1 mm
Signal A = SE2
Mag = 10.00 K X
Date :11 Dec 2013 Time :10:54:56

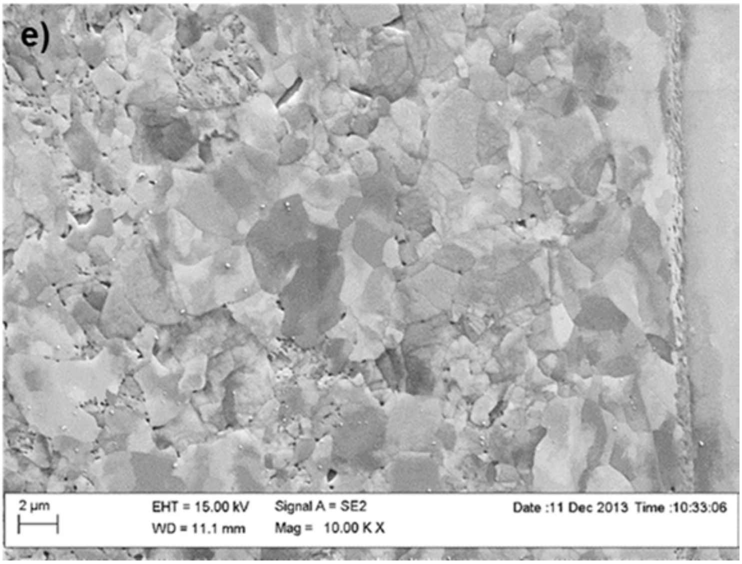

Figure 80. SA 508 HAZ microstructure of the as-welded condition of Alloy 52 NG DMW, with a) base metal showing coarse ferrite grains with bainite clusters, b) HAZ at 360 µm from the fusion line, c) grain refining zone at 120 µm from the fusion line, d) grain refining zone at 50 µm from the fusion line and e) grain coarsening zone and fusion line with Alloy 52.

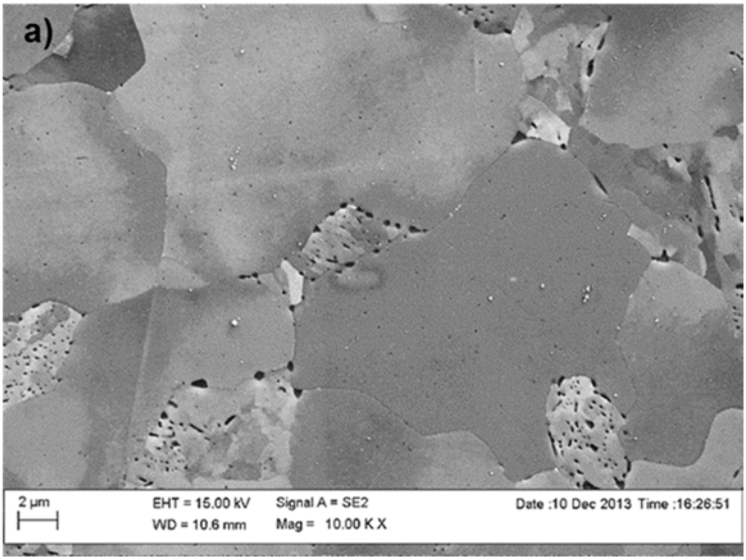

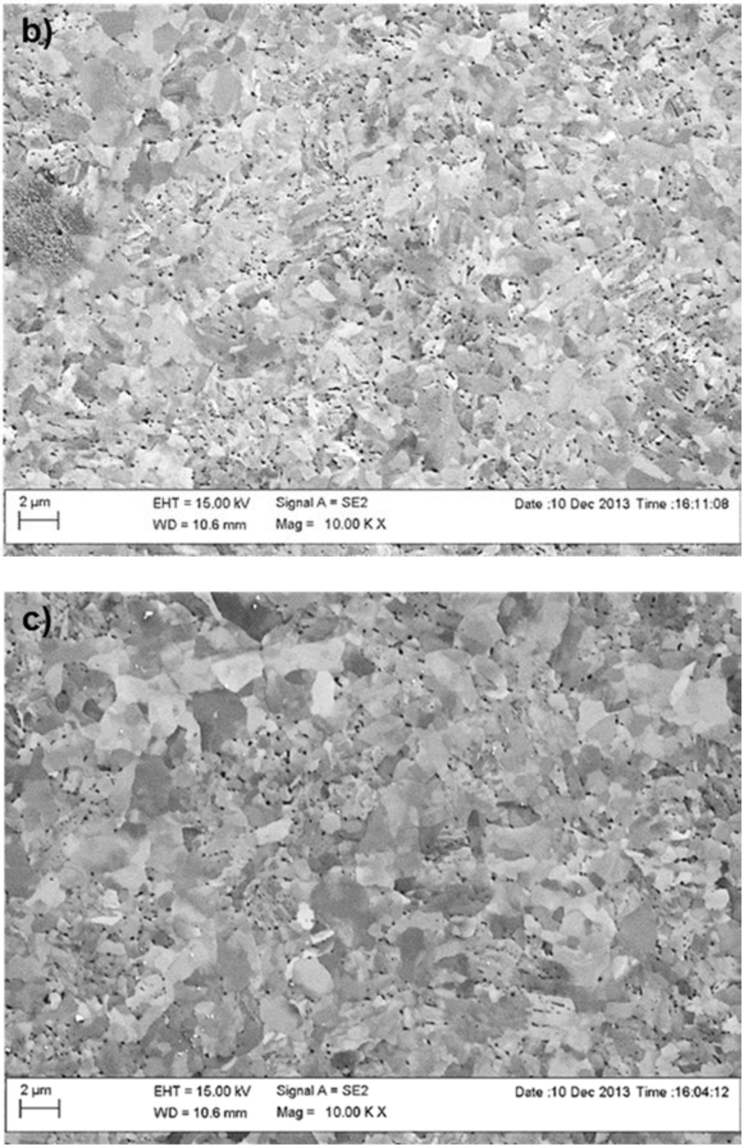
b)
2 µm
EHT = 15.00 kV
WD = 10.6 mm
Signal A = SE2
Mag = 10.00 K X
Date :10 Dec 2013 Time :16:11:08
c)
2 µm
EHT = 15.00 kV
WD = 10.6 mm
Signal A = SE2
Mag = 10.00 K X
Date :10 Dec 2013 Time :16:04:12

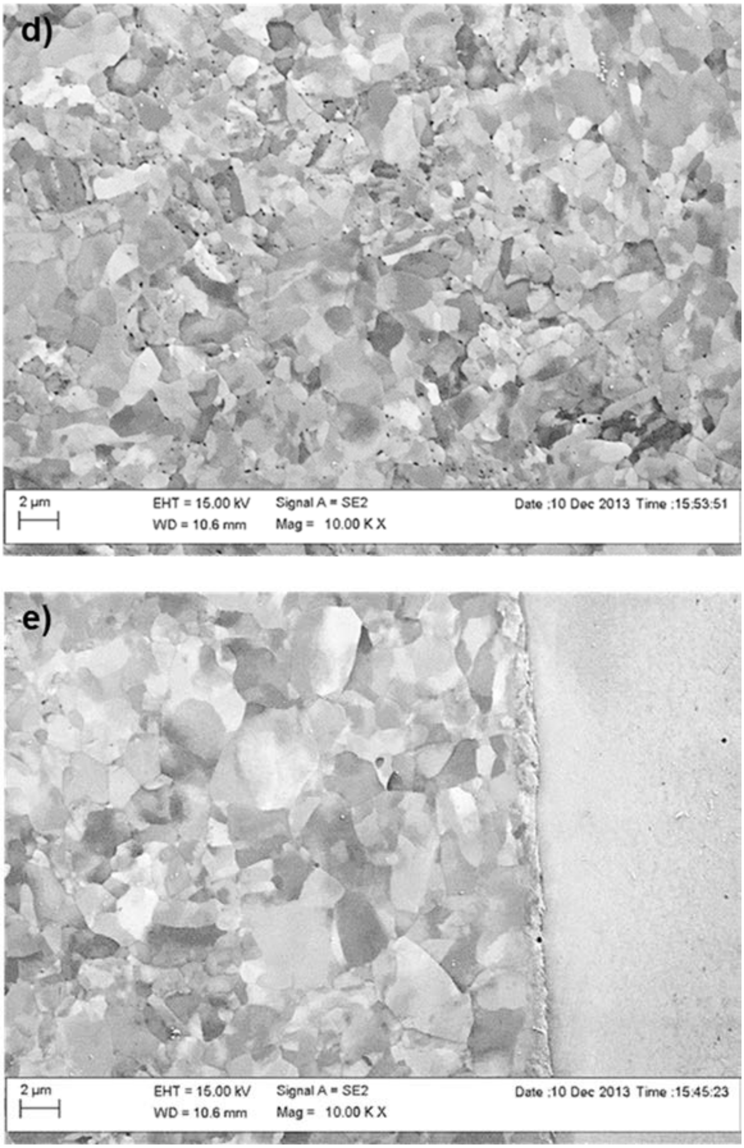

Figure 81. SA 508 HAZ microstructure of the PWHT condition of Alloy 52 NG DMW, with a) base metal showing coarse ferrite grains with bainite clusters, b) HAZ at 360 µm from the fusion line, c) grain refining zone at 120 µm from the fusion line, d) grain refining zone at 50 µm from the fusion line and e) grain coarsening zone and fusion line with Alloy 52.

In both condition, grain refining occurs from the SA 508 base metal toward the fusion line due to increasing experienced temperatures during welding. Grain coarsening and carbon depletion occur at the fusion line: no carbides and only ferrite grains remain in the LAS side. No difference is noted between the base materials (Figure 80a and 81a) and the beginning of the grain refining zones (Figure 80b and 81b) after PWHT. However, when comparing the microstructures closer to the fusion line (Figures 80c and d and 81c and d) and the fusion lines (Figure 80e and 81e), PWHT appears to increase carbon depletion. At 120 µm from the fusion line, the PWHT condition shows already slightly less carbides. At 50 µm and closer, it becomes obvious that almost no carbides remain after PWHT while they are still numerous in the as-welded condition. The CDZ in SA 508 HAZ is increased from about 30 to 80 µm by PWHT.

SEM pictures in Figure 82 and 83 show a comparison between AW and HT Alloy 52 NG DMW, respectively. PWHT and consequent carbon migration from the base metal seem to increase carbide precipitation in the weld metal side. A featureless layer about 8 µm wide is found on the weld metal side of the PWHT fusion line (Figure 83a and b). It is free of any precipitates. Carbides start to appear after this layer in the dendritic structure. A similar layer has been associated with a planar growth zone with carbon pile-up, responsible for very high hardness levels [Alexandrov et al. 2013]. White precipitates are observed at the end of this layer (Figure 83c). Another layer is found in the as-welded condition (Figure 82b and c), but is much smaller (2 µm) and could result from cathodic protection during etching.

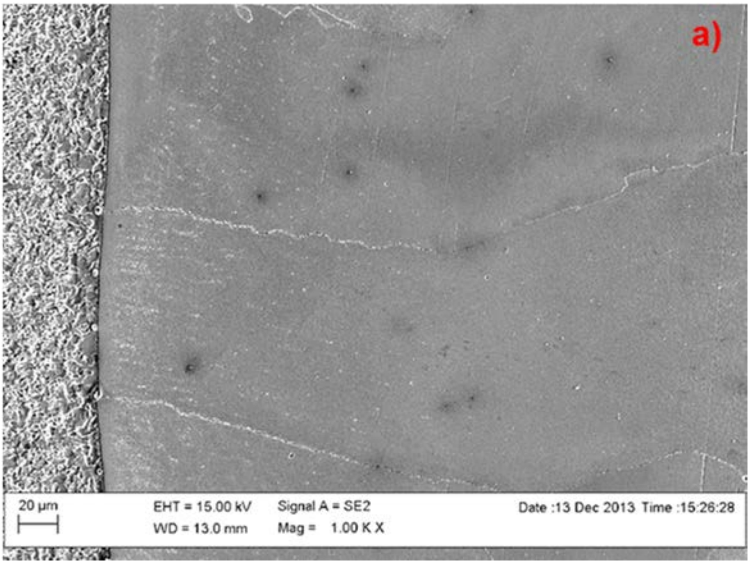

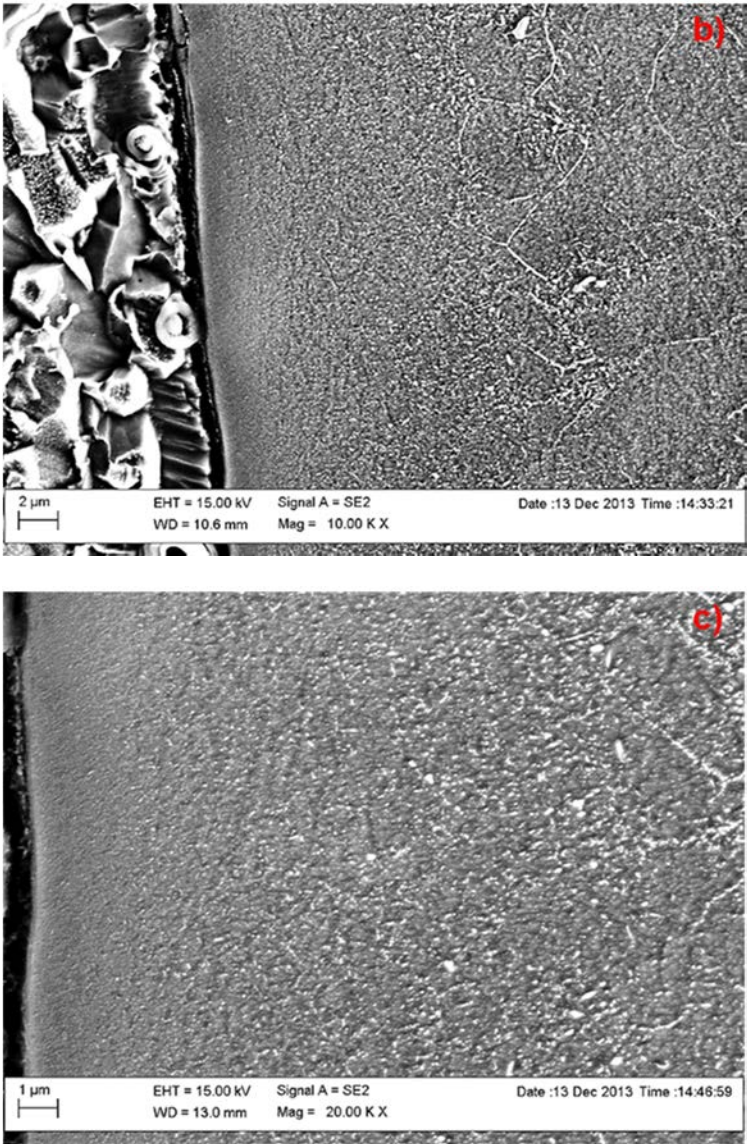

Figure 82. Fusion line and Alloy 52 weld metal side of the as-welded Alloy 52 NG DMW, with different magnifications.

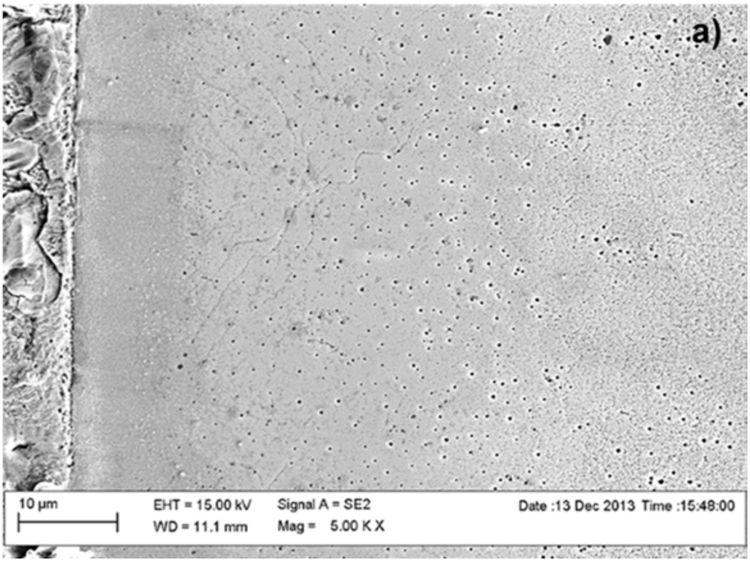
a)
10 µm
EHT = 15.00 kV
WD = 11.1 mm
Signal A = SE2
Mag = 5.00 K X
Date :13 Dec 2013 Time :15:48:00

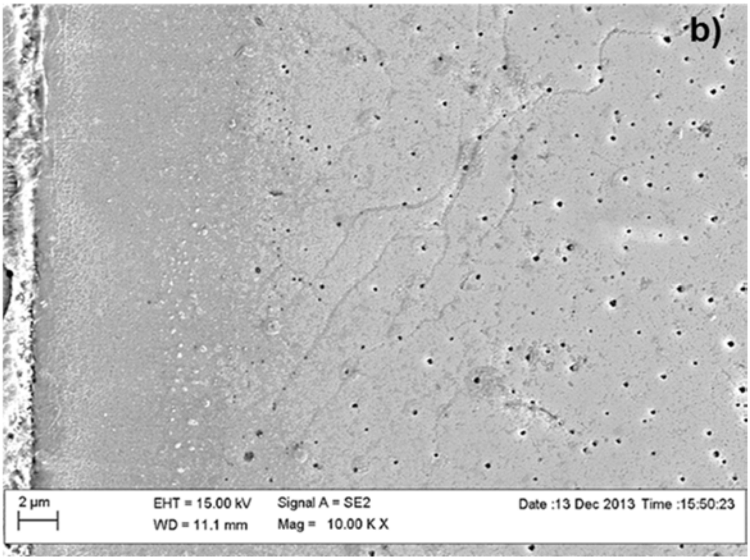
b)
2 µm
EHT = 15.00 kV
WD = 11.1 mm
Signal A = SE2
Mag = 10.00 K X
Date :13 Dec 2013 Time :15:50:23

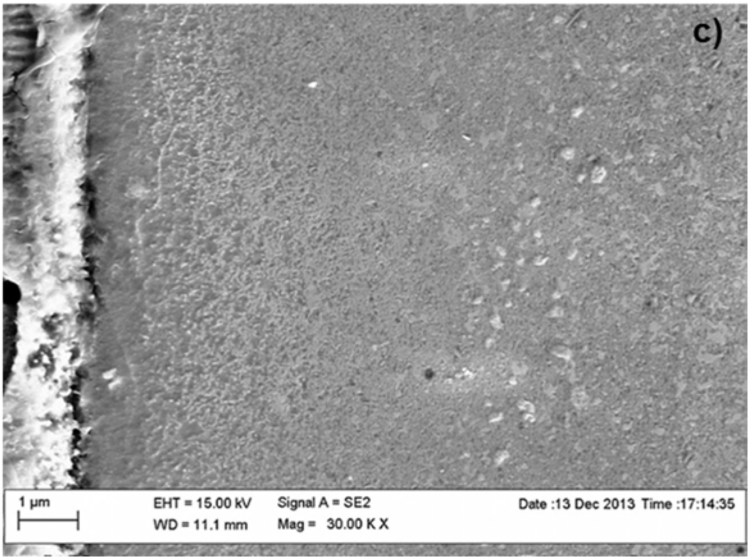

Figure 83. Fusion line and Alloy 52 weld metal side of the PWHT Alloy 52 NG DMW, with different magnifications.

3.2.3 Electron backscattering diffraction (EBSD)

EBSD maps of the microstructures of the different weld zones of as-welded and PWHT states of Alloy 52 NG-DMW are shown in Figures 84 and 85, respectively. Grain size (GS) of the SA 508 base metal a) is around 4.3 µm and the grain size of the grain refining zone b) is around 1.5 µm. The difference in grain size of the partially grain refining zone c) is just a statistical difference and, thus, the PWHT does not have an effect on the grain structure of the SA 508 HAZ fusion line d).

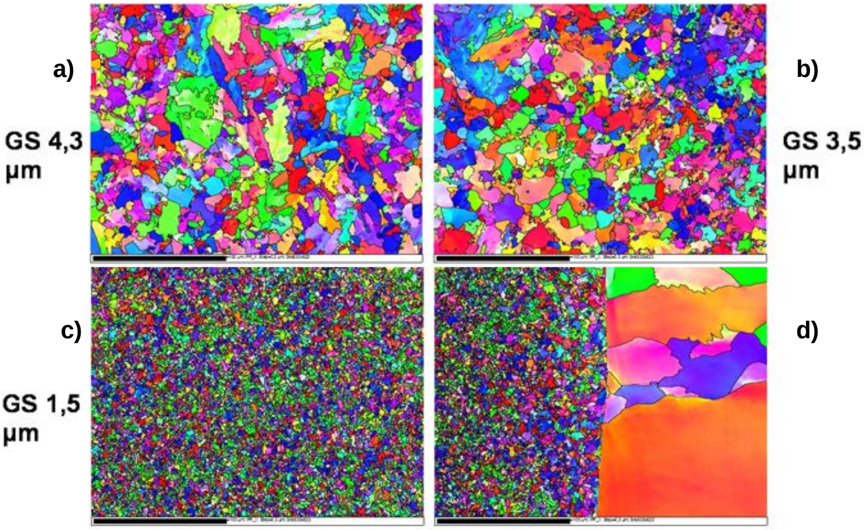

Figure 84. SA 508 HAZ microstructure of the as-welded state Alloy 52 NG DMW, a) SA 508 base metal, b) grain refining zone, c) partially grain refining zone and d) SA 508 HAZ fusion line.

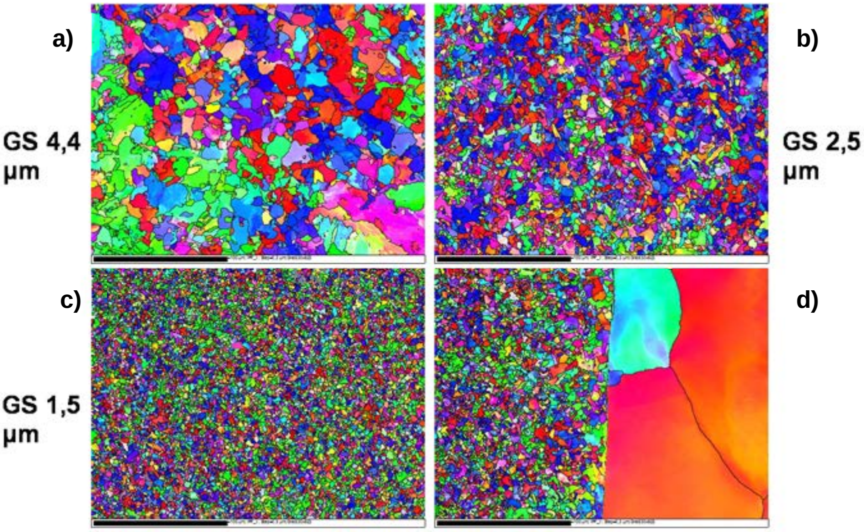

Figure 85. SA 508 HAZ microstructure of the PWHT state Alloy 52 NG DMW, a) SA 508 base metal, b) grain refining zone, c) partially grain refining zone and d) SA 508 HAZ fusion line.

Figure 86 shows EBSD maps of a location at the fusion line in which there are a partially melted zone (PMZ) and a Type II boundary present. The Type II boundary was not continuously present at the fusion line region. The size of the PMZ varied along the fusion line as well. Figure 87 shows EBSD maps of the fusion line at a location in which there is no Type II boundary present and the PMZ is observably smaller than in Figure 86. Figure 88 shows closer EBSD images of the PMZ at the SA 508 – Alloy 52 fusion line.

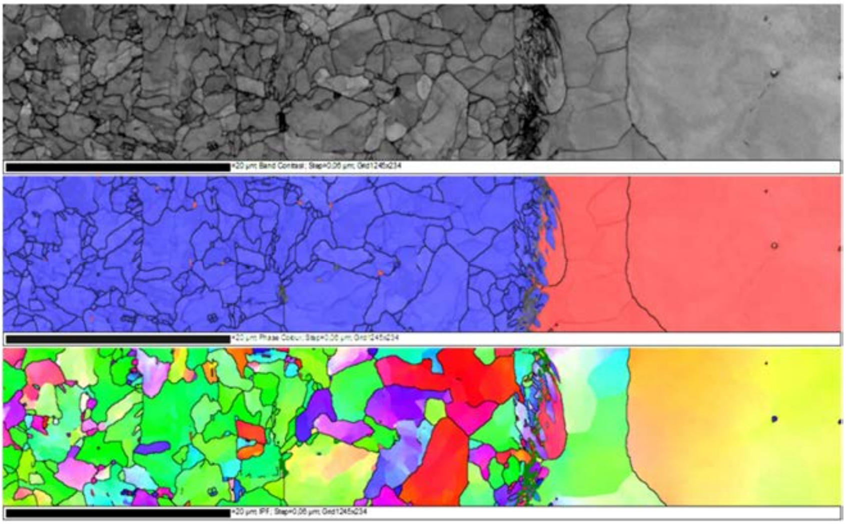

Figure 86. EBSD maps of the SA 508 – Alloy 52 fusion line with partially melted zone (PMZ) and Type II boundary.

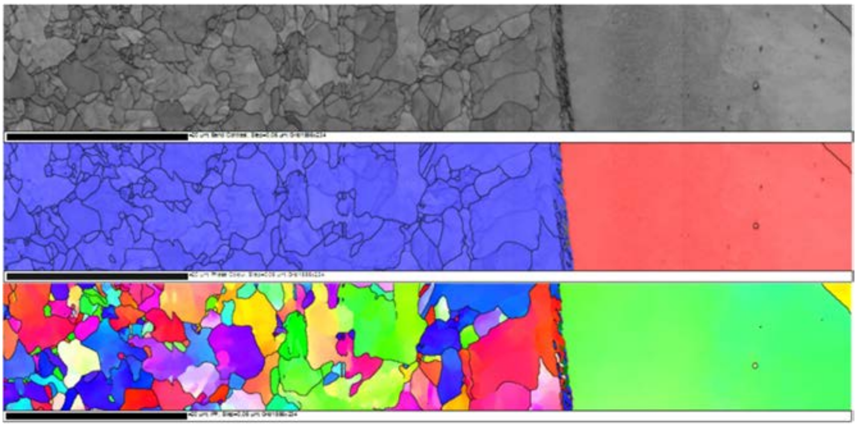

Figure 87. EBSD maps of the SA 508 – Alloy 52 fusion line region without clear PMZ and Type II boundary.

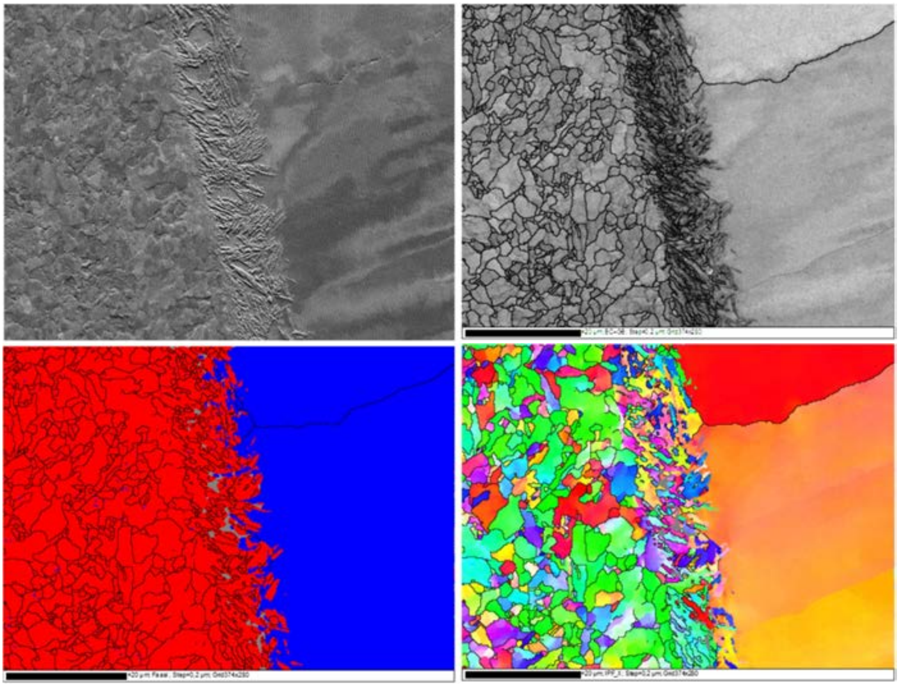

Figure 88. EBSD maps showing the PMZ at the SA 508 – Alloy 52 fusion line.

3.2.4 Energy dispersive X-ray spectroscopy (EDS)

The dilution of the main alloying elements Fe, Cr, and Ni within the SA 508 – Alloy 52 interface of the as-welded and PWHT NG-DMW can be seen from the EDS line scans presented in Figures 89 and 90, respectively. The dilution seemed to take place in a very narrow zone right next to the fusion line and the gradients of Fe, Cr, and Ni composition change are very steep. The composition gradients show some variation depending on the location in which they were measured. However, there seemed to be no noticeable trend which would indicate a significant effect of the PWHT to the width of the dilution zone at the SA 508 – Alloy 52 interface.

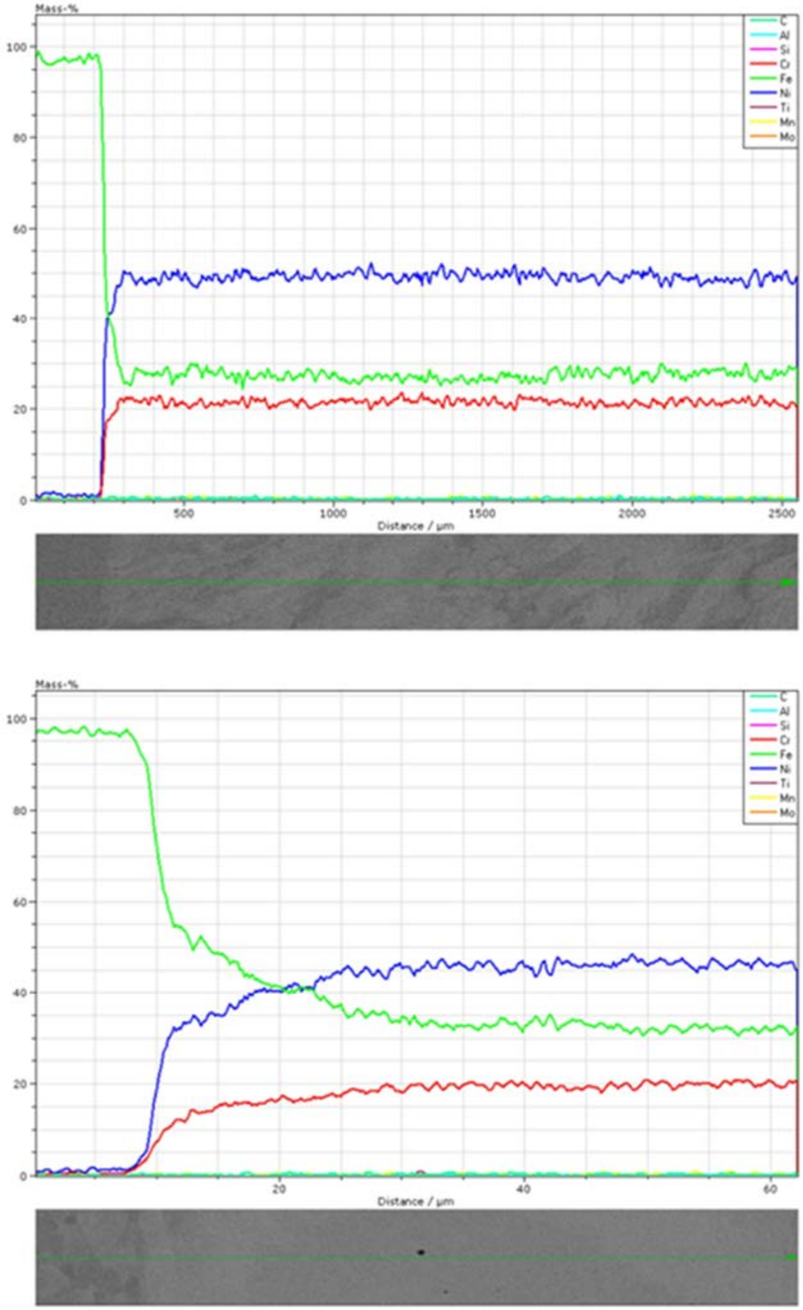

Figure 89. EDS line scans over the SA 508 – Alloy 52 interface of an as-welded state NG-DMW mock-up.

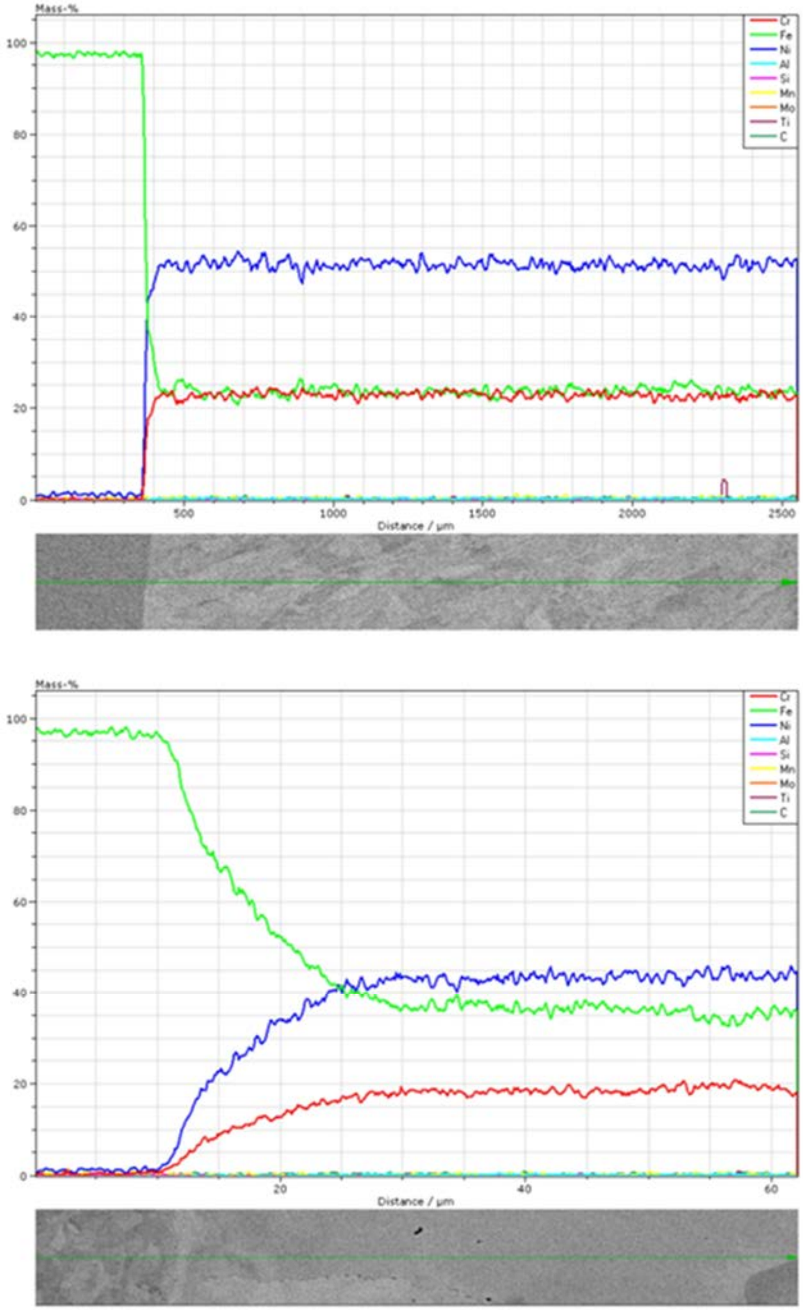

Figure 90. EDS line scans over the SA 508 – Alloy 52 interface of a PWHT state NG-DMW mock-up.

Figures 91 and 92 show EDS line scans over the SA 508 – Alloy 52 interface of the NG-DMW of as-welded and PWHT states, respectively. EDS line scans show a very steep gradient in Fe, Cr, and Ni compositions at the fusion line in locations in which the PMZ is not present. In the locations in which the PMZ is present, the change in Fe, Cr, and Ni compositions is more gradual.

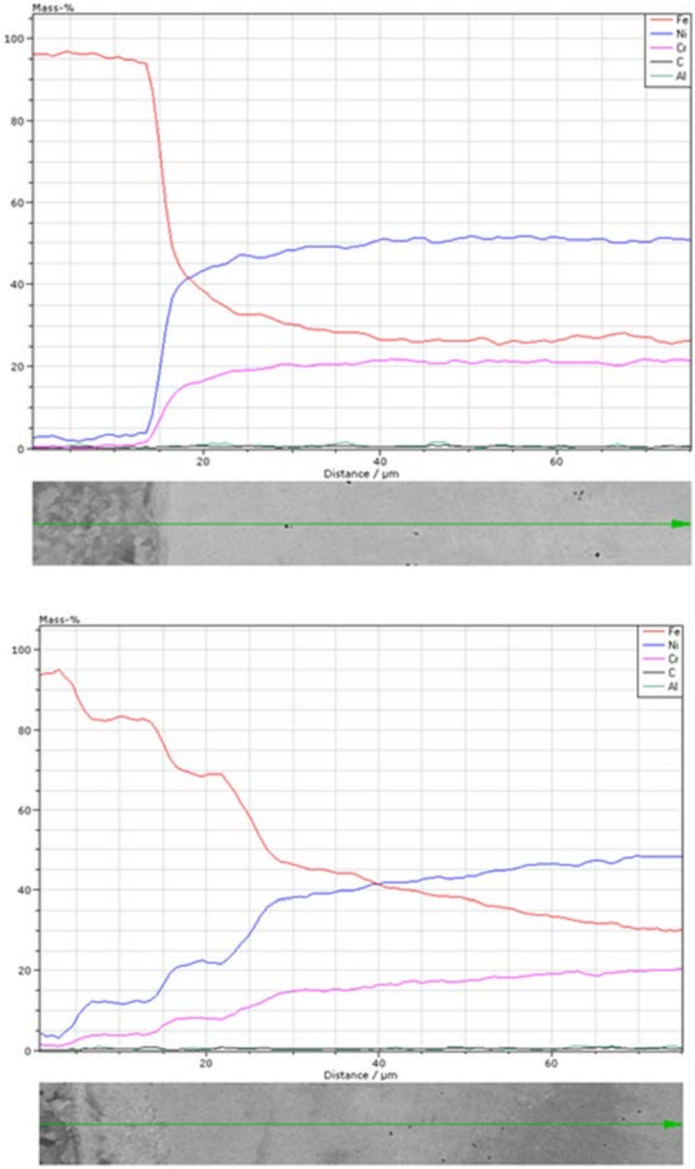

Figure 91. Dilution zone variation in as-welded Alloy 52 NG-DMW.

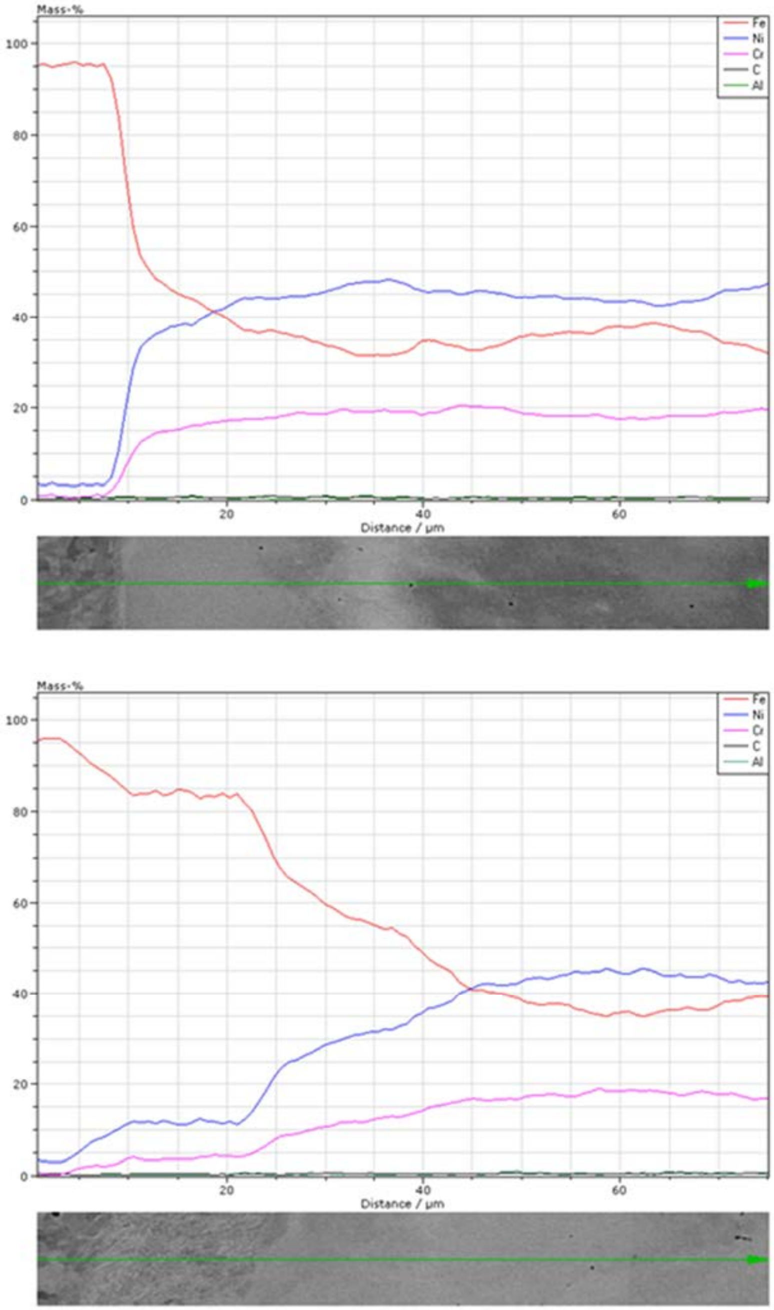

Figure 92. Dilution zone variation in PWHT Alloy 52 NG-DMW.

EAC mock-up EDS line scans were performed across the weld from three different locations of the cross-section: 1. near the surface of the weld (just below the carbon steel from the interface of the AISI 309 and AISI 308 cladding), 2. from the middle of the weld and 3. from the root of the weld (above the root backing weld). EDS line scans were taken from the locations presented with blue dotted lines in Figure 93.

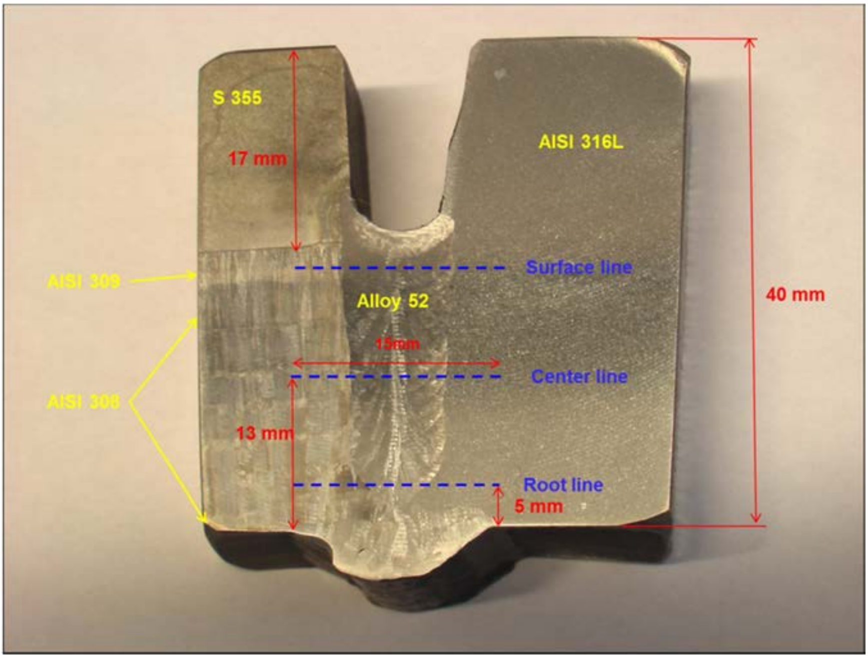

Figure 93. EAC mock-up EDS element line scan locations (marked with blue dotted lines).

In addition to the measurements across the whole weld, two more detailed line scans were made from each three locations: across the interfaces between the cladding and the weld and between the weld and the stainless piping steel. Results of the EDS line scans are presented in Figures 94 to 102. In general, the Ni composition is lower and the Fe composition higher in Alloy 52 weld metal compared to the nominal weld metal composition. Dilution zone in both interfaces is very narrow.

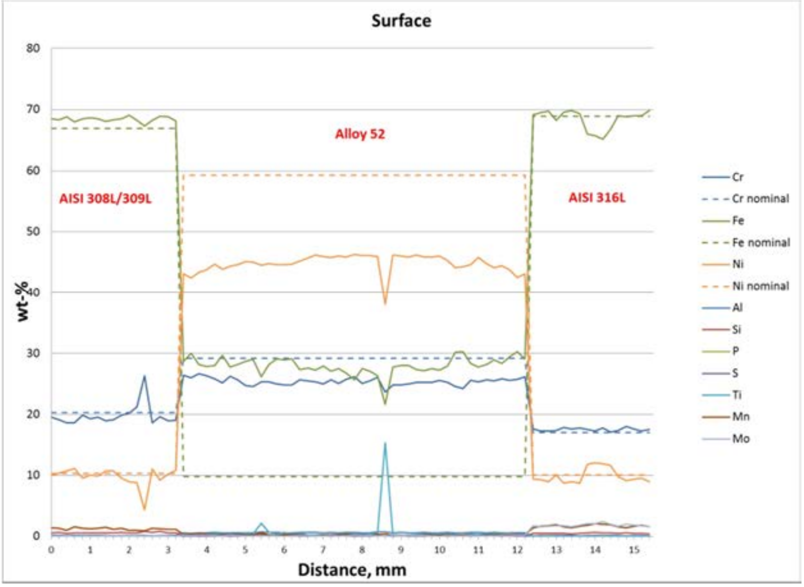

Figure 94. EDS element line scan from EAC mock-up across the weld surface. Nominal composition is marked with dotted lines.

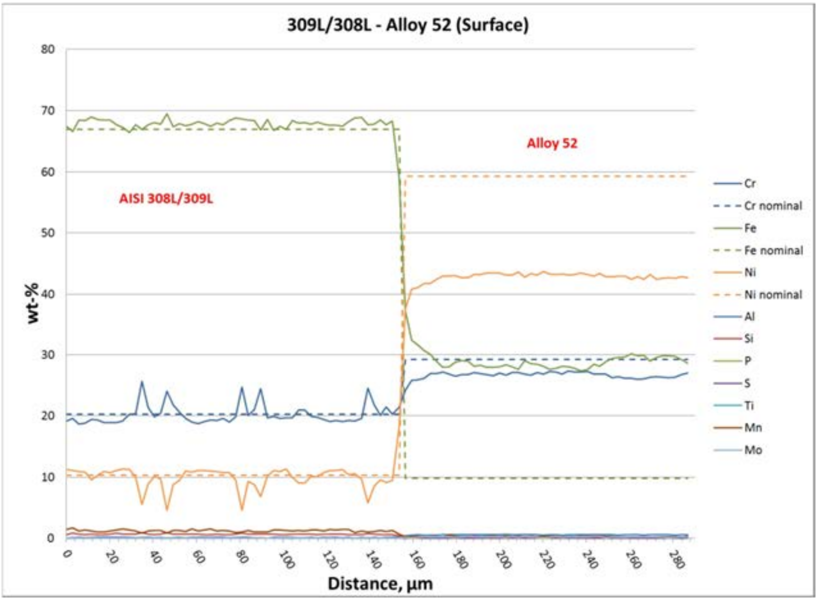

Figure 95. EDS element line scan from EAC mock-up weld surface across the Alloy 308L/309L and Alloy 52 interface. Nominal composition is marked with dotted lines.

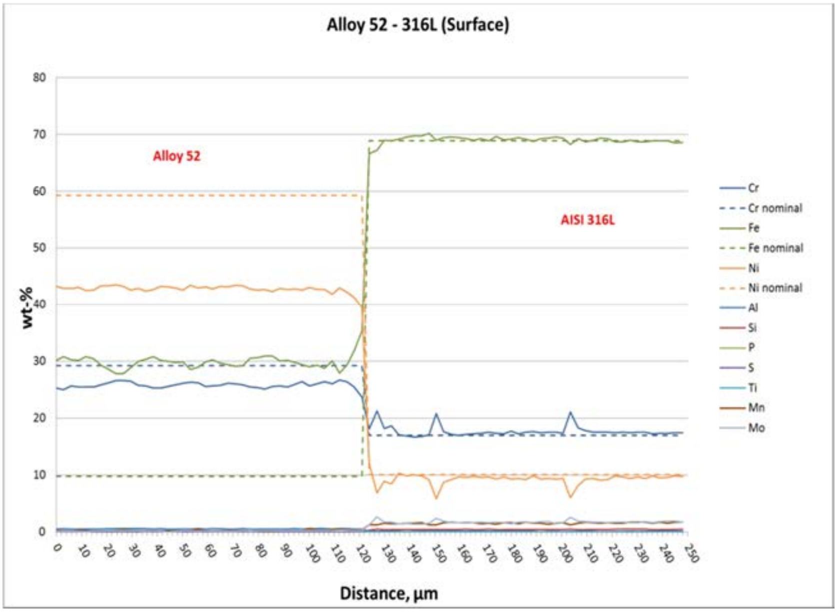

Figure 96. EDS element line scan from EAC mock-up weld surface across the Alloy 52 and AISI 316L interface. Nominal composition is marked with dotted lines.

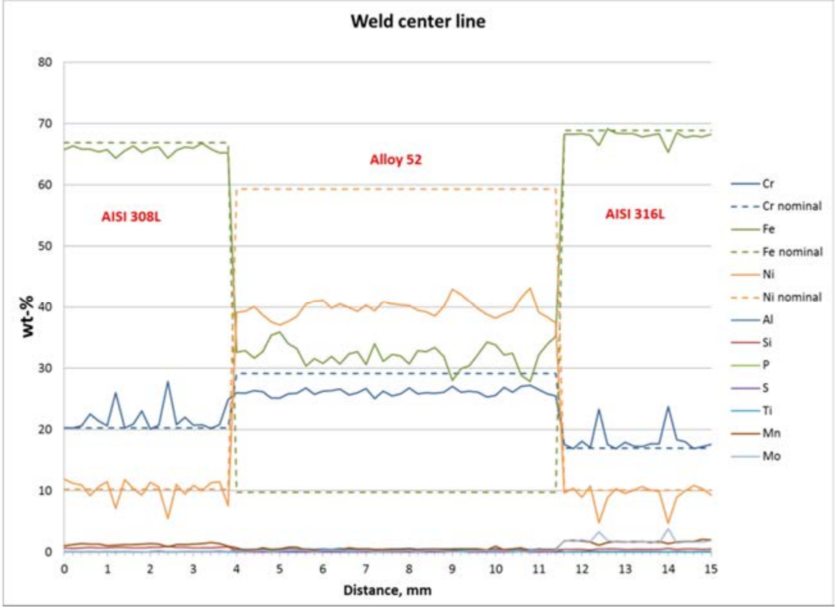

Figure 97. EDS element line scan from EAC mock-up across the weld center line.

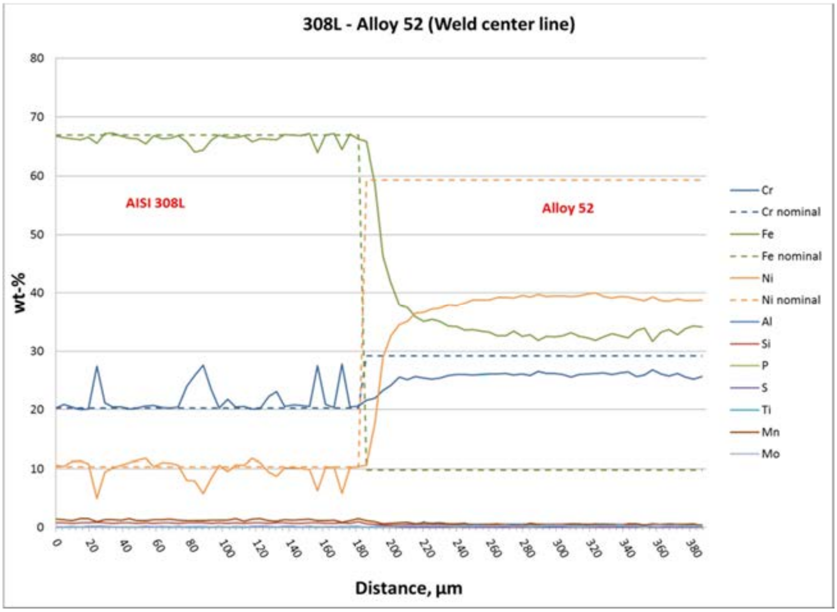

Figure 98. EDS element line scan from EAC mock-up weld center line across the Alloy 308L and Alloy 52 interface. Nominal composition is marked with dotted lines.

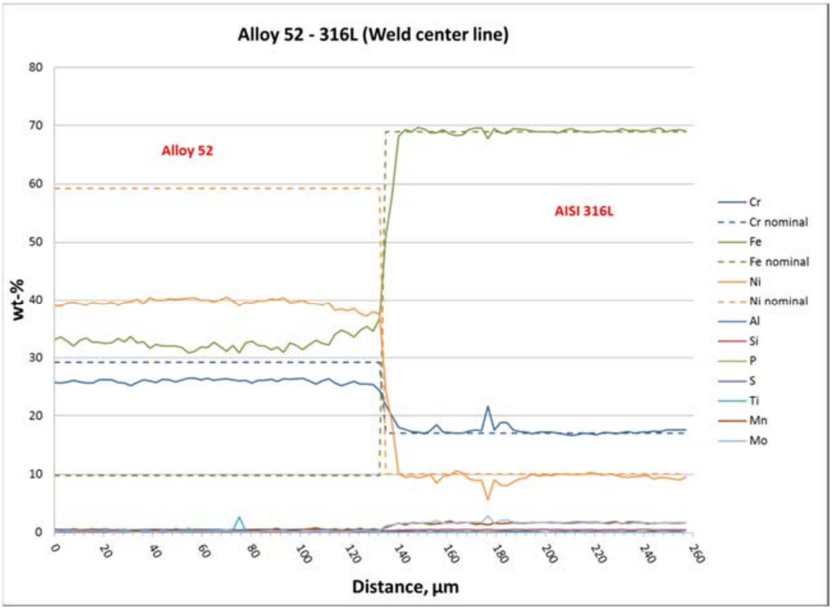

Figure 99. EDS element line scan from EAC mock-up weld centerline across the Alloy 52 and AISI 316L interface. Nominal composition is marked with dotted lines.

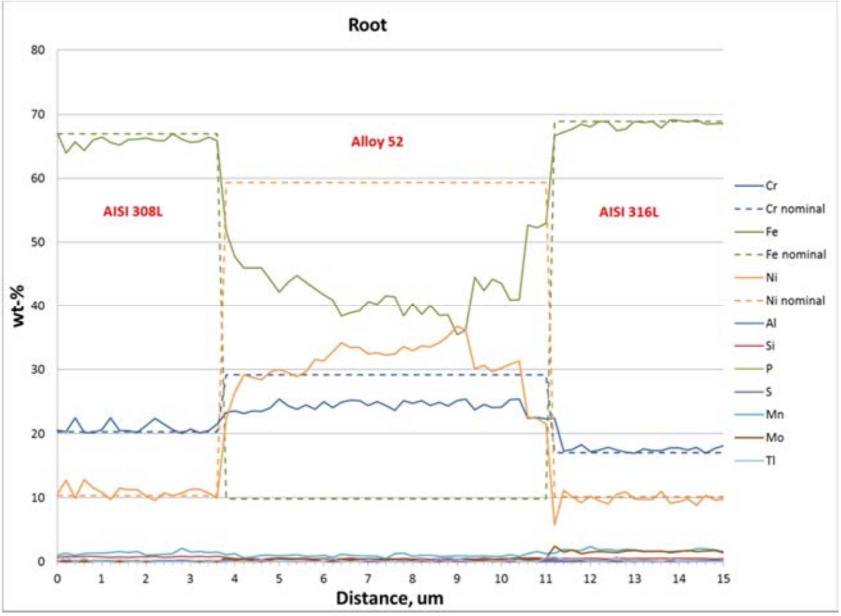

Figure 100. EDS element line scan from EAC mock-up across the weld root.

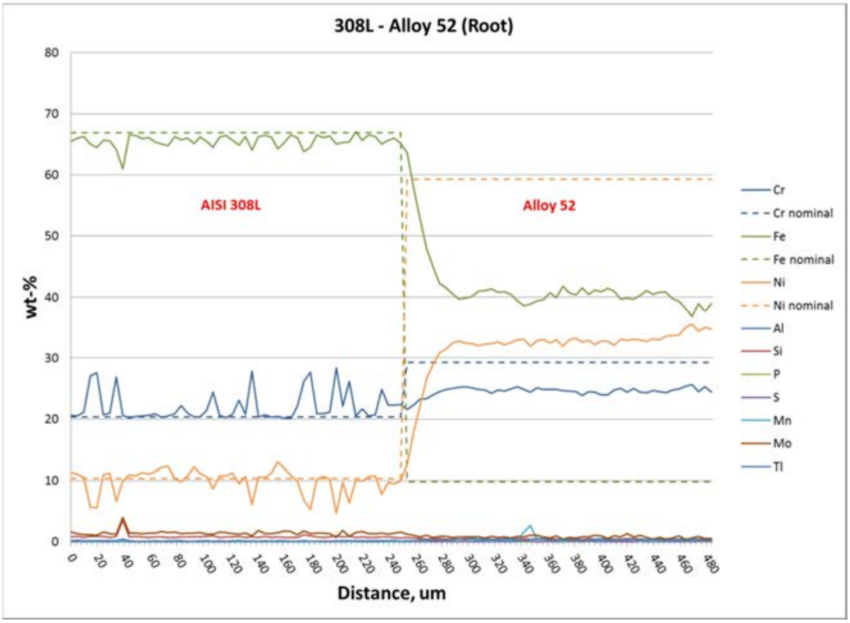

Figure 101. EDS element line scan from EAC mock-up weld root across the Alloy 308L and Alloy 52 interface. Nominal composition is marked with dotted lines.

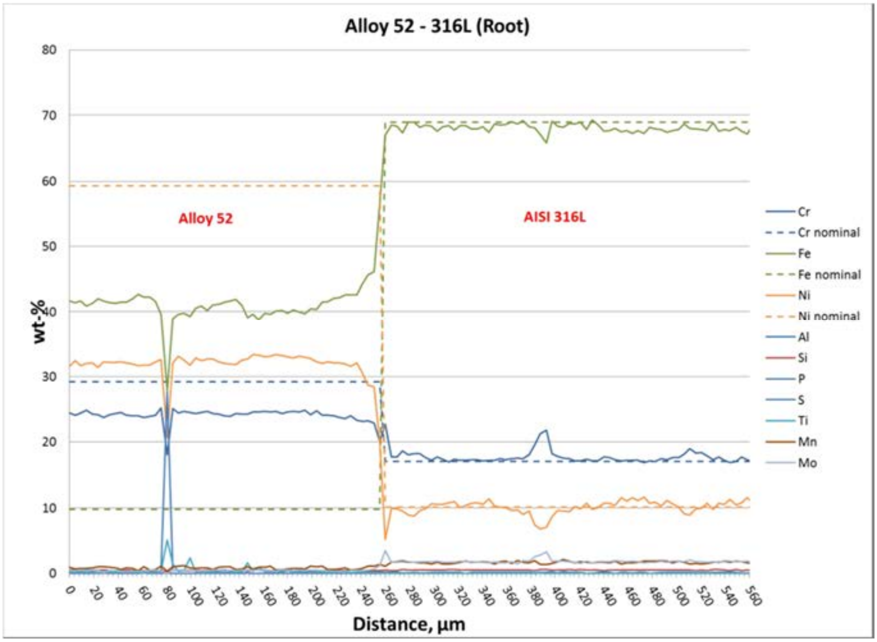

Figure 102. EDS element line scan from EAC mock-up weld root across the Alloy 52 and AISI 316L interface. Nominal composition is marked with dotted lines.

3.3 Hardness measurements

Hardness tests were conducted for both as-welded (AW) and heat-treated (HT) samples to show the hardness profiles across the SA 508/Alloy 52 interface. Microhardness tests were done with 1 mm step and 0.5 kg load, to characterize the average hardness levels and the influence of the LAS HAZ (see Figure 103 for the as-welded sample and Figure 104 for the heat-treated sample). Measurements were also made with 0.2 mm step and 0.1 kg load in order to characterize narrow zones formed at the interface (see Figures 105 and 106, respectively). Nanoindentation tests were performed to further characterize the narrow zone across the fusion line. Nanoindentation tests were performed at the AW and HT interfaces with 15 mN maximum load and 50 µm steps (Figures 107 and 108), and with 5 mN load and 25 µm steps (Figures 109 and 110). It has to be noted that the nanoindentation hardness values are calculated with the Oliver&Pharr method and cannot be directly compared to the values of the other hardness measurements.

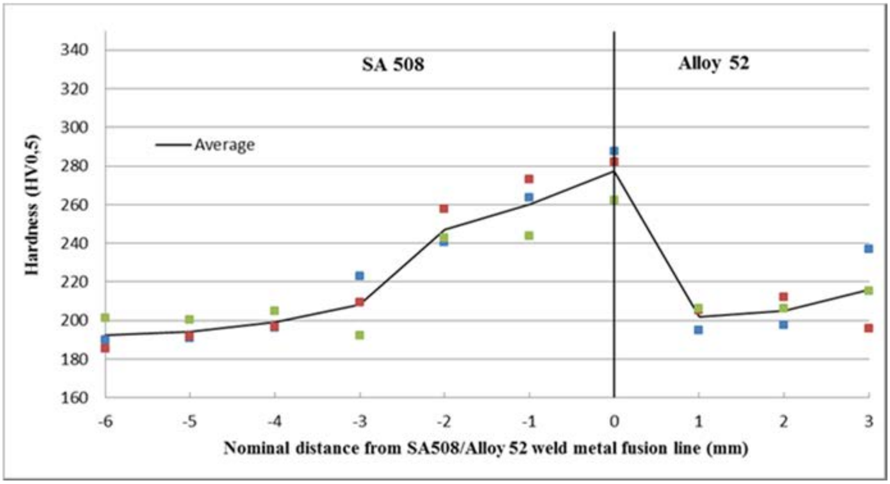

Figure 103. Microhardness profile of the AW SA 508/Alloy 52 interface.

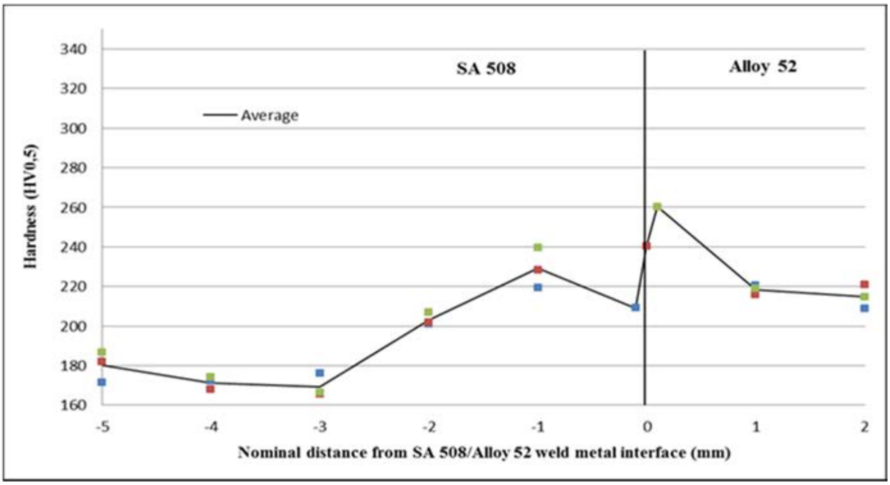

Figure 104. Microhardness profile of the HT SA 508/Alloy 52 interface.

In the AW sample, hardness increases from 190 HV in the LAS base metal to 270 HV in the LAS HAZ. Close to the fusion line, the microhardness measurements show that hardness drops to 230 HV in the LAS CGZ and CDZ. The weld metal hardness is about 210 HV. In the HT sample, hardness increases from 170 HV in the SA508 base metal to 230 HV in the grain-refined LAS HAZ. A drop to 210 HV is seen on the LAS side of the fusion line due to grain-coarsening zone and CDZ. Hardness in the weld metal is 215 HV. A hardness peak is present on the weld metal side of the fusion line. This is confirmed by the microhardness testing done with 0.2 mm step and 0.1 kg load: hardness is the lowest on the LAS CGZ and CDZ (190–210 HV) and increases drastically on the weld metal side (330 HV) close to the fusion line (less than 50 µm distance). Hardness levels are lower than in the AW sample due to tempering and grain coarsening. However, PWHT affects the microstructures at the fusion line leading to a strong mismatch from 190 HV in the LAS to 340 HV in the weld metal.

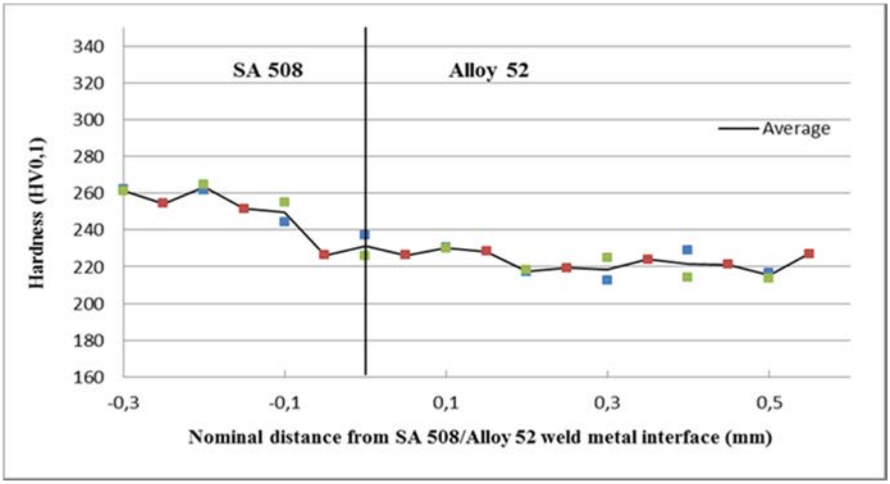

Figure 105. Microhardness profile across the AW SA 508/Alloy 52 interface.

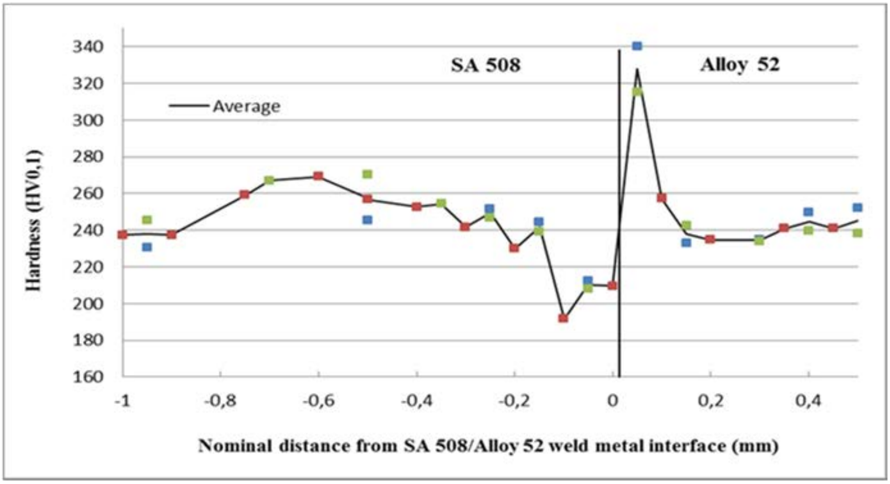

Figure 106. Microhardness profile across the HT SA 508/Alloy 52 interface.

The parameters used for the nanoindentation tests with 50 µm steps were:

- Acquisition rate: 20 Hz
- Maximum load: 15 mN
- Linear loading
- Loading/ unloading rate: 20 mN/min
- Pause: 15 s
- Step: 50 µm.

The parameters used for the nanoindentation test with 25 µm steps were:

- Acquisition rate: 20 Hz
- Maximum load: 5 mN
- Linear loading
- Loading/ unloading rate: 15 mN/min
- Pause: 10 s
- Step: 25 µm.

The nanoindentation test results in Figures 107 and 108 are done with 50 µm step and in Figures 109 and 111 with 25 µm step to confirm that the hardness peak forms in the weld metal very close to the interface after PWHT. No peak is detected in the AW condition. Figure 110 shows the corresponding indentations with 25 µm step for the HT sample. Figures 112 and 113 show that the hardness decrease in the HAZ CGC and CDZ is accentuated by PWHT. This is related to increased carbon migration from the LAS to the weld metal. With 10 µm step, the nanoindentation test in Figure 114 shows clearly the hardness peak in the HT condition. Similar hardness levels are found further away in the weld metal in both conditions. Hardness starts to increase at about 30 µm from the fusion line in the weld metal, and has highest value closest to the fusion line. The hardest zone is about 5 µm distance from the fusion line.

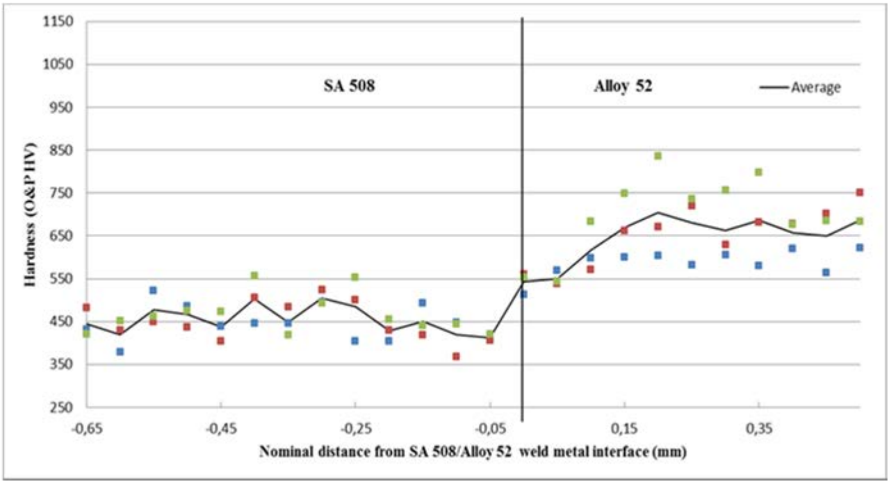

Figure 107. Nanoindentation profile across the AW SA 508/Alloy 52 interface.

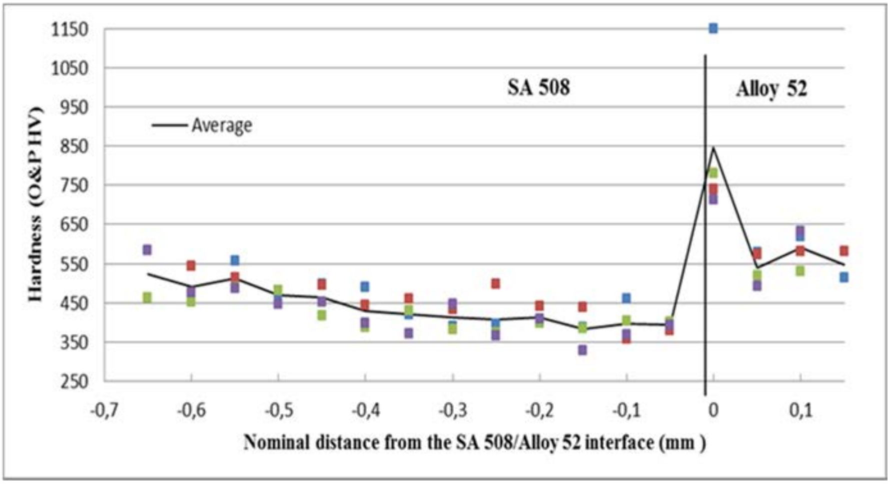

Figure 108. Nanoindentation profile across the HT SA 508/Alloy 52 interface.

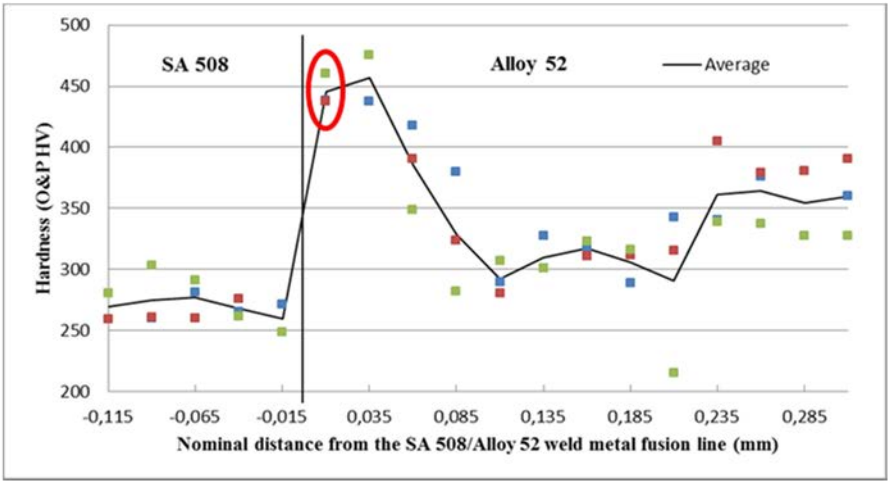

Figure 109. Nanoindentation profile across the HT SA 508/Alloy 52 interface with 5 mN load.

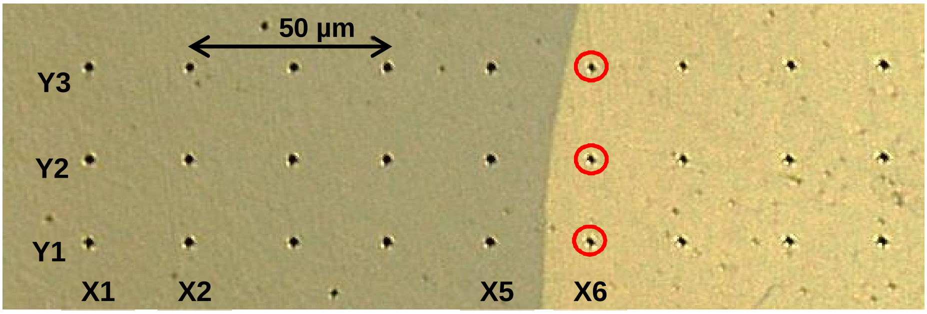

Figure 110. Corresponding 5 mN load nanoindentations across the HT SA 508/Alloy 52 interface. The red circles indicate the indentation locations inside the weld metal close to the fusion line (shown in nanoindentation profile with red circle in Figure 109).

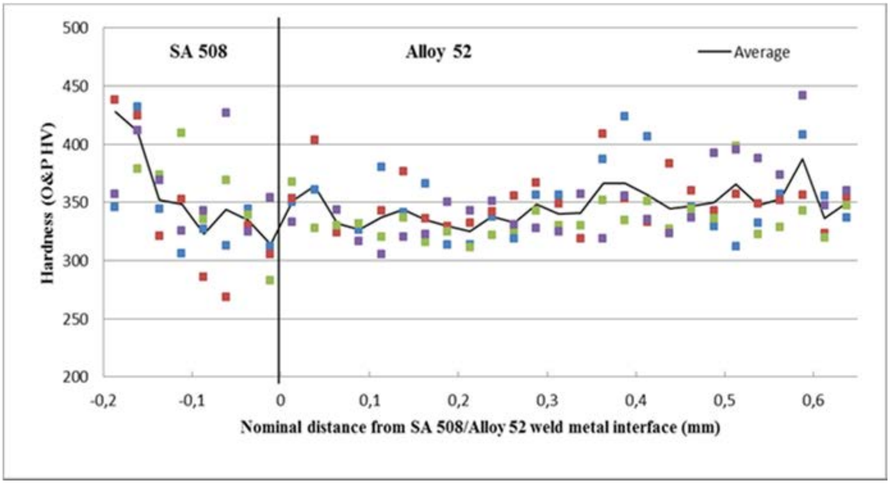

Figure 111. Nanoindentation profile across the AW SA 508/Alloy 52 interface with 5 mN load.

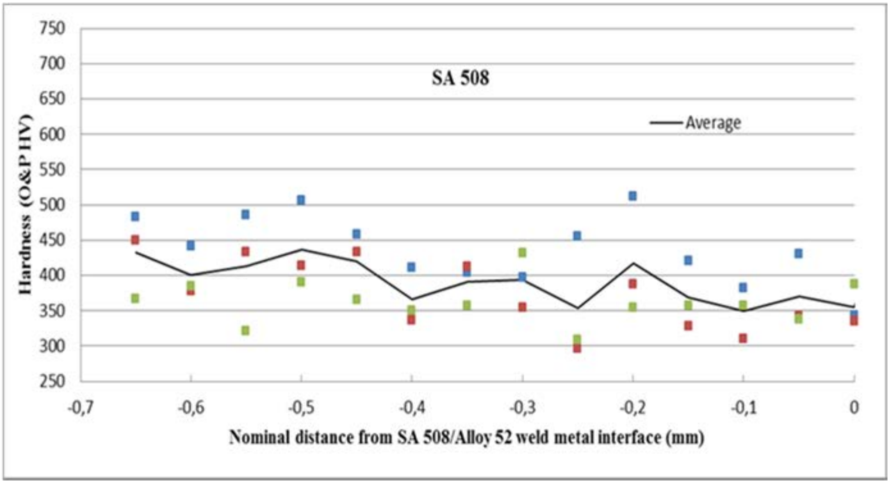

Figure 112. Nanoindentation profile across the AW SA 508 HAZ. The fusion line is reached at 0 mm.

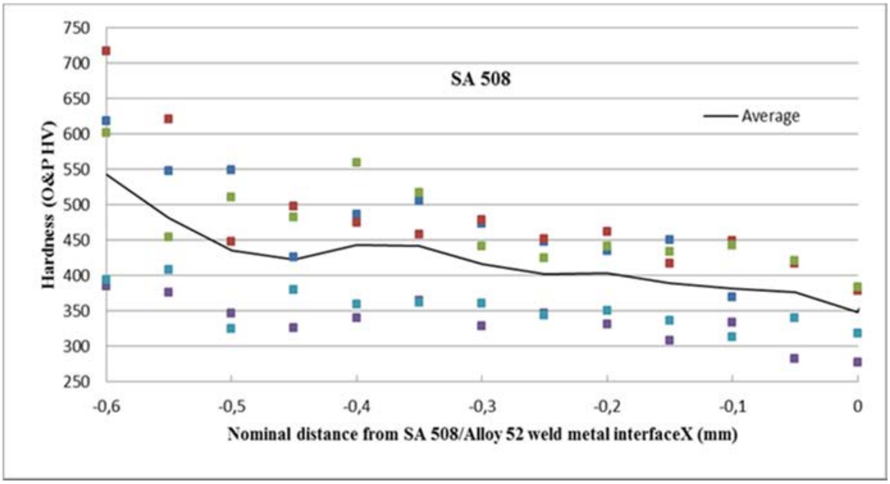

Figure 113. Nanoindentation profile across the HT SA 508 HAZ. The fusion line is reached at 0 mm.

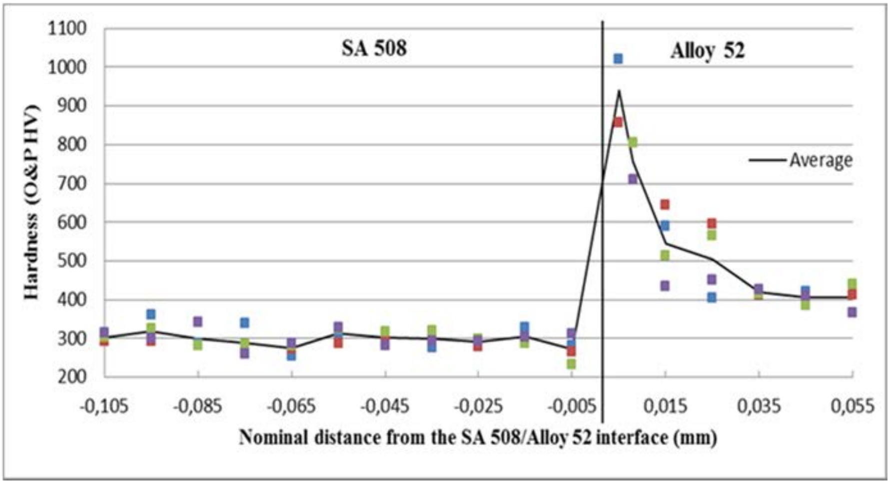

Figure 114. Nanoindentation profile across the HT SA 508/Alloy 52 interface with 5 mN load and 10 µm steps.

To conclude, PWHT increases metallurgical changes at the SA 508/Alloy 52 weld metal interface. Increased carbon migration from the LAS leads to a wider CDZ and lower hardness in the LAS HAZ. Simultaneously, carbon pile-up in the weld metal leads to high hardness levels. It happens close to the fusion line due to the low diffusivity of carbon in the nickel matrix. This hardness peak was confirmed by micro- and nanoindentation tests and has been related to a light-etched band inside the weld metal. Its presence emphasizes the mechanical mismatch between the LAS and the weld metal at the interface, and may affect the cracking behavior at the fusion line region.

3.4 Tensile testing

Tensile tests of Alloy 52 NG weld mock-up materials were performed with a Robcon and MTS servohydraulic testing machines at room temperature. Both standard round bar tensile specimens with a diameter of 8 mm and an original gauge length of 30 mm, Figure 30, and miniature flat tensile test specimens with 1 x 2 mm cross-section and 8 mm gauge length, Figure 32, were used.

Specimen elongation of flat tensile specimens was measured between the specimen ends with a symmetric extension rig having two LVD-gauges on opposite sides of the specimen. Average reading of the two gauges was used as the extension value. The tests were performed under displacement control with constant velocity. Beyond the yield point the loading velocity was increased stepwise.

The tensile tests were performed according to the standard “EN ISO 6892-1:2009 Metallic materials. Tensile testing, Part 1: Method of test at room temperature”.

All tensile test specimens were cut using electric discharge machining (EDM). Round tensile specimens were cut from SA 508 base material and Alloy 52 weld metal parallel to the welding direction.

Miniature flat tensile specimens were cut parallel to the welding direction in 7 locations; from the fusion line between Alloy 52 weld metal and SA 508 base material, and from the HAZ (heat affected zone) at distances of 1 mm, 2 mm and 2.3 mm from the fusion line towards the SA 508 base material, from the SA 508 base material, the Alloy 52 weld metal as well as from AISI 308 cladding. In addition, transverse tensile specimens were cut in 2 locations, i.e., across the fusion line from SA 508 base material to Alloy 52 weld metal, and from the AISI 308 cladding material to Alloy 52 weld metal, Figure 115.

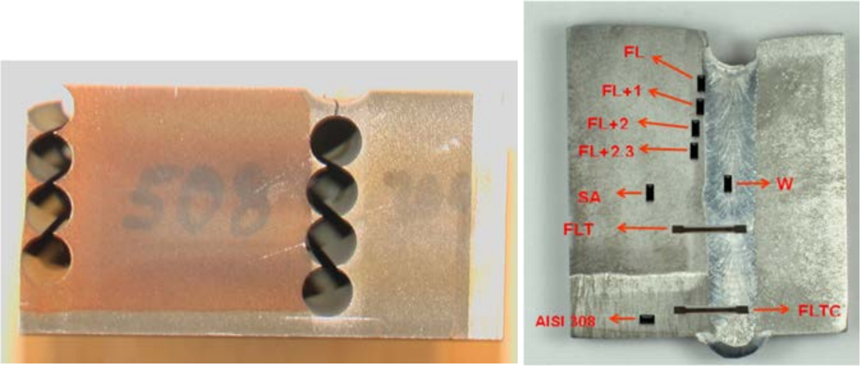

Figure 115. Cutting of standard size round bar tensile specimens from SA 508 base material and Alloy 52 weld metal and miniature tensile test specimens of Alloy 52 NG weld mock-up.

Three to seven miniature tensile tests were performed at each zone, summing up 32 miniature tensile tests. All tensile tests were made at room temperature following the practices presented in the standard SFS-EN 10 002-1 “Metallic materials. Tensile testing. Part 1: Method of test (at room temperature)”. The test matrix for the tensile tests is presented in Table 9.

Table 9. Test matrix for tensile tests performed on Alloy 52 NG.

Material / zone	Test specimen ID	Test specimen type	Orientation
Ferritic pressure vessel steel, SA 508	SA 508_1	miniature flat	longitudinal (acc. weld)
	SA 508_2		
	SA 508_3		
	1	standard size round bar	
	2		
	3		
	4		
2,3 mm from fusion line, SA 508 / Alloy 52	FL2.3_1	miniature flat	
	FL2.3_2		
	FL2.3_3		
	FL2.3_4		
	FL2.3_5		
	FL2.3_6		
	FL2.3_7		
	FL2.3_8		
2 mm from fusion line,SA 508 / Alloy 52	FL2_1	miniature flat	
	FL2_2		
	FL2_7		
1 mm from fusion line,SA 508 / Alloy52	FL1_1	miniature flat	
	FL1_2		
	FL1_7		
Fusion line, SA 508 / Alloy 52	FL_1	miniature flat	
	FL_5		
	FL_8		
Weld metal, Alloy 52	WM_1	miniature flat	
	WM_2		
	WM_3		
	WM_4		
	5	standard size round bar	
	6		
	7		
	8		
Cladding, AISI 308	308_1	miniature flat	
	308_2		
	308_3		
Across the fusion line, SA 508/weld metal	FLTC_1	miniature flat	transverse
	FLTC_2		
	FLTC_3		
Across the fusion line, AISI 308 / weld metal	FLT_1	miniature flat	
	FLT_2		
	FLT_3		

The tensile tests using miniature flat specimens were performed using a servohydraulic testing machine MTS 810, with load capacity of 100 kN. The load cell was calibrated down to 0–2 kN load range. The elongation was measured using an inductive sensor calibrated to 0–5 mm range. The approximate loading rates applied in the tests were 34 MPa/s (linear portion), 1.7%/min (linear portion), 35–40%/min (max load). The elongation percentage, non-proportional elongation at maximum force, and A_g (uniform elongation) were calculated from the plotted load-elongation curve.

3.4.1 Miniature tensile test analysis

The yield and tensile strength values, i.e. R_{p02}- and R_m-values, are measured relatively accurately with flat tensile specimens but the measured elongation values may depend slightly on specimen geometry and hence deviate from the round specimen values, because stress-strain distribution and deformation pattern depend on specimen geometry. Specimen elongation is measured in the test between the specimen ends. Hence the measured elongation includes in addition to the elongation of the uniform section of the specimen also the elongation of the rounded ends. With a correction procedure the elongation of the uniform section is calculated by subtracting the elongation of the rounded portion from the measured total elongation by an iterative procedure. The procedure takes into account the influence of rounded ends on elongation values [Valo 2014].

Two sets of measured values are calculated. In the first analysis it is assumed that only the reduced section of the specimen deforms. In the second analysis a corrected load-elongation curve is created. The correction is calculated as follows:

$$\mathrm{L}_{\mathrm{corrected}}(\mathrm{L}_0) = \mathrm{L}_{\mathrm{measured}} - 2 \cdot \sum_{\mathrm{i}=1}^{\mathrm{n}} \Delta_{\mathrm{i}}, \tag{2}$$

where

$L_{corrected}(L_0)$	corrected elongation of the reduced section length L_0,
$L_{measured}$	measured elongation value from specimen ends including the reduced section length and the rounded ends,
Δ_i	elongation of slice i in the rounded end.

The rounded end is divided into 10 equally thick slices and the elongation of each slice is calculated based on the measured load-elongation curve. The iterations are continued until the sum of corrections to the elongation values from zero up to load maximum does not change more than 0.01 mm (~ no iteration error remains).

Estimation of the elongation of slice i in the rounded end is based on the reduced stress of this slice due to increased cross-section and the relative length of the slice compared to gauge length:

$$\Delta_i = \frac{\Delta l_i}{L_0} \cdot L_m(F_m) = \frac{\Delta l_i}{L_0} \cdot L_m\left(\frac{A_0}{A_i} \cdot F_i\right), \tag{3}$$

where

$L_m(F_m)$	the corrected load-elongation curve,
Δ_l	elongation of slice i due to specimen load,
F_i	load acting on the specimen,
A_0	cross-section of the reduced section of the specimen,
A_i	cross-section of a slice in the rounded end,
Δl_i	thickness of slice i in the rounded end,
L_0	length of the reduced section of the specimen.

Even if only elongation values are corrected, the load-elongation curve will change and hence also the R_{p02}-value changes slightly. The correction is significant only in relatively soft, strain hardening materials.

All given elongation values refer to the standard EN 10002-1 with gauge length of 5 times the specimen diameter. The rectangular cross-section is transformed into an equivalent round cross-section and the elongation is calculated based on gauge length of the round specimen. Uniform elongation is measured correctly with all applied gauge lengths independently of specimen geometry. It is assumed that specimen elongation can be divided into uniform elongation and local contraction. Based on this and the equivalent round specimen radius, total elongation is calculated as:

$$A = A_g + 100 \cdot \frac{l_{tot} - l_g}{10\sqrt{\frac{a \cdot b}{\pi}}}, \tag{4}$$

where

A	total elongation,
A_g	uniform elongation,
l_{tot}	the measured total elongation,
l_g	the measured uniform elongation (up to load maximum),
a, b	cross-sectional dimensions of a flat specimen.

3.4.2 Results and discussion

The flat tensile specimen test data of Alloy 52 weld mock-up was analysed by using the nominal gauge length of $L_0 = 8$ mm and by applying the correction procedure defined above. Results for different materials / zones are shown in Table 10. Engineering stress-strain curves are presented in Figures 116–124. Average yield and tensile strengths and uniform and total elongations, based on corrected elongations, are presented in Figures 125 and 126. Yield strength divided by tensile strength describing the strain hardening capacity of a material is presented in Figure 127.

The lowest average strength of Alloy 52 NG weld mock-up, if AISI 308 cladding material is not taken into account, is in Alloy 52 weld metal with the average yield strength of 365 MPa and tensile strength of 565 MPa. Highest average strength, 668 and 753 MPa yield and tensile strength, was found in the heat affected zone 1 mm from the fusion line of base material SA 508 and weld metal Alloy 52. Fusion line area has almost as high strength values than HAZ, having average yield and tensile strength of 643 MPa and 727 MPa.

Strain hardening capacity of Alloy 52 NG weld mock-up is the highest in AISI 308 cladding and quite high in Alloy 52 weld metal. Fusion line or HAZ near fusion line (SA 508 / Alloy 52) has the lowest strain hardening capacity, Figure 127.

Average tensile strength determined with flat miniature specimens as a function of average hardness $HV_{0.5}$-values for Alloy 52 weld mock-up shows good linear correlation in case of base material SA 508 and HAZ in a distance of 1 mm and 2 mm from fusion line, Figure 128. Observed tensile strength vs. hardness correlation is in line with correlations presented in literature [Gaško & Rosenberg 2011, Pavlina & van Tyne 2008], Figure 128 and Table 11. Fusion line and weld metal average tensile strength vs. hardness seems not follow the same trend as base material SA 508 and its HAZ, Figure 128. As fusion line and weld metal are inhomogeneous, hardness and tensile test are more likely to find material volumes with different properties, thus providing firstly much bigger scatter than base material or HAZ. Secondly, strain hardening capacity may have an effect on the form of tensile strength vs. hardness correlation.

All tensile tests and hardness measurements show that mismatch is greatest near the fusion line, Figures 125, 129 and 130, Table 12. Hardness measurements show greater mismatch near the interface area than tensile testing, Figures 129 and 130. This is due to the fact that hardness test can capture more local microstructural variations than tensile test specimen. Tensile test results represent more averaged value over greater volume of material or zone. Degree of mismatch becomes different based on hardness data and strength data, but the location is the same, i.e. near the interface area. For structural integrity assessment, mismatch between two adjacent microstructural zones may be more significant than mismatch based on comparison with parent steel properties. The greatest mismatch between adjacent zones is also the near interface area, Table 12 and Figure 129. The elongation correction reduces the elongation values of flat specimens approximately as is expected.

Table 10. Results of the tensile tests of Alloy 52 NG weld mock-up.

Material / zone	Test specimen ID	Calculated with L_0				Corrected elongation			
		R_{p02}	R_m	A_g	A	R_{p02}	R_m	A_g	A
		[MPa]	[MPa]	[%]	[%]	[MPa]	[MPa]	[%]	[%]
Pressure vessel steel, SA 508	508_1	427	587	12.3	25.1	427	587	11.4	24.1
	508_2	400	575	11.7	22.1	400	575	10.7	21.2
	508_3	420	579	11.5	23.4	420	579	10.6	22.4
	average	416	580	11.9	23.5	416	580	10.9	22.6
	std deviation	11	5	0.4	1.2	11	5	0.3	1.2
Pressure vessel steel, SA 508 (standard size specimen)	1	430 / 415	583		29				
	2	445 / 415	585		32				
	3	430 / 410	584		30				
	4	420 / 395	575		32				
	average	431 / 409	582		31				
	std deviation	10.3 / 9.5	5		1				
2.3 mm from fusion line (SA 508 / Alloy 52)	FL2.3_2	438	597	13.5	24.7	438	597	12.3	23.7
	FL2.3_3	400	567	21.5	27.0	400	567	19.8	25.9
	FL2.3_4	400	561	13.7	26.7	400	561	12.6	25.5
	FL2.3_7	420	596	12.1	24.2	420	596	11.1	23.2
	FL2.3_8	520	631	13.4	27.3	520	631	12.4	26.2
	average	436	590	14.9	25.4	436	590	8.4	18.3
	std.dev.	45	25	3.4	1.2	45	25	3.1	1.2
2 mm from fusion line (SA 508 / Alloy 52)	FL+2_1	672	776	9.1	19.1	672	776	8.4	18.3
	FL+2_2	599	672	12.3	23.1	599	672	11.3	22.2
	FL+2_7	579	685	8.7	18.6	579	685	8.0	17.9
	average	617	711	10.0	21.1	617	711	9.2	20.3
	std.dev.	40	46	1.6	2.0	40	46	1.5	2.0
1 mm from fusion line (SA 508 / Alloy 52)	FL+1_1	720	807	8.1	17.8	720	807	7.5	17.1
	FL+1_2	643	727	9.8	20.0	643	727	9.0	19.2
	FL+1_7	640	727	9.8	20.0	640	727	9.0	19.2
	average	668	753	9.3	18.9	668	753	8.5	18.1
	std.dev.	37	38	0.8	1.1	37	38	0.7	1.1
Fusion line between SA 508 and Alloy 52	FL_1	520	652	24.8	33.5	520	652	23.2	32.2
	FL_5	683	750	9.6	18.6	683	750	8.8	17.9
	FL_8	725	779	9.1	20.0	725	779	8.4	19.2
	average	643	727	14.5	26.0	643	727	13.5	25.0
	std.dev.	88	54	7.3	7.5	88	54	6.9	7.1
Weld metal, Alloy 52	WM_1	285	505	37.8	43.8	285	505	33.0	42.0
	WM_2	384	585	32.0	36.3	384	585	32.8	34.9
	WM_3	427	606	24.0	29.6	427	606	32.9	28.5
	average	365	565	31.2	40.1	365	565	32.9	38.5
	std.dev.	59	43	5.6	3.8	59	43	0.1	3.5
Weld metal, Alloy 52 (standard size specimen)	5	385	626		44				
	6	460	669		40				
	7	460	660		37				
	8	430	639		38				
	average	434	649		40				
	std.dev.	35	20		3				

Cladding, AISI 308	308_1	280	517	33.9	36.8	280	517	31.6	35.2
	308_2	280	518	59.1	60.4	280	518	55.0	58.2
	308_3	280	518	57.1	60.0	280	518	53.2	57.7
	average	280	518	50.0	48.6	280	518	46.6	46.7
	std.dev.	0	1	11.4	11.8	0	1	10.6	11.5
Across the fusion line SA 508 base material / Alloy 52 weld metal	FLT_1	271	547	23.7	31.0	271	547	21.8	29.8
	FLT_2	400	542	11.7	22.1	400	542	10.7	21.3
	FLT_3	400	533	21.5	27.0	400	533	19.8	25.9
	average	336	545	17.7	26.6	336	545	16.3	25.5
	std.dev.	65	2	6.0	4.4	65	2	5.5	4.3
Across the fusion line AISI 308 cladding / Alloy 52 weld metal	FLTC_1	363	491	19.0	26.8	363	491	17.5	25.6
	FLTC_2	292	404	8.8	NA	292	404	8.1	
	FLTC_3	285	509	27.0	32.9	285	509	24.9	31.6
	average	313	468	18.2	29.8	313	468	16.8	28.6
	std.dev.	35	46	7.5	3.1	35	46	6.9	3.0

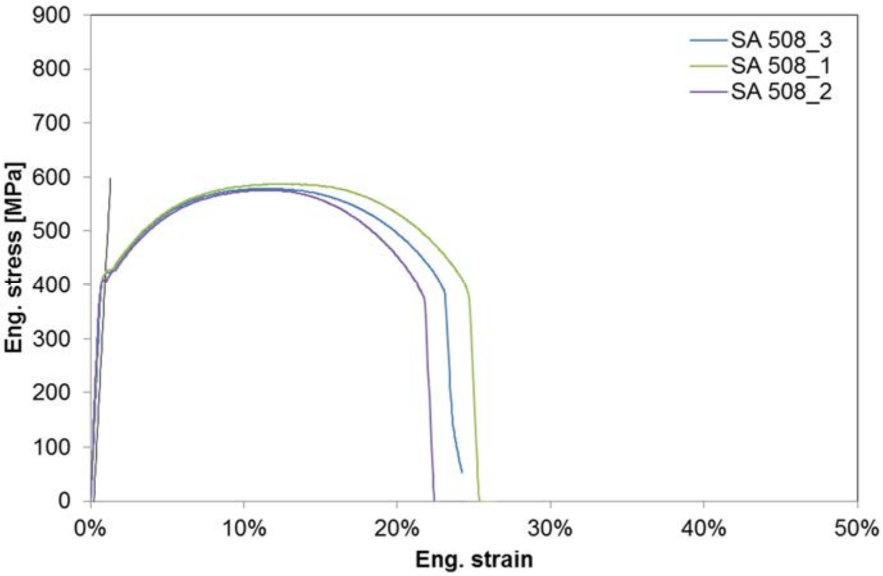

Figure 116. Miniature tensile specimen stress-strain curves of pressure vessel steel SA 508.

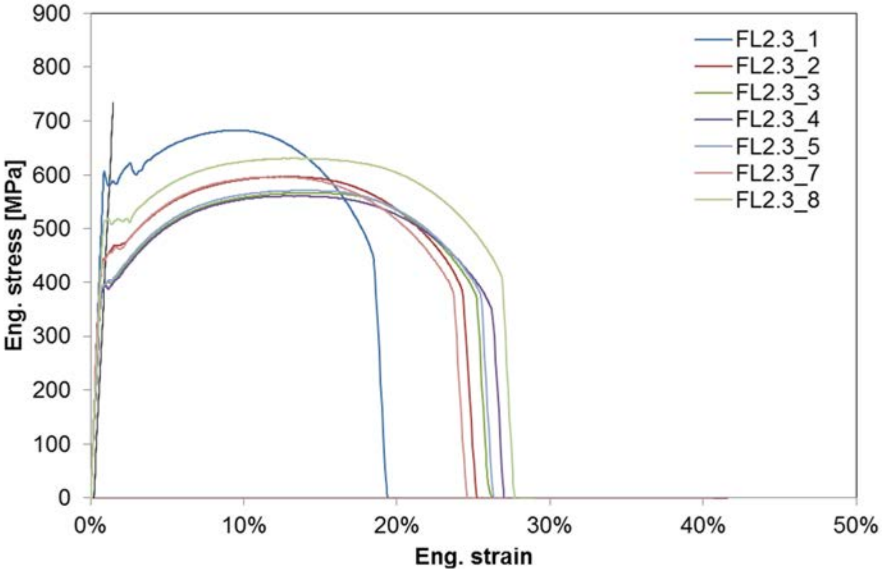

Figure 117. Miniature tensile specimen stress-strain curves of the zone about 2.3 mm from SA 508 / Alloy 52 fusion line.

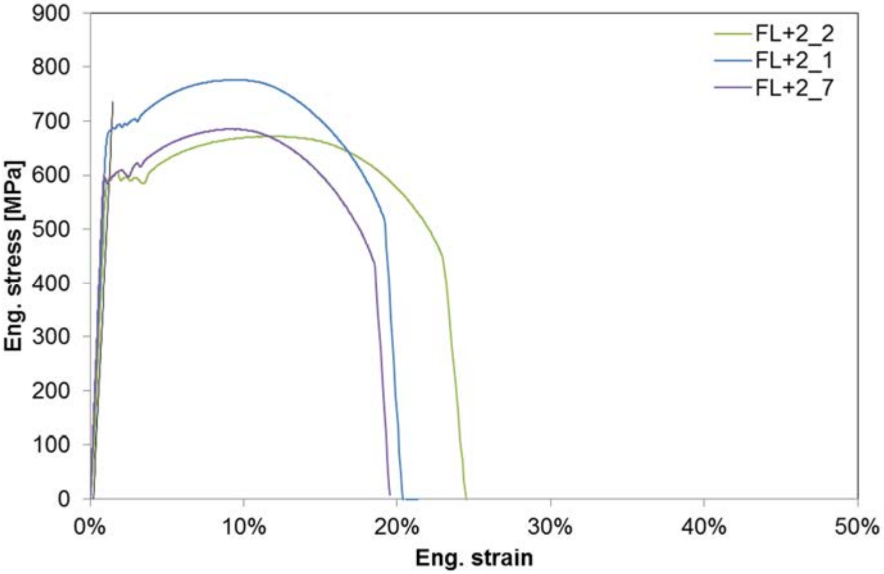

Figure 118. Miniature tensile specimen stress-strain curves of the zone about 2 mm from SA 508 / Alloy 52 fusion line.

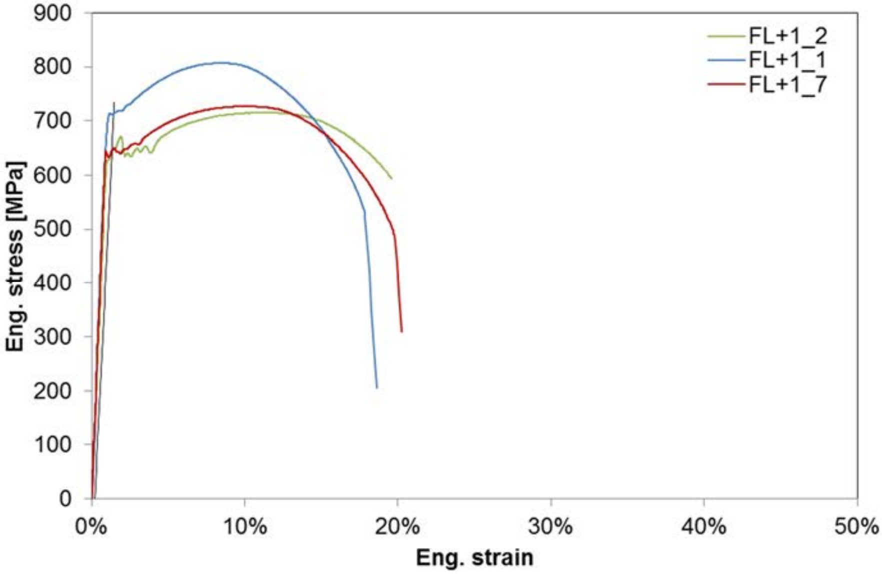

Figure 119. Miniature tensile specimen stress-strain curves of the zone about 1 mm from SA 508 / Alloy 52 fusion line.

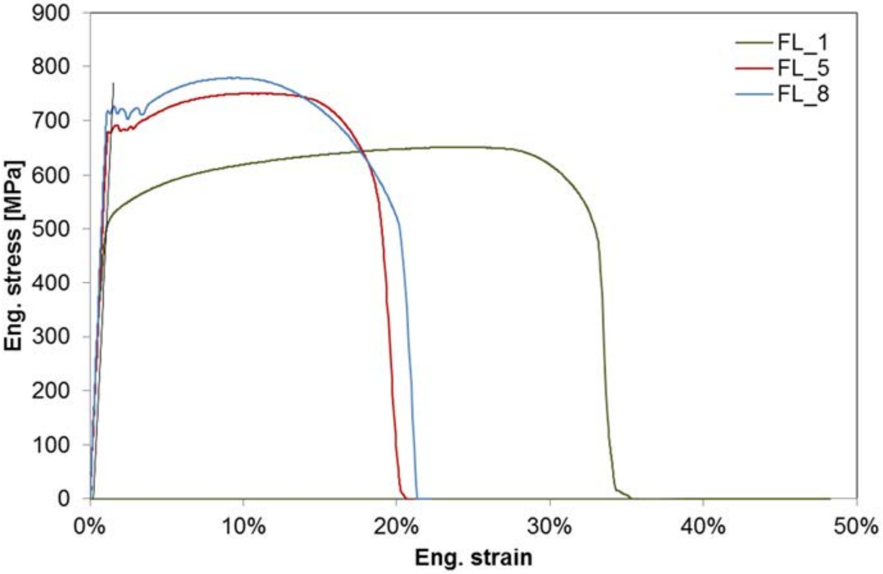

Figure 120. Miniature tensile specimen stress-strain curves of the SA 508 / Alloy 52 fusion line.

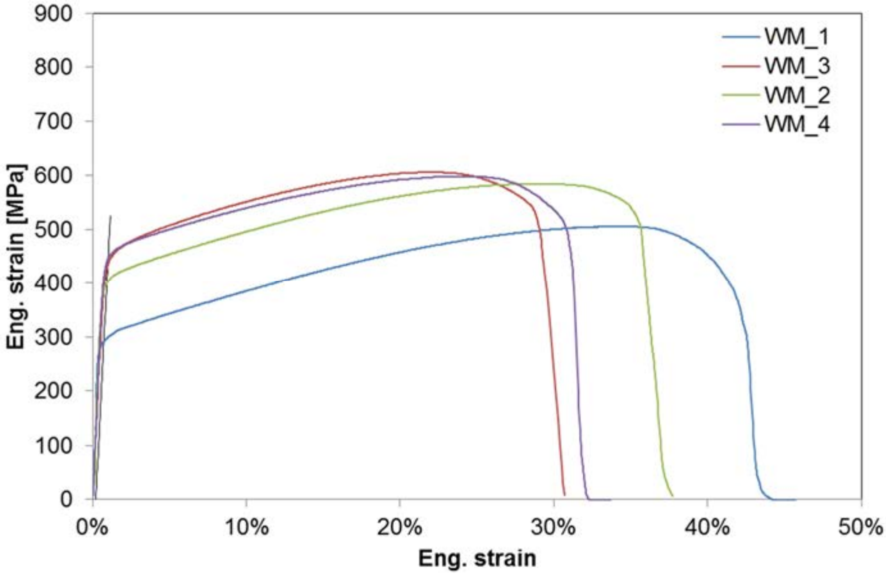

Figure 121. Miniature tensile specimen stress-strain curves of the Alloy 52 weld metal.

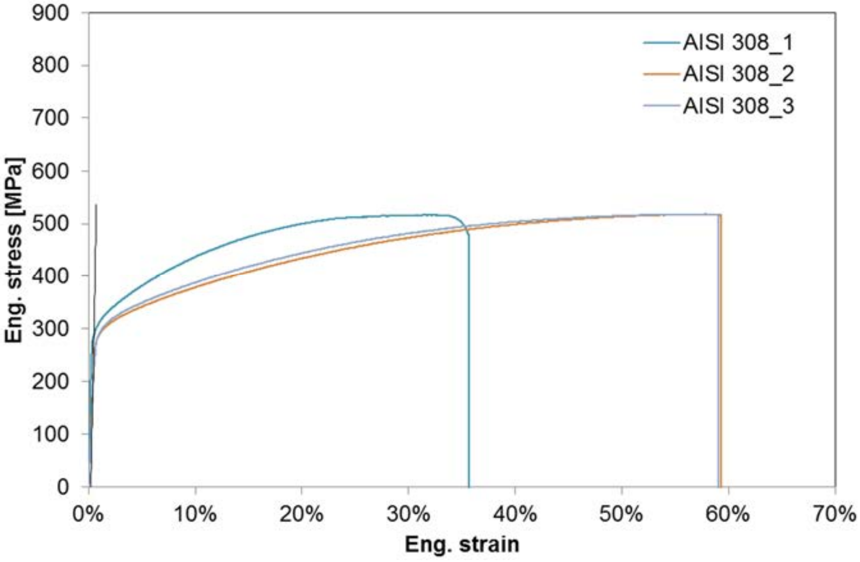

Figure 122. Miniature tensile specimen stress-strain curves of the AISI 308 cladding. Specimen total elongation could not be determined because linear variable displacement transducer (LVDT)-gauge was out-of-range.

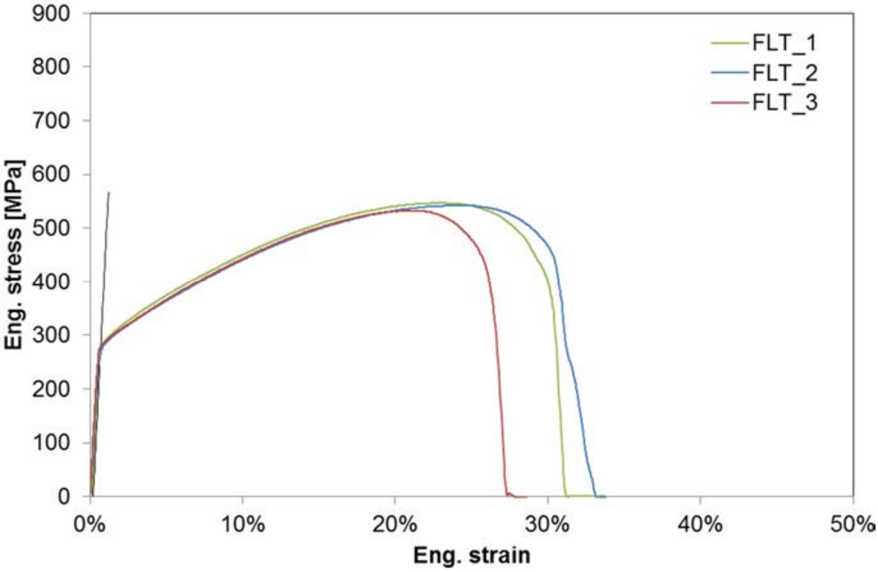

Figure 123. Miniature tensile specimen stress-strain curves across the SA 508 base material / Alloy 52 weld metal fusion line.

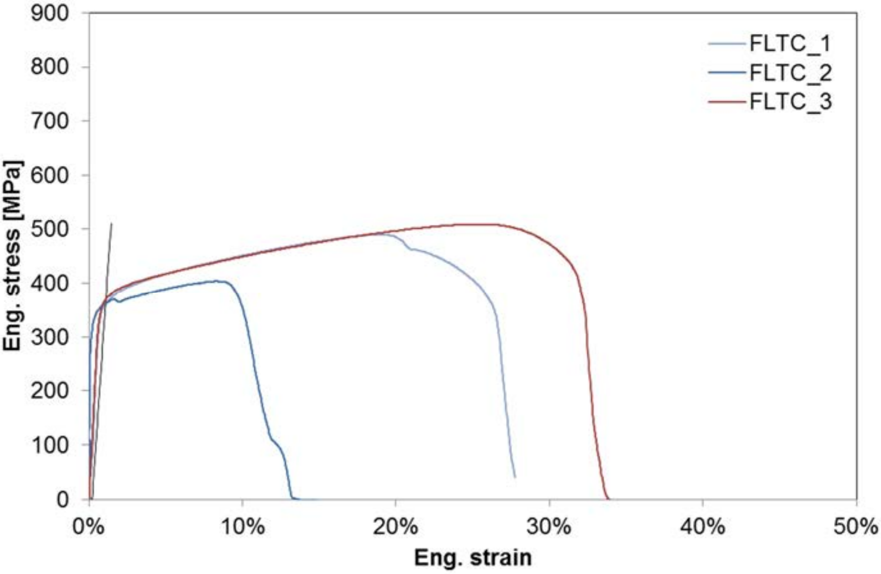

Figure 124. Miniature tensile specimen stress-strain curves across the AISI 308 cladding / Alloy 52 weld metal fusion line.

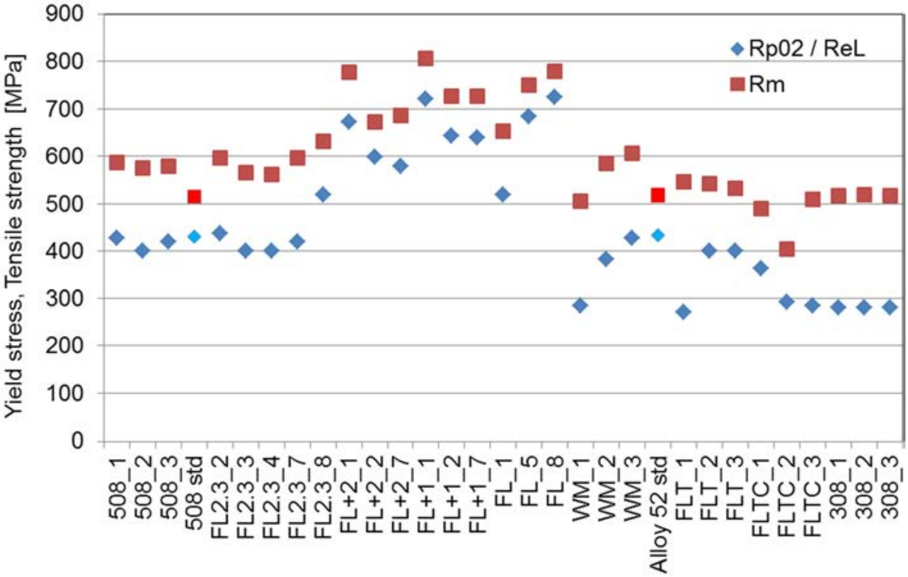

Figure 125. Yield and tensile strengths of Alloy 52 NG weld mock-up. Strength mismatch is the greatest near the interface area.

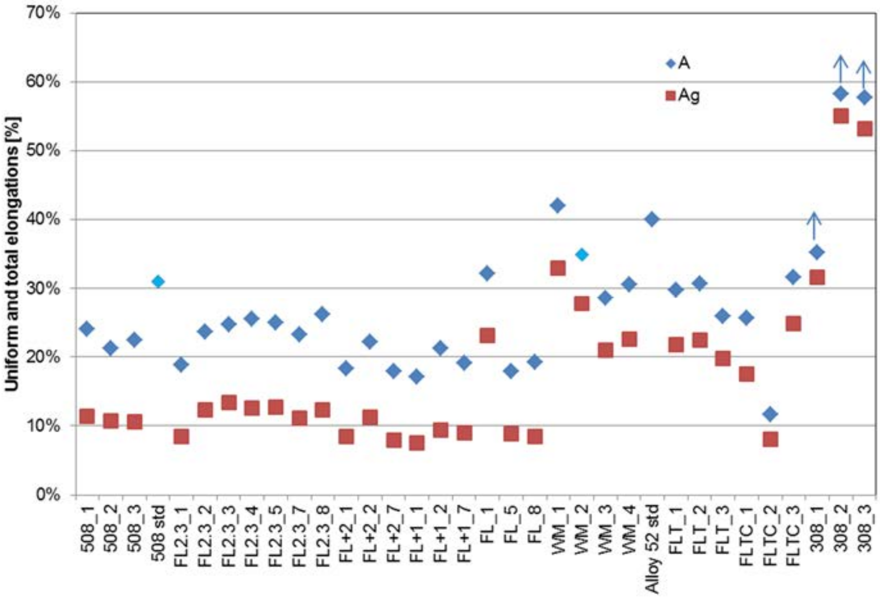

Figure 126. Uniform and total elongations of Alloy 52 NG weld mock-up. Note: Total elongation of the AISI 308 cladding could not be measured reliably because LVDT-gauge was out-of-the-range in the end of the tests.

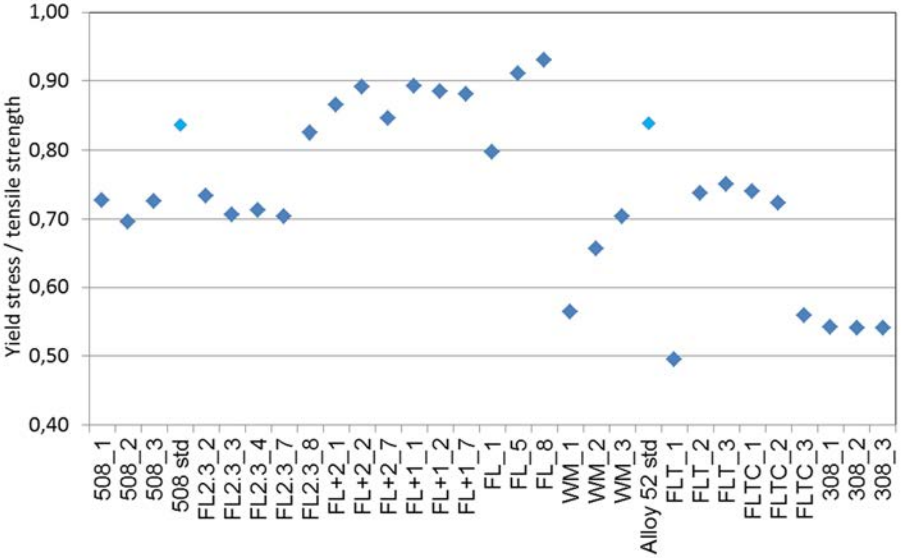

Figure 127. Yield stress divided by tensile strength of Alloy 52 weld mock-up describes strain hardening capacity of materials / zones.

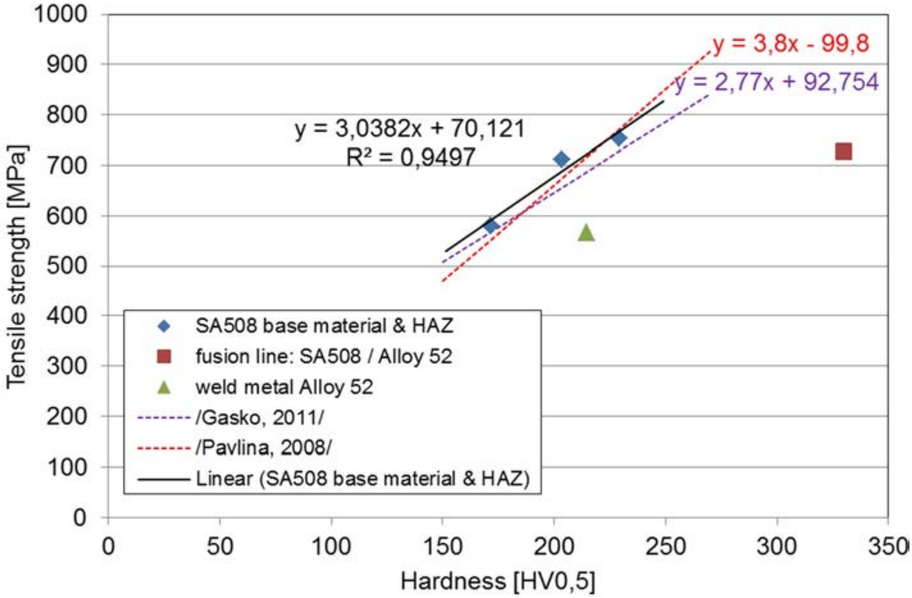

Figure 128. Tensile strength determined with miniature flat tensile specimen compared to hardness measurements of Alloy 52 NG weld mock-up.

Table 11. Linear fitting function for tensile strength determined with miniature flat tensile specimen as a function of hardness measurements of Alloy 52 NG weld mock-up.

Material / zone	**Average hardness [$HV_{0,5}$]**	**Average tensile strength, R_m [MPa]**	**Average yield strength [MPa]**	**Linear fitting $Rm = A*HV_{0.5}+B$**	
				A	**B**
SA 508	171	580	416	3.04	70.12
FL+2	203	711	617		
FL+1	229	753	668		
FL	330	727	643		
Weld metal, Alloy 52	215	565	365		
[Gaško & Rosenberg 2011]				2.77	92.754
[Pavlina & van Tyne 2008]				3.8	-99.8

Table 12. Strength mismatch of Alloy 52 NG weld mock-up based on average strength values. M = mismatch factor, R_p = yield strength, R_p_SA 508 = yield strength of base material SA 508 pressure vessel steel, R_m = tensile strength, R_m_SA 508 = tensile strength of base material SA 508 pressure vessel steel, adjasent zones = FL, FL+1, FL+2 and FL+2.3.

Material / zone	**R_{p02}/R_{eL}**	**R_m**	**Mismatch: yield strength vs. base material**	**Mismatch: tensile strength vs. base material**	**Mismatch: yield strength adjacent zone**	**Mismatch: tensile strength adjacent zone**
			M = R_p/R_p_SA 508	**M = R_m/R_m_SA 508**	**M = R_{p1}/R_{p2}**	**M = R_{m1}/R_{m2}**
SA 508	416	580	1.00	1.00		
FL+2,3 / SA 508					1.05	1.02
FL+2,3	436	590	1.05	1.02		
FL+2 / Fl+2,3					1.42	1.20
Fl+2	617	711	1.48	1.23		
Fl+1 / FL+2					1.08	1.06
FL+1	668	753	1.61	1.30		
FL / FL+1					0.96	0.97
FL	643	727	1.55	1.25		
WM Alloy 52 / FL					0.57	0.78
WM Alloy 52	365	565	0.88	0.97		
AISI 308 / WM Alloy 52					0.77	0.92
AISI 308	280	518	0.67	0.89		

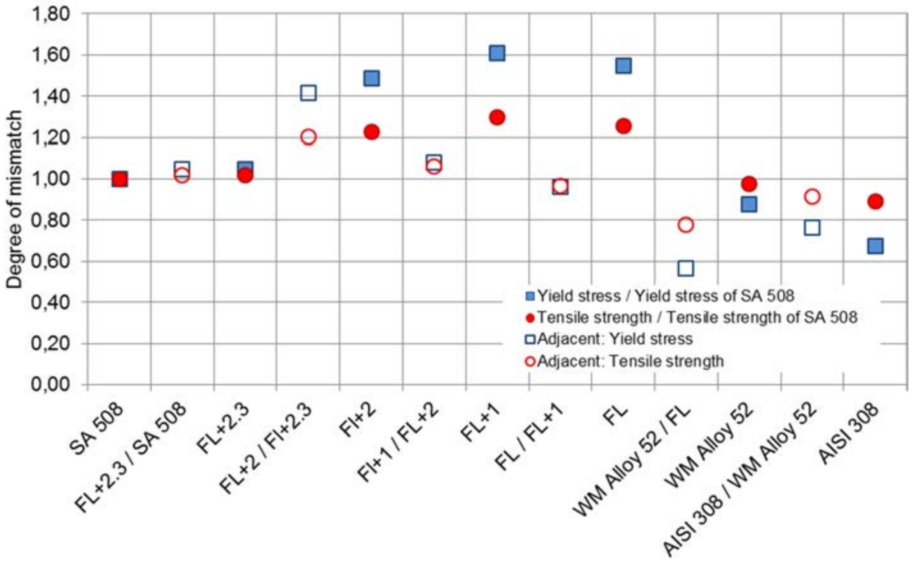

Figure 129. Strength mismatch of Alloy 52 NG weld mock-up. Strength mismatch is presented as each zone strength divided by the SA 508 base material strength (filled symbols) and as each zone strength divided by strength of adjacent zone, FL, FL+1, FL+2 and FL+2.3 (open symbols).

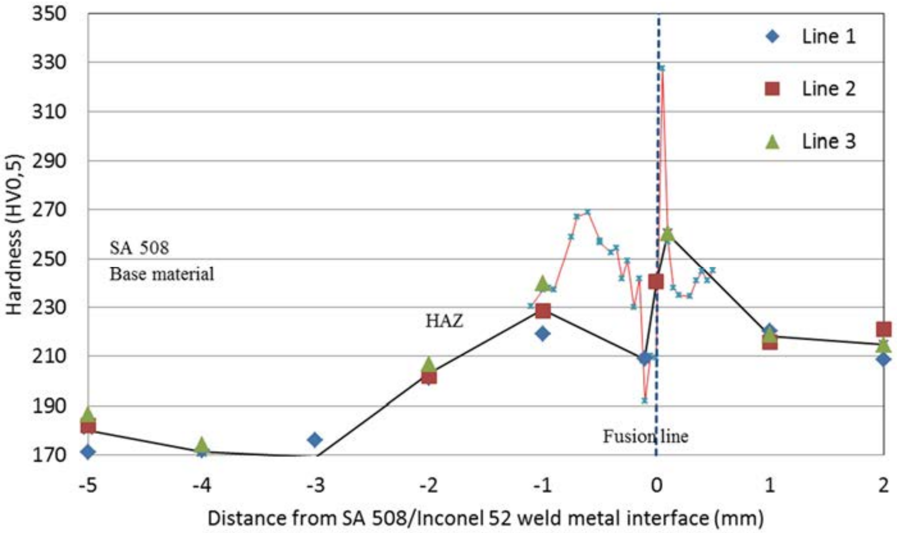

Figure 130. Hardness measurements of Alloy 52 NG weld mock-up show greatest mismatch near the interface area.

3.5 Fracture toughness testing

The experiments were performed with guidance of the ASTM E 1820-99a standard at VTT. The experiments were done at room temperature with the unloading compliance method. Both specimen dimensions were side-grooved prior to the pre-fatigue of the initial crack, in order to direct the crack into the preferred microstructural zone. The Alloy 52 NG-DMW fracture mechanical specimens were extracted from the fusion line, 1 mm from the fusion line into the HAZ of SA 508 (FL + 1), and 1 mm from the fusion line into the Alloy 52 weld metal (FL - 1). The extraction locations of the fracture mechanical specimens are shown in Figure 131 and list of Alloy 52 NG-DMW fracture mechanical test specimens is presented in Table 13.

Figure 131. Extraction locations of the SE(B) specimens used in fracture mechanical testing.

Table 13. Alloy 52 NG-DMW fracture mechanical specimens.

Weld Zone	10x20x100 mm SE(B)		5x10x55 mm SE(B)	
	n	Specimen notations	n	Specimen notations
As-welded fusion line	4	AWFL_i1 – AWFL_i4	8	AWFL_p1 – AWFL_p8
As-welded weld metal (FL - 1 mm)	4	AWFL-1_i1 – AWFL-1_i4	8	AWFL-1_p1 – AWFL-1_p8
As-welded HAZ (FL + 1 mm) of SA 508	4	AWFL+1_i1 – AWFL+1_i4	8	AWFL+1_p1 – AWFL+1_p8
PWHT fusion line	4	HTFL_i1 – HTFL_i4	8	HTFL_p1 – HTFL_p8
PWHT weld metal (FL - 1 mm)	4	HTFL-1_i1 – HTFL-1_i4	8	HTFL-1_p1 – HTFL-1_p8
PWHT HAZ (FL + 1 mm) of SA 508	4	HTFL+1_i1 – HTFL+1_i4	8	HTFL+1_p1 – HTFL+1_p8

3.5.1 Fracture resistance curves

Fracture resistance curves of the 10x20x100 SE(B) Alloy 52 NG-DMW weld metal, fusion line, and HAZ specimens are shown in Figures 132, 133, and 134, respectively. Fracture resistance of the Alloy 52 weld metal is very high and, as can be seen, the PWHT seems to increase the fracture resistance of the Alloy 52 weld metal. The lowest J values of the as-welded and PWHT weld metal specimens at 1 mm crack extension are 958 kJ/m^2 and 1146 kJ/m^2, respectively. Fracture resistances of the HAZ and fusion line area are high as well, although clearly lower than the fracture resistance of the Alloy 52 weld metal. In contrast to the weld metal, the PWHT seems to decrease the fracture resistance of the HAZ and fusion line area. The lowest J values of the as-welded and PWHT HAZ specimens at 1 mm crack extension are 714 kJ/m^2 and 521 kJ/m^2, respectively, and the lowest J values of the as-welded and PWHT fusion line specimens at 1 mm crack extension are 485 kJ/m^2 and 240 kJ/m^2, respectively.

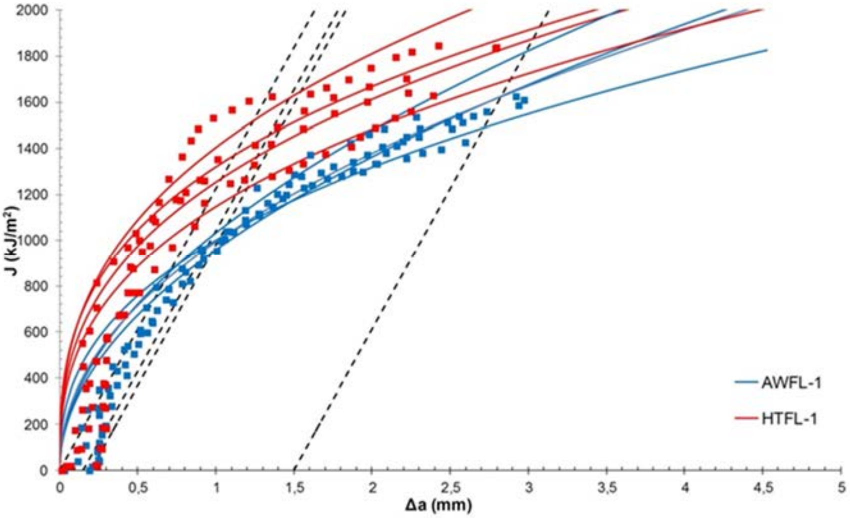

Figure 132. Fracture resistance curves of WM NG-DMW specimens.

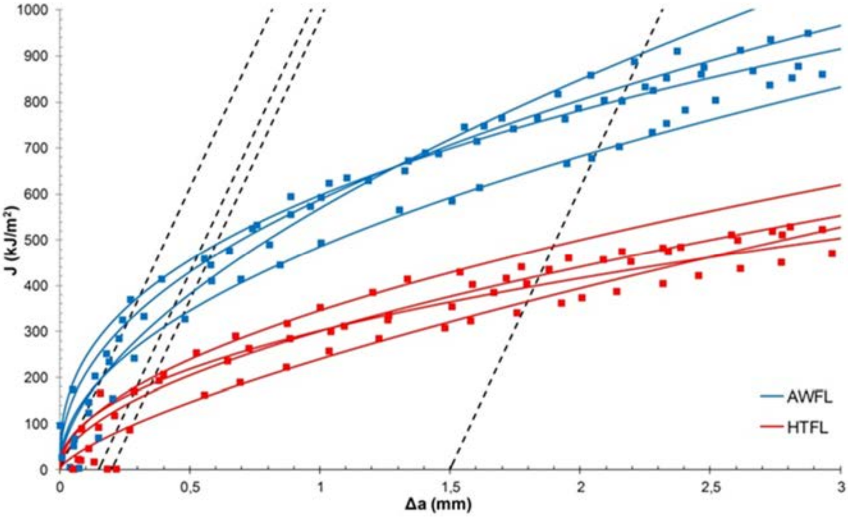

Figure 133. Fracture resistance curves of FL NG-DMW specimens.

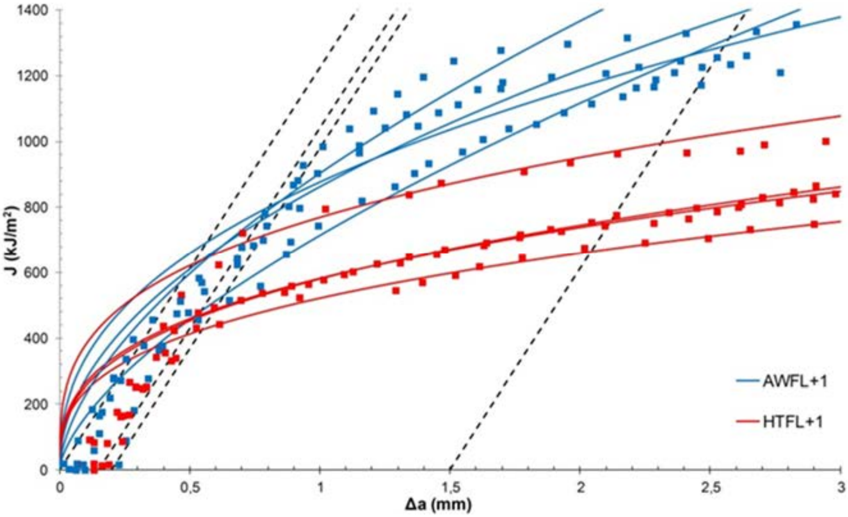

Figure 134. Fracture resistance curves of HAZ NG-DMW specimens.

Fracture resistance curves of the sub-sized 5x10x55 mm Alloy 52 NG-DMW SE(B) specimens are shown in Figures 135 through 137. As can be seen, the 5x10x55 mm SE(B) specimens show quite similar results as 10x20x100 mm SE(B) specimens. However, especially the fusion line specimens, show large scatter compared to the fracture resistance curves of the normal-sized specimens. Effect of the specimen size on fracture resistance requires significantly more research.

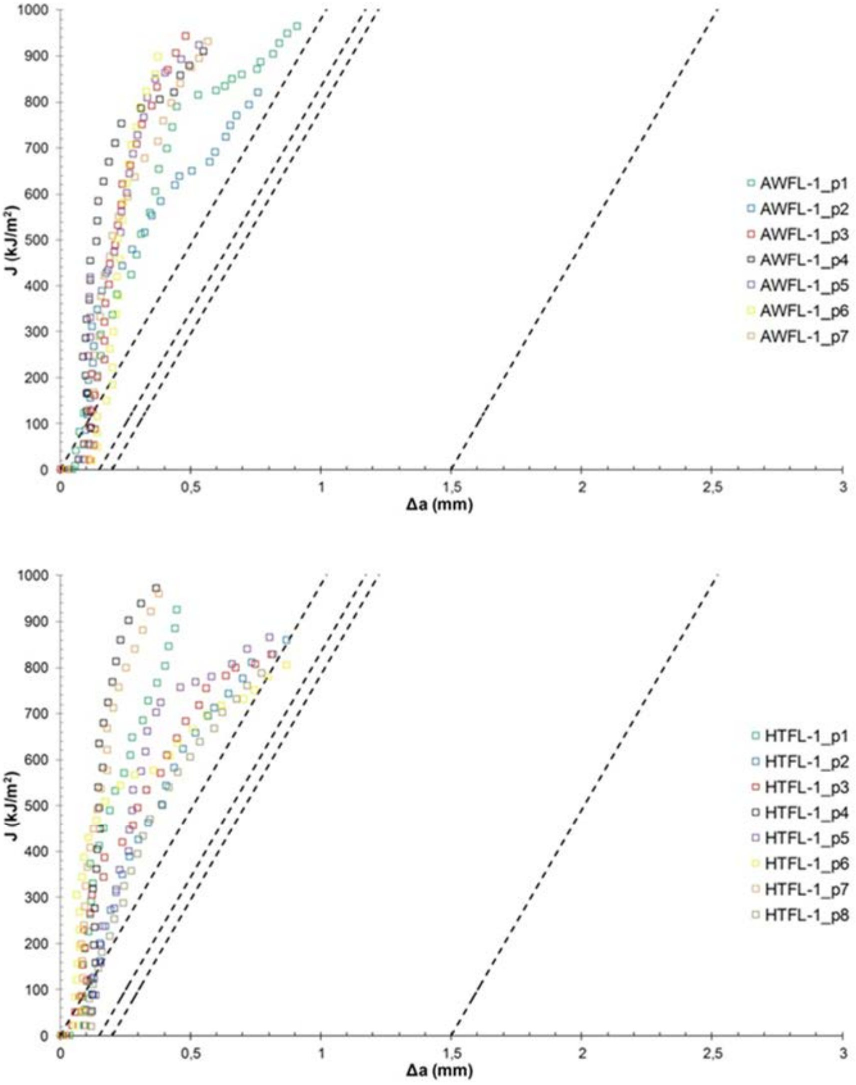

Figure 135. Fracture resistance curves of miniature WM NG-DMW specimens.

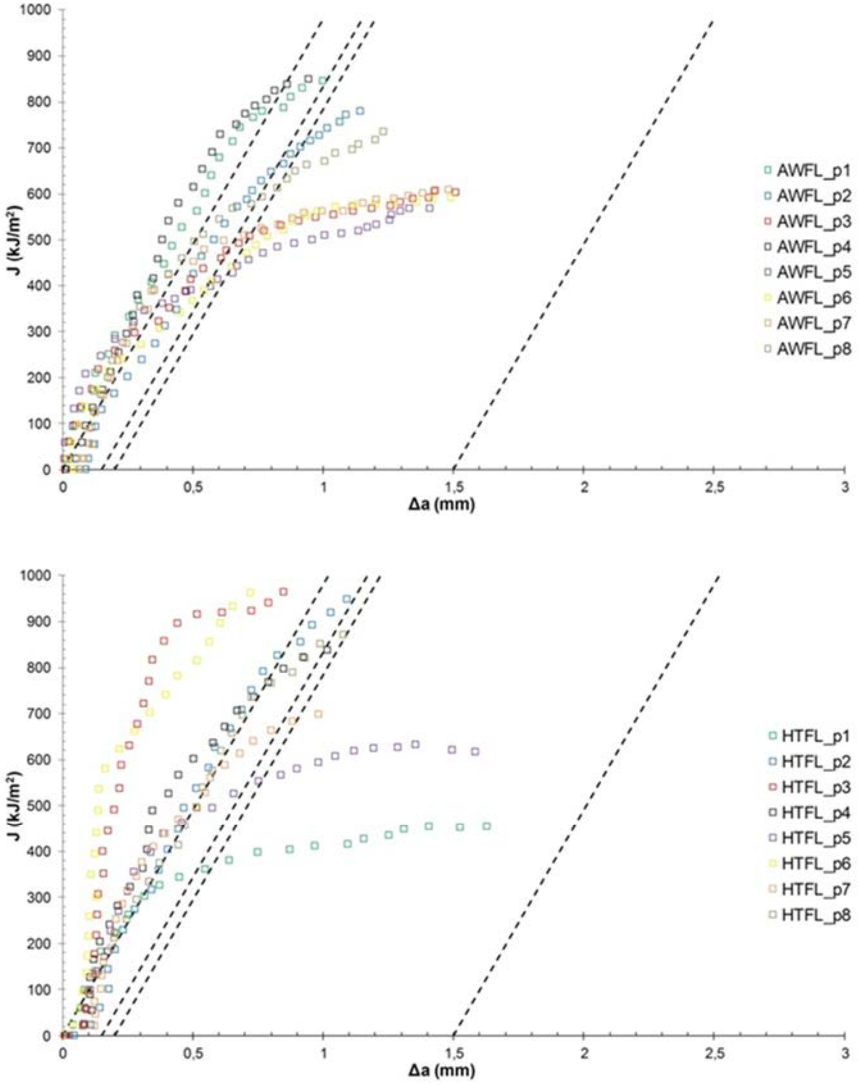

Figure 136. Fracture resistance curves of miniature FL NG-DMW specimens.

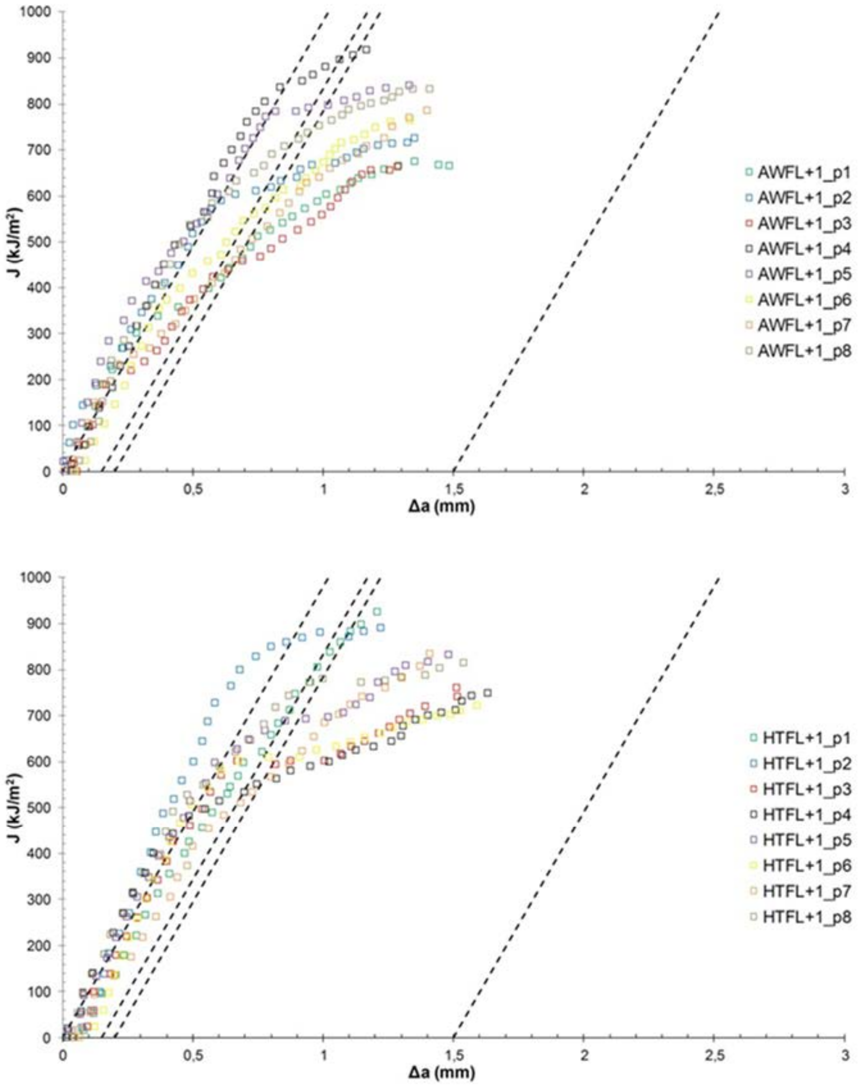

Figure 137. Fracture resistance curves of miniature HAZ NG-DMW specimens.

3.5.2 Fracture surface characterization

Figure 138 shows fracture surfaces of the Alloy 52 weld metal specimens of as-welded and PWHT states. The red arrows in the pictures show the pre-fatigue crack tip and the crack growth direction during the testing. Typical fracture surface structures found from the weld metal specimens are shown in Figure 139. Fracture surfaces show high amount of deformation and mostly ductile fracture. Images of typical fracture surface structure of the weld metal specimens are presented in Figures 139a and 139b. Some of the as-welded state weld metal specimen fracture surfaces showed bands of dendritic-like structures, shown in Figure 139e, and the surfaces of these dendritic-like structures were covered with small, presumably aluminum oxide particles, shown in Figure 139f. Also, solidification cracking-like surfaces with sizes of around 100 µm, shown in Figure 139g, were found from a few weld metal specimens. The surfaces of the solidification-like cracks were covered with small, presumably aluminum oxide particles, shown in Figure 139h. It should be noted, that even though there were some flaws found from the fracture surfaces of the Alloy 52 specimens, the fracture resistance of the specimens was still very high.

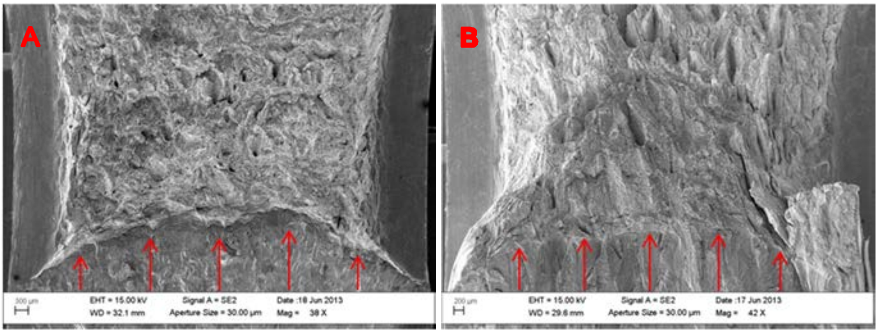

Figure 138. Fracture surfaces of the Alloy 52 weld metal specimens of as-welded (A) and PWHT (B) states.

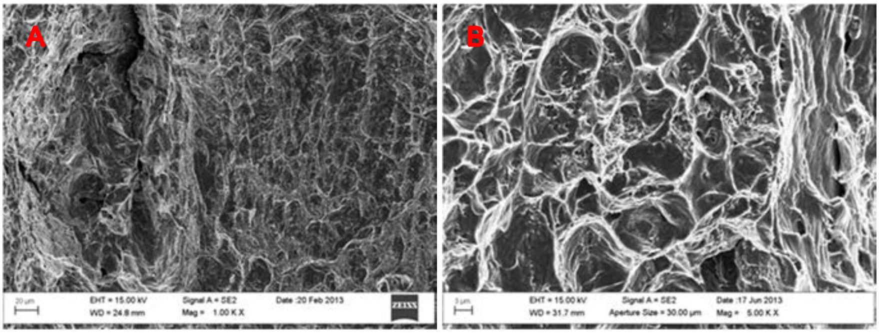

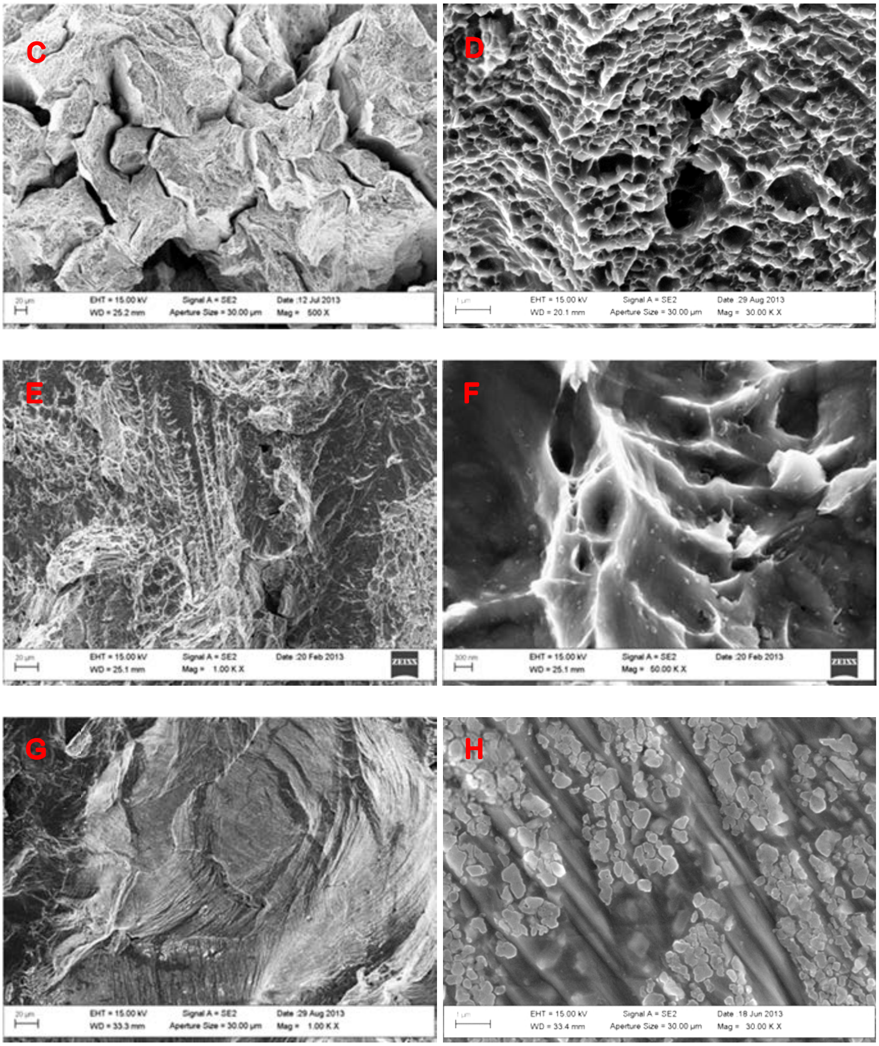

Figure 139. Typical fracture surface structures found from the Alloy 52 weld metal specimens.

Figure 140 shows fracture surfaces of Alloy 52 miniature-sized weld metal specimens of as-welded and PWHT states. The fracture surfaces of the miniature-sized weld metal specimens show very similar characteristics to those of the normal-sized weld metal specimens.

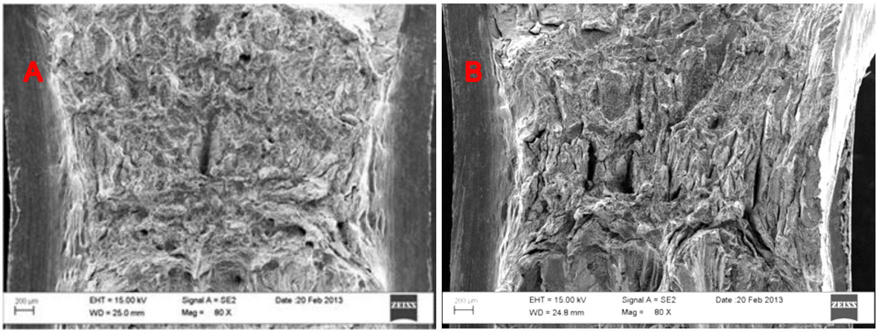

Figure 140. Fracture surfaces of Alloy 52 miniature-sized weld metal specimens of as-welded (A) and PWHT states (B).

Fracture surfaces of Alloy 52 NG-DMW fusion line specimens of as-welded and PWHT states are shown in Figure 141. In both specimens, the cracks continue to propagate near the fusion line. However, in the as-welded state specimens, the crack occasionally jumps to the weld metal side of the fusion line while in the PWHT specimens, the crack propagates along the SA 508 side of the fusion line. Figure 142 shows typical fracture surface characteristics found from the fusion line specimens. Weld defects or pores are found from the bottom of the large dimples formed to the Alloy 52 weld metal side of the fusion line (Figures 142a and 142b). The weld defects have initiated a dimple formation in the weld metal and caused the crack to jump across the fusion line. Unlike in the as-welded specimens, the cracks in the PWHT specimens do not jump across the fusion line. This is likely due to the wider and softer carbon depleted zone (CDZ) in the PWHT weld, which also explains the lower fracture resistance of the PWHT fusion line specimens. Figures 142c and 142d show the fracture surface structure of the SA 508 HAZ. The dimple size is much smaller than in the weld metal and in the bottom of each dimple there is a small MnS inclusion (EDS spectra shown in Figure 143). The distribution of the MnS inclusions is likely the controlling factor in the fracture behavior of the fusion line area.

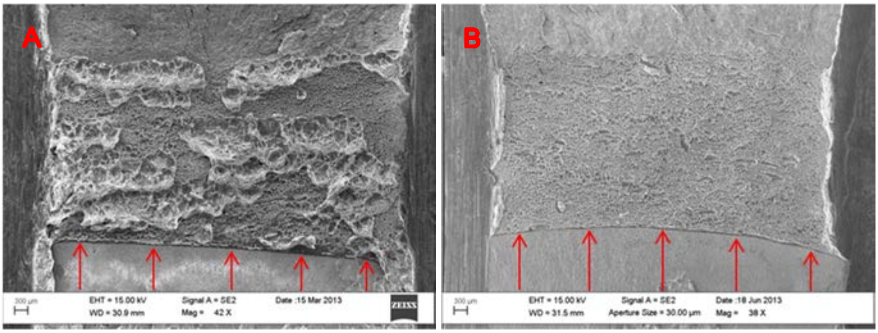

Figure 141. Fracture surfaces of the Alloy 52 NG-DMW fusion line specimens of as-welded (A) and PWHT (B) states.

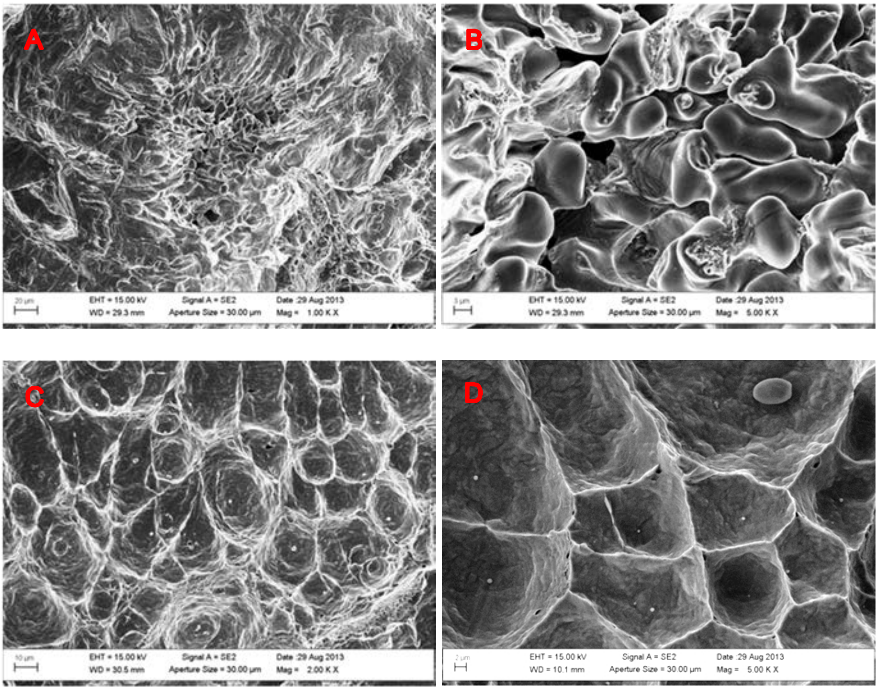

Figure 142. Typical fracture surface structures found from the Alloy 52 NG-DMW fusion line specimens.

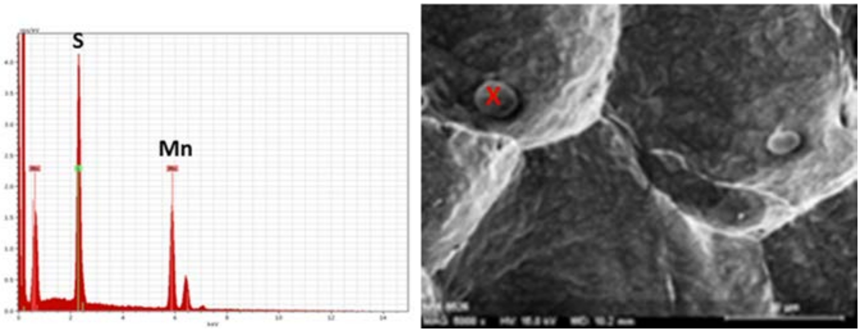

Figure 143. EDS spectrum showing the chemical composition of the precipitates in the bottom of the dimples located in the fusion line region of the NGW.

Fracture surfaces of Alloy 52 NG-DMW miniature-sized fusion line specimens are shown in Figure 144. The exact location of the pre-fatigue crack has a significant effect on the fracture resistance of the miniature specimen. In the specimens with higher fracture resistance, the pre-fatigue crack has likely been so deep in the weld metal side of the fusion line that it has continued its propagation in the weld metal. Thus, the fracture resistance curves of the miniature-sized specimens, especially the fusion line specimens, show significantly higher scatter compared to the normal-sized specimens.

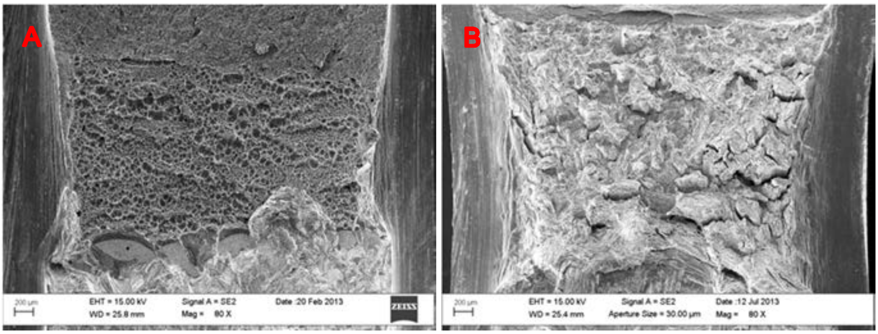

Figure 144. Fracture surfaces of the Alloy 52 NG-DMW miniature-sized specimens.

Figure 145 shows the fracture surfaces of the normal-sized HAZ specimens as-welded and PWHT states. Fracture surfaces of the HAZ samples showed only ductile fracture. In the specimens of both heat treatment conditions, the cracks propagated towards the fusion line and the propagation seemed to happen in shorter distance in the PWHT specimens. However, in one as-welded state specimen, the crack propagated towards the SA 508 base metal (fracture surface shown in Figure 146). This can be explained by the exact location of the pre-fatigue crack tip in that specimen. The tip of the pre-fatigue crack in that specimen was located at 1.59 mm from the fusion line into the SA 508 base metal and the distance has likely been so much that instead of propagating to the softer CDZ into the fusion line, the crack has propagated to the softer base metal. Figure 147 shows typical fracture surface characteristics found from the HAZ specimens. In SA 508, the fracture surface contains larger sized MnS inclusions, shown in Figure 147c. When the crack propagation has achieved the fusion line, the fracture surface shows characteristics similar to those of the fusion line specimens.

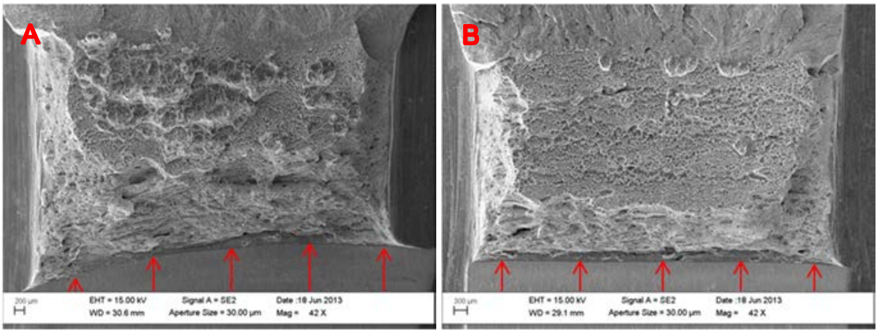

Figure 145. Fracture surfaces of the SA 508 HAZ specimens of as-welded (A) and PWHT (B) states.

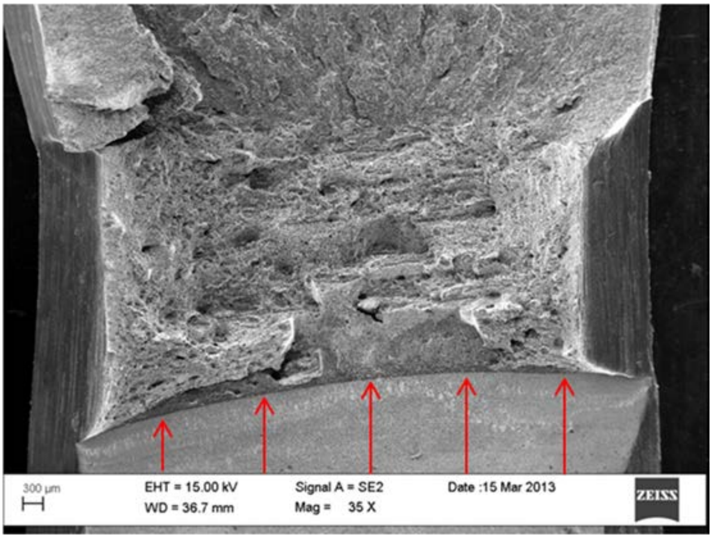

Figure 146. Fracture surface of the as-welded state specimen in which the crack has propagated towards the base metal.

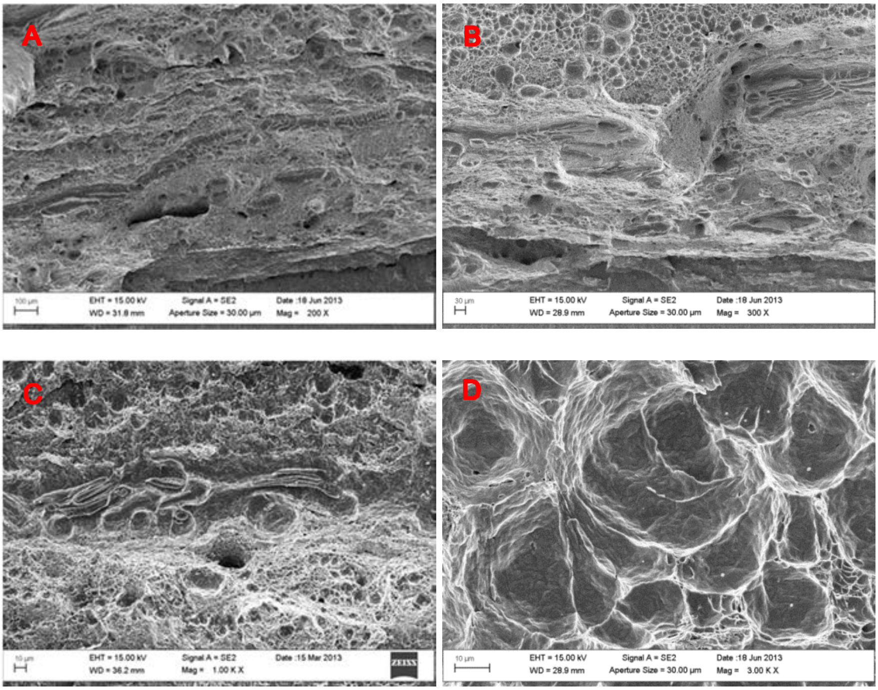

Figure 147. Typical fracture surface characteristics found from the SA 508 HAZ specimens.

Figure 148 shows the fracture surfaces of two miniature-sized SA 508 HAZ specimens. As shown in Figure 137, there was some scatter in the fracture resistance curves of the miniature-sized specimens and the MnS inclusion distribution appears to have an effect on the fracture resistance of the HAZ, especially in the miniature-sized HAZ specimens. In the specimens with lower fracture resistance, the fracture surface showed higher amounts of larger MnS inclusions.

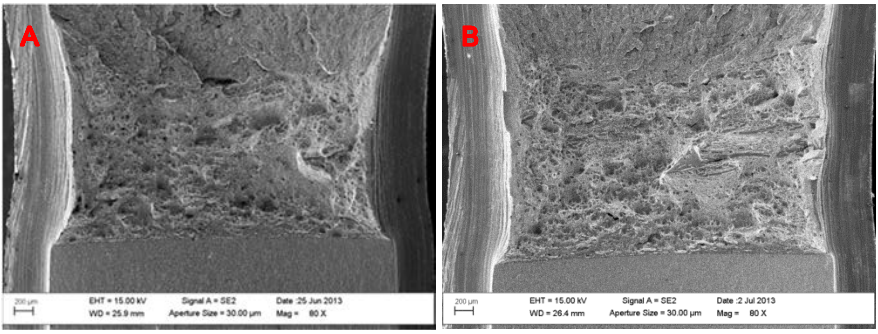

Figure 148. Fracture surfaces of the miniature-sized SA 508 HAZ specimens.

3.5.3 3D profilometry and crack path examination

Fracture surfaces of the J-R tested SE(B) fracture toughness specimens were analysed using 3D profilometry. The measurements were performed for the weld metal side halves of the fractured specimens for NGW mock-up. The attained results from the 3D profilometry measurements were a 3D topography map of the fracture surface and a line profile, which was measured in crack growth direction at mid-thickness of the fracture surfaces. Topography maps for narrow-gap Alloy 52 mock-up samples start at the notch, 2 mm before the start of the pre-crack, and end at the final fatigue. The maps are shown in such orientation that the notch of the specimen is located on the left and the crack (pre-crack, J-R test and final fatigue) grows to the right. The maps for narrow gap Alloy 52 mock-up samples cover almost the whole breadth of the fracture surface excluding the side grooves. The differences in altitude of a fracture surface are illustrated with a colour scale from blue to red, where the blue tones correspond to the lowest points of a fracture surface and the red to the highest. It must be pointed out that the colours of the 3D maps are scaled separately for each specimen and therefore the colours of the different fracture surface maps are not directly comparable in absolute units.

Sensofar Plμ 2300 is a non-contact optical imaging profiler. Both confocal and interferometry techniques can be used to illuminate the surface and create a 3D topography by detecting the reflection. Measurement of larger areas (i.e. extended topography) is also possible by using X-Y motor stage. The objective used in this study was 20x which has an optical resolution of 64 µm. The maximum inclination of the studied surface that the equipment can measure is 42°. The fracture surfaces were mainly measurable with the equipment except for a few specimens where the crack grows in the weld and the cracks have locally steeper inclinations than 42°. In addition, side-grooved areas could not be included in the map because of their inclination, which is 45°, related to the fracture surface. The hight scale of each profile is dependent on the degree of topography.

Both as-welded (AW) and post-weld heat-treated (HT) J-R tested 20x10x100 mm specimens were studied. Nominal fatigue pre-crack tip locations were ±1 mm from the fusion line (FL+1 and FL-1) and at the fusion line (FL). The actual pre-crack tip distances from the fusion line were measured from cross-section cut at mid-width and they are presented in Table 14 with J_{1mm} values. In as-welded fusion line specimens the actual pre-crack tip location ranged from close to zero to 0.34 mm, towards the low-alloy steel (LAS). In heat-treated fusion line samples the actual pre-cracks were about 0–0.47 mm from the fusion line, in the LAS in each case. In as-welded +1 mm specimens, where the crack tip was nominally in the heat affected zone (HAZ) of the low-alloy steel, 1 mm from the fusion line, the actual locations ranged between 1.44 and 1.59 mm from the FL. In post-weld heat-treated +1 mm samples the actual pre-crack locations were close to the nominal 1 mm (0.91–1.1 mm). In -1 mm samples the exact pre-crack tip locations were not measured, but the cracks grew only in the weld metal during pre-cracking, J-R testing and final fatigue. All the FL +1 mm specimens exhibited a step towards the

FL early in the J-R test, except for one specimen which had the largest pre-crack tip distance from the FL.

Table 14. The actual pre-crack tip distances from the fusion line and measured J_{1mm} values.

AW/HT	Specimen number	J-integral value at 1 mm crack growth	Nominal distance of pre-crack tip from FL (mm)	Measured distance of pre-crack tip from FL (mm)	Crack jumps towards the FL in J-R test
AW	1	569	0	0.34	x
AW	2	485	0	0.28	x
AW	3	588	0	~0	x
AW	4	597	0	0.20	x
AW	1	903	+1	1.48	x
AW	2	877	+1	1.59	
AW	3	714	+1	1.50	x
AW	4	862	+1	1.44	x
AW	1	1000	-1	in weld	
AW	2	1032	-1	in weld	
AW	3	958	-1	in weld	
AW	4	993	-1	in weld	
HT	1	300	0	0.47	x
HT	2	301	0	0.03	x
HT	3	240	0	~0	x
HT	4	345	0	~0	x
HT	1	521	+1	0.91	x
HT	2	769	+1	1.10	x
HT	3	580	+1	0.91	x
HT	4	582	+1	0.92	x
HT	1	1253	-1	in weld	
HT	2	1320	-1	in weld	
HT	3	1147	-1	in weld	
HT	4	1404	-1	in weld	

Pre-crack tips of the FL specimens were nominally at the fusion line. The actual pre-crack tip locations ranged from about zero to 0.34 mm from the fusion line. An example of the obtained 3D profiles for AWFL specimen fracture surfaces is presented in Figure 149, and a cross-section of the same specimen fracture surface with a measured line profile is presented in Figure 150. The scale shown in the Figures is the scale of the SEM pictures. The fracture surface profile at mid-width has been laid over the SEM picture and size is adjusted to mimic the SEM picture.

Pre-crack grows slightly towards the low-alloy steel in all AWFL specimens. When the J-R test starts, the crack grows partly on a rather smooth plane which is located close to the fusion line (about 0–50 µm) but also makes occasional steps towards the weld (Figures 151 and 152). SEM examination showed that the jumps were induced by small welding defects, shown in Figure 142. All AWFL specimens showed the similar behaviour.

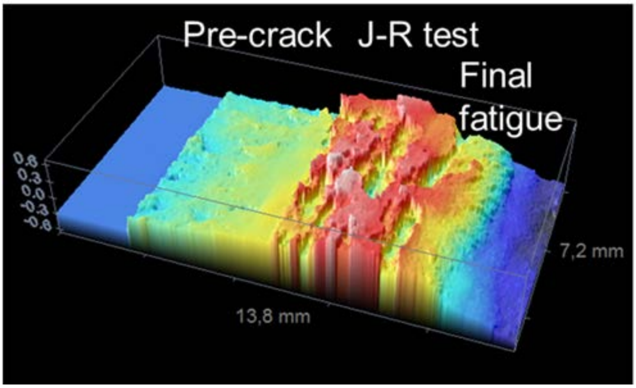

Figure 149. 3D topography map of specimen AWFL_3. Notch, pre-crack, J-R test and final fatigue can approximately be distinguished from the image. The 3D map illustrates how the crack makes occasional steps towards the weld during J-R testing.

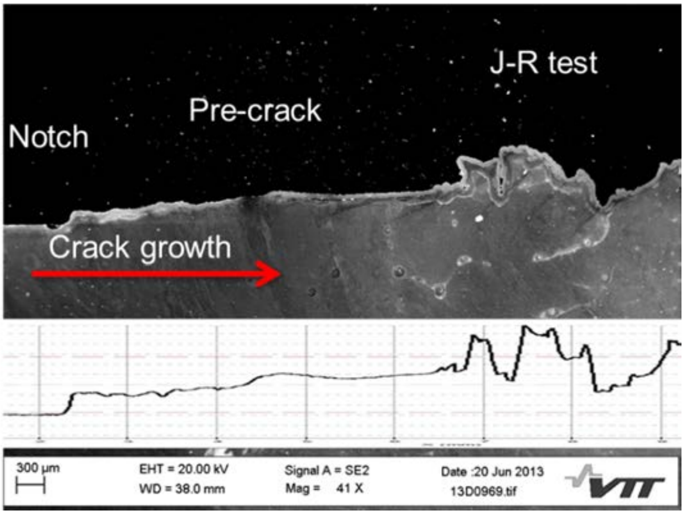

Figure 150. A SEM image of the polished mid-thickness cross-section of the fracture surface of specimen AWFL_3 and a mid-thickness line profile obtained from 3D profilometry measurement.

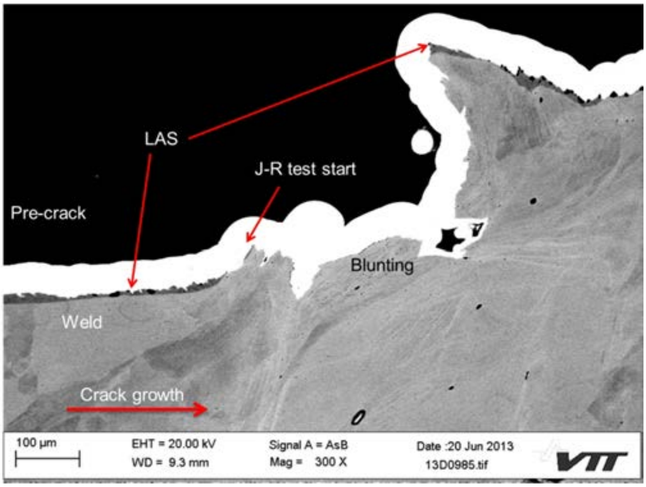

Figure 151. A SEM image of a detail of the fracture surface cross-section at the location where the J-R test starts. Significant plastic deformation and crack tip blunting occurs when the J-R test is started. A thin layer (< 50 µm) of low-alloy steel was observed both on the pre-crack and the J-R test part of the fracture surface.

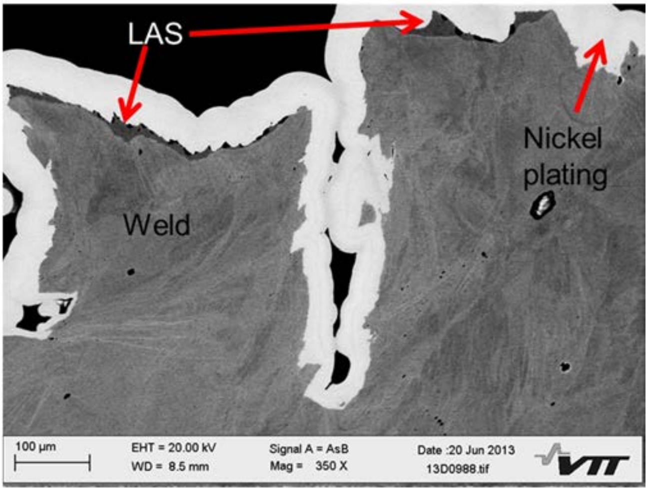

Figure 152. A SEM image of a detail of the polished cross-section. An example of a crack step which was widely observed in as-welded specimens during J-R testing.

Heat-treated FL specimens showed smoother fracture surfaces than those of as-welded specimens. No steps to weld metal during J-R tests were observed. An example of a HTFL specimen fracture surface topography is presented in Figure

153. The fracture has advanced on a rather smooth plane, which appears to be very close (< 150 µm, for the most part < 50 µm) to the fusion line, as can be observed in Figures 154 and 155. A detail from the J-R test region of the fracture surface showing a thin layer of low-alloy steel is presented in Figure 156. All the studied HTFL specimen fracture surfaces showed a similar behaviour.

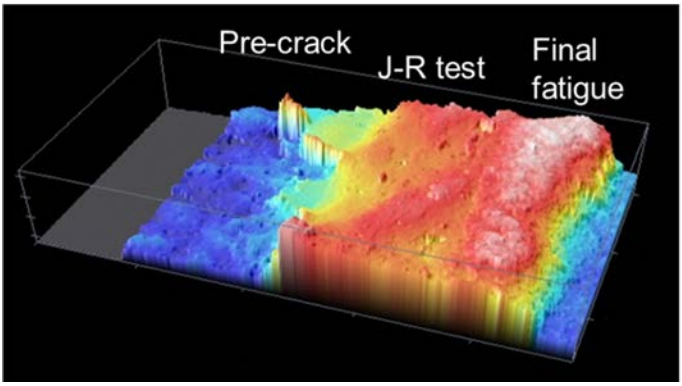

Figure 153. 3D topography map of the specimen HTFL_4. Notch, pre-crack, J-R test and final fatigue can approximately be distinguished from the image. The 3D map illustrates that marcoscopically the specimen fracture surface has a smooth appearance in the J-R test region.

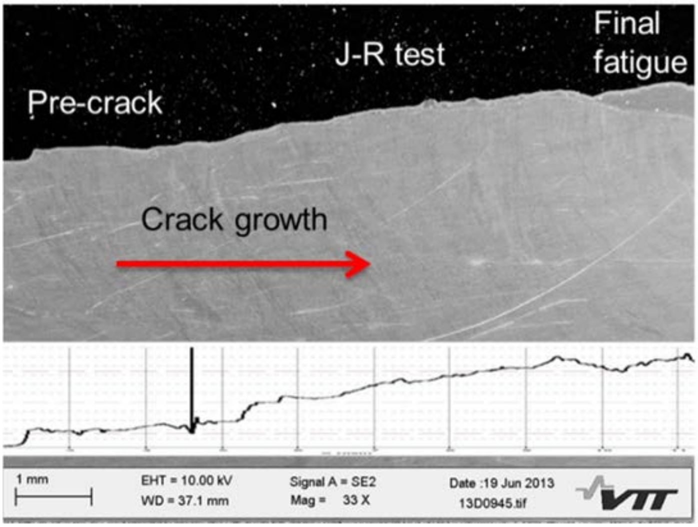

Figure 154. A SEM image of the mid-thickness cross-section of the fracture surface of specimen HTFL_4 and a mid-thickness line profile obtained from 3D profilometry measurement. The peak in the pre-crack region of the line profile is a measurement error.

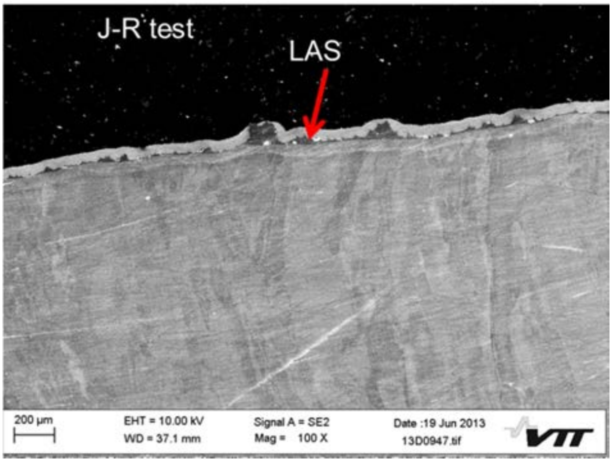

Figure 155. A SEM image of the fracture surface cross-section at the J-R test region. A thin layer (< 150 µm) of low-alloy steel was observed on the J-R test part of the fracture surface.

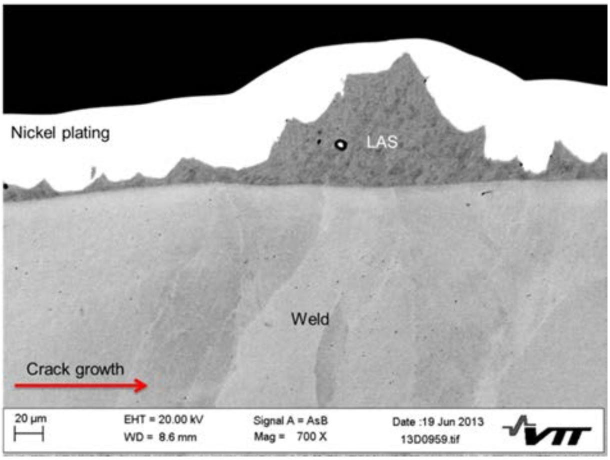

Figure 156. A SEM image of a detail at the J-R test region of the fracture surface showing a thin layer of low-alloy steel. The thickness of the low-alloy steel layer in this specimen ranges from about 2 µm to about 150 µm.

Three of the four AWFL +1 specimens showed a similar behaviour, where the crack found its way close to the fusion line early in the J-R test. However, in one case the crack did not grow close to the fusion line but instead grew further towards the low-alloy steel. The 3D topography map of the fracture surface of that specimen is presented in Figure 157. The polished cross-section of the fracture surface and a mid-thickness line profile obtained from 3D profilometry measurement are presented in Figure 158. Figure 159 shows how the crack grows steeply towards the low-alloy steel side early in the J-R test.

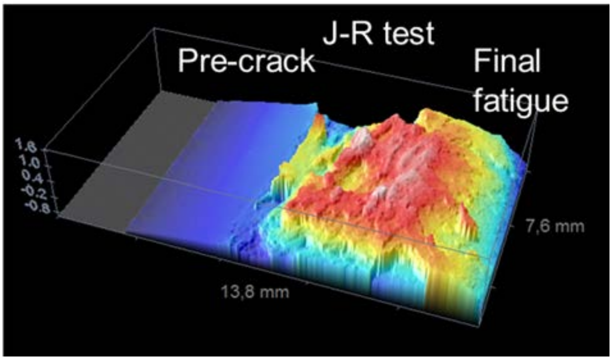

Figure 157. 3D topography map of specimen AWFL +1_2. Notch, pre-crack, J-R test and final fatigue can approximately be distinguished from the image. Crack grows towards the low-alloy steel during the J-R test.

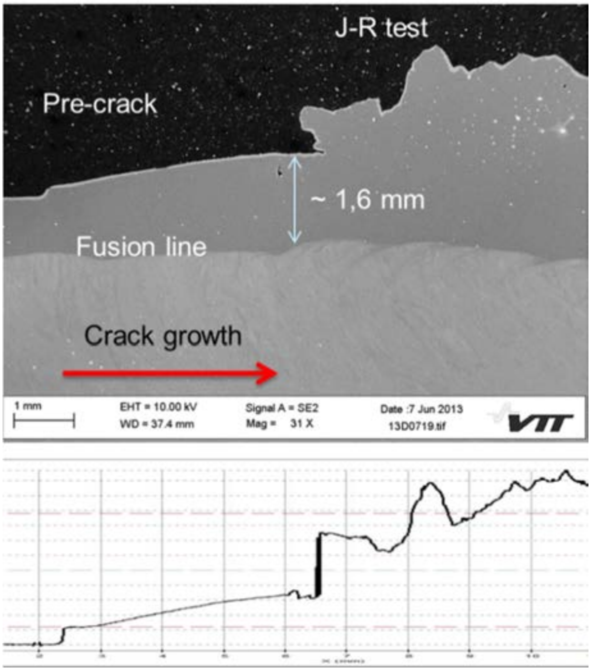

Figure 158. A SEM image of a polished mid-thickness cross-section of the fracture surface of specimen AWFL +1_2 and a mid-thickness line profile obtained from 3D profilometry measurement. The crack grows further towards the low-alloy steel during the J-R test.

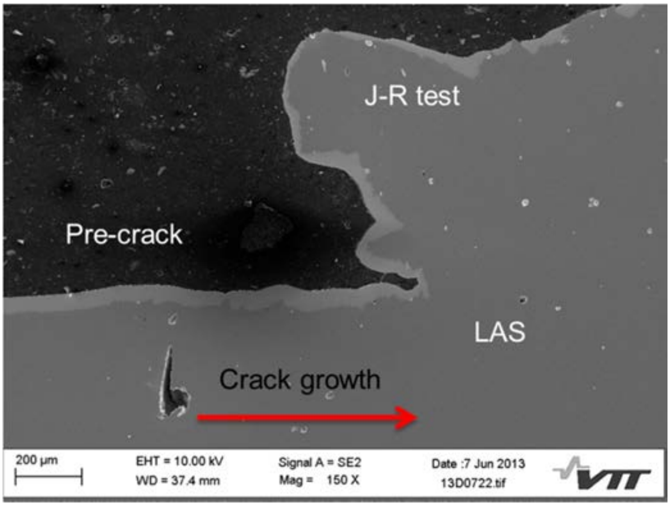

Figure 159. A SEM image of a detail of the polished fracture surface cross-section at the location where the J-R test starts. The crack grows further towards the low-alloy steel.

Pre-crack tip locations were close to the nominal 1 mm in the case of post-weld heat-treated fusion line +1 mm specimens. The fracture surfaces appeared to be rather smooth according to the 3D maps. A 3D map for one specimen (HTFL+1_3) is shown in Figure 160. In all cases, cracks step close to the fusion line early in the J-R test and continue to grow in that region (Figures 161 and 162). In some cases the crack finds a weld bead boundary and makes a small step through the fusion line and then returns to the low-alloy steel side, as shown in Figure 163.

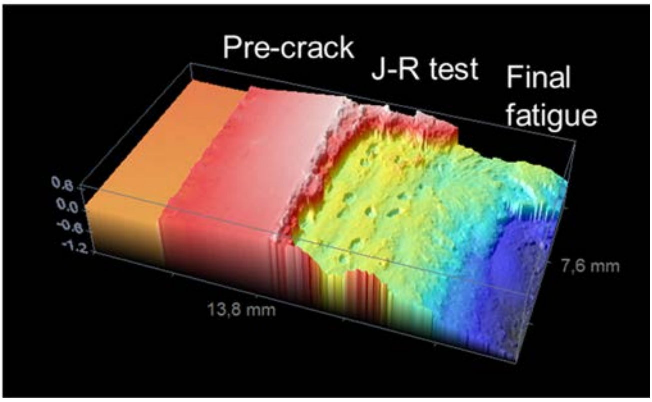

Figure 160. 3D topography map of specimen HTFL +1_3. Notch, pre-crack, J-R test and final fatigue can approximately be distinguished from the image. Crack grows on a rather smooth plane during the J-R test.

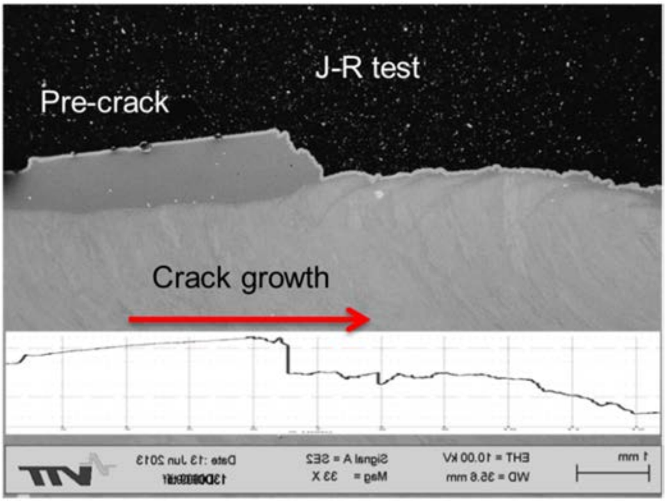

Figure 161. A SEM image of a polished mid-thickness cross-section of the fracture surface of specimen HTFL +1_3 and a mid-thickness line profile obtained from 3D profilometry measurement.

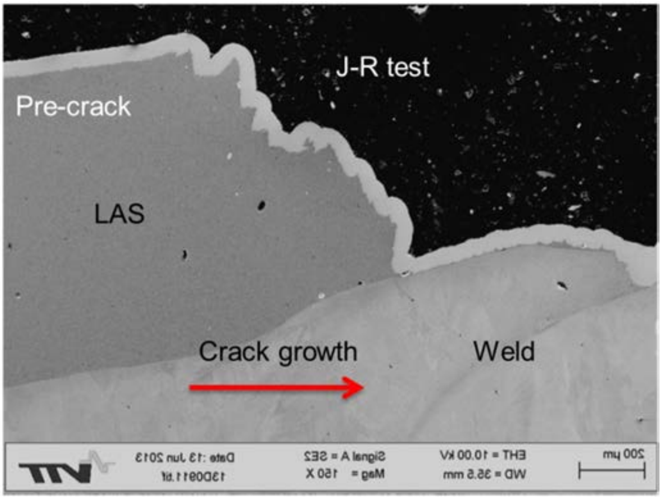

Figure 162. A SEM image of a detail of the polished fracture surface cross-section of specimen HTFL +1_3 at the location where the J-R test starts. Crack finds the fusion line early in the J-R test.

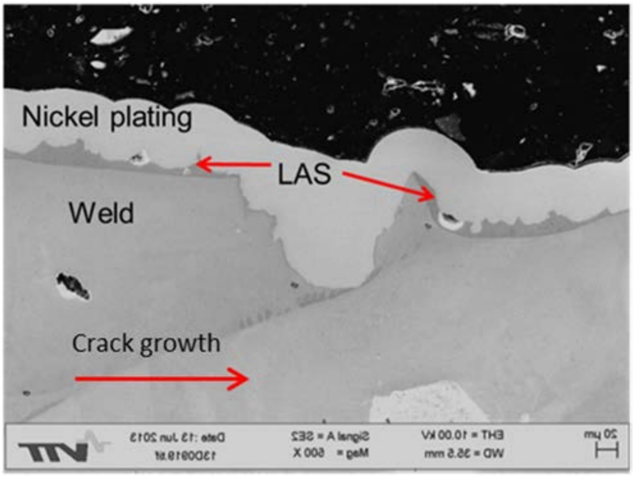

Figure 163. A SEM image of a detail of the polished fracture surface cross-section of specimen HTFL +1_3 at J-R test region. Crack grows in low-alloy steel close to the fusion line (<100 µm). At some locations, the crack occasionally finds a weld bead boundary and then returns to the low-alloy steel side.

In specimens where the pre-crack tip located in the weld cracks grew further to the weld during J-R testing. An example of a 3D profile of those specimens is presented in Figure 164.

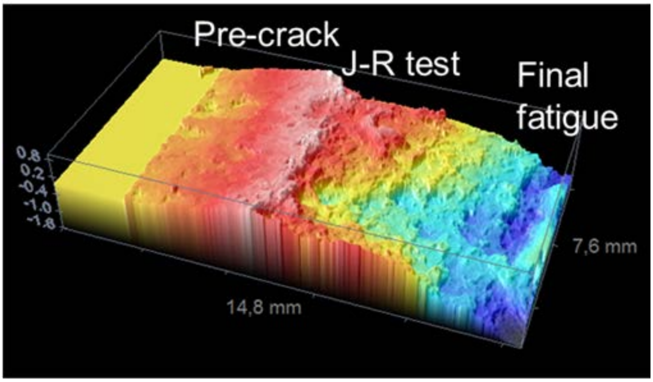

Figure 164. 3D topography map of specimen AWFL-1_1 fracture surface. Notch, pre-crack, J-R test and final fatigue can approximately be distinguished from the image. Crack grows towards the weld in the J-R test.

The 3D profilometer was unable to measure the fracture surfaces of HTFL-1 specimens due to too rough topography including steep inclinations on the fracture surfaces.

All the miniature 5x10x55 SE(B) specimens were studied using 3D profilometry. Representative examples of the results for each specimen series are presented in the following. Cross-sections were prepared from two specimens of each series of tests in order to clarify the actual pre-crack tip locations and crack paths. The selection of the specimens is based on different J-R test behaviour. The specimens that showed the most diverging J-R curves within a series of specimens were selected to be studied. Mid-thickness cross-sections of those specimens were examined using optical microscopy.

Cross-sections were manufactured from two as-welded fusion line samples (AWFL_4 and AWFL_5). 3D topography maps for those specimens are presented in Figures 165 and 166, respectively. Optical microscope images of the polished cross-sections are presented in Figures 167 and 168 and the detailed views of the transition from fatigue pre-crack to J-R test in Figures 169 and 170.

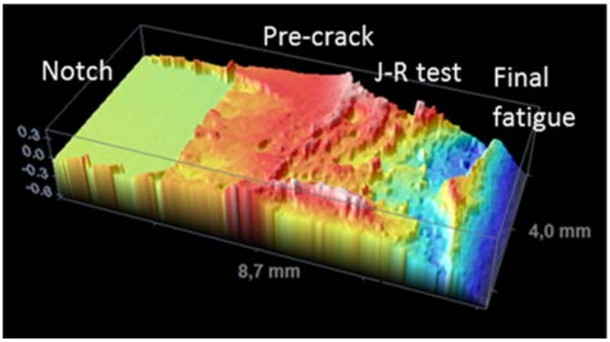

Figure 165. 3D topography map of the miniature-size specimen AWFL_4 fracture surface. Notch, pre-crack, J-R test and final fatigue can approximately be distinguished from the image. Fracture surface has a rough appearance in the J-R test region.

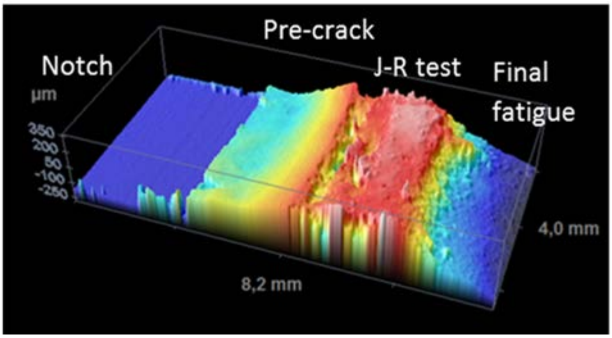

Figure 166. 3D topography map of the miniature-size specimen AWFL_5 fracture surface. Notch, pre-crack, J-R test and final fatigue can approximately be distinguished from the image. Crack makes steps early in J-R test but then finds a smooth plane.

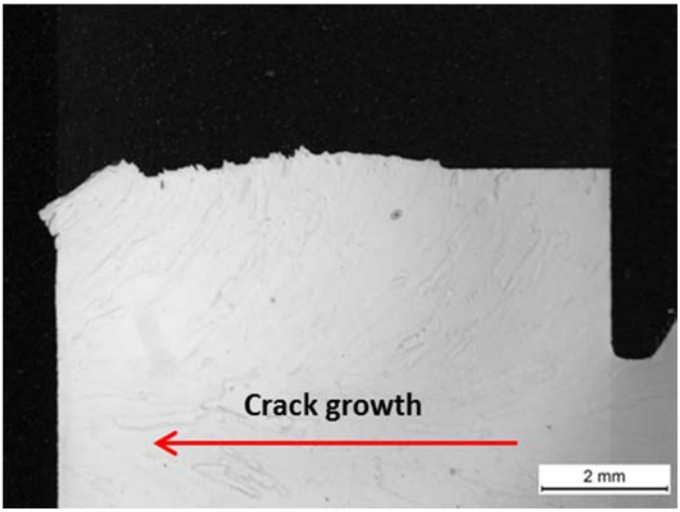

Figure 167. An optical microscope image of the polished fracture surface cross-section of specimen AWFL_4. Pre-crack tip is in the weld and the crack grows in the weld metal during the J-R test.

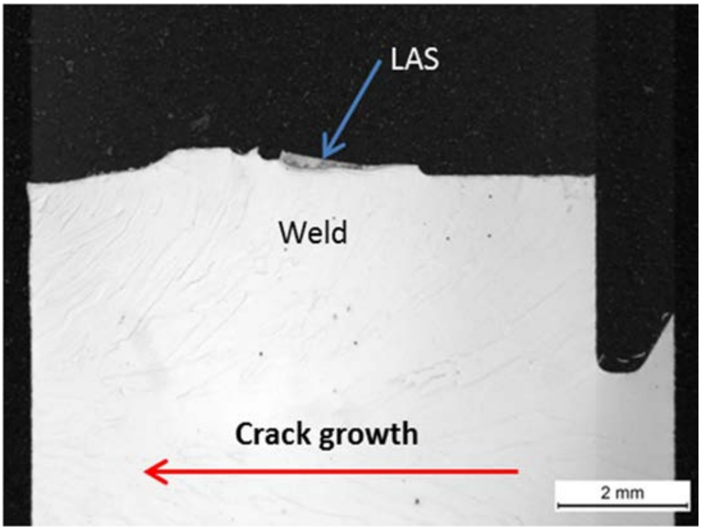

Figure 168. An optical microscope image of the polished fracture surface cross-section of specimen AWFL_5. Pre-crack tip is in low-alloy steel and the crack grows close to the fusion line during the J-R test.

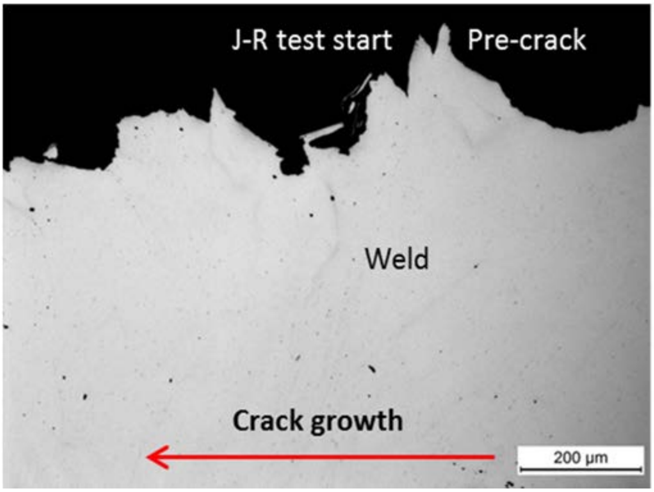

Figure 169. An optical microscope image of a detail of the polished cross-section of specimen AWFL_4. Pre-crack tip is in the weld and the crack grows in the weld during the J-R test. Crack path is tortuous.

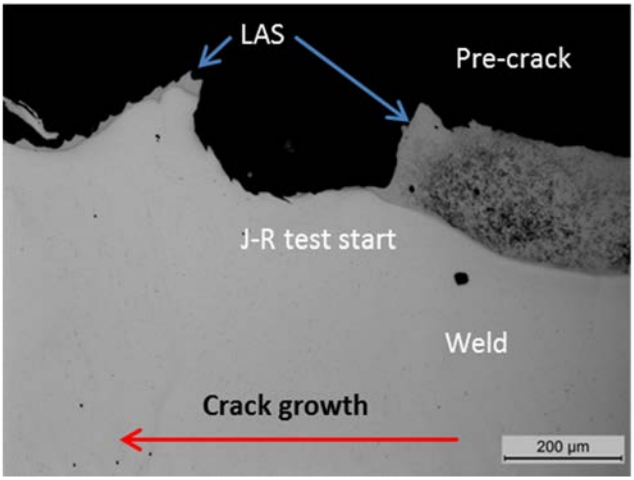

Figure 170. An optical microscope image of a detail of the polished cross-section of specimen AWFL 5. Crack makes a step to the fusion line region early in the J-R test and continues to grow in low-alloy steel close to the fusion line.

Cross-sections were manufactured from two heat-treated fusion line specimens (HTFL_1 and HTFL_3). 3D topography maps of the specimens are presented in Figures 171 and 172. Optical microscope images of the polished cross-sections are presented in Figures 173 and 174 and the detailed views of the transition from fatigue pre-crack to J-R test in Figures 175 and 176.

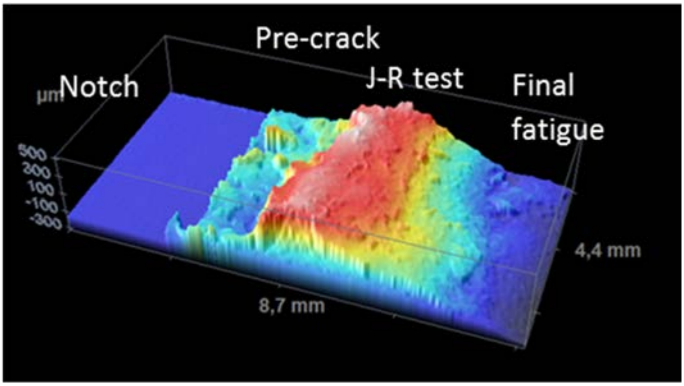

Figure 171. 3D topography map of the miniature-size specimen HTFL_1 fracture surface. Notch, pre-crack, J-R test and final fatigue can approximately be distinguished from the image. Fracture surface has a rather smooth appearance in the J-R test region.

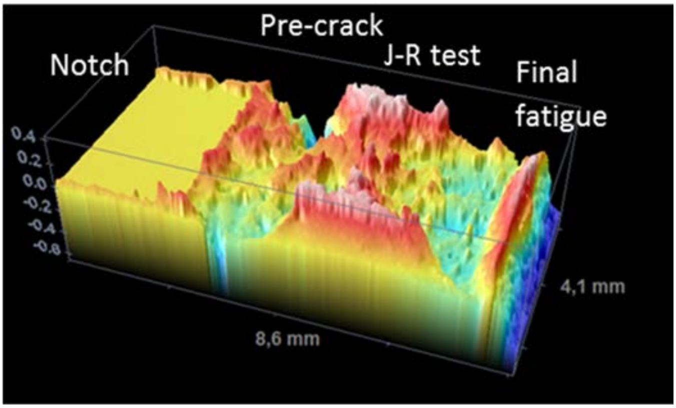

Figure 172. 3D topography map of the miniature-size specimen HTFL_3 fracture surface. Notch, pre-crack, J-R test and final fatigue are not clearly distinguishable from the image. Fracture surface has a rough appearance in the J-R test region.

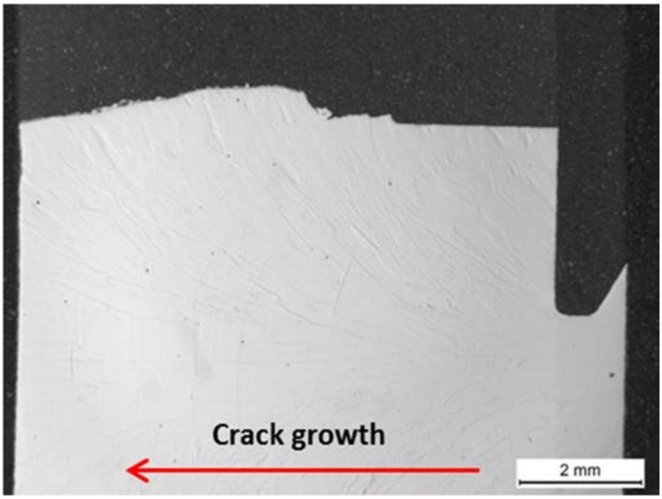

Figure 173. An optical microscope image of the polished fracture surface cross-section of specimen HTFL_1. Pre-crack tip is in the weld but the crack makes a step to the low-alloy steel side early in the J-R test and continues to grow in the LAS close to the fusion line.

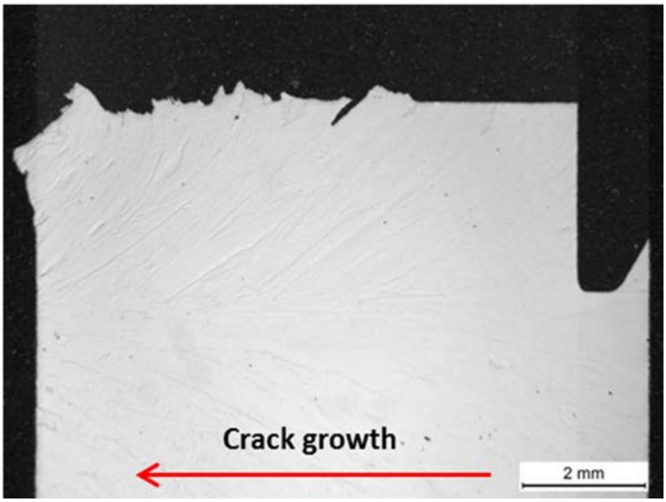

Figure 174. An optical microscope image of the polished fracture surface cross-section of specimen HTFL_3. Pre-crack tip is in the weld and the crack grows in the weld during the J-R test. The crack path is tortuous.

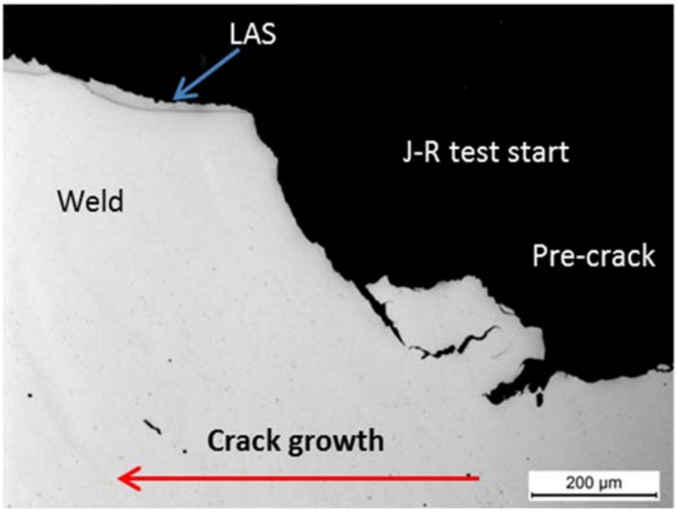

Figure 175. An optical microscope image of a detail of the polished cross-section of specimen HTFL_1. Pre-crack tip is in the weld but the crack makes a step to the low-alloy steel side early in the J-R test and continues to grow in LAS close to the fusion line.

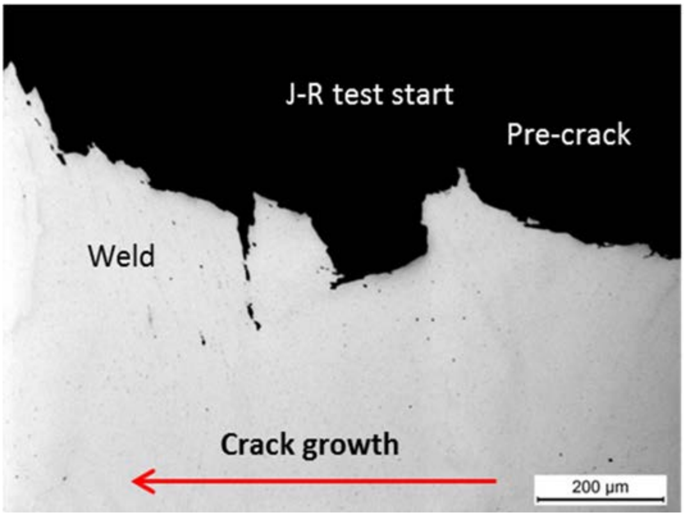

Figure 176. An optical microscope image of a detail of the polished cross-section of specimen HTFL_3. Pre-crack tip is in the weld and the crack grows in the weld during the J-R test.

Cross-sections were manufactured of two as-welded fusion line +1 mm specimens (AWFL +1_3 and AWFL +1_4). 3D topography maps of the specimens are presented in Figures 177 and 178. Optical microscope images of the polished cross-sections are presented in Figures 179 and 180. Figure 181 shows the start of the J-R test of specimen AWFL +1_3. The step to the fusion line region during the J-R test in specimen AWFL +1_4 is presented in Figure 182.

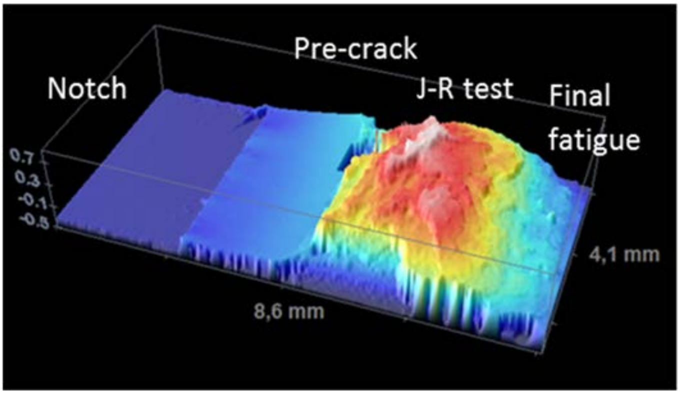

Figure 177. 3D topography map of the miniature-size specimen AWFL +1_3 fracture surface. Notch, pre-crack, J-R test and final fatigue can approximately be distinguished from the image.

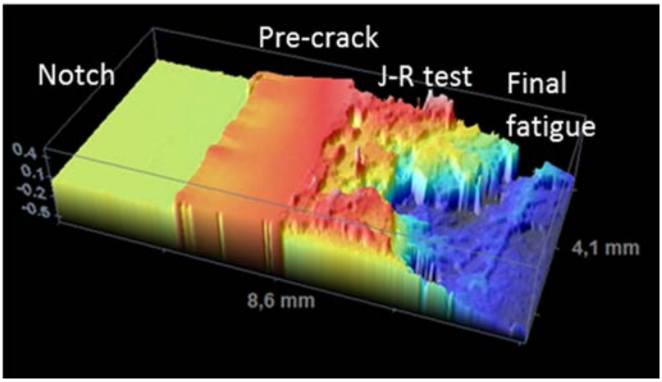

Figure 178. 3D topography map of the miniature-size specimen AWFL +1_4 fracture surface. Notch, pre-crack, J-R test and final fatigue can approximately be distinguished from the image.

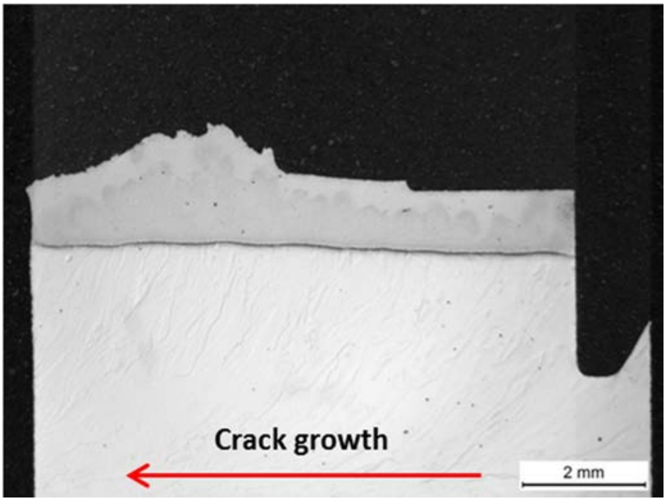

Figure 179. An optical microscope image of the polished fracture surface cross-section of specimen AWFL +1_3. Pre-crack tip is in the low-alloy steel and the crack grows in the LAS during the J-R test.

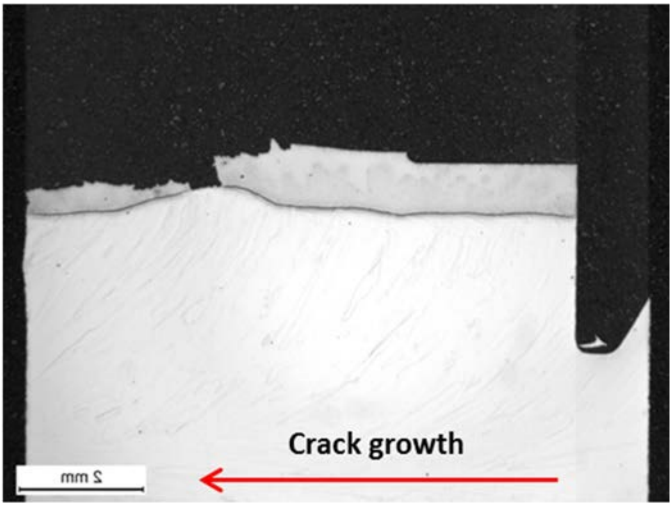

Figure 180. An optical microscope image of the polished fracture surface cross-section of specimen AWFL +1_4. Pre-crack tip is in low-alloy steel and the crack grows in the LAS during the J-R test. At one point, crack makes a step close to the fusion line during the J-R test but stays in the low-alloy steel side.

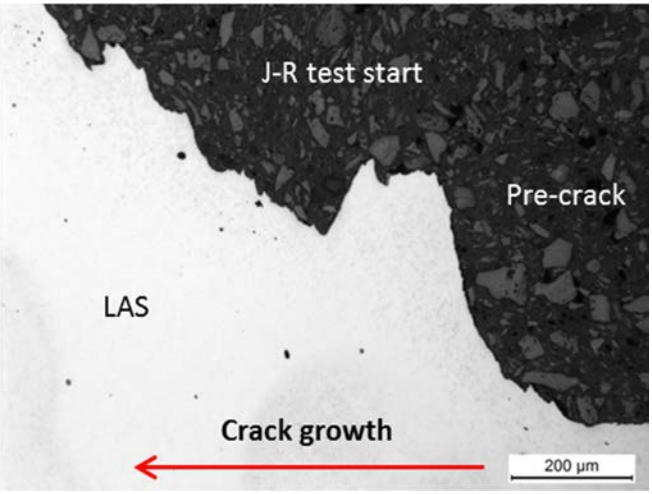

Figure 181. An optical microscope image of a detail of the polished cross-section of specimen AWFL +1_3. Crack grows in the low alloy steel.

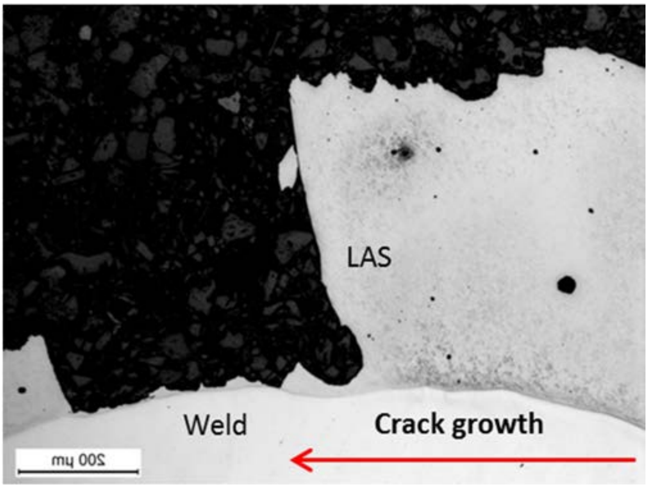

Figure 182. An optical microscope image of a detail of the polished cross-section of specimen AWFL +1_4. Crack grows in the low-alloy steel but makes a jump close to the fusion line during the J-R test.

Cross-sections were manufactured of two-post weld heat-treated fusion line +1 mm specimens (HTFL +1_2 and HTFL +1_4). 3D topography maps of the specimens are presented in Figures 183 and 184. Optical microscope images of the polished cross-sections are presented in Figures 185 and 186 and the detailed views of transition from fatigue pre-crack to J-R test in Figures 187 and 188.

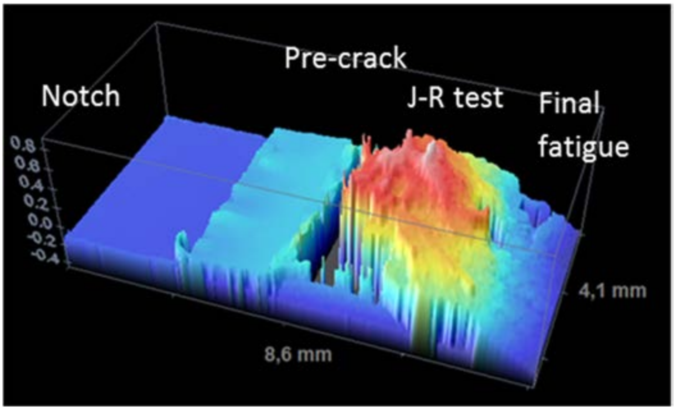

Figure 183. 3D topography map of the miniature-size specimen HTFL +1_2 fracture surface. Notch, pre-crack, J-R test and final fatigue can approximately be distinguished from the image. Some areas of the fracture surface are not covered in the 3D map because of steep inclinations that were not measurable.

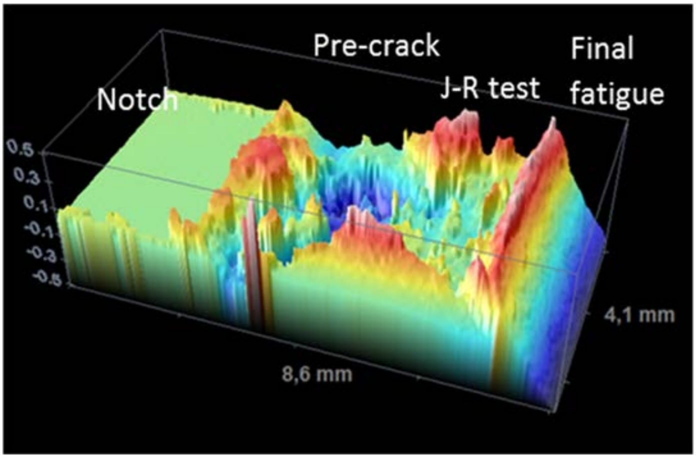

Figure 184. 3D topography map of the miniature-size specimen HTFL +1_4 fracture surface. Notch, pre-crack, J-R test and final fatigue are not clearly distinguishable from the image because of very rough and tortuous appearance of the fracture surface.

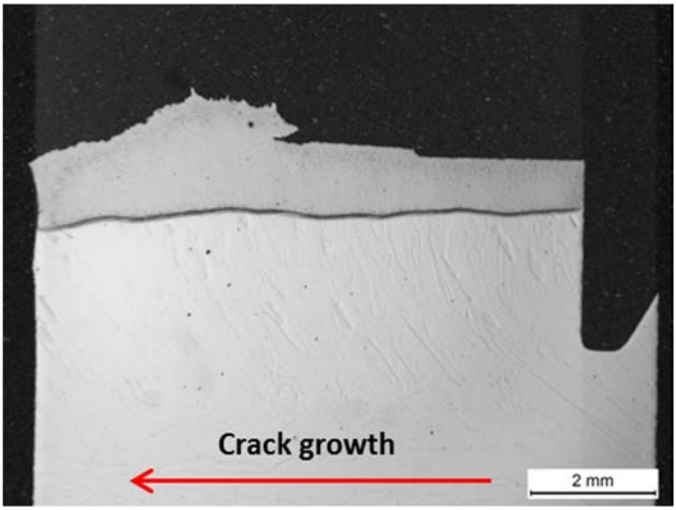

Figure 185. An optical microscope image of the polished fracture surface cross-section of specimen HTFL +1_2. Pre-crack tip is in the low-alloy steel and the crack grows in the LAS during the J-R test.

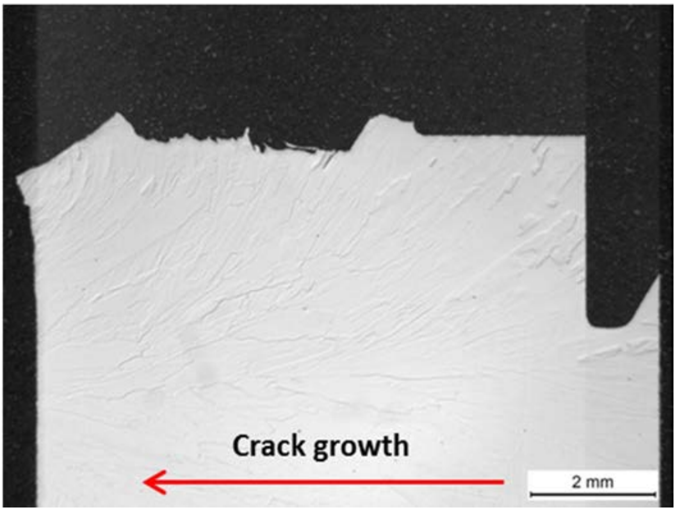

Figure 186. An optical microscope image of the polished fracture surface cross-section of specimen HTFL +1_4. Pre-crack tip is in the weld and the crack grows in the weld during the J-R test.

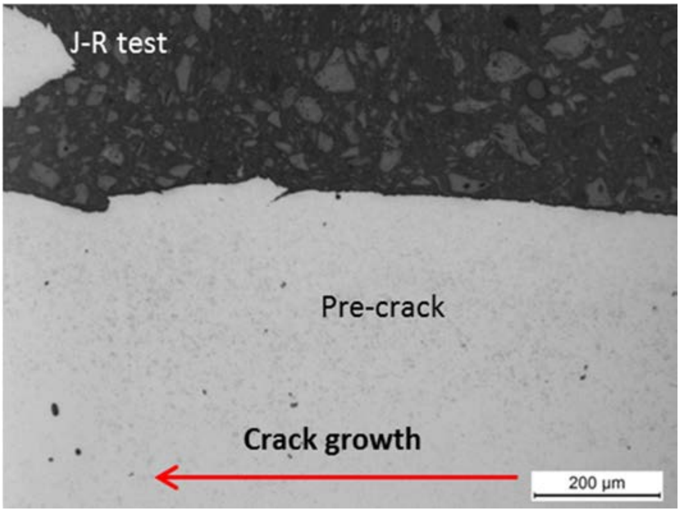

Figure 187. An optical microscope image of a detail of the polished cross-section of specimen HTFL +1_2. Crack grows in the low-alloy steel.

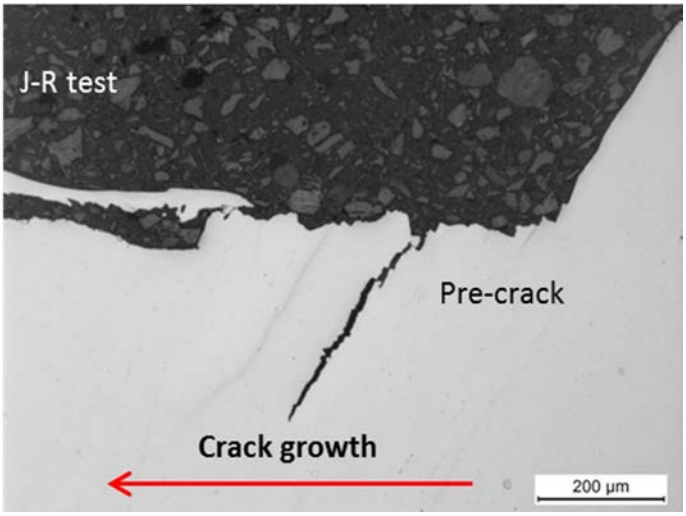

Figure 188. An optical microscope image of a detail of the polished cross-section of specimen HTFL +1_4. Crack grows in the weld.

Cross-sections were manufactured from two as-welded fusion line -1 mm specimens (AWFL -1_2 and AWFL -1_4). 3D topography maps of the specimens are presented in Figures 189 and 190. Optical microscope images of the polished cross-sections are presented in Figures 191 and 192.

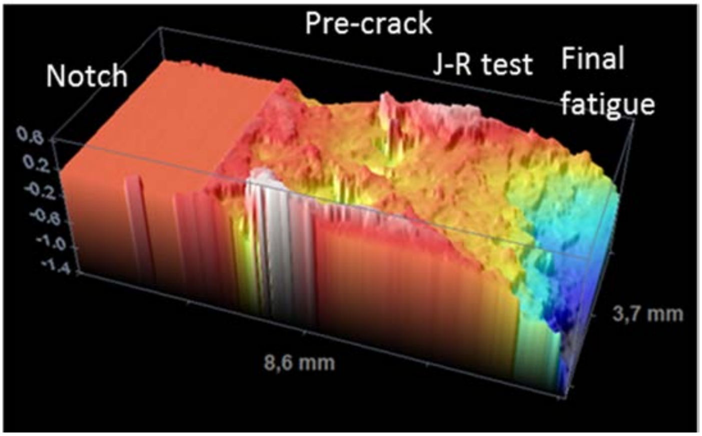

Figure 189. 3D topography map of the miniature-size specimen AWFL -1_2 fracture surface. Notch, pre-crack, J-R test and final fatigue are difficult to distinguish from the 3D map.

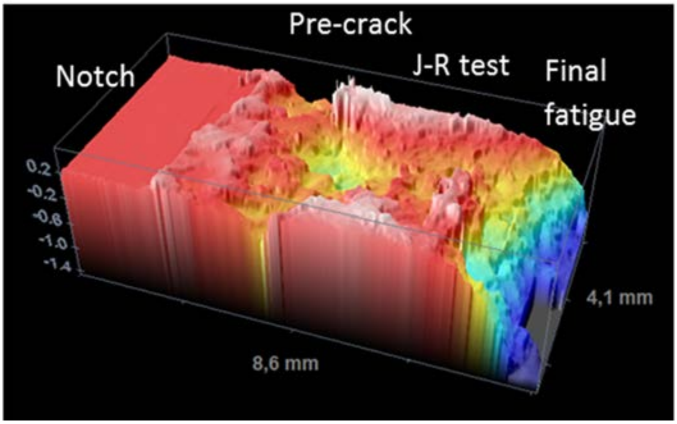

Figure 190. 3D topography map of the miniature-size specimen AWFL -1_4 fracture surface. Notch, pre-crack, J-R test and final fatigue are difficult to distinguish from the 3D map.

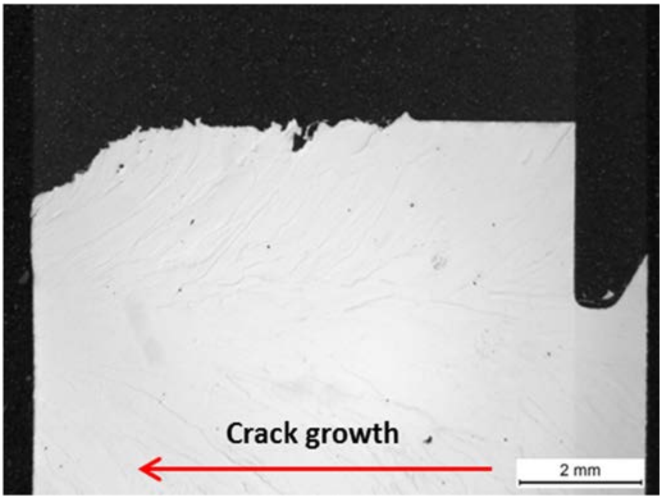

Figure 191. An optical microscope image of the polished fracture surface cross-section of specimen AWFL -1_2. Pre-crack tip is in the weld and the crack grows in the weld during the J-R test.

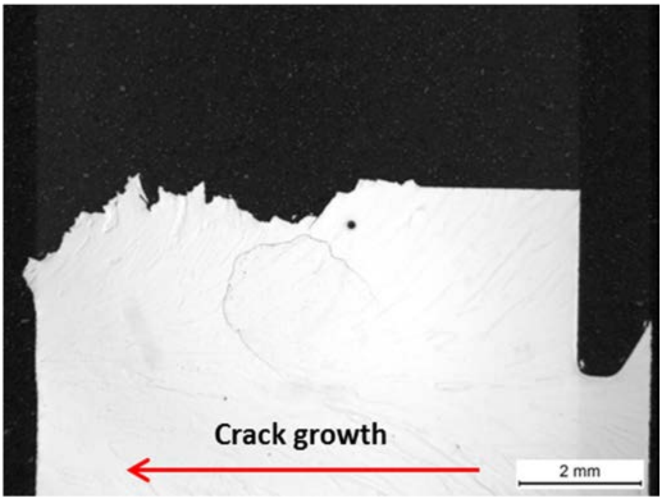

Figure 192. An optical microscope image of the polished fracture surface cross-section of specimen AWFL -1_4. Pre-crack tip is in the weld and the crack grows in the weld during the J-R test.

Cross-sections were manufactured from two post-weld heat-treated fusion line -1 mm specimens (HTFL -1_4 and HTFL -1_8). 3D topography maps of the specimens are presented in Figures 193 and 194. Optical microscope images of the polished cross-sections are presented in Figures 195 and 196.

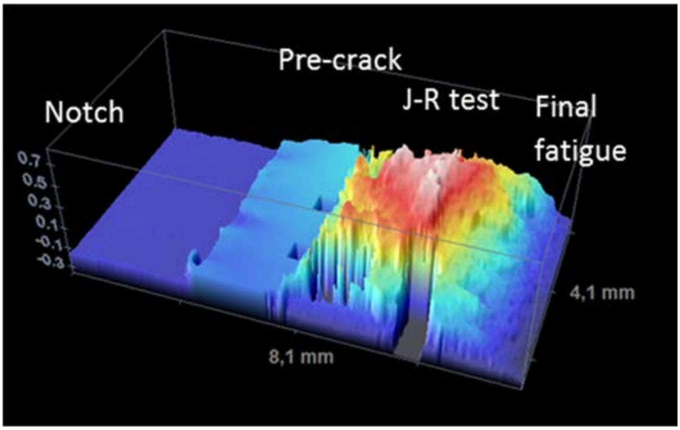

Figure 193. 3D topography map of the miniature-size specimen HTFL -1_4 fracture surface. Some areas of the fracture surface are not covered in the 3D map because of steep inclinations that were not measurable.

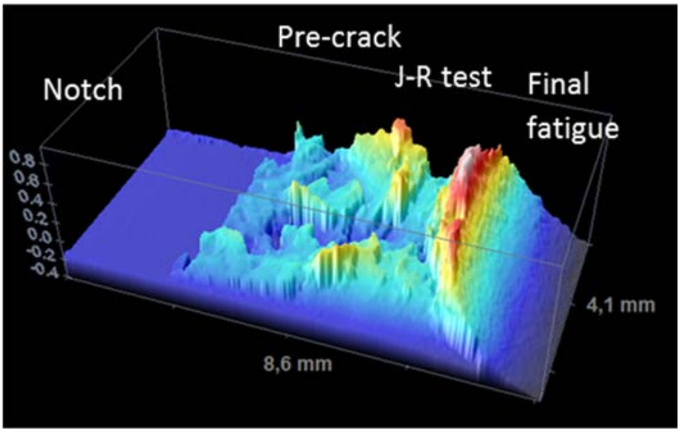

Figure 194. 3D topography map of the miniature-size specimen HTFL -1_8 fracture surface. Notch, pre-crack, J-R test and final fatigue are difficult to distinguish from the 3D map.

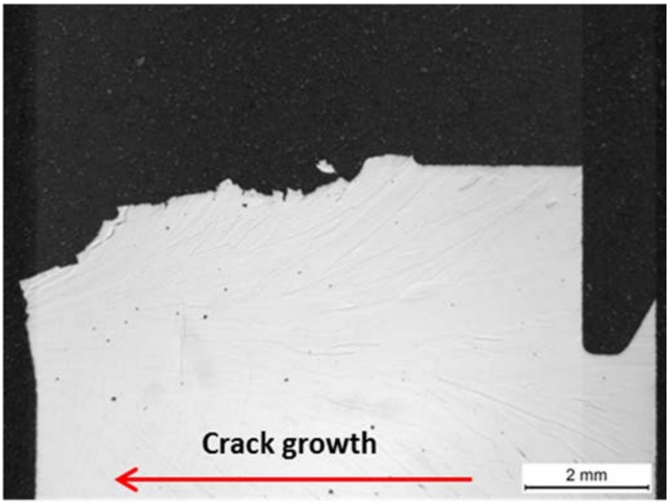

Figure 195. An optical microscope image of the polished fracture surface cross-section of specimen HTFL -1_4. Pre-crack tip is in the weld and the crack grows in the weld during the J-R test.

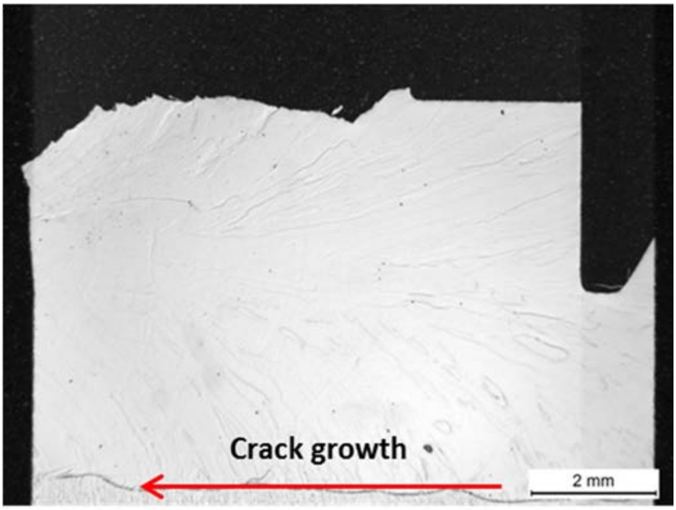

Figure 196. An optical microscope image of the polished fracture surface cross-section of specimen HTFL -1_8. Pre-crack tip is in the weld and the crack grows in the weld during the J-R test.

Cracks propagated mostly in the LAS side in carbon-depleted zone during J-R testing, but in the case of AW specimens cracks also made steps to the weld metal side. The reason for the steps seems to be small welding defects that were detected on the fracture surfaces of AW specimens. However, these steps were not observed in PWHT samples. As it can be seen in 3D topography maps, the fracture surfaces of PWHT specimens have a smooth appearance and the cracks propagate always close (2–150 µm) to the fusion line. Figures 197–200 show that there is a thin zone (thickness about 2–5 µm) right next to the fusion line in PWHT samples that has a white appearance in optical microscope images (Figures 197 and 198). The hardness measurements indicate that this white zone is very hard. A local hardness mismatch in the fusion line region in the heat-treated specimens is larger than in as-welded specimens, based on the nano-hardness measurements, and it appears that the cracks do not tend to propagate through the hard white zone in J-R testing.

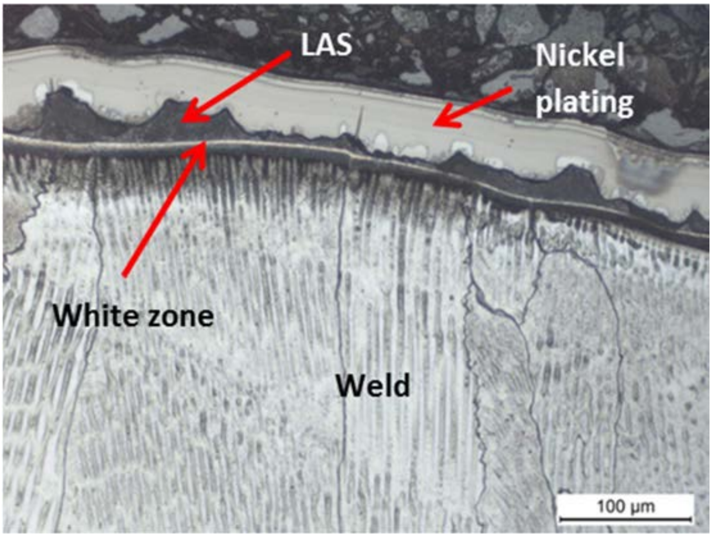

Figure 197. An optical image of the polished and electrolytically etched cross-section of the fracture surface of a J-R tested specimen (HTFL_1) showing the crack path and the fusion line region microstructure. A white zone was detected close to the fusion line on the weld metal side.

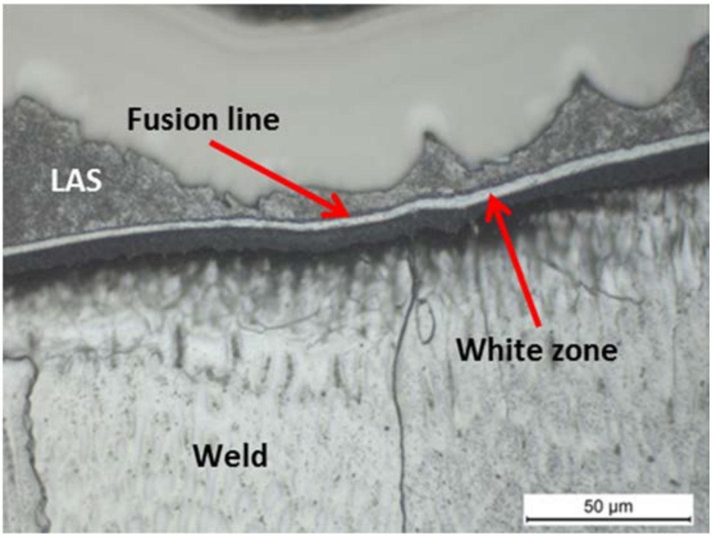

Figure 198. A detailed view of the polished and electrolytically etched cross-section of the fracture surface of a J-R tested specimen (HTFL_1). The white zone is about 2–5 µm thick.

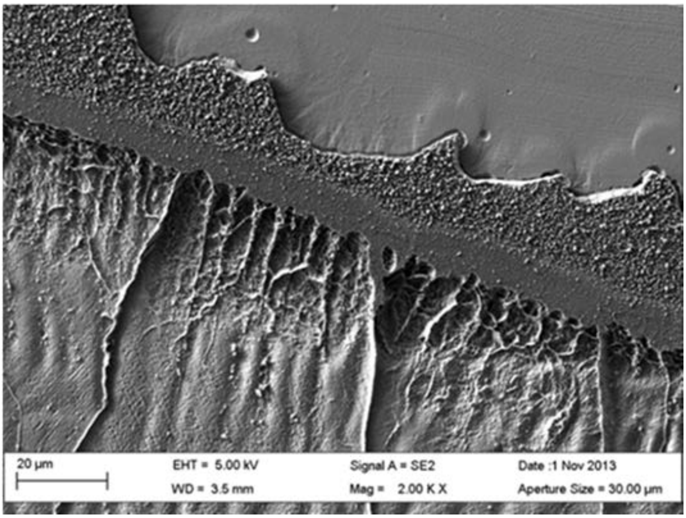

Figure 199. A SEM image illustrating the fusion line region of the polished and electrolytically etched cross-section of a J-R tested specimen (HTFL_1).

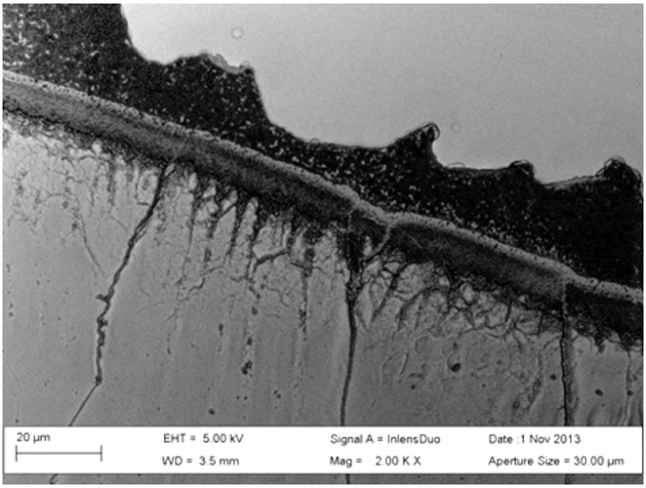

Figure 200. A SEM image illustrating the fusion line region of the polished and electrolytically etched cross-section of a J-R tested specimen (HTFL_1).

A fracture surface of a PWHT specimen (HTFL_1) was gradually grinded and polished in a direction shown in Figure 201, in order to study the white zone and the fusion line region. The grinding plane of this sample is nominally parallel to the fusion line but the fusion line region becomes locally visible because the FL is not straight. Figure 202 shows an area of the fracture surface that has been grinded and polished until the fusion line region unfolds. That area was studied in more detail using SEM. Figures 203 and 204 illustrate the fusion line region. Based on the appearance of the microstructure in SEM images there seems to be some martensite in the weld metal side close to the fusion line.

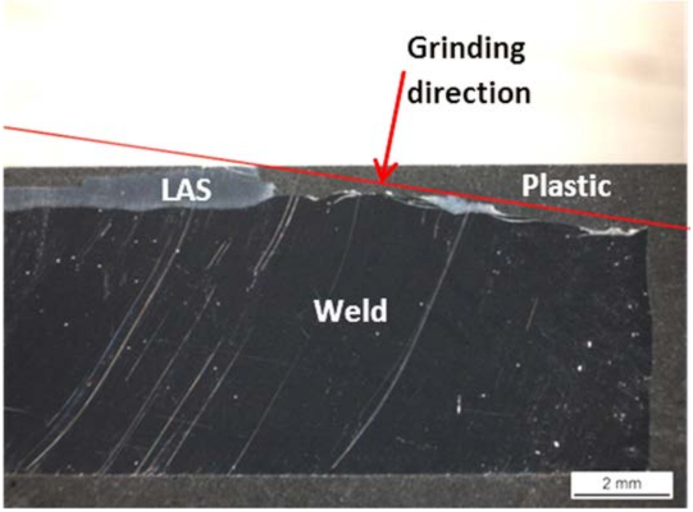

Figure 201. The fracture surface of the J-R tested specimen (HTFL_1) was ground and polished as shown in the picture with a red line.

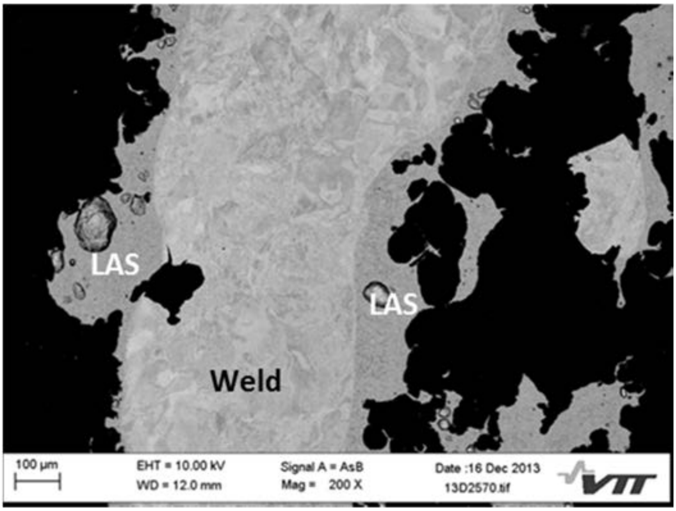

Figure 202. An area of the fracture surface of the studied J-R tested specimen (HTFL_1). The fracture surface was ground and polished until the fusion line region was reached. The image illustrates an unfolded area where the middle part consists of weld metal and the perimeters consist of low-alloy steel. The black areas are plastic that the fracture surface was cast in.

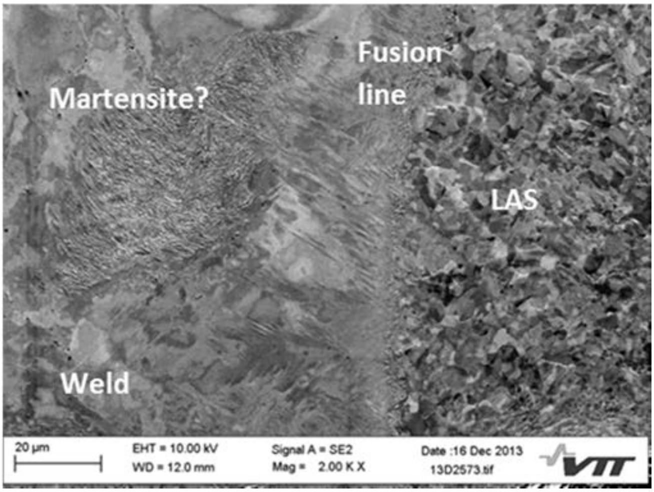

Figure 203. A SEM image showing the fusion line region. Some areas with martensitic appearance were observed.

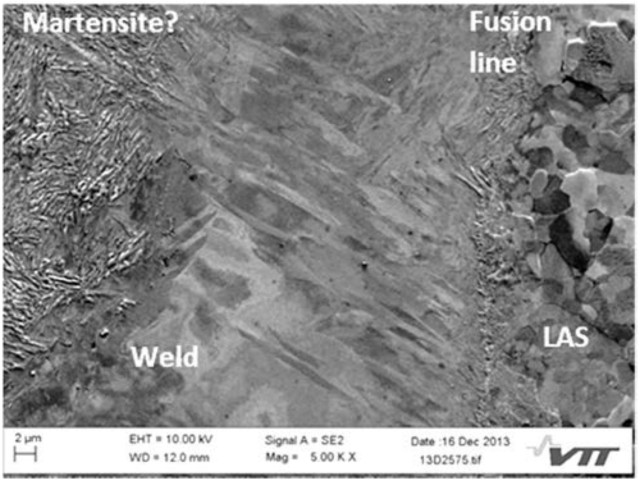

Figure 204. A detailed view of the fusion line region showing the LAS and weld metal sides and a possible martensitic area (on the left).

The chemical composition of the white zone region was analysed using EDS line analysis shown in Figure 205. The EDS did not show evidence of a higher carbon content next to the fusion line at Alloy 52 weld metal side and, thus, the EDS results do not explain the high hardness values measured from the area of the white zone. However, the amount of carbon is very low, and may be below the sensitivity of the EDS-method.

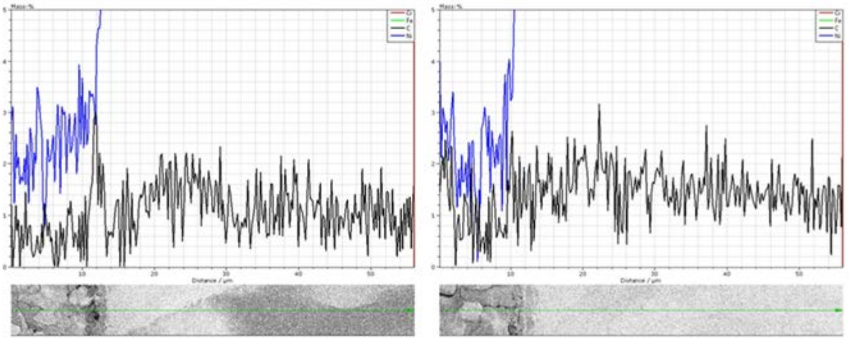

Figure 205. EDS line scans over the SA 508 – Alloy 52 interface of a PWHT state fracture mechanical specimen (carbon content shown in black).

3.6 Conclusions

The microstructural examination of the fusion line area of the NG-DMW specimens revealed the following characteristics:

1. A CDZ (carbon-depleted zone) was found from the SA 508 side of the fusion line and the PWHT increased the width of the CDZ from around 30 to around 80 µm,
2. a discontinuous type II boundary was found from the weld metal from about 10 to few tens of µm from the fusion line,
3. a PMZ (partially melted zone), which seemed martensite-like, located between the Type II boundary and the fusion line,
4. and a HAZ with microstructural zones typical of low-alloy steel (LAS) was detected from the SA 508 side of the fusion line.

The Type II boundary and the PMZ were not continuous along the fusion line and the distance of the Type II boundary from the fusion line varied. According to EDS, the weld dilution seemed to take place in a very narrow zone right next to the fusion line and the gradients of Fe, Cr, and Ni composition change were very steep in locations in which the PMZ was not present. In the locations in which the PMZ was present, the change in Fe, Cr, and Ni compositions was more gradual.

Hardness measurements showed a hardness peak at the SA 508 HAZ of the as-welded NG-DMW. The PWHT decreased the hardness of the SA 508 HAZ; however, the PWHT caused formation of a narrow hard zone to the Alloy 52 weld metal side of the fusion line. The hardness peak in the SA 508 HAZ is caused by the grain refining microstructure that has formed next to the fusion line as a result of the rapid cooling from high peak temperatures above A3 during the welding process. The narrow hard zone in the Alloy 52 weld metal in PWHT state has been caused by increased carbon mitigation across the fusion line due to the

PWHT and likely a formation of carbon pile-up right next to the fusion line. Next to the narrow carbon pile-up zone, a precipitate-rich zone was found from the Alloy 52 weld metal which also causes an increased hardness in the Alloy 52 weld metal side of the fusion line.

The lowest average yield stress and tensile strength of Alloy 52 NG weld mock-up is in Alloy 52 weld metal, and the highest values near (at a distance of +1 mm) or at the fusion line between SA 508 base material and Alloy 52 weld metal. Strain hardening capacity of Alloy 52 NG weld mock-up is the highest in AISI 308 cladding and quite high in Alloy 52 weld metal. Fusion line or HAZ near the fusion line (SA 508/Alloy 52) has the lowest strain hardening capacity. Average tensile strength determined with flat miniature specimens as a function of average hardness $HV_{0.5}$-values for Alloy 52 weld mock-up show good linear correlation in case of base material SA 508 and HAZ in at the distance of 1 mm and 2 mm from the fusion line. The correlation is in line with correlations presented in literature [Gaško & Rosenberg et al. 2011, Pavlina & van Tyne 2008]. Fusion line and weld metal average tensile strength vs. hardness seems not to follow the same trend as SA 508 base material and its HAZ. As fusion line and weld metal are inhomogeneous, hardness and tensile test are more likely to find material volumes with different properties, thus providing firstly much bigger scatter than base material or HAZ. Secondly, strain hardening capacity may have an effect on the form of tensile vs. hardness correlation.

All tensile tests and hardness measurements show that mismatch is greatest near the fusion line. Hardness measurements show greater mismatch near the interface area than tensile testing. This is due to the fact that hardness test can capture more local microstructural variations than tensile test specimen. Tensile test results represent more averaged value over greater volume of material or zone. Degree of mismatch becomes different based on hardness data and strength data, but the location is the same i.e. near the interface area. For structural integrity assessment, mismatch between two adjacent microstructural zones may be more significant than mismatch based on comparison with parent steel properties. In this case mismatch between adjacent zones has its highest values near the interface area.

The fracture mechanism of the fracture mechanical test specimens was ductile and no brittle behavior was found in the studied zones. Fracture resistance of all the weld zones was high and the PWHT increased the fracture resistance of the Alloy 52 weld metal. The PWHT seemed to have a negative effect on the fracture resistance of the SA 508 side of the weld since the PWHT SA 508 HAZ and FL specimens showed lower fracture resistance values than those of the as-welded state. The crack propagation occurred from the SA 508 HAZ towards the fusion line. Once the crack had reached the fusion line area, it continued its propagation along the SA 508 side of the fusion line in the PWHT specimens. In the as-welded specimens, the crack made occasional jumps across the fusion line into the Alloy 52 weld metal side. The ductile tearing in the SA 508 side of the fusion line seemed to be controlled by the distribution of MnS particles in the microstructure. MnS particles near the fusion line were small and finely distributed whereas the

MnS particle distribution farther away from the fusion line was coarser and the size of the MnS inclusions was larger. The width and hardness of the CDZ and the existence of the narrow hard zone in the Alloy 52 side of the fusion line in PWHT state weld may offer an explanation for the crack propagation behavior. The wider and softer CDZ in the PWHT state weld causes the crack to propagate along the SA 508 side of the fusion line and the existence of the hard zone in the Alloy 52 prevents the crack propagation across the fusion line into the Alloy 52 side of the weld. In the as-welded state weld, the CDZ is narrower and harder and, thus, the crack occasionally jumped across the fusion line into the Alloy 52 weld metal.

4. Crack initiation testing

A limited amount of laboratory EAC initiation test results is available for the new material combinations of dissimilar metal welds of nuclear power plants. A test has been developed to enhance cracking of Ni-base alloys and their weld metals at 400 °C. According to Staehle and Gorman [2004], the initiation time of low potential stress corrosion cracking (LPSCC) follows monotonic 1/T dependence from hydrogenated steam to water. This suggests that the mechanistic processes in water and steam are the same, at least for pure water, Figure 206. As crack initiation takes a very long time (years or decades) in actual LWR water at relevant operating temperatures, the accelerated tests have been conducted at 400 °C in steam doped with hydrogen, sodium chloride, sodium sulphate and sodium fluoride [Staehle & Gorman 2004].

Jacko et al. [2003] performed an accelerated laboratory test series in an environment consisting of hydrogenated 400 °C steam doped with fluoride, chloride and sulphate anions. Comparison tests were performed using Alloy 600 and Alloy 182 weld metal. Alloy 52M welds, prepared to simulate the Ringhals 4 field repairs of the reactor pressure vessel outlet nozzle, exhibited complete resistance to stress corrosion crack initiation in laboratory exposure times exceeding 45 effective full-power years (EFPYs) equivalent service times. Stress corrosion cracks initiated in Alloy 182 welds in exposure times less than one-fifth of the total exposure time of the Alloy 52M specimens. Crack initiation was also observed in specimens of Alloy 600 CRDM nozzle material in the doped steam environment. The specimens used by Jacko et al. [2003] were prepared as flat plates and they were bolt loaded in specially designed four-point bending fixtures. Analysis indicated that the degradation observed after 89000 EFPHs at 317 °C in Ringhals 4 was duplicated with 289 h exposure at 400 °C to sulphate, chloride and fluoride doped hydrogenated steam. This translates to an acceleration factor of 308. For other temperatures Jacko et al. adjusted the acceleration factor using an activation energy of Q = 55 kcal/mole [Jacko et al. 2003]. The activation energy was estimated by assuming Arrhenius type dependence for cracking probability between Alloy 600 in Ringhals 4 and Alloy 600 in laboratory tests at 400 °C in doped steam [Rao et al. 2002].

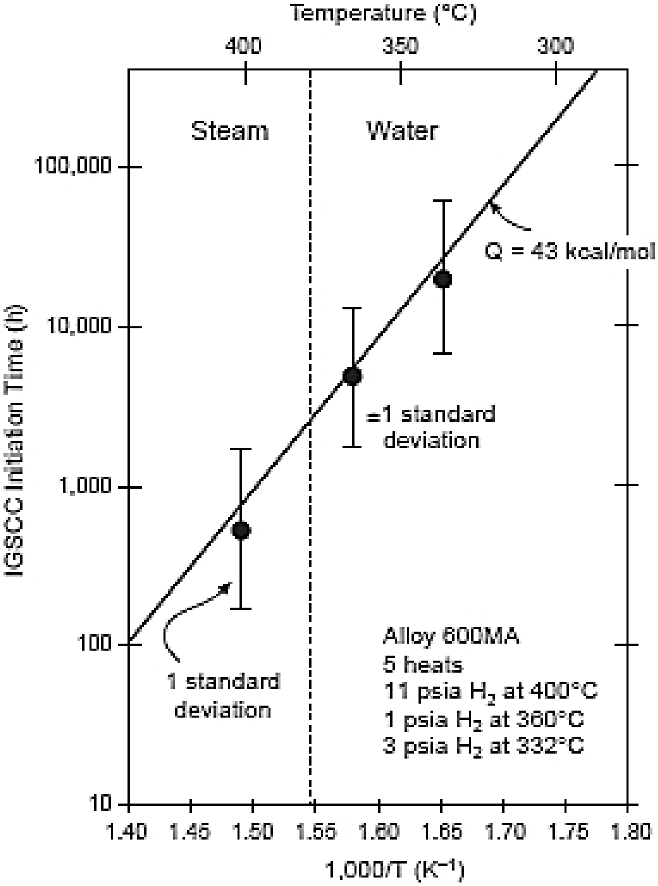

Figure 206. 1/T dependence of the LPSCC crack initiation time of Alloy 600 in water and steam [Staehle & Gorman 2004].

The approach of Jacko et al. [2003] was followed in the previous projects, ERIPARI and PERDI, realised at VTT and Helsinki University of Technology (presently part of Aalto University) in 2003–2006 and 2006–2009 [Hänninen et al. 2007B, 2011, 2007A, 2009]. The specimens were safe-end weld mock-ups containing weld metals Alloy 52, 152, and 182 and pure weld metals 52, 152, 82 and 182. The specimens were loaded to 0.35 or 1% strain in the ERIPARI project and 1.1% in the PERDI project. In those tests the first clear crack indications were observed after 240 h exposure in Alloys 82 and 182. No clear difference could be distinguished in the initiation times between the specimens strained to 0.35 and ~1%. In Alloys 52 and 152 indications were also present, but they resulted from the initial mechanical loading that opened pre-existing hot cracks or other weld defects.

Detailed fractography of broken pure Alloy 182 and 82 specimens showed that the outer surface and fracture surface were covered with an oxide layer. However, a metallic Ni film had formed on the top of the oxide layer within the cracks and covered almost completely the fracture surface close to the specimen surface. In the middle of the crack the formation of NiO was also observed as small particles growing laterally on the oxide covered surface together with larger Fe-rich spinel oxide particles. Close to the crack tip no metallic Ni or NiO was observed and the fracture surface was covered only by a thin Cr-rich oxide layer. In the cross-sections of the cracks the intergranular propagation of the fracture was evident [Hänninen et al. 2009].

In the SINI project the crack initiation in a number of nickel-based dissimilar metal welds (Alloys 182, 82 and 52) and mill-annealed Alloy 600 were studied. Testing was performed in pure and doped steam as well as in PWR water. Pure and doped steam testing was done at 400 °C and 150 bar pressure with a target value for H_2 pressure, which according to the Ellingham diagram presents the Ni-NiO stability line in these conditions. The tests in PWR water were done at 360 °C.

The test series had two objectives:

1. Reproduce cracks in pure steam for comparison with the cracks observed in doped steam tests performed within the ERIPARI and PERDI projects.
2. Reproduce cracks in relevant PWR reactor water for comparison with the cracks formed in doped and pure steam.

4.1 Materials and specimens

The specimens were prepared by plane milling. Mechanical polishing by 600 grit emery paper was performed after milling in order to remove the roughness of the specimen surfaces. The specimens were, initially, bolt-loaded in 4-point bend loading. Strain was calculated from the bending radius of a 3.5 mm thick plate. The initial target strain for the specimens was 1.1%. Later some of the specimens were further loaded to ~5% strain and bolt loaded to U-shape. Specimens which were cut from the weld mock-ups were cut from the weld root side of the mock-up, Figure 207a. Pure welds were welded on a groove made to a AISI 304 steel block, Figure 207b, and the specimens were cut so that the 20 mm wide pure weld was located in the middle of the test bars in the 4-point bend fixtures, Figure 207c. The U-bend loading geometry of the specimens tested in the later phase of the project is shown in Figure 207d. In Figure 208 are presented in red rectangles EAC sample locations in a) Alloy 52 and b) EAC mock-up. Different combinations of nickel-base dissimilar metal welds were tested. The combinations together with the number of specimens and test environment are shown in Table 15.

a)

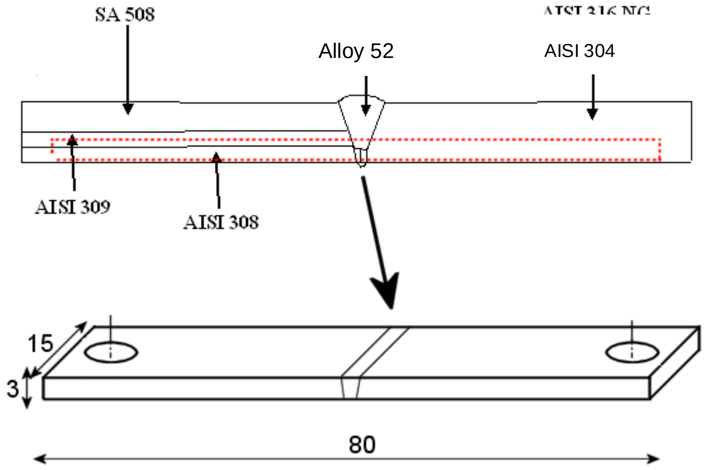
SA 508
AISI 316 NG
Alloy 52
AISI 304
AISI 309
AISI 308
15
3
80

b)

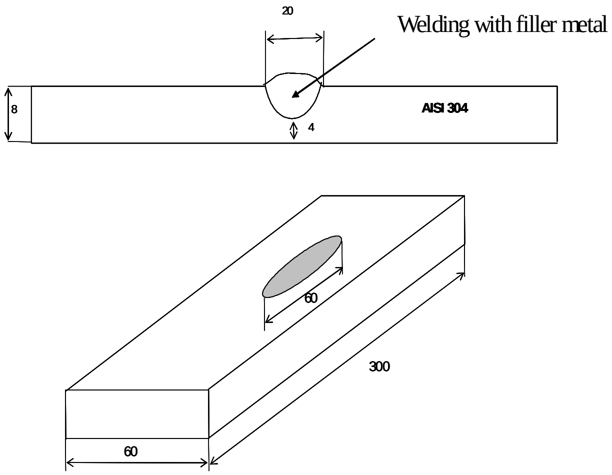
20
Welding with filler metal
8
AISI 304
4
60
300
60

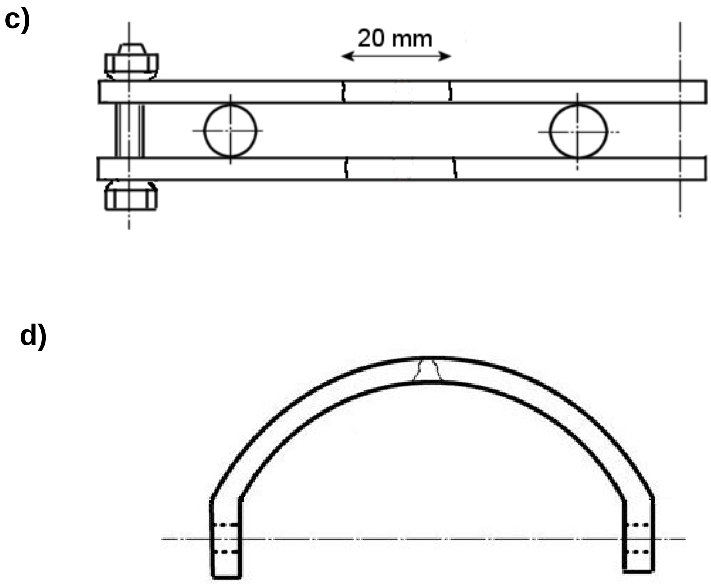

Figure 207. Cutting plan and dimensions of the weld mock-up test bars a), pure weld preparation b), initial loading geometry of the test bars (length of the pure weld shown) c), and U-bend shape loading geometry used in the later phase of the project d).

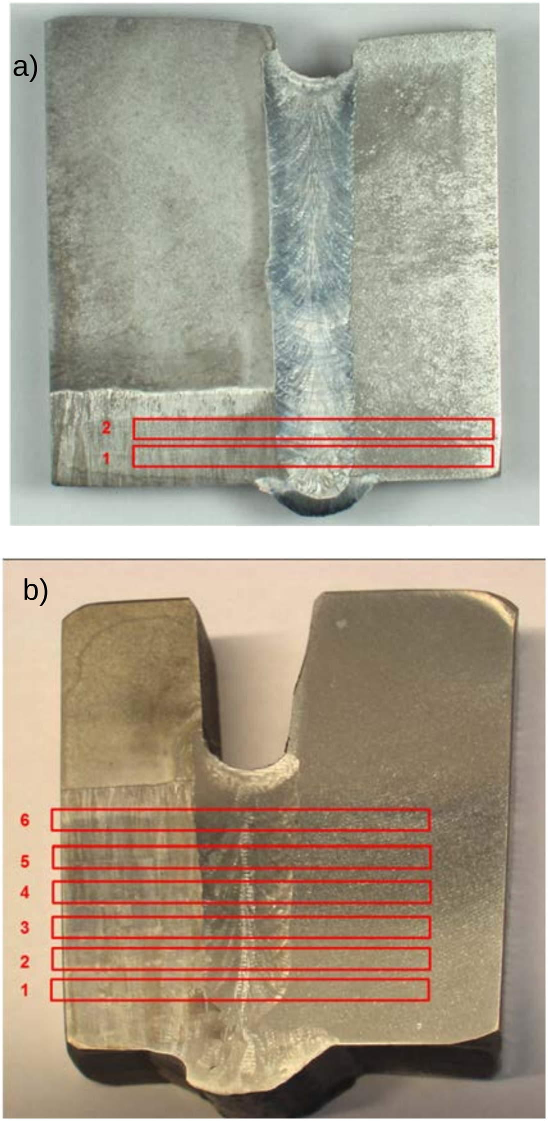

Figure 208. EAC sample locations in a) Alloy 52 mock-up and b) EAC mock-up.

Table 15. Number of each type of specimens, material combinations and test environment.

No. of specimens	Weld type	Environment
4	308/butter 182	Steam, 400 °C
3	Butter 182/82/304	Steam, 400 °C
6	Pure 82	Steam, 400 °C
6	Pure 182	Steam, 400 °C
2	LAS/root 52/316	Steam, 400 °C
15	52 narrow gap	Steam, 400 °C
4	Alloy 600	Steam, 400 °C
6	Pure 82	PWR, 360 °C
6	Pure 182	PWR, 360 °C
4	Alloy 600	PWR, 360 °C
3	52 oxidation plates	Steam, 400 °C /PWR 360 °C
3	182 oxidation plates	Steam, 400 °C /PWR 360 °C

*At a later stage of the project, the steam test specimens were divided to two groups. Tests of one group were continued in doped steam after the pure steam exposure and tests of the other group were continued in pure steam, but with a higher strain, ~5%.

Specimens were prepared also for oxide layer analysis using XPS (see Chapter 5). These specimens were made of Alloy 52 and 182 welds. The dimensions of the specimens were about 10x10x1 mm. The surfaces of the specimens were polished before the exposure with diamond paste.

4.2 Experimental methods

Crack initiation in a number of nickel-based dissimilar metal welds (Alloys 182, 82 and 52) and mill-annealed Alloy 600 were studied. Testing was performed in pure and doped steam as well as in PWR water. Pure and doped steam testing was done at 400 °C and 150 bar pressure with a target value for H_2 pressure which according to the Ellingham diagram presents the Ni-NiO stability line in these conditions. The tests in PWR water were done at 360 °C. High susceptibility to crack initiation and growth was observed with Alloy 600 and Alloy 182 and 82 weld metals, while Alloy 52 weld metal showed no crack initiation.

4.2.1 Tests in steam

Tests were started using 4-point bend specimens strained to 1.1% in pure steam. Later the specimens were divided to two groups of about the same number of identical material combinations in each. One group was further loaded from 1.1% to ~5% strain and the test in pure steam was continued. At this point, the loading geometry was U-bend. The other group was used for testing in doped steam. In the doped steam test, the strain remained at 1.1%.

The steam for the pure steam tests was generated by injecting de-ionized O_2-free water into the autoclave. The target pressure was 150 bar. Target value for H_2 partial pressure was 0.56 bar, which according to the Ellingham diagram represents the Ni-NiO equilibrium at this temperature and steam pressure. The steam pressure was maintained using a high performance liquid chromatography (HPLC) pump feeding replacement water to the autoclave operated under constant pressure mode. The H_2 partial pressure was measured using a Pd-membrane sensor inside the autoclave. The H_2 partial pressure was controlled by a PID controller connected to a pressure sensor and a high pressure solenoid valve connected to the tube between the autoclave and the hydrogen container. The autoclave temperature was controlled using a PID controller and a commercial K-type thermocouple. A schematic picture of the test configuration is shown in Figure 209.

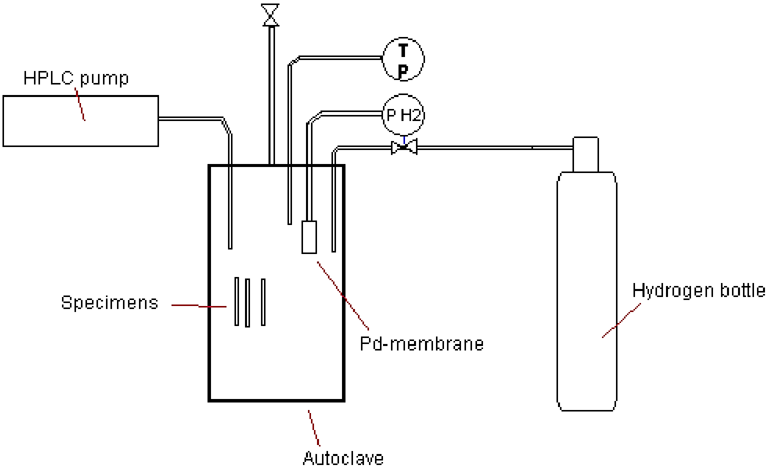

Figure 209. A schematic picture of the test equipment configuration.

The steam for the doped steam test was generated from de-ionized water doped with 30 ppm SO_4^{2-} (added as Na_2SO_4), 30 ppm F^- (added as NaF) and 30 ppm Cl^- (added as NaCl). The test implementation was performed as follows:

- the specimens were washed in de-mineralized water and ethanol,
- the specimens were installed into the autoclave,
- autoclave lid was closed,
- air was replaced by N_2 (pressure was raised to 3 bar, autoclave was emptied through a valve, and this cycle was repeated 10 times),
- the autoclave was pressured to 2 bar with N_2,

- the autoclave was heated to the test temperature,
- the autoclave was de-pressurized,
- water feeding was started (with or without the doping compounds),
- when the steam pressure was 150 bar, hydrogen injection was started,
- 400 °C/150 bar steam pressure/0.56 bar H_2 pressure was maintained until the exposure time was complete,
- at the end of the exposure, the steam-H_2 mixture was replaced with N_2,
- the autoclave was cooled down,
- the autoclave was opened, specimens were taken out and washed in demineralized water and ethanol,
- liquid penetrant test was performed for the specimens and the indications were inspected with an optical microscope.

4.2.2 Tests in PWR water

Tests in PWR water were also started on 4-point bend specimens strained to 1.1%. Later the specimens were further loaded to ~5% strain and the test in PWR water was continued. As in the second phase of the pure steam tests, the loading geometry was U-bend in the second phase of the PWR tests. The test temperature was 360 °C. The PWR water was de-ionized water with 1200 ppm B (added as boric acid) and 2 ppm Li (added as LiOH). The hydrogen concentration was 25–28 cc/kg and oxygen concentration < 5 ppb during the tests. The testing equipment used in this investigation consists of a water re-circulation loop, which is used to control the test environment, and a materials testing autoclave which is connected to the loop. Hydrogen, oxygen and conductivity levels were measured using commercial equipment. The test implementation was performed as follows:

- the specimens were washed in de-mineralized water and ethanol,
- the specimens were installed into the autoclave, autoclave lid was closed,
- the recirculation loop and autoclave were filled with de-ionized water and water was circulated in the loop through the autoclave and a mixed bed ion-exchanger until the conductivity was < 0.1 µS/cm,
- boric acid and lithium hydroxide were injected into the loop,
- pressure was raised to 200 bar,
- oxygen was replaced by N_2 after which H_2 was injected into the mixing tank (partial pressure 1.5–1.6 bar),
- the autoclave was heated to the test temperature,

- the conditions were followed and controlled during the exposure,
- at the end of the exposure, the autoclave was cooled down,
- H_2 was replaced with N_2,
- water recirculation was stopped and the pressure was decreased to ambient pressure,
- the autoclave was opened, specimens were taken out and washed in demineralized water and ethanol,
- liquid penetrant test was performed for the specimens.

4.3 Results and discussion

The 1.1% strained 4-point bend specimens were examined after every ~500 or ~1000 h exposure to pure steam or PWR water. The maximum total exposure time in pure steam was 2580 h and in PWR water 2500 h. Some of the specimens contained crack indications already before the exposures. The indications resulted from the opening of weld defects during the initial loading of the specimens. The crack indications were mainly in Alloy 52 welds, but some indications were also in Alloy 82 welds. No new post-test crack indications were observed. The existing opened weld defects did not grow during the exposures. The results are shown in Table 16 and examples of the liquid penetrant tested specimens in Figure 210.

Table 16. Exposure times of the specimens in pure steam and PWR water.

No. of speci-mens	Weld type	Environment	Exposure time, h	Post-test indications
4	308/butter 182	Steam, 400 °C	2580	No indications
3	Butter 182/82/304	Steam, 400 °C	2580	No indications
6	Pure 82	Steam, 400 °C	1860–2580	No indications
6	Pure 182	Steam, 400 °C	1860–2580	No indications
2	LAS/root 52/316	Steam, 400 °C	2580	No indications
15	52 narrow gap	Steam, 400 °C	2100–2580	No indications
4	Alloy 600	Steam, 400 °C	1500	No indications
6	Pure 82	PWR, 360 °C	2500	No indications
6	Pure 182	PWR, 360 °C	2500	No indications
4	Alloy 600	PWR, 360 °C	1500	No indications
2	182 and 52 oxidation specimens	Steam, 400 °C	1000	-
2	182 and 52 oxidation specimens	PWR 360 °C	1000	-

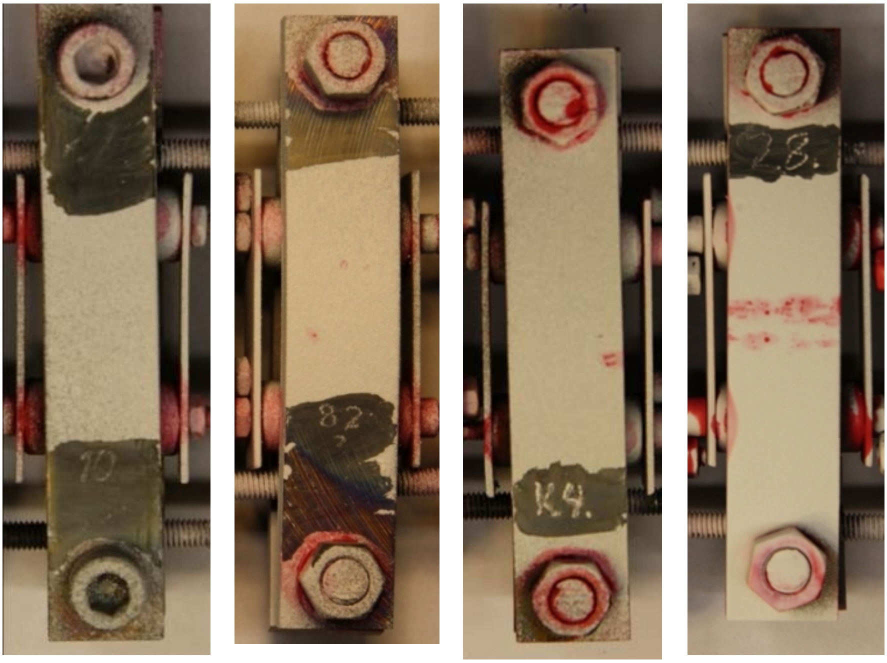

a) **b)** **c)** **d)**

Figure 210. Liquid penetrant tests on pure weld metal of Alloy 182 a) and Alloy 82 b), LAS/root 52/316L mock-up c) and Alloy 52 narrow gap weld mock-up d) specimens after 2580 h exposure to pure steam at 400 °C. Steam pressure was 150 bar and H_2 partial pressure ~0.56 bar during the exposures. The crack indications originate from the opening of weld defects in bending prior to the exposure.

Because no cracking was observed either in pure steam or in PWR water, the strain of some of the pure steam and all PWR specimens was increased to ~5%. Because this was not possible to realize with the 4-point bend fixtures, the specimens were bent to U-shape and loaded with bolts extending from the one end to the other end of the specimen as shown in Figure 207d. In order to check that the material condition regarding the SCC susceptibility was similar as in the previous ERIPARI and PERDI studies, some of the specimens exposed to the pure steam were exposed also to the doped steam environment used in the previous testing using 1.1 strain.

The weld type, environment, exposure time, applied strain, prior exposure time to the previous environment and observed crack indications for the doped steam tests on 1.1% strained specimens, pure steam on 5% strained specimens and PWR water on 5% strained specimens are shown in Tables 17, 18 and 19, respectively. Examples of liquid penetrant tested specimens before and after doped steam test with 1.1% strained specimens and pure steam test with 5% strained specimens are shown in Figures 211 and 212, respectively.

Extensive cracking was observed after doped steam tests on specimens containing Alloy 82 or 182 welds. Small but numerous indications were observed in

Alloy 600 specimens. No indications were observed in specimens containing Alloy 52 welds. The total exposure time in doped steam was 998 h. The specimens were checked after the first 434 h, but no indications were observed.

Specimens with 1.1% strain exposed to pure steam up to 2580 h and subsequent further loading to 5% strain and exposure to the pure steam for 1000 h had less or smaller indications than those exposed to the doped steam except for the Alloy 600 base metal specimens. The size and number of the cracks in Alloy 600 specimens were about the same after the exposure to both environments after ~1000 h. It should be noted, however, that the strains of the specimens were different, i.e. 1.1% in doped steam and 5% in pure steam, respectively.

No indications (except for weld defects which opened during the initial loading) were observed after exposure to PWR water. The total exposure time of these specimens was 3500–4500 h. However, the further loading from 1.1% to 5% strain after the initial testing has possibly changed the surface of the specimen. If there were microcracks/preferable initiation sites after the initial exposure with 1.1% strain, these sites probably blunted in bending representing no more favorable initiation sites.

Table 17. Results of tests in doped steam.

No. of specimens	Weld type	Environment	Exposure time, h	Strain %	Prior exposure to pure steam, h	Post-test indications
2	308/butter 182	Doped steam	998	1.1	2580	Extensive cracking in 1, clear indication in 1
2	Butter 182/82/304	Doped steam	998	1.1	2580	Extensive cracking in both specimens
4	Pure 82	Doped steam	998	1.1	1860–2580	Extensive cracking in 2, no indication in 2
3	Pure 182	Doped steam	998	1.1	1860–2580	Extensive cracking in 1, small indication in 1, no indication in 1
2	LAS/root 52/316	Doped steam	998	1.1	2580	No indications
9	52 narrow gap	Doped steam	998	1.1	2100–2580	No indications
2	Alloy 600	Doped steam	998	1.1	1500	Numerous indications in both specimens
2	182 and 52 oxidation specimens	Doped steam	998	-	-	-

Table 18. Results of tests in pure steam on specimens strained to 5%.

No. of specimens	Weld type	Environment	Exposure time, h	Strain %	Prior exposure to pure steam (1.1% strain), h	Post-test indications
2	308/butter 182	Pure steam	1000	5	2580	No indications
1	Butter 182/82/304	Pure steam	1000	5	2580	One small indication
2	Pure 82	Pure steam	1000	5	2580	No indications
2	Pure 182	Pure steam	1000	5	2580	One small, one large indication
6	52 narrow gap	Pure steam	1000	5	2100–2580	No indications
2	Alloy 600	Pure steam	1000	5	1500	Numerous indications in both specimens

Table 19. Results of tests in PWR water on specimens strained to 5%.

No. of specimens	Weld type	Environment	Exposure time, h	Strain %	Prior exposure to PWR (1.1% strain), h	Post-test indications
6	Pure 82	PWR	2000	5	2500	No indications
6	Pure 182	PWR	2000	5	2500	No indications
4	Alloy 600	PWR	2000	5	1500	No indications

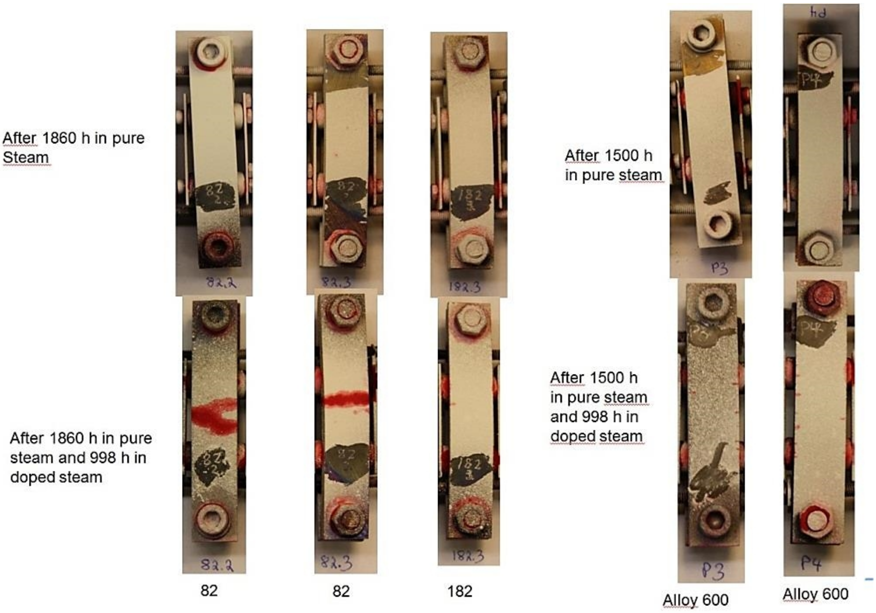

Figure 211. Liquid penetrant indications in Alloy 82, 182 and 600 specimens after exposure to pure steam and subsequent 998 h exposure to doped steam. Indications after the pure steam exposure in one Alloy 82 specimen are a result of weld defects which opened during the initial loading.

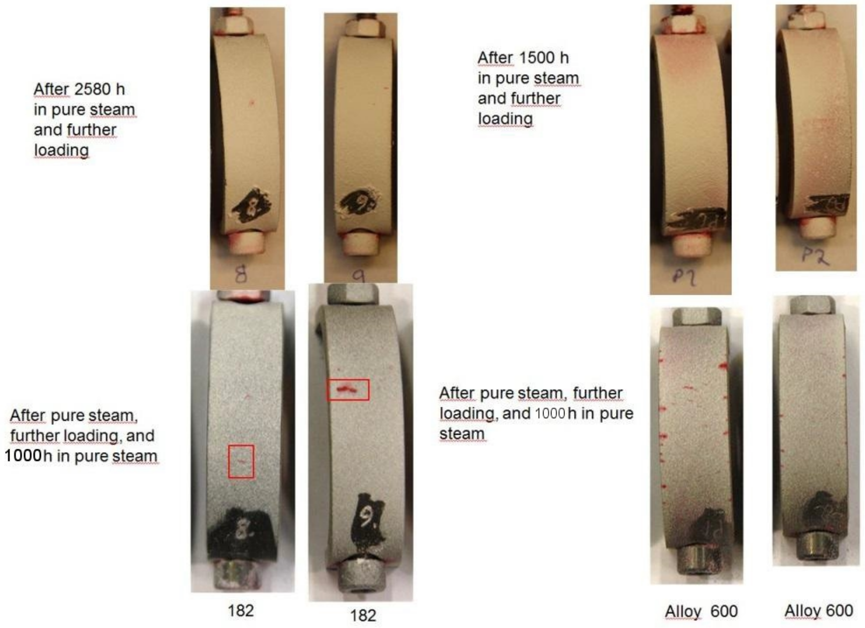

Figure 212. Liquid penetrant indications in Alloy 182 and 600 specimens strained to 1.1%, 2580 h or 1500 h exposure to pure steam and further loading to 5% strain (above) and subsequent exposure to pure steam for 1000 h (below). Indications after the pure steam exposure in Alloy 182 specimens are a result of weld defects which opened during the initial loading.

4.4 EAC oxide and crack characterization

Alloy 82/182/600 samples with exposures to different environments had significant differences in their oxide scales. Figure 213 shows the oxide scales on the surface of Alloy 82 weld metal samples after exposures to doped steam and pure steam. The oxide scale on the surface of the doped steam sample is around a few µm thick and consists of layers of Cr-rich oxides with metallic Ni deposits inside the Cr-rich oxide layers (Figure 214). Figure 214 also shows a starting oxide penetration into Alloy 82. Figure 213b shows the oxide scale on the surface of Alloy 82 weld metal after 2580 h exposure to pure steam and further 1000 h exposure to pure steam with higher loading. As can be seen, the oxide scale is, compared to the doped steam specimen, overall significantly thinner and consists of external, Cr-rich oxide layer with Ni deposits inside the oxide layer (Figure 215). Oxide scales of Alloys 182 and 600 were very similar to those found on the surface of Alloy 82.

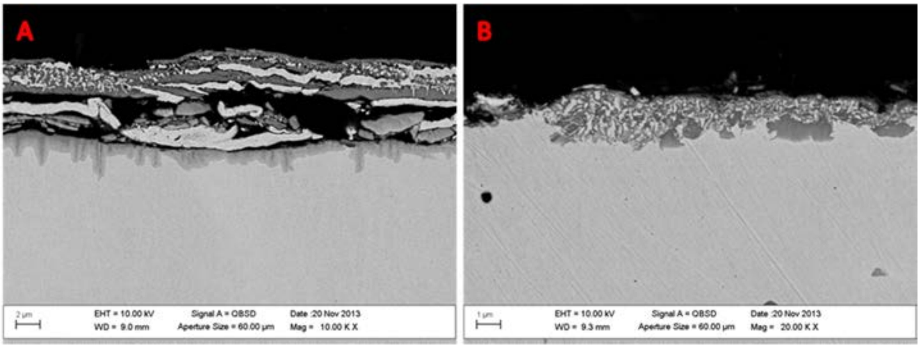

Figure 213. SEM images of the oxide scales on the surface of Alloy 82 weld metal after 2580 h exposure to pure steam and a) further 998 h exposure to doped steam with 1.1% strain and b) further 1000 h exposure to pure steam with 5% strain.

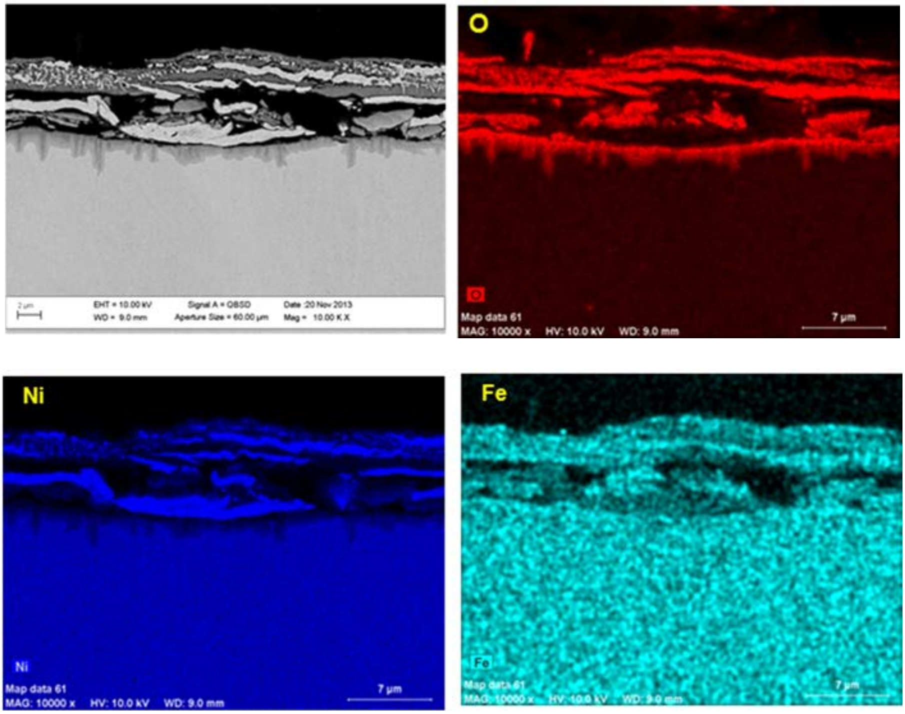

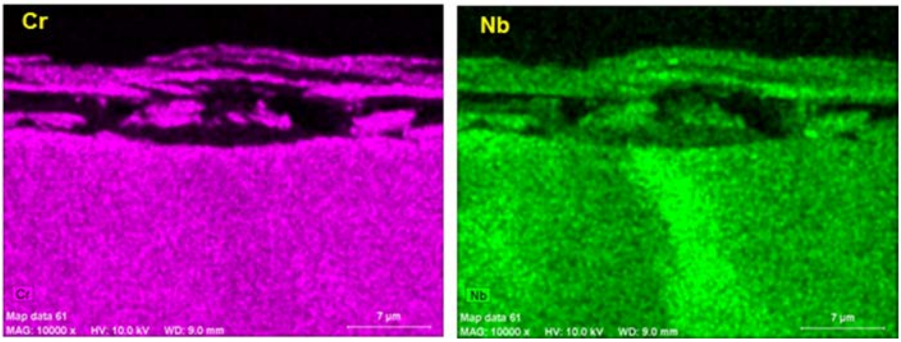

Figure 214. EDS maps of the oxide scale on the surface of Alloy 82 weld metal after 2580 h exposure to pure steam and 998 h exposure to doped steam.

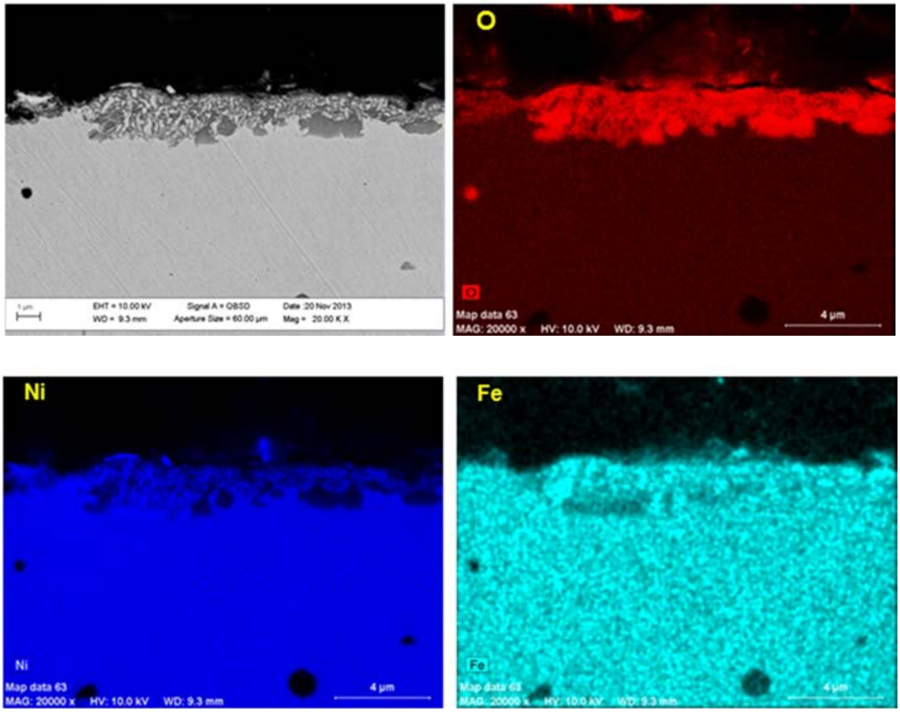

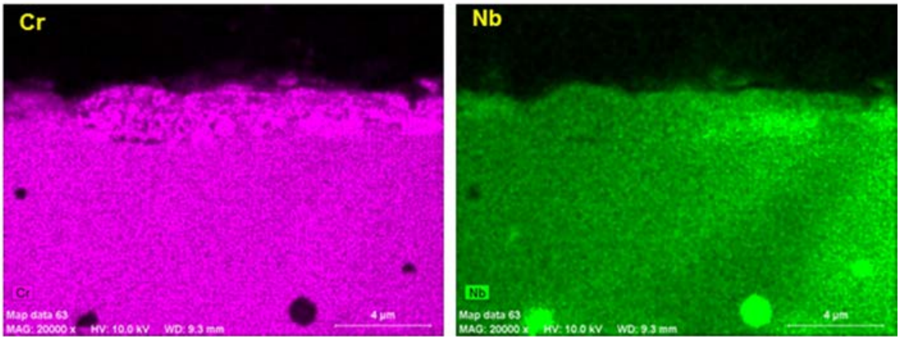

Figure 215. EDS maps of the oxide scale on the surface of the Alloy 82 weld metal after 2580 h exposure to pure steam and further 1000 h exposure to pure steam with 5% strain.

Alloy 52, on the other hand, did not have such significant differences in its oxide scale after different environmental exposures. Figure 216 shows SEM images of the oxide scale on the surface of Alloy 52 weld metal samples after exposures to doped steam and pure steam. As can be seen, the oxide scale is clearly thicker after the exposure to doped steam. However, in both cases, the oxide scale composition is very similar and the oxide scales consist of thin, external layer of Cr-rich oxides with small, metallic Ni deposits inside the Cr-oxide layer (Figures 217 and 218).

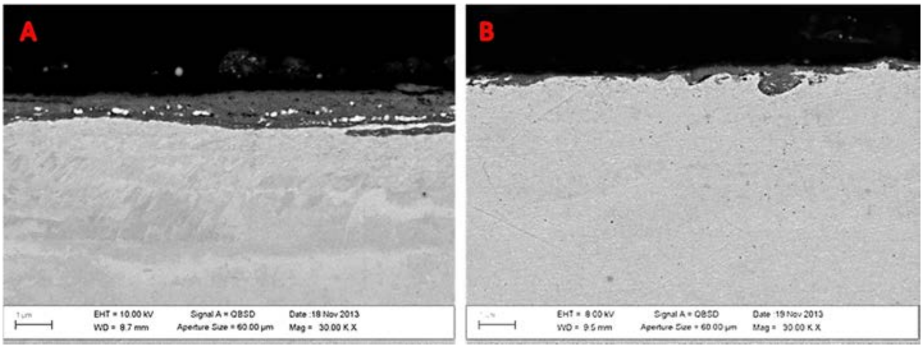

Figure 216. SEM images of the oxide scales on the surface of Alloy 52 weld metal after 2580 h exposure to pure steam and a) further 998 h exposure to doped steam with 1.1% strain and b) further 998 h exposure to pure steam with 5% strain.

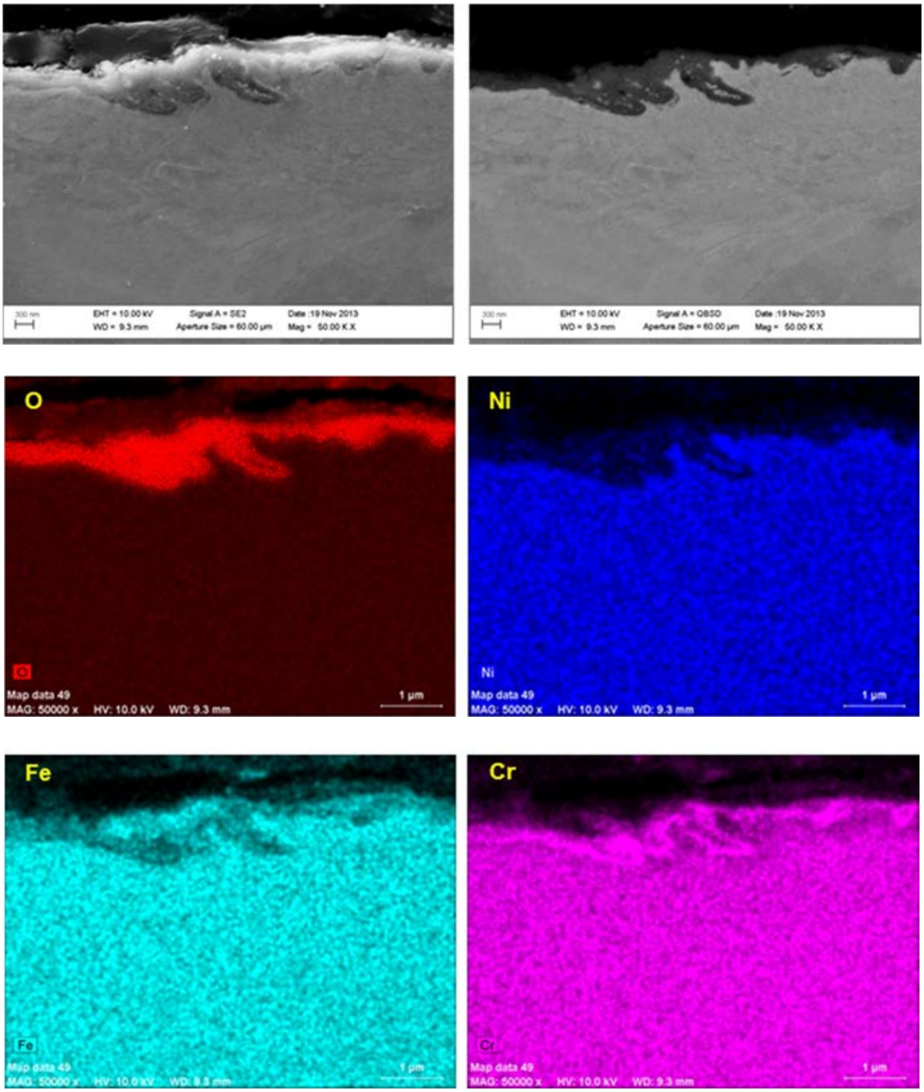

Figure 217. EDS maps of the oxide scale on the surface of Alloy 52 weld metal after 2580 h exposure to pure steam and further 998 h exposure to doped steam.

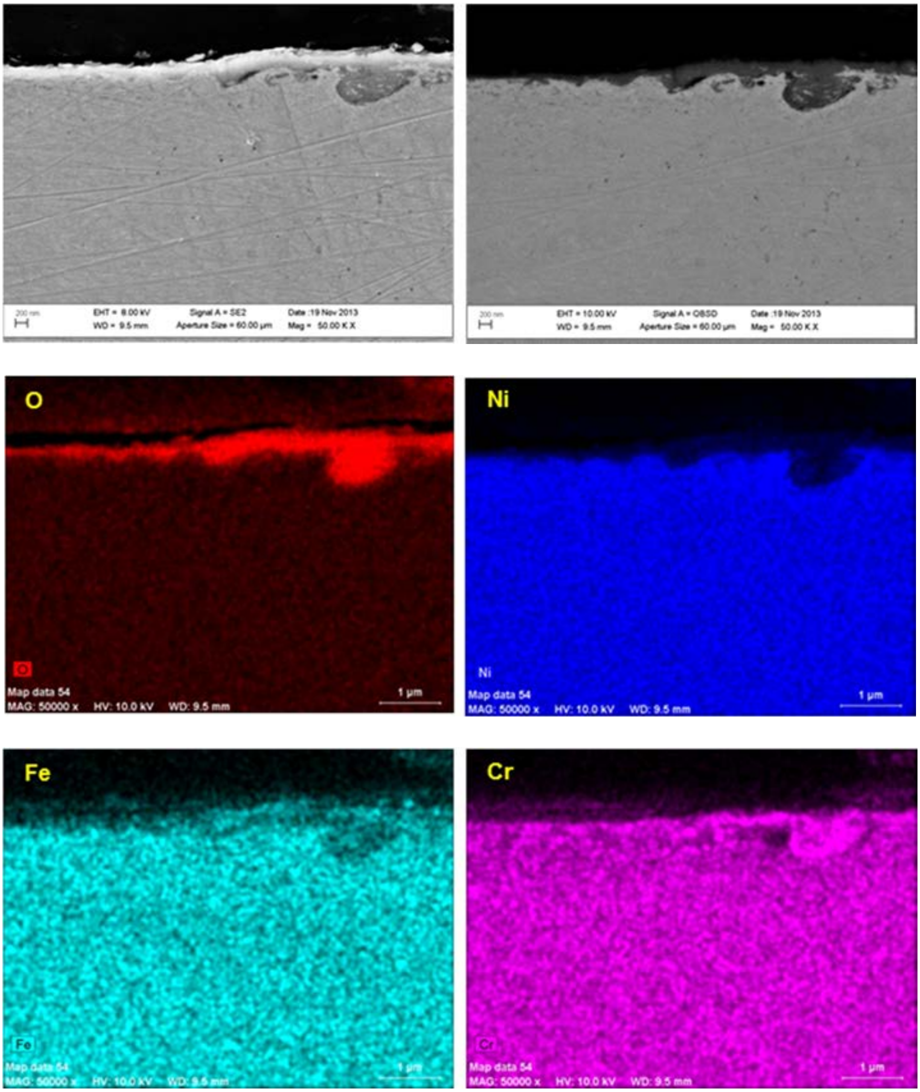

Figure 218. EDS maps of the oxide scale on the surface of Alloy 52 weld metal after 2580 h exposure to pure steam and further 1000 h exposure to pure steam.

As mentioned above, Alloys 82 and 182 showed significant crack initiation after the exposure to doped steam. Figure 219 shows SEM images of cracks observed in an Alloy 182 doped steam specimen. The cracks consisted of Cr-rich oxide layers with metallic Ni deposits inside the Cr-oxide layers. Cracks also contained Nb-rich particles within the middle of the oxide layers, as can be seen from Figure 220.

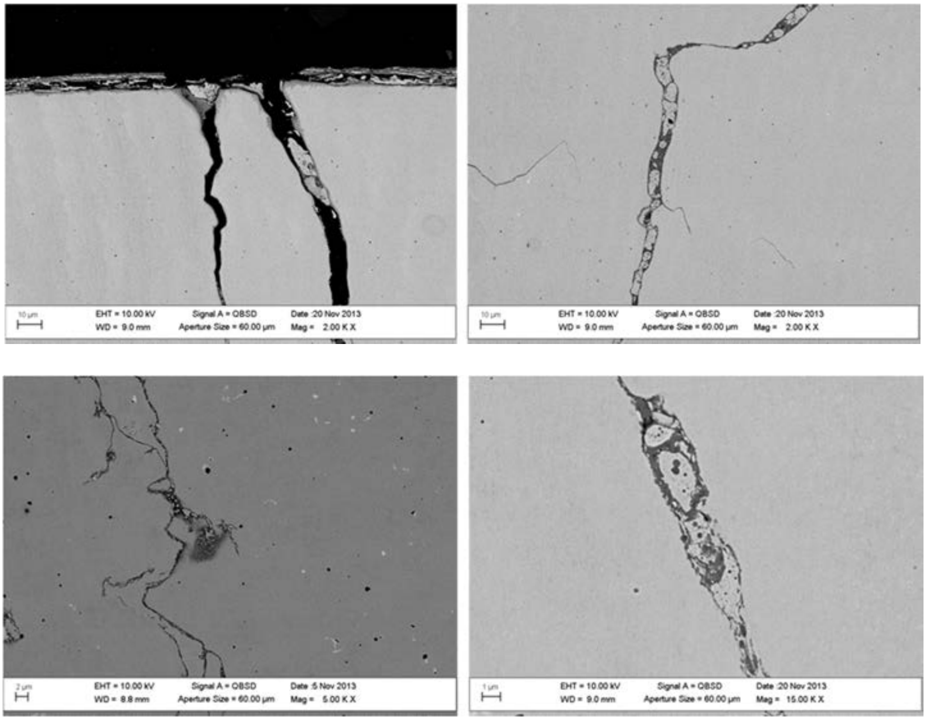

Figure 219. SEM images showing cracks in Alloy 182 weld metal after 2580 exposure to pure steam and further 998 h exposure to doped steam.

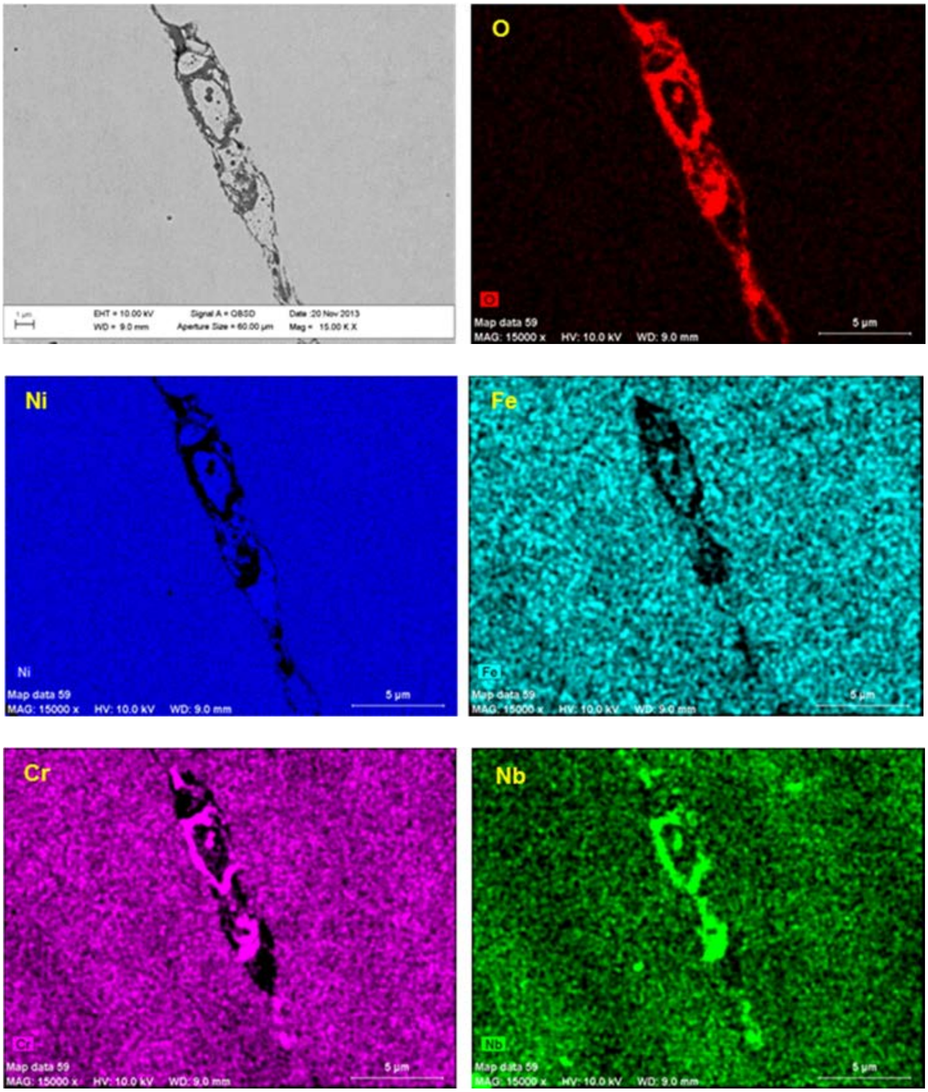

Figure 220. EDS maps of an EAC crack in Alloy 182 weld metal after 2580 h exposure to pure steam and further 998 h exposure to doped steam.

Alloy 600 samples showed crack indications after exposures to doped steam with 1.1 strain and also pure steam with higher strain. SEM images of cracks observed from the Alloy 600 doped steam and pure steam samples are shown in Figures 221 and 222, respectively. As can be seen from Figures 223 and 224, which shows EDS maps of an EAC crack in Alloy 600 doped steam sample, the composition of an EAC crack in Alloy 600 is quite similar to those found from the Alloy 82/182 samples. The cracks are noticeably more closed in the pure steam samples when comparing to the cracks found from the doped steam samples. Figures 225 and 226 show EBSD IPF maps of EAC cracks found from the Alloy 600 doped steam and pure steam samples, respectively. As can be seen, the EAC crack growth in both exposures is clearly intergranular.

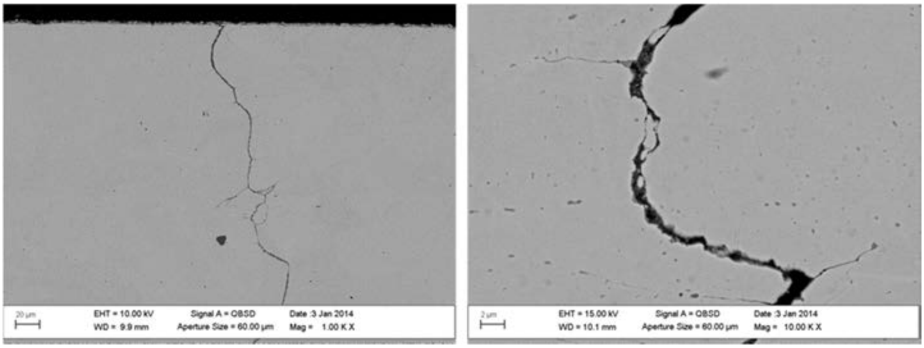

Figure 221. Crack in Alloy 600 specimen after 1500 h exposure to pure steam and further 998 h exposure to doped steam.

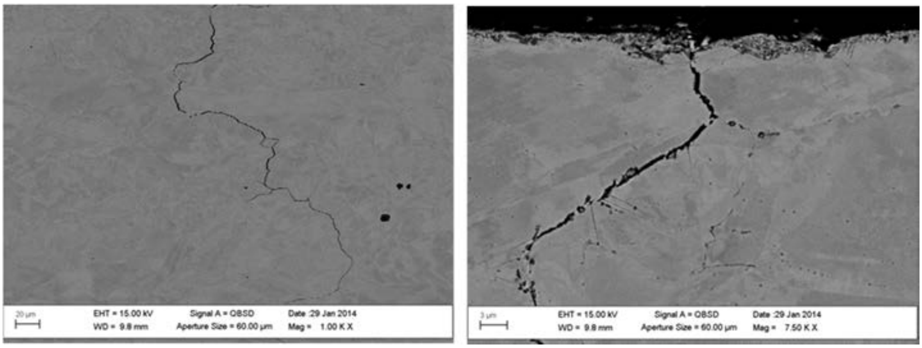

Figure 222. Cracks in Alloy 600 specimen after 1500 h exposure to pure steam and 1000 h further exposure to pure steam.

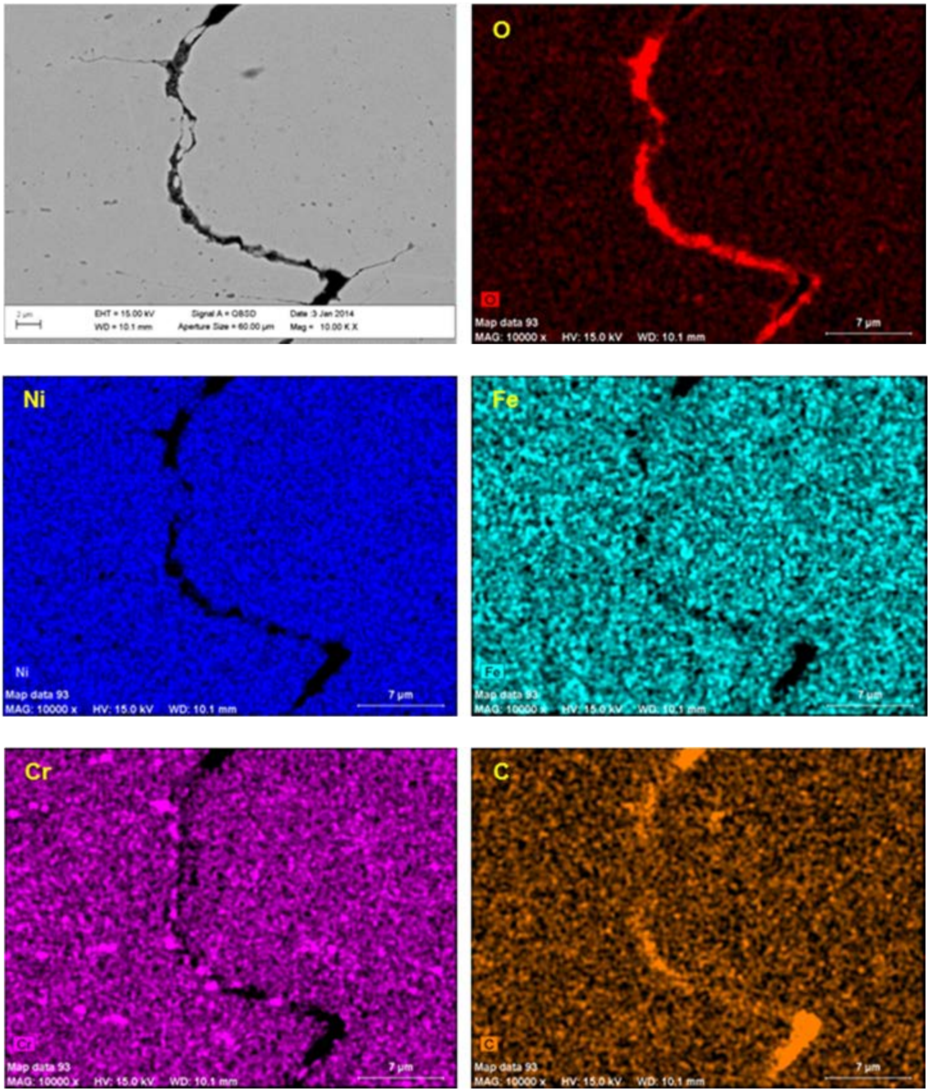

Figure 223. EDS maps of an EAC crack in Alloy 600 specimen after 1500 h exposure to pure steam and further 998 h exposure to doped steam.

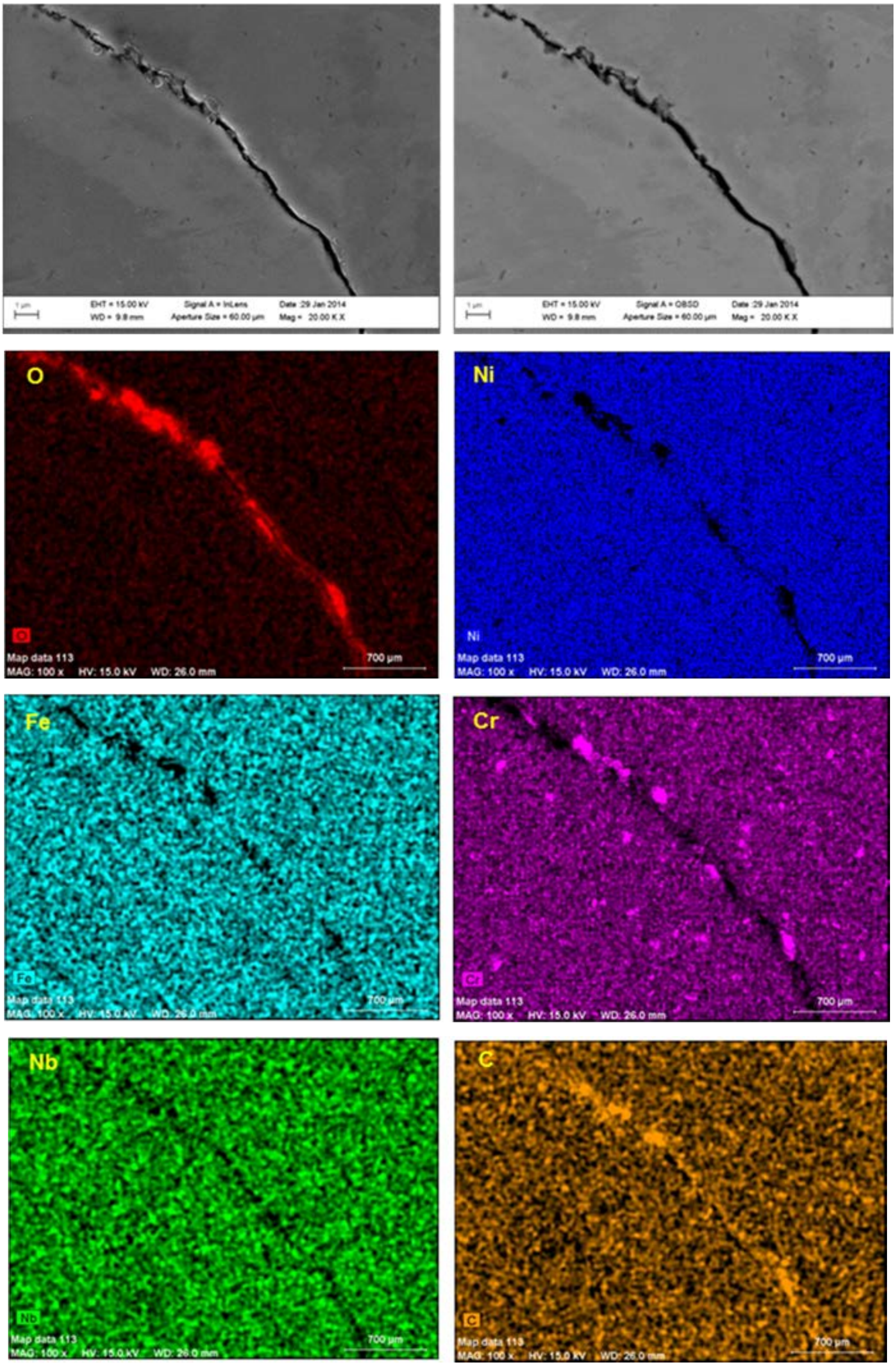

Figure 224. EDS maps of an EAC crack in Alloy 600 specimen after 1500 h exposure to pure steam and further 1000 h exposure to pure steam.

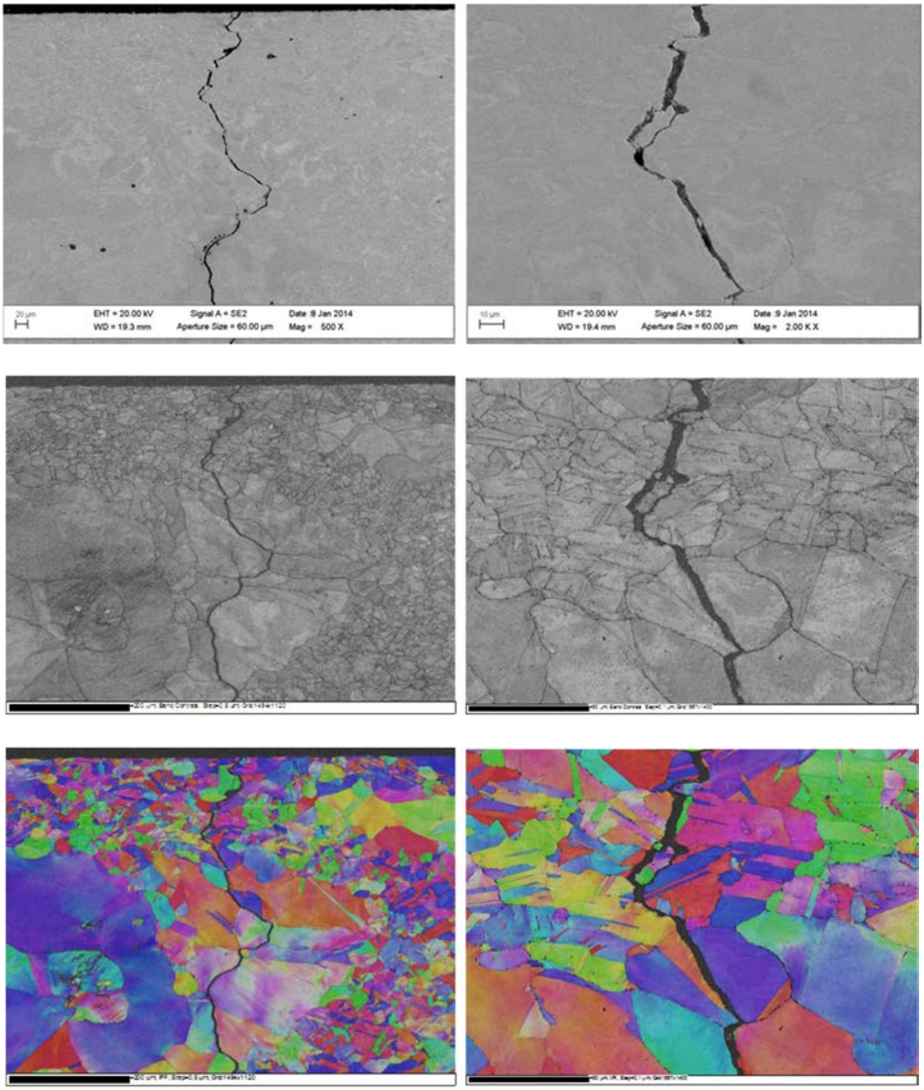

Figure 225. EBSD maps showing an intergranular EAC crack in Alloy 600 specimen after 1500 h exposure to pure steam and further 998 h exposure to doped steam.

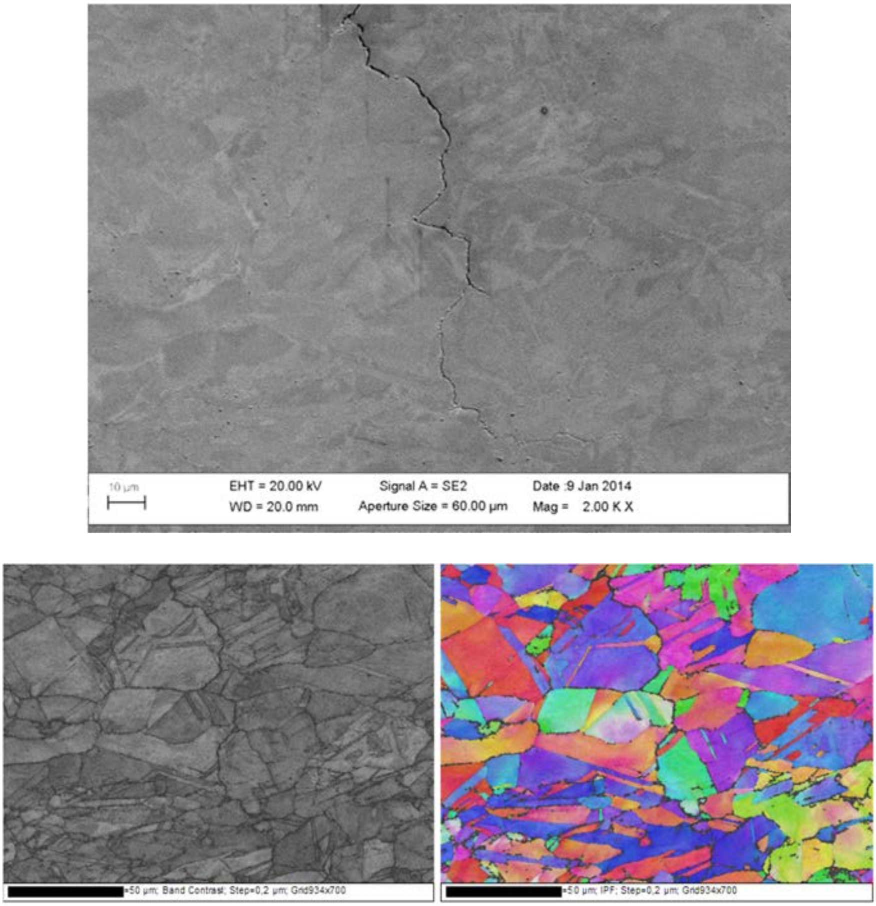

Figure 226. EBSD maps showing an intergranular EAC crack in Alloy 600 specimen after 1500 h exposure to pure steam and further 1000 h exposure to pure steam.

4.5 Conclusions

EAC crack initiation in Alloy 52 weld metal takes clearly longer time than in Alloys 82, 182 or 600 in steam and PWR water. No EAC cracks were observed in Alloy 52 whereas cracks were observed in all other tested alloys at least after exposure to doped steam.

Crack initiation in Alloys 82, 182 and 600 is considerably slower in pure steam than in doped steam: >2580 h in pure steam vs. <998 h in doped steam within this project and ~250 h in doped steam within the previous PERDI project using 1.1% strained specimens. Difference between the initiation times between the present tests and the tests performed during the previous PERDI project result probably from stress relaxation during the prior long exposure to the pure steam before the doped steam exposure. The specimens of the previous PERDI project were exposed directly to the doped steam environment.

In order to initiate EAC cracks in pure steam, longer than 2600 h exposure times are needed if low, 1.1%, strains are used. A considerably shorter testing time can be achieved by using a 5% strain.

Longer tests or higher strains are needed also for EAC crack initiation in PWR water than was used in this study. Even as long as 4500 h total exposure time (2500 with 1.1% strain and subsequent 2000 h with 5% strain) at 360 °C did not result in crack initiation in any of the tested alloys.

Exposure in doped steam has caused a slightly thicker oxide scale on Alloy 52 than exposure in pure steam; however, the oxide scales were very thin after both exposures, thickness varying from 200 nm to 1 µm in the thickest parts. Alloys 82, 182, and 600 showed significantly thicker oxide scales after exposure to doped steam, thickness varying around a few µm. The oxide scales on Alloys 82, 182, and 600 were substantially thinner after exposure in pure steam than in doped steam. The oxide scales of Alloy 52 in both exposures consisted of chromium-rich oxide with small Ni deposits inside the oxide layer. The oxide scales of Alloys 82, 182, and 600 in doped steam consisted of lamellar layers of chromium-rich oxides and metallic Ni. Cracks in Alloys 82, 182, and 600 after the exposure to doped steam contained metallic Ni and Nb-rich deposits surrounded by chromium-rich oxide layers. The crack compositions observed in the Alloy 600 pure steam samples were similar to those observed in the doped steam samples with the exception that the cracks seemed to be more closed in the pure steam samples. The cracks found from the samples of both exposures were intergranular.

5. Oxide film characterization

The oxide layers formed on Alloy 600 (Alloy 182) and Alloy 690 (Alloy 52) in primary PWR water are similar in nature. They were found to be made up of two layers, a Cr-rich inner layer and a Ni- and Fe-rich outer layer. The inner layer is believed to be protective; however, this layer may comprise of two components. The first component observed at the metal / oxide interface is obviously a thin remnant layer of an air-born oxide with a high Cr content, probably of Cr_2O_3 oxide [Sennour et al. 2010]. Cr oxide layer is formed rapidly even at ambient temperatures on all Cr containing alloys. The second component is a Cr-rich spinel type oxide forming the main constituent of the inner layer overlying the Cr_2O_3 sub-layer. The thickness and composition of the inner oxide layer varies according to the nature of the base metal and the corrosion potential. This is attributed to the presence of a perturbed layer with a large density of defects and / or to surface cold work accelerating diffusion. On Alloy 600, the thickness of the internal oxide layer exhibits a maximum near the Ni-NiO equilibrium potential. The Cr content of this layer is much higher than that of the base metal and is somewhat higher on Alloy 690 compared to Alloy 600. The Ni content of the film is very low at low corrosion potential and becomes significant near the Ni-NiO equilibrium. The outer layer consists of separate crystallites spread over the surface. These crystals are usually much coarser than the chromium-rich spinel crystals of the inner oxide layer. Obviously this layer does not contribute to protection of the base metal, and it may be completely absent in some instances. The oxide crystallites of the outer layers are almost Cr-free and contain mostly Fe and Ni. On Ni-base alloys it is generally made of $(Ni_xFe_{1-x})Fe_2O_4$, i.e., nickel ferrite. Formation and growth of this layer depends on the saturation of the environment by Fe and Ni cations. In unsaturated test loops and solutions, this layer may not be formed at all while in saturated solutions it can incorporate Fe or Ni ions from the base metal as well as those dissolved in the bulk environment [Combrade et al. 2005, Ziemniak & Hanson 2006, 2003, Delabrouille et al. 2005].

Oxide film on nickel-based materials exposed to simulated reactor coolant environment reflects both the environment and the chemical composition as well as the surface microstructure of the alloy used for crack initiation tests. Oxide films and oxide structure on nickel-based weld metal DMW samples were characterized after exposure to test environments used for crack initiation. Steam tests were carried out using a static stainless steel autoclave which was heated before the steaming water was introduced. Correspondingly, the steam was vented out before cooling the autoclave in order to avoid deposition reactions. Deposition of dissolved ions in steam tests are believed to be insignificant. Tests in simulated PWR environment were carried out using recirculating stainless steel test loop, where the specimens exposed to coolant were heated up to test temperature. Correspondingly, specimens with the coolant were cooled down after the exposure time was complete enabling deposition of dissolved ions with decreasing loop temperature. This test arrangement enabled deposition of dissolved species on the specimen surface. Oxide film samples for XPS analysis were exposed to the test environments together with 4 PB specimens. Samples for surface film SEM analysis were cut from the exposed 4 PB test specimens. The idea was to analyze surface films on sample surfaces corresponding to real surface finish existing on components. However, after first analysis conducted for doped steam specimens of Alloy 182 and Alloy 52 using surface sensitive methods (ESCA, Auger and X-ray) it became evitable, that sputtering did not progress smoothly due to too rough surface finish and thus oxide profiling was not reliable. Next specimens used for oxide film characterization after exposure to pure steam and to simulated PWR environments were manufactured separately from the 4PB specimens and the machined surface was finished by diamond paste polishing. For oxide film characterization only weld metals Alloy 52 and Alloy 182 were selected. ESCA and Auger measurements were conducted in the University of Turku and the GI-XRD analysis was conducted in the University of Wisconsin-Madison.

5.1 Test materials

Samples for oxide film analysis were cut after exposure of the 4PB specimens to the doped steam environment. Specimen preparation process for the 4 PB crack initiation specimens:

- Plane-milling to the dimensions of 15x80x3.5 mm^3,
- Polishing with Roloc surface conditioning disc, grade A VFN (polishing agent: aluminum oxide), corresponds roughly to 600 grit emery paper
- cold work to 1% strain by bending
- Exposure to 400 ºC/150 bar doped steam with ~0.6 bar H_2
- Cutting of about 10x10x1 mm^3 representative weld metal piece for oxide film analysis.

Samples for doped steam oxide film characterization of Alloy 182 were cut from the 4PB specimen after about 750 h total exposure time to doped steam. Samples for oxide analyses for the pure steam exposure and simulated PWR environment exposure were manufactured separately paying attention to surface smoothness. The surface of these specimens was finished by diamond polishing after machining.

A sample for doped steam oxide film characterization of Alloy 52 was cut from the 4PB specimen after about 2175 h total exposure time to doped steam.

5.2 Test methods

Two surface sensitive techniques with an option to carry out depth profiling by Ar^+ ion sputtering were used: Electron Spectroscopy for Chemical Analysis (ESCA), i.e., X-ray photoelectron spectroscopy (XPS) and Auger electron spectroscopy (AES). XPS uses soft X-rays (Al Kα with 1486 eV, for example) to excite photoelectrons from the sample surface. The binding energy of the photoelectrons contains information on the chemical environment of sample atoms. Also the concentration can be obtained by comparing the number of photoelectrons emitted from different atoms. The sampling depth of XPS is about 5 nm. AES is based on measuring the kinetic energy of the Auger electrons excited by the electron beam. The atomic concentration of the surface can be analyzed within about the same detection limits and error bars as with XPS. However, the chemical state of the atoms cannot be studied in most of the cases. The advantages of AES compared to XPS are small spot size and good sensitivity for light elements. The sampling depth of AES is about 5 nm.

Surface sensitivity means that these techniques are very sensitive to surface contamination. A base pressure in the UHV region is needed to avoid contamination and oxidation of metallic samples. Sputtering sample with Ar^+ ions in the same chamber where the measurements are performed can be used to remove surface atoms layer by layer. This method can be used to clean the sample surface or carry out depth profiling of the sample with alternating sputtering and measurement cycles. The surface left after sputtering is analyzed by AES or XPS. Small analysis spot size of AES minimizes crater edge effects and allows higher sputtering speeds as ion beam can be focused to a smaller area. Ion sputtering is mostly used for depths less than the order of 1 µm.

Sputtering speed data is needed to calibrate the depth scale of the profile. It was estimated from the time needed to sputter through a 100 nm thick Ta_2O_5 oxide layer (from Physical Electronics). Ion bombardment causes topographical and compositional changes in the sample surface. The original surface roughness has a significant influence on depth resolution. Sputtering yield dependence on grain orientation may also cause roughness of the poly-crystalline sample surface. These sputtering effects are seen in the measured profile as an additional broadening. Preferential sputtering leads to compositional changes in the sample surface during depth profiling.

5.2.1 ESCA (XPS)

Measurements were done with a PHI 5400 spectrometer using twin anode Al Kα and Mg Kα excitations. X-ray source with dual anode allows use of Mg Kα and Al Kα radiation. Hemispherical analyzer was used in constant pass energy mode.

Wide scan spectra were recorded with 89.45 eV and selected narrow regions with 35.75 eV pass energy. The energy scale was calibrated with Ag 3d at 368.2 eV and Cu 2p at 932.6 eV lines or with Au 4f7 / 2 at 84.0 eV. Diameter of the analyzed area was about 1.5 mm. The base pressure in the analyzer chamber was 5 x 10^{-10} torr during data collection and 2x10^{-8} torr during ion bombardment. Sputtering was done with Ar ions using 3 keV beam energy, and 2 µA beam current. Sample was tilted so that the takeoff angle of the photoelectrons was 60º measured from the sample surface.

Specimens were mounted to sample holder using screws. Aluminum mask protected other parts of the sample from sputtering and re-deposition of sputtered species, as the same sample surfaces were used for both XPS and AES analysis. Pure steam samples were measured as delivered without any cleaning. For PWR 182 sample the inhomogeneous outer layer was removed. The inhomogeneous layer was removed using nylon brush under ion exchanged water. Surface atomic compositions were calculated from peak intensities. A Shirley type background correction was applied. In Shirley method the background intensity is assumed to be proportional to the intensity of the peak area above background. Relative sensitivity factors were tabulated values for the spectrometer. Due to overlapping Auger lines, Fe 2p1/2 and Mn 2p1/2 line areas were used for iron and manganese.

Many oxides are reduced to lower oxidation states as a result of preferential sputtering. Therefore profiles were divided only to metallic and oxidized components. For metallic phase asymmetric line shape of a clean metal was used. Curve fitting was done with Unifit program.

The metallic reference samples were cleaned by sputtering and oxide pellets (NiO, Cr_2O_3 and Fe_2O_3) were scraped under vacuum to remove contaminants. Hydroxide powders were pressed to a small stainless steel slot for the measurements. Line shifts caused by the sample charging were corrected using C 1s line at 284.8 eV.

5.2.2 Auger (AES)

A PHI 610 spectrometer was used for AES analysis. Electron source uses LaB_6 emitter and electrostatic optics. Electron gun was run at 5 keV beam energy, beam current was 70 nA and it was rastered over an area of 5 x 5 µm^2. Cylindrical mirror electron analyzer was used in constant retardation ratio mode with 0.6% resolution. Base pressure during the measurements was 1×10^{-9} torr. Sputtering was done with a differentially pumped argon ion gun. Fine focused ion beam was rastered over sample surface area of 4 x 4 mm^2 at an angle of 40º from the sample surface. A rastered ion beam will produce a more uniform ion current distribution. Ion beam energy was 3 keV and current 2 µA. Pressure in the analysing chamber was 2 x 10^{-8} torr during sputtering. The sputtering rate was calibrated using a 100 nm thick Ta_2O_5 oxide layer as a reference sample. The estimated etching rate was 6.5 nm / min. Area for profiling was selected from SED figure. For depth profiling kinetic energy region 400–950 eV was measured. Depth profiling was done in alternating mode. Sputtering time between the measurements was 1 min. Used energy region covers all metallic elements of the samples and also oxygen. Intensities were determined from the peak-to-peak heights of the differentiated spectra. The Savitzky-Golay algorithm was employed to differentiate measured spectra. Auger line energies used for the concentration determination were: O 512 eV, Fe 650 eV, Ni 849 eV, Cr 528 eV and Mn 638 eV.

5.2.3 X-ray diffraction

In addition to the surface sensitive analysis techniques small angle X-ray diffraction analysis (GI-XRD) was applied. The XRD curves can be recorded in multiple ways. This work concentrates on the asymmetric grazing incidence (GI) XRD measurements, which especially is sensitive to the near surface properties (coatings, oxides, etc.) of the examined samples. The measurements are done by fixing the angle of incidence, α, while collecting the data by scanning the detector angle, 2θ. As compared to the symmetric scan with α and 2θ constantly changing to keep the diffraction vector direction constant, the diffraction vector direction rotates upon the scan in the GI-XRD setup. However, at the same time, the probing depth stays nearly constant for all the reflections at the GI-XRD, Figure 227.

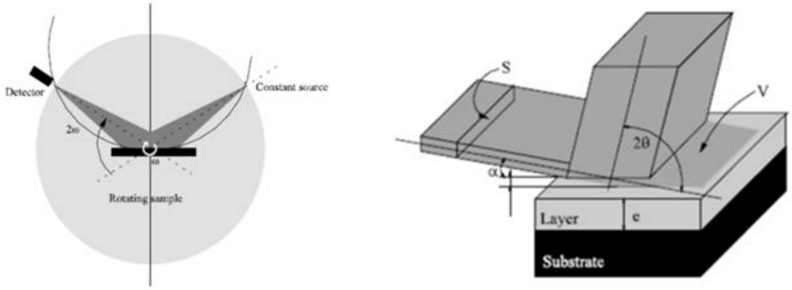

Figure 227. Probing depth for XRD reflections located at 2θ = 30, 45, and 60 degrees. The data points with black large circles represent the typical probing depths for the symmetric ω-2θ scans [Guinebretiere 2007].

A Siemens Stoe X-ray diffractometer using Cu K_α radiation (40 kV, 2.5 mA) was used in omega-2 theta and grazing incidence geometry. The GI-XRD measurements were used to depth profile the observed XRD features. The X-ray probing depth was calculated using a geometric relation, Equation 5:

$$p = -\frac{1}{\mu}\left[\ln\left(\frac{I}{I_0}\right)\right]\left[\frac{\sin(\omega)\sin(2\theta-\omega)}{\sin(\omega)+\sin(2\theta-\omega)}\right], \qquad (5)$$

where μ is the linear absorption coefficient, I and I_0 are the diffracted and incoming intensity, ω is the angle between the sample surface and the incoming X-ray beam (GI angle), and 2θ is angle between the incoming beam and the detector. A criterion for probing depth was set to be $I/I_0 = 1/e$, i.e., once the diffracted intensity falls 1/e of its initial values it was assumed negligible. The $\mu = 4 \times 10^2$ cm^{-1} for Ni-based alloys at the energy of Cu K_α (about 8 keV) was taken from the tabulated mass absorption coefficients, by assuming the samples consisted solely of Ni with a density of 8.908 g/cm^3. The calculated probing depth for three reflections is shown in Figure 228. The probing depth calculation does not take into account total reflection, which takes place at very small GI angles.

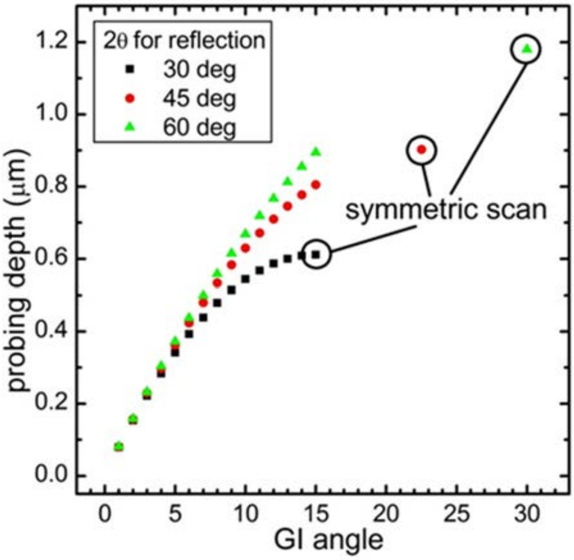

Figure 228. Probing depth for XRD reflections located at 2θ = 30, 45, and 60 degrees. The data points with black large circles represent the typical probing depths for the symmetric ω-2θ scans [Guinebretiere 2007].

5.3 Doped steam exposures

The first oxide samples originate from PERDI project and were exposed to doped steam containing 30 ppm Cl^-, 30 ppm F^-, 30 ppm SO_4^{2-} (all added as sodium salts), at the temperature of 400 °C. The nominal steam pressure in the autoclave was adjusted to 150 bar and additionally the partial hydrogen pressure was adjusted to 0.6 bar. By this pressure at the test temperature the potential of nickel-based weld metal corresponds to the thermodynamic boarder between metallic nickel and nickel oxide (Ni-NiO). In practice, the hydrogen pressure decreased during the test and was adjusted by adding hydrogen in the loop. Steam test environment fluctuated between partial formation pressure of NiO and metallic nickel. This fluctuation and the heating and cooling practice resulted in not a well developed outer oxide layer. Thus, the oxide film analysis was conducted only on the continuous inner layer.

5.3.1 ESCA analysis of the inner layer oxide film on Alloy 182 and Alloy 52 formed during doped steam exposure

The chemical compositions of the oxides on samples Alloy 182 and Alloy 52, as determined by ESCA measurements, as a function of the depth, are shown in Figure 229. The surface part of the Sample 52 included more Cr than the surface of the Sample 182. The inner oxide on Alloy 52 was thinner than on Alloy 182, although, the method applied for oxide thickness definition was not specified. Due to uneven sputtering mainly caused by the rough surface finish in the analyzed samples oxygen was recorded still in the base metal. ESCA profile for Alloy 182 shows near the surface fluorine and silicon, which were not reported for Alloy 52.

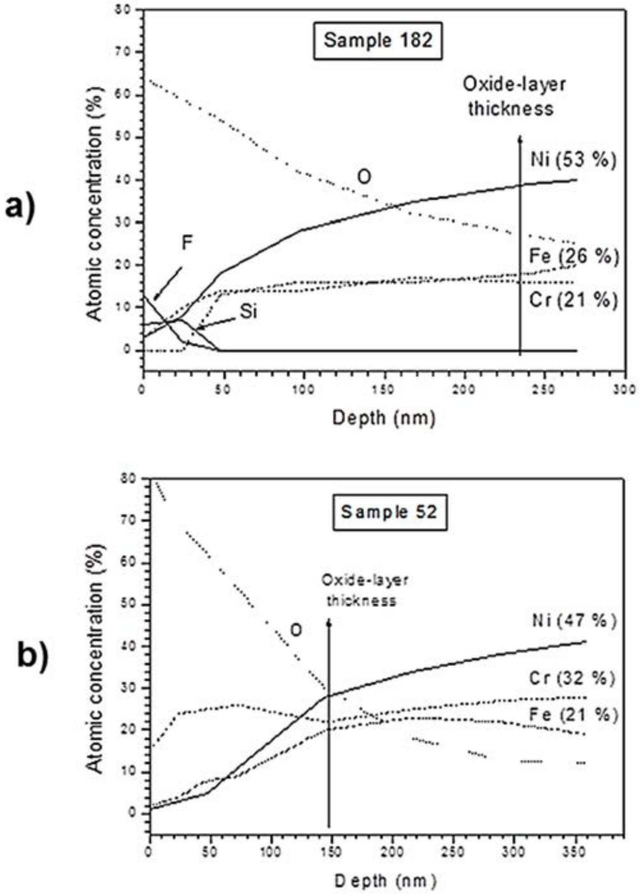

Figure 229. ESCA composition profiles of the inner surface film a) on Alloy 182 and b) Alloy 52 after 750 h and 2175 h exposure, respectively, to doped steam.

The oxidation-state analysis of Cr, Fe, and Ni is shown as a function of the depth in Figure 230.

a)

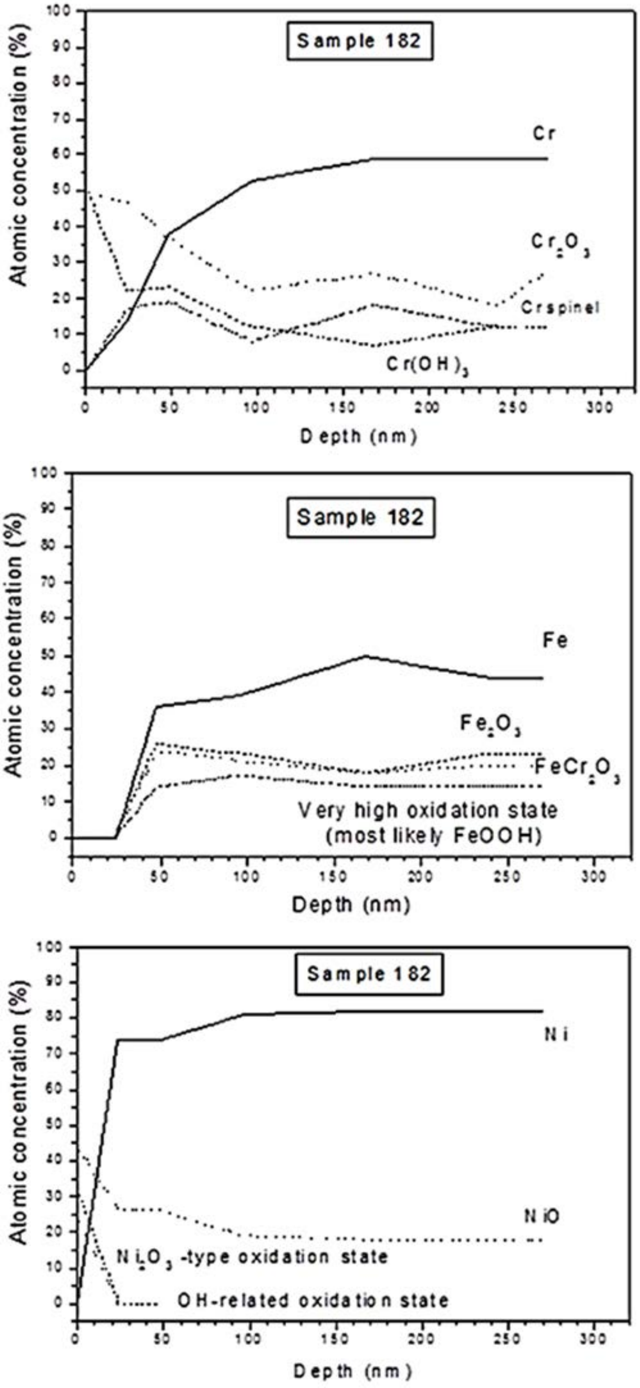
Sample 182
Atomic concentration (%)
Depth (nm)
Cr
Cr_2O_3
Cr spinel
$Cr(OH)_3$
Sample 182
Atomic concentration (%)
Depth (nm)
Fe
Fe_2O_3
$FeCr_2O_3$
Very high oxidation state
(most likely FeOOH)
Sample 182
Atomic concentration (%)
Depth (nm)
Ni
NiO
Ni_2O_3 -type oxidation state
OH-related oxidation state
0
10
20
30
40
50
60
70
80
90
100
0
50
100
150
200
250
300

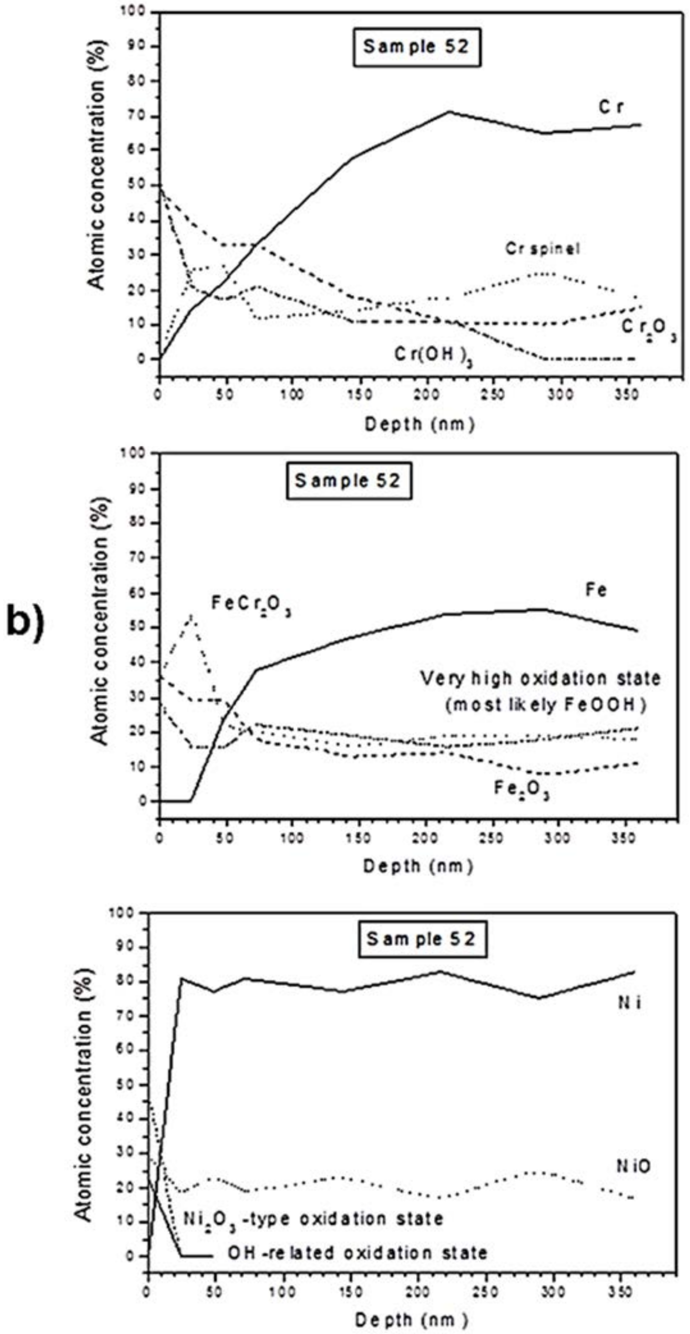

Figure 230. Oxidation states of main components in the inner oxide layer formed during exposure to doped steam a) on Alloy 182 and b) Alloy 52.

The comparison to the identification of the various Cr and Fe oxides clearly shows that the Cr, Fe, and Ni atoms all have the OH-type bonding near the surface. The OH-bonding of Ni atoms appears only in the surface parts of oxide layer. Metallic phase is the reference which has the smallest binding energy. It is also expected that the spinel compounds have a lower binding energy than the pure M_2O_3 phases. Both metal surfaces were oxidized (i.e., no pure metallic areas or phase). Among Cr, Fe, and Ni, the metallic phase appeared first for Ni in the both samples.

5.3.2 Auger analysis of the inner layer oxide film on Alloy 182 and Alloy 52 formed during doped steam exposure

The Auger spectra for Alloy 182 and Alloy 52 indicate thicker oxide film on Alloy 52. However, the Auger spectra were collected on area where smooth, local area of single surface oxide was observed as shown in Figure 231. The XPS signals are averaged over a large area (about 1 mm^2), and contain contributions from the different areas seen in the SEM images in Figure 232.

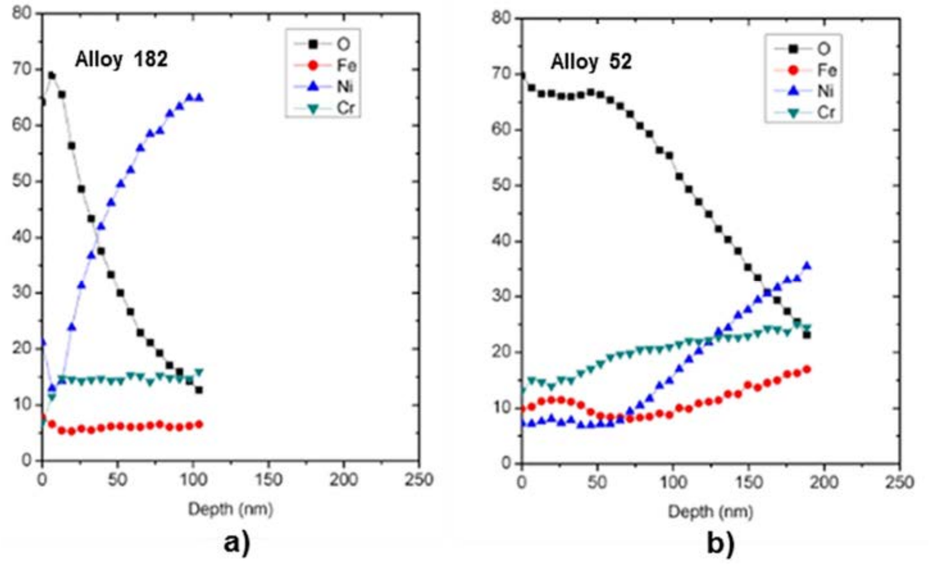

Figure 231. Auger profiles of the inner film for a) Alloy 182 and b) Alloy 52 exposed to doped steam for 750 and 2175 hours, respectively.

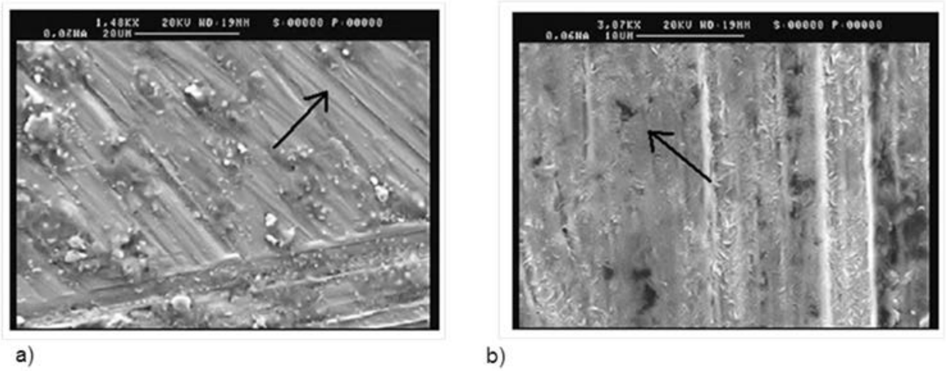

a)

b)

Figure 232. SEM micrographs of smooth surface areas indicated by arrows. Smooth area on a) Alloy 182 and b) Alloy 52, where the Auger spectra were collected.

5.3.3 GI-XRD analysis of the oxide film formed on doped steam exposed Alloy 182 and Alloy 52

XRD scans in symmetric omega-2theta and asymmetric GI-XRD modes were conducted. The spectra are collected in Figures 233 (a) and (b) for Alloy 182 and Alloy 52, respectively. With the smallest GI-angle of 0.5 degrees, the matrix-related XRD reflections are the weakest in both cases. Upon increasing the angle of incidence, the matrix-reflections increase in intensity and the oxide contribution (inside the black boxes in Figure 233) becomes smallest, as expected, in the symmetric omega-2theta scan with the deepest probing depth. The experimental results were compared to reference spectra from the XRD library, the lower lines in Figure 233, the main emphasis being if a dual oxide spinel layers were resolvable in the GI-XRD.

Clearly, oxide reflections are detected in the low GI angle spectra for the both studied samples. The Alloy 52 sample shows slightly higher intensity for the oxide reflections at around 2θ = 60 degrees as compared to the Alloy 182.

The observation indicates better organized or thicker oxide layer for Alloy 52 than for Alloy 182. The two spinel oxides, $NiFe_2O_4$ and $FeCr_2O_4$, show a variety of peaks but because the overlap of the peaks further analysis remains to be done with methods that are more sensitive for elemental composition (such as SEM/TEM-EDS or XPS) than the crystal lattice spacing. Also, smaller GI angles than 0.5 degree may need to be used, but that would require perfectly flat sample surfaces.

Oxides were clearly detected in both Alloy 182 and Alloy 52 surfaces. Due to the peak overlap between the spinel phases, more careful analysis is required to determine the dual layer nature of the studied oxides. Furthermore, techniques with a spatial elemental sensitivity are required for thorough analysis, but GI-XRD can be considered as a complementary technique for further characterization.

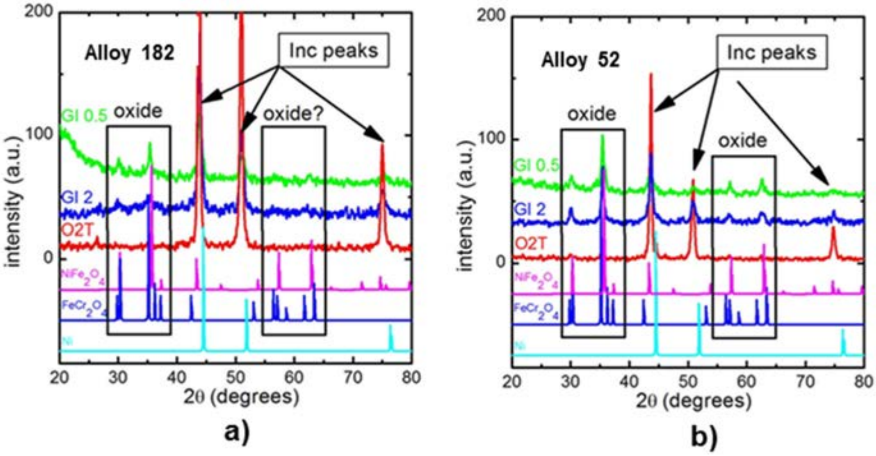

Figure 233. XRD peaks obtained using various grazing angles for oxide layers a) on Alloy 182 and b) Alloy 52 after oxidation in doped steam.

5.4 Pure steam exposures

Pure steam exposure was conducted at 400 °C, at the nominal steam pressure of about 150 bar and partial hydrogen pressure of about 0.6 bar correspondingly to the doped steam test. Surface smoothness of specimens was improved by polishing the machined and ground surface before exposure.

5.4.1 ESCA analysis of the inner oxide layer on Alloy 182 and Alloy 52 formed during pure steam exposure

ESCA analysis shown in Figure 234 gave about the same thickness for the inner chromium-rich oxide layer formed on Alloy 182 as on Alloy 52. Oxide thickness is defined as the depth where the oxygen reaches ½ the surface concentration. In pure steam the outer oxide surface on both specimens was spotty and uneven. Thus, the ESCA and Auger analyses cover only the inner layer of the oxide. Based on the ESCA profile the inner film on Alloy 52 is slightly thicker than on Alloy 182. In general, both samples have very thin chromium-enriched oxide layer. Oxygen content remains high in the base metal depths which is an indication of too rough surface finish for a successful sputtering.

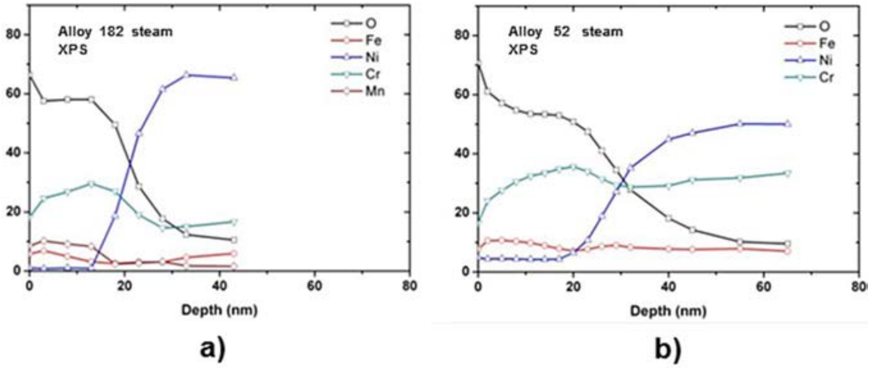

Figure 234. ESCA composition profiles for a) Alloy 182 and b) Alloy 52 exposed to pure steam for 998 hours.

5.4.2 Auger analysis of the inner oxide layer on Alloy 182 and Alloy 52 formed during pure steam exposure

Based on the Auger analysis results the thickness of chromium-rich film is slightly thicker on Alloy 52 than on Alloy 182, Figure 235. Polishing specimen surface with diamond paste was not adequate for successful sputtering. Oxide tail is visible under the inner layer oxide both in the ESCA and Auger analyses.

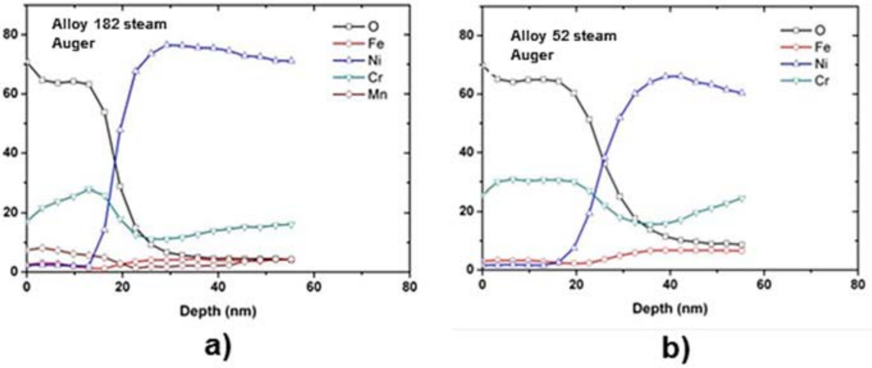

Figure 235. Auger profiles for a) Alloy 182 and b) Alloy 52 exposed to pure steam for 998 hours.

5.5 Simulated PWR environment exposures

The outer surface on Alloy 182 after PWR coolant exposure was covered by the nickel-, iron- and chromium-rich needles, loosely attached precipitates which were removed by nylon brush before conducting ESCA analysis, Figure 236. Nickel-, iron- and chromium-rich precipitates cover also partly Alloy 52 surface after PWR coolant exposure, Figure 237. ESCA analyses were conducted on an area between precipitates. The ESCA results concerning Alloy 182 and 52 cover only the inner, chromium-rich layer. Test arrangement and heating and cooling of specimens with the PWR loop resulted obviously in deposition of the dissolved ions on top of the grown oxide layers.

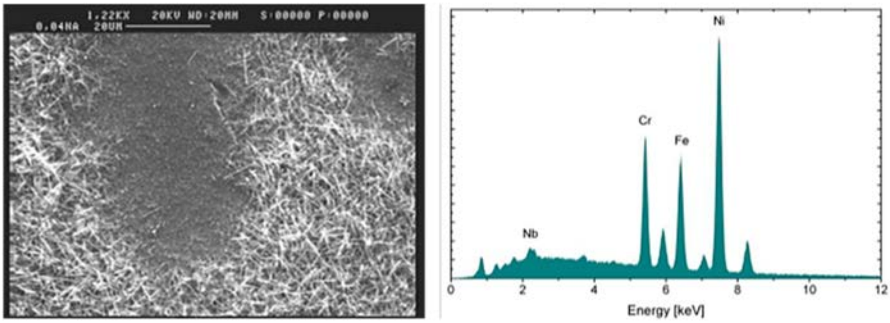

Figure 236. Surface of Alloy 182 sample after PWR exposure. Nickel-, iron- and chromium-rich precipitates cover partly the sample surface. ESCA analyses were conducted on an area between precipitates.

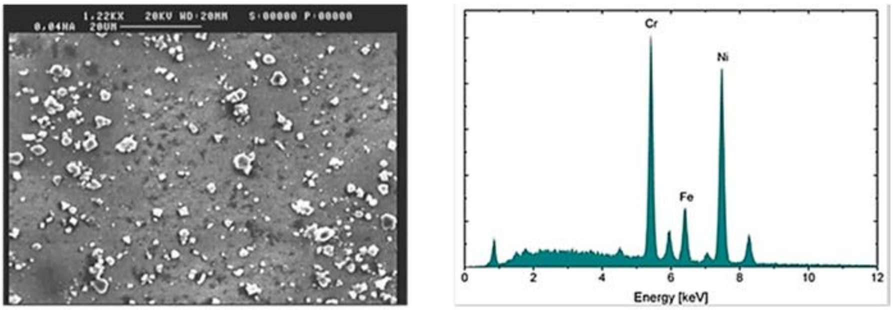

Figure 237. Surface of Alloy 52 sample after PWR exposure. Nickel-, iron- and chromium-rich precipitates cover partly the sample surface. ESCA analyses were conducted on an area between precipitates.

5.5.1 ESCA analysis of the inner oxide structure on Alloy 182 and Alloy 52 formed during simulated PWR coolant exposure

ESCA analysis indicates larger inner oxide thickness on Alloy 182 than on Alloy 52. Oxide thickness is defined as the depth where the oxygen concentration reaches ½ the surface concentration. In the case of both PWR exposed samples surface ESCA analysis shown in Figure 238 may include traces of the deposited phases.

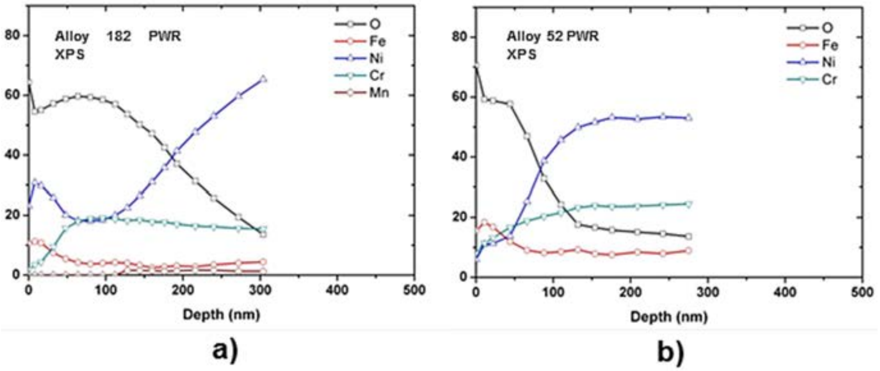

a) b)

Figure 238. ESCA composition profiles of the inner oxide film for a) Alloy 182 and b) Alloy 52 exposed to PWR coolant at 360 ºC for 998 hours.

5.5.2 Auger analysis of the inner oxide structure on Alloy 182 and Alloy 52 formed during simulated PWR coolant exposure

Auger analysis gives the same inner oxide thickness as ESCA results and shows similar increase of iron and nickel contents on Alloy 182 on sample surface, Figure 239.

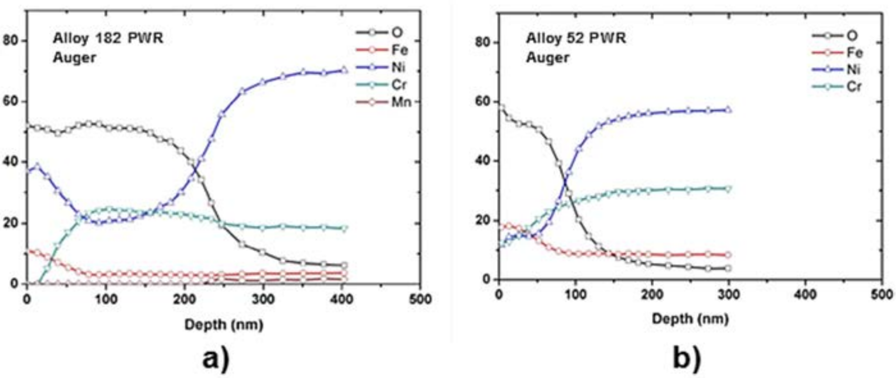

a) b)

Figure 239. Auger profiles for a) Alloy 182 and b) Alloy 52 exposed to PWR coolant at 360 ºC for 998 hours.

5.6 Scanning electron microscopy (SEM) of oxide film cross-sections

Scanning electron microscopy of the oxide in 4 PB specimen cross-section was applied for the oxide thickness evaluation. Especially, specimens which after pure steam experienced exposure continued exposure to pure steam with increased strain or exposed to doped steam for crack initiation were analyzed using SEM. Cross-section of Alloy 182 specimen exposed first for 1860 hours in pure steam with 1.1% strain, and after that in doped steam for additional 998 hours with the original 1.1% strain revealed marked changes in the oxide structure, as well as crack initiation after short doped steam exposure, Figure 240.

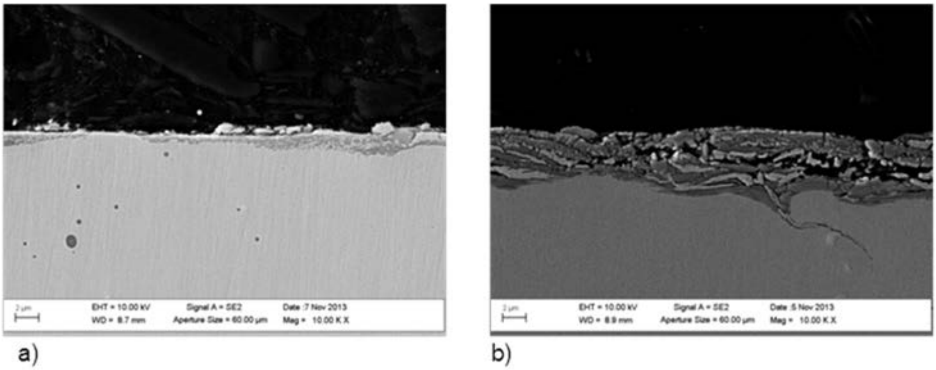

a) b)

Figure 240. a) Alloy 182 with 1.1% strain for 1860 h in pure steam continued with 5% strain for 998 h in pure steam and b) Alloy 182 with 1.1% strain for 1860 h in pure steam continued with 1.1% strain for 998 h in doped steam.

The continued exposure of Alloy 52 applying either increased strain in pure steam or original strain in doped steam environment did not change the appearance of the oxide film. Either exposure time was too short or the chromium content of the material requires even higher temperature, Figure 241.

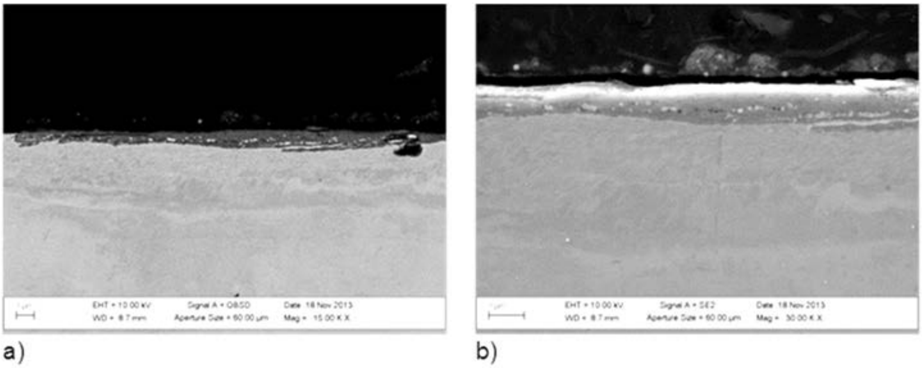

a) b)

Figure 241. a) Alloy 52 loaded with 1.1% strain for 1860 h in pure steam continued with 5% strain for 998 h in pure steam and b) Alloy 52 loaded with 1.1% strain exposed for 1860 h in pure steam continued for 998 h in doped steam.

The appearance of the oxide film on Alloy 52 did not change after continued exposure to doped steam. Nor did the increased strain combined with continued exposure to pure steam change the oxide appearance of the oxide layer on Alloy 182, Figure 242.

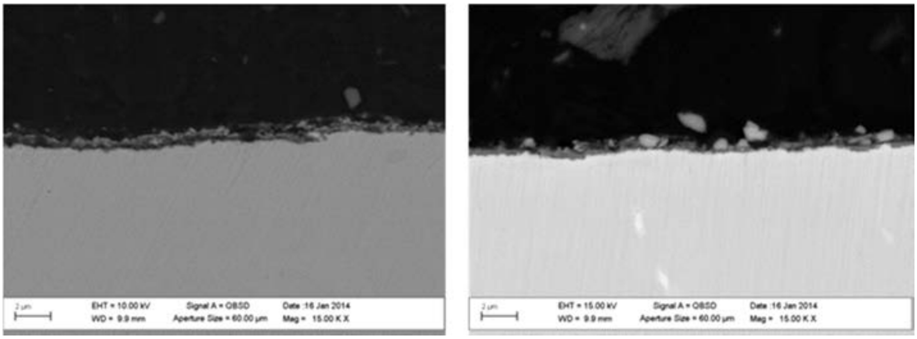

Figure 242. Alloy 182 with 1.1% strain for 1860 h in PWR water continued with 5% strain for 998 h in PWR environment.

5.7 Summary

The temperatures and oxidation periods applied for Alloy 182 and Alloy 52 in different environments varied. Inner oxide thickness depends on the chromium content of the alloy. Additionally, besides the exposure temperature, material microstructure and surface finish affect the oxidation kinetics. Oxidation environment affects the outer layer of the oxide film.

5.7.1 Oxides formed in pure steam

Pure steam provided only an inner oxide layer during the applied test time and temperature on studied alloys. Duplex film existed locally on Alloy 182 samples but the conducted ESCA and Auger analyses did not cover the observed separate precipitates. Thus, the pre-stage of the observed outer oxide layers were not systematically analyzed because the various test procedures applied affected the appearance of the outer oxide layer structure. Strain increase in pure steam did neither affect the oxide film structure nor initiate cracks in the studied Ni-based alloy weld metals.

5.7.2 Oxides formed in doped steam

Doped steam initiated cracks, but the analyzed oxide structure did not correspond to any structure normally observed in NPP environments. In doped steam Alloy 182 had thinner inner oxide layer than Alloy 52. Doped steam test after long-term pure steam exposure modified totally the film structure on Alloy 182 during 998 hours exposure. Oxide on Alloy 52 became also thicker but no cracks were initiated. Doped steam exposure with 1.1% strain and preceding pure steam exposure of Alloy 182 changed the oxide film thickness and appearance and initiated cracks. The doped steam oxide samples cut from the 4 PB specimens had experienced after exposure the liquid penetrant testing and removal of the developer used. Additionally, the sample surface was washed several times before surface film analysis using ESCA or Auger techniques. Obviously, these surface treatments have removed the outer oxide layer deposited on sample surface. Sample 182 included still some fluorine (F) as well as small amounts of sulfur. Fluorine and sulfur are visible on Alloy 182 but not on Alloy 52 even though samples have been exposed to the same environment. It is obvious that outer layers of the oxide film have been affected by washing, wiping or some other mechanical treatments after autoclaving before ESCA analysis. The inner layer of the oxide on Alloy 52 included about five times more Cr than the inner layer on Alloy 182. The inner layer on Alloy 52 can be chromite, e.g., $FeCr_2O_4$. All main elements of the studied samples showed hydroxides after doped steam exposure on the outer surface.

5.7.3 Oxides formed in simulated PWR coolant

Simulated PWR coolant environment exposures were assumed to provide precipitates on the inner oxide layer. Oxide films formed in simulated PWR coolant consisted of duplex oxide film on Alloy 182. The outer layer in this oxide was needle-shaped and contained mainly nickel, iron and chromium. The oxide structure on Alloy 52 contained local nickel-ferrite precipitates on the chromium-rich inner oxide layer. The continued exposure with increased strain in PWR environment did not produce any observable changes in the oxide.

5.8 Conclusions

Machined surface was not applicable to detailed oxide structure analysis utilizing sputtering. Rough surface resulted in uneven sputtering penetration and mixing of element ions at different levels in analysis results.

Doped steam provides fast oxide film growth initiating cracking. Crack initiation was observed only in alloys with low chromium content. Thickness of the inner chromium-rich layer may not be a measure of the corrosion resistance. However, observed thick outer oxide layer correlates with crack initiation. The thickness of the inner layer depends only on the chromium content of the alloy, i.e., Alloy 52 < Alloy 182.

Nickel hydroxide was observed in the outmost layers on Alloy 182 exposed to doped steam. Doped steam test may include the catalytic effects of impurities on oxidation reactions, producing rapid growth of the outer oxide layer. Oxide layers on Alloy 52 samples exposed to the applied test environments consist only of chromium-rich layers. It is possible that surface films vary locally on sample surface.

6. Rigidity comparison of Alloy 52 narrow-gap weld plate and tubular safe-end mock-up

The goal of this study was to computationally estimate the effect of geometry and boundary conditions on structural rigidity, stresses, strains and further on the possible risk for hot cracking in the case of narrow-gap welding. Two different mock-ups were examined, the first was a plate mock-up and the second a nozzle mock-up.

The computation was performed as follows:

- Specifically tailored finite element, Abaqus [Abaqus Theory Manual 2011], analyses were utilised;
- The non-linear characteristics of material were taken into account;
- Temperatures, deformations, stresses and strains were computed during and after welding.

The overall geometry of the plate mock-up is shown in Figure 243. Beams were welded to the bottom of the plates which were narrow-gap welded together. The nozzle mock-up was a tubular specimen having inner diameter of approximately 750 mm and wall thickness of approximately 110 mm, Figure 244. The flange-like part of the nozzle mock-up was only partly modelled as shown in Figure 244.

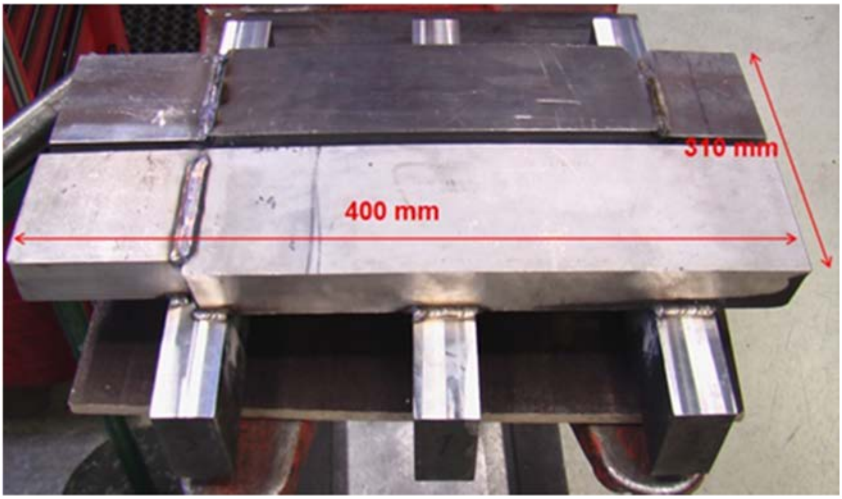

Figure 243. The plate mock-up. Plate thickness is approximately 50 mm.

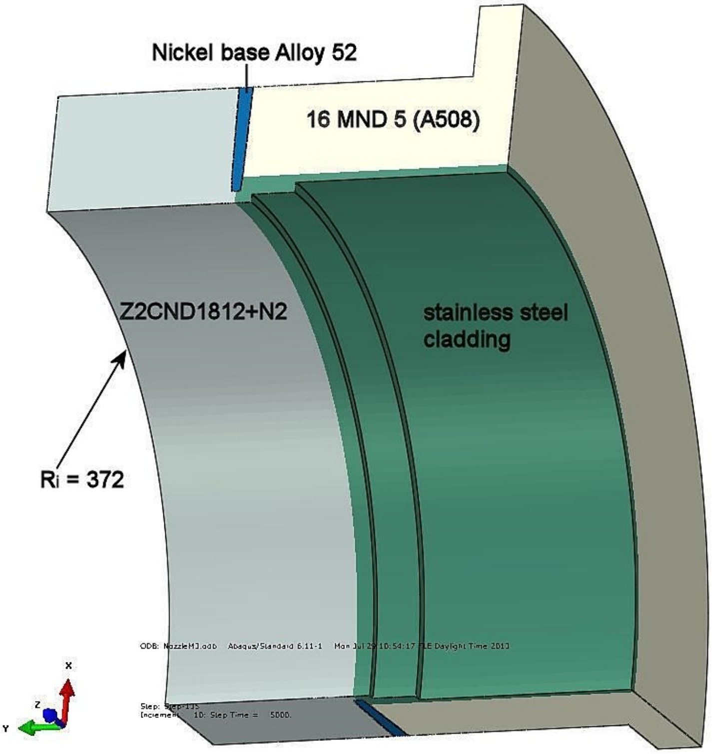

Figure 244. The nozzle mock-up (one quarter of it). Only part of the flange-like part was modelled as is shown.

The materials of the plate mock-up were ferritic steel SA 508 and austenitic steels AISI 304, AISI 308 and AISI 309. The weld metal was Alloy 52. The welding parameters were selected with the help of welding experts. Cracking of the weld occurred in the first 7 weld passes. After that no cracking was observed. Total shrinkage measured from the top of the groove was 2.5 mm after welding. The filling per weld bead was approximately 0.9–1.2 mm.

The materials, weld geometry and welding parameters of the nozzle mock-up were similar. The wall thickness was approximately twice that of the plate mock-up. The weld groove was slightly different. Initially there was also material under the first weld bead.

The material properties for the analysis were taken from references [International Weld Residual Stress Round Robin Problem Statement 2009, Crooker & Rathbun 2011, Zang et al. 2009]. These properties include also the material parameters for combined isotropic/kinematic hardening material model of Abaqus [Abaqus Theory Manual 2011]. The combined isotropic/kinematic hardening material model was first introduced by Armstrong and Frederick [1966] and later expanded by Chaboche [1989]. The combined isotropic/kinematic model is more suitable to cyclic loading conditions (such as occurs in multi-pass welding) than the conventional kinematic hardening model.

The materials which were utilised in the analyses are:

- SA508 (16 MND 5), ferritic material. Same properties were utilised for both ferritic materials.
- Alloy 52 (Inconel 52), weld metal.
- AISI 304 (pipe and cladding). Same properties were used for AISI 309, AISI 308, Z2CND and cladding materials.

Figure 245 shows stress-strain curves for the materials at room temperature (constant strain amplitude 0.01).

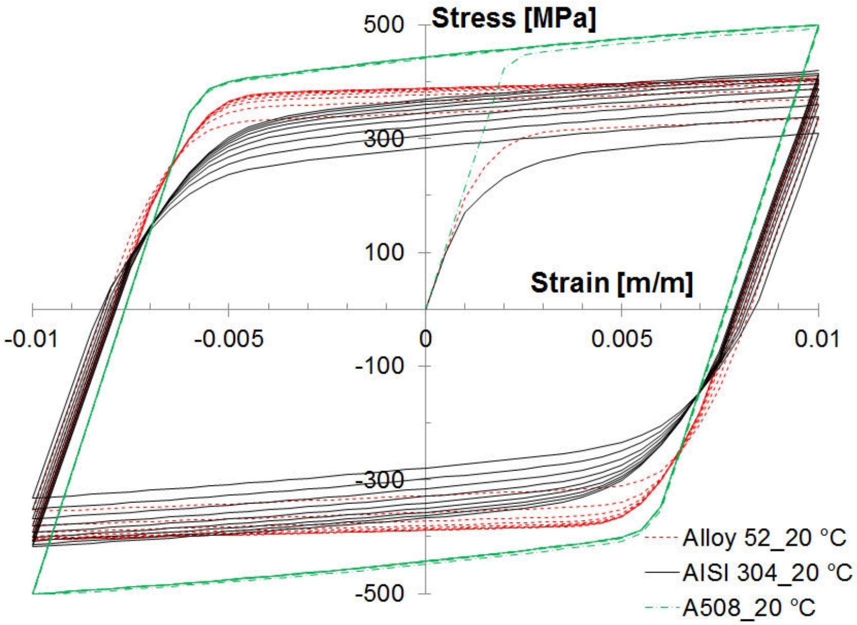

Figure 245. Stress-strain curves for the materials at room temperature (constant strain amplitude 0.01).

Abaqus 6.11-1 software [Abaqus Theory Manual 2011] was utilised in the analyses. Thermal and mechanical analyses were performed separately. In-house codes were used to generate some of the input data, see Figure 246.

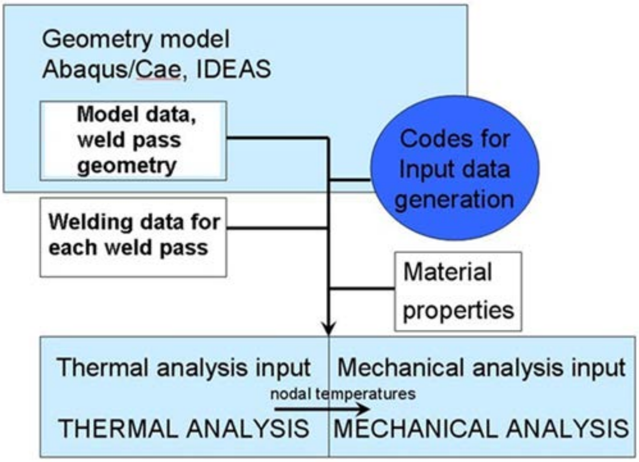

Figure 246. Flow chart of the analysis procedure.

Second order (parabolic) reduced integration hybrid finite elements were used in order to avoid volumetric locking[1] (Abaqus axisymmetric element type CAX8RH and generalized plane strain element type CPEG8RH). The generalised plane strain formulation involves a model that lies between two planes that can move with respect to each other and, hence, cause strain in the axial direction of the model. This formulation is considered to be necessary in the case of different materials and temperature change. Small strains and displacements were assumed. The model of the plate mock-up is shown in Figure 247 and nozzle mock-up in Figure 248.

In the mechanical analysis, double elements (two sets of similar elements on top of each other) were used in the areas which were not yet active in the computation. The additional elements were modelled with remarkably low elastic modulus and material strength properties. Those elements were needed to track the accumulated deformation of the weld nodes, which are not yet active in the model. Otherwise the computed deformed shape would be highly distorted. Pass by pass modelling was performed adding the corresponding elements to the model (”model change, add” option of Abaqus code).

In the thermal analysis the heat input was modelled using uniform internal heat generation and an exponential time function. The length of the time function was approximately chosen so, that the length of the heat input area was approximately 12 mm. In addition, the initial temperature of 1400 °C of the weld metal was modelled to simulate the initially molten weld metal and its heat content. The amount of the heat input *Q* [J/s]) was obtained using the welding parameters and thermal efficiency η as:

$$Q = \eta \times U \times I \text{ ,} \qquad (6)$$

where U is voltage and I is current. The value of the thermal efficiency η of 80% was assumed. It was selected in such a way that realistic size of the molten zone was obtained.

---

[1] At each integration point of an element the volume remains almost constant and hence overconstrains the kinematically admissible displacement field. This results in overconstraining of mesh, also known as “Locking”. It can be avoided using reduced integration resulting to fewer volumetric constrains. Hybrid elements work by including the hydrostatic stress distribution as an additional unknown variable, which is computed at the same time as the displacement field. This allows the stiff terms to be removed from the system of finite element equations.

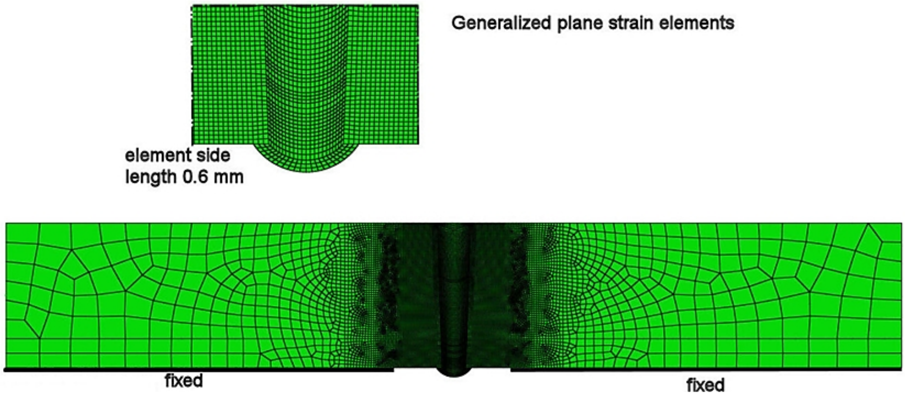

Figure 247. The plane strain finite element model of the plate mock-up. The thickness of the plate is 50 mm and width is 310 mm. Thus, the whole width of the real plate was modelled.

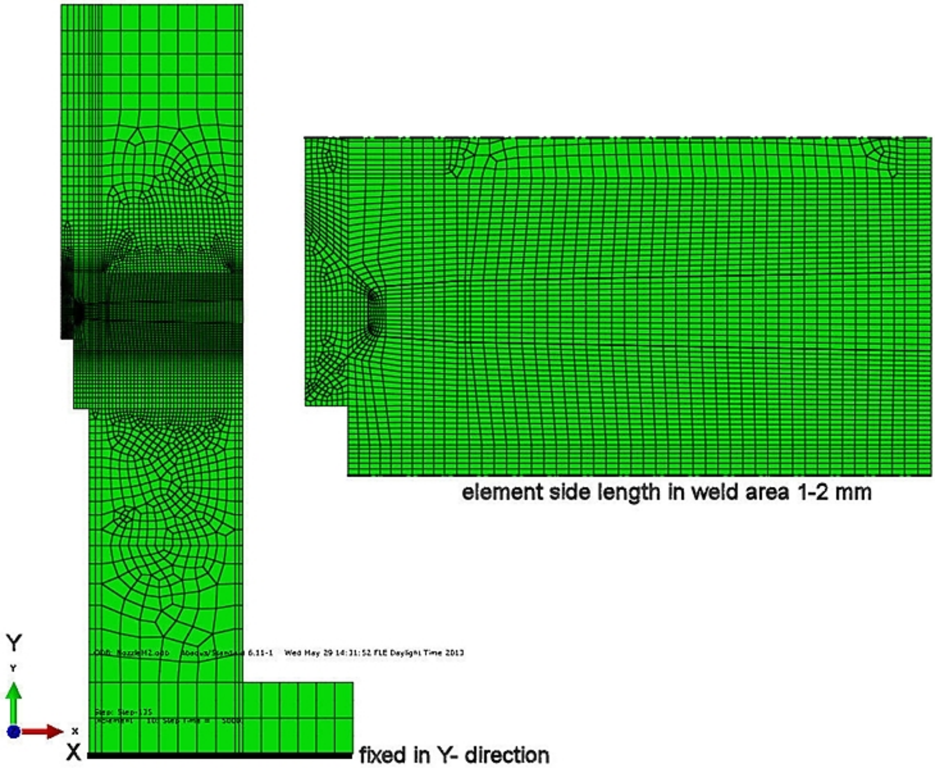

Figure 248. The axisymmetric finite element model of the nozzle mock-up.

Concerning surface heat losses convection was modelled using heat transfer coefficient value of 100 W/m^2K. The ambient temperature was 20 °C. No heat losses from weld pool were modelled. Radiation was not modelled. An efficiency of 80% was assumed in the welding.

In the mechanical analysis, mixed hardening material model of Abaqus including both isotropic and kinematic hardening was utilised. An annealing temperature of 1400 °C was utilised. The annealing procedure simulates the relaxation of stresses and plastic strains due to material behaviour near or in the melting temperature. Physically, annealing is the process of heating a metal part to a high temperature to allow the microstructure to recrystallize, removing dislocations caused by cold working of the material. During the annealing procedure the analysis code Abaqus sets all appropriate state variables to zero (in this case stresses, back stresses, and plastic strains).

In the welding simulation the actual weld elements were added to the model in the stress-free state having an initial temperature of 1400 °C. Temperatures were read from the thermal analysis results.

The mechanical cause of hot cracking is a combination of both a tensile strain and reduced material resistance to cracking [Computational Weld Mechanics Simulation of Hot Crack Nucleation 2012]. In this case the reduced material resistance to deformation cannot compensate localized tensile strain. The reduced material resistance is only experienced within certain temperature ranges. There are different reasons for the reduction in material resistance and accordingly hot cracking can be classified (Figure 249) as follows [Computational Weld Mechanics Simulation of Hot Crack Nucleation 2012]:

- Ductility dip cracking (DDC) in heat affected zone, hot cracking of HAZ. DDC occurs in a completely solid phase, e.g., for austenitic alloys DDC is observed approximately at half of the absolute solidus temperature.
- Liquation cracking (LC) in partially melted zone. Hot cracking occurs at the boundary between fusion zone and HAZ. At a higher temperature range, some metallic materials are at risk of liquation cracking. This type of cracking occurs in a solid-liquid coexistent region. Resistance to LC drops, because above the local solidus temperature the grain boundary melts, but the grain centre remains solid.
- Solidification cracking (SC) in fusion zone and hot cracking of fusion zone. Like liquation, solidification cracking occurs in the solid-liquid coexistent region. Resistance drops because below local liquidus, dendrites growing in completely liquid phase are surrounded by a liquid film.

The risk of hot crack nucleation can be predicted using the experimentally determined resistance. The prediction is based on a balance between resistance and driving force. The driving force is the strain increment in the susceptible temperature range.

Figure 250 shows experimentally determined critical strain for ductility dip cracking of Alloy 82 at different temperatures obtained from reference [Chen & Hao 2010].

In the same figure the experimentally determined critical strain for ductility dip cracking from reference [Hänninen et al. 2006] for Alloy 82 and 52 is also shown. The weld metals of the mock-ups was Alloy 52 both for the plate- and the nozzle mock-ups. The critical strain shown for Alloy 52 in Figure 250 is utilised later.

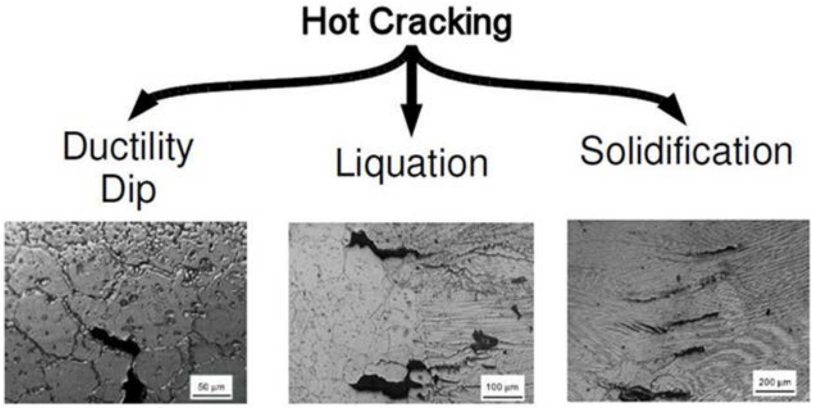

Figure 249. The classification of hot cracking [Computational Weld Mechanics Simulation of Hot Crack Nucleation 2012].

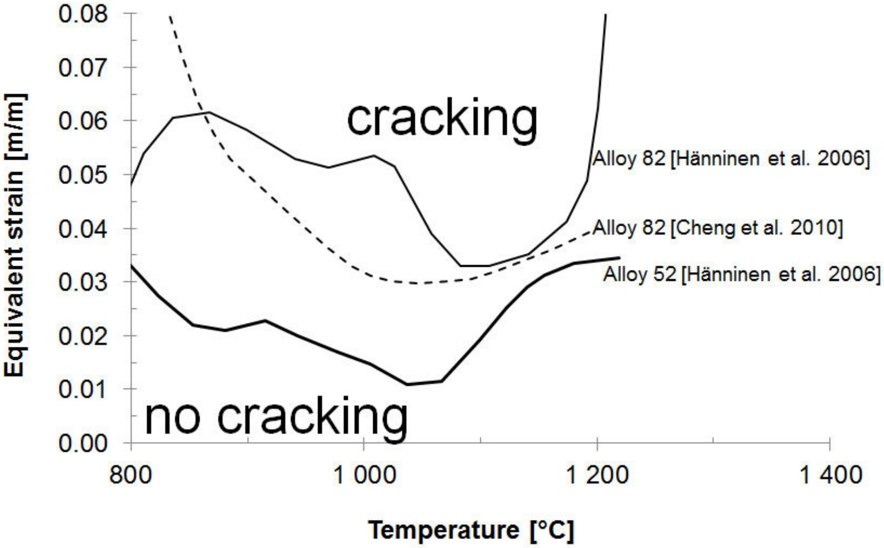

Figure 250. Critical strain for ductility dip cracking of Alloy 82 at different temperatures from reference [Chen & Hao 2010] together with the critical strain for Alloy 82 and 52 from reference [Hänninen et al. 2006].

Concerning thermal results, the maximum temperature at each node of the computation model was searched through the computation history. This was performed with the postprocessor Abaqus/Viewer and a written script. The results show the temperature distribution and the fusion zone (T > 1400 °C) after welding, see Figure 251 (plate mock-up).

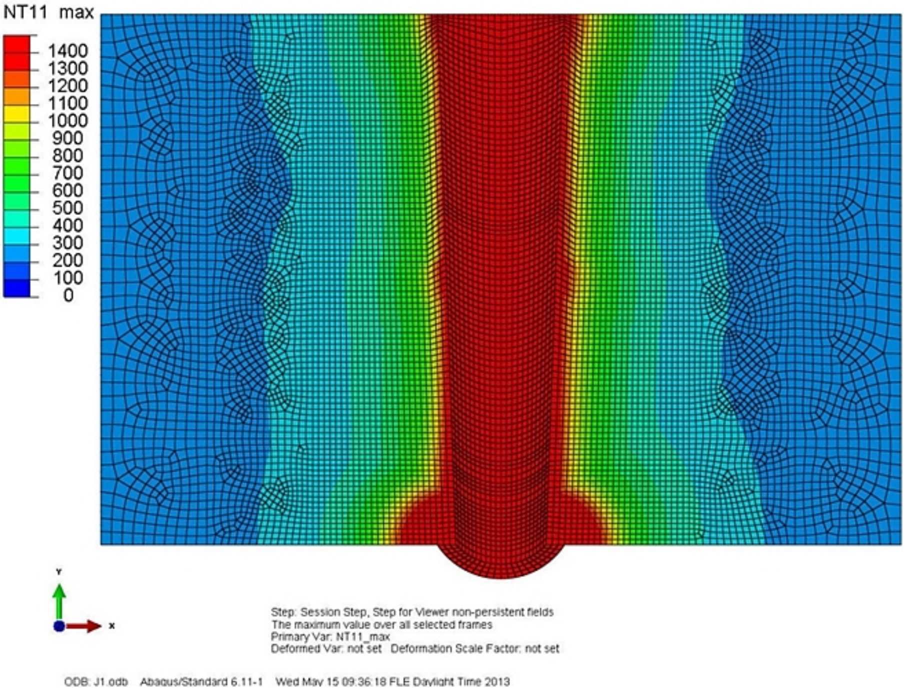

Figure 251. Computed fusion zone for the plate mock-up.

The computed circumferential residual stresses after welding at room temperature for the nozzle mock-up are presented in Figure 252. The computed transverse and longitudinal residual stresses after welding at room temperature for the plate mock-up are presented in Figure 253.

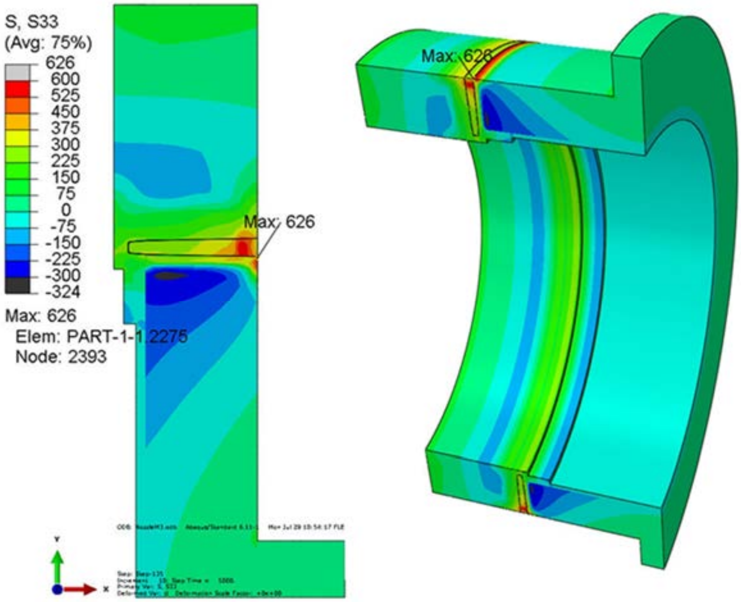

Figure 252. The computed circumferential residual stresses [MPa] for the nozzle mock-up after welding at room temperature. The axisymmetric results were swept to get three-dimensional presentation (right).

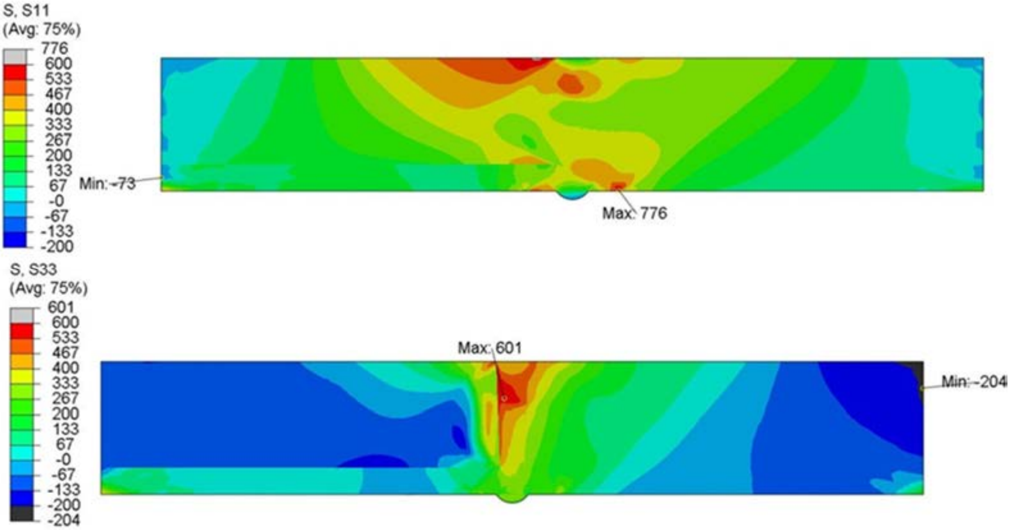

Figure 253. The computed transverse (upper figure) and longitudinal residual stresses [MPa] for the plate mock-up after welding at room temperature.

In the case of the plate mock-up the support beams were cut away and 5 mm layers were machined from the surfaces. The process was simulated so, that first the other half of the fixed boundary conditions on the lower surface were removed. The stress state was mapped to a new model allowing the surface layer removal. The rest of the lower surface boundary conditions were removed and new boundary conditions were applied to two nodes on the right end of the model. Finally the surface layers (5 mm) were removed.

The computed transverse and longitudinal residual stresses after surface layer removal are presented in Figure 254. Figure 255 shows the stresses along the lower surface at the end of the analysis after surface layer removal.

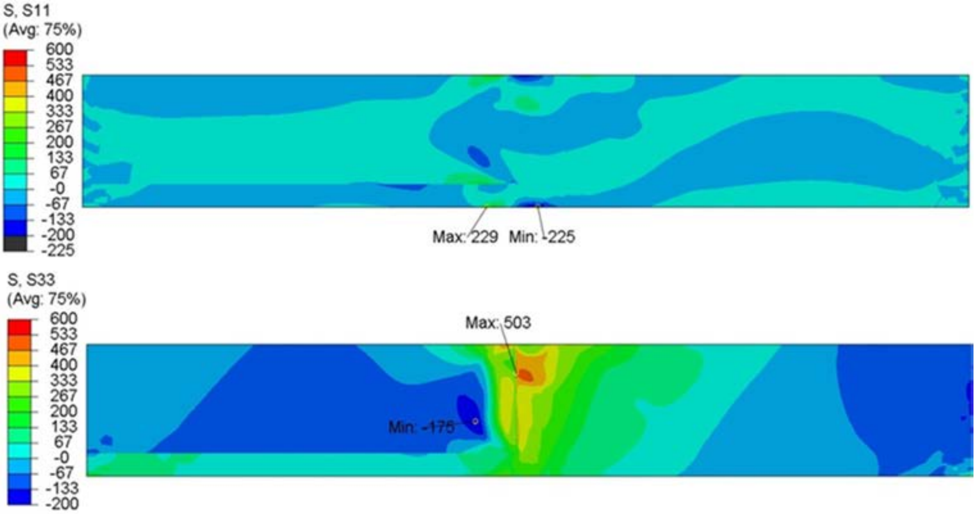

Figure 254. The computed transverse (upper figure) and longitudinal residual stresses [MPa] for the plate mock-up after surface layer removal.

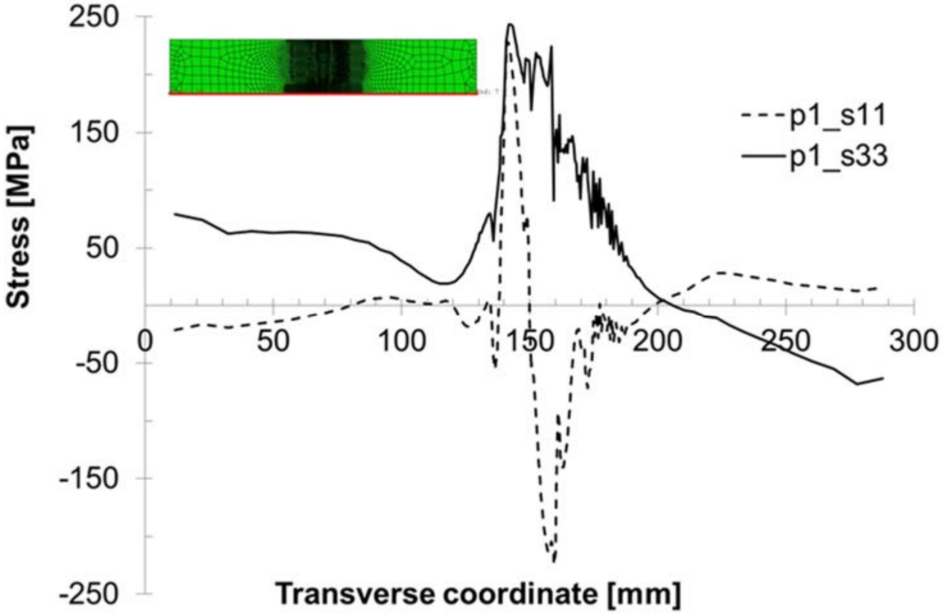

Figure 255. The stresses along the lower surface (from left to right) at the end of the analysis after surface layer removal. S11 = transverse stress, S33 = longitudinal stress.

The risk of hot cracking was estimated in the same way as in references Computational Weld Mechanics Simulation of Hot Crack Nucleation [2012] and Chen and Hao [2010]. In each location the computed equivalent plastic strain was plotted against temperature. This was performed only for one weld pass in the location of interest. The critical strain for ductility dip cracking (Figure 250) is plotted together with the computed results in Figure 256 and Figure 257. This critical strain curve was utilised for the both mock-ups due to lack of material specific data. In the case of plate mock-up the computed strains exceed the critical strain curve. Thus, hot cracking is considered to be possible. Although all the pass-results were not examined, it is estimated, that the risk for hot cracking decreases approximately after the first 15 passes.

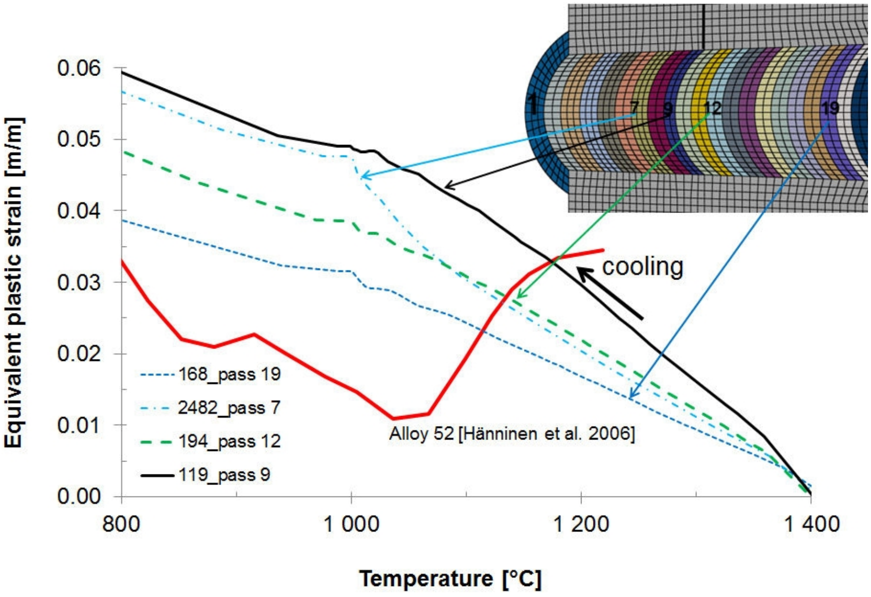

Figure 256. The computed equivalent plastic strain as function of temperature together with the critical strain for ductility dip cracking (Alloy 52 curve in Figure 250). Results for four locations of the plate mock-up.

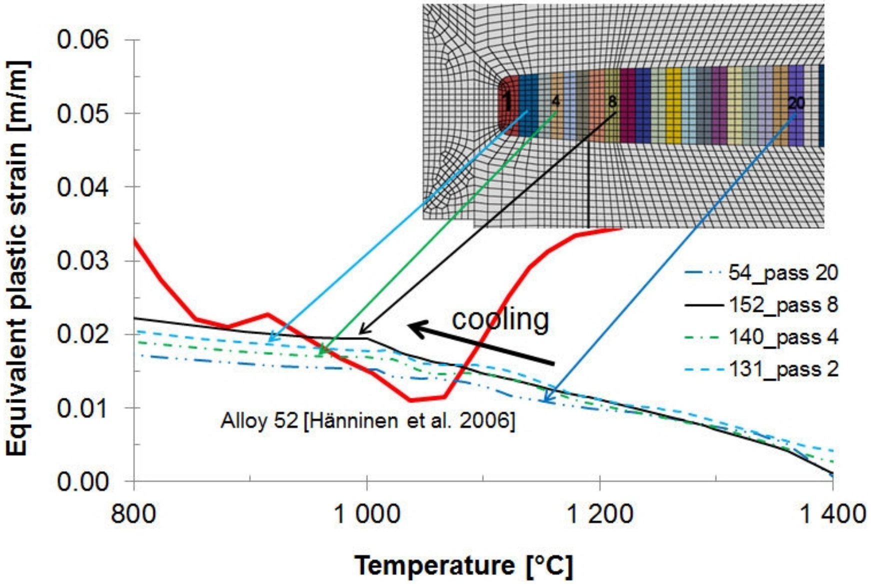

Figure 257. The computed equivalent plastic strain as function of temperature together with the critical strain for ductility dip cracking (Alloy 52 curve in Figure 250). Results for four locations of the nozzle mock-up.

On the basis of the thermal results the size of the computed fusion zone was reasonable. The computed residual stresses of the plate mock-up include the effect of support beams and surface removal. The way of modelling those phases may affect the results, e.g. in which order the boundary conditions are released. This could be numerically studied in the future.

The use of three-dimensional models, although being much more time consuming, would give more detailed results. The utilised plane or axisymmetric models are simplifications of the real structure.

The utilised von Mises mixed hardening material model does not include effect of microstructural behaviour, e.g. phase changes except in the values of the certain material parameters. Also the material model is developed for the lower temperature range. At higher temperatures the creep/relaxation and even material flow near or above melting temperature should be modelled, although this is usually not needed in the welding residual stress computations.

The critical strain curve for ductility dip cracking of filler metal Alloy 52 [Hänninen et al. 2006] was utilised in the estimation of the risk of hot cracking. The actual critical strain curve for the present weld material should be experimentally determined. The computation shows, however, that the strains in the weld center of the plate mock-up are approximately twice larger than the strains of the nozzle mock-up.

The reason for the computed higher risk for hot cracking of the plate mock-up is most probably due to different structural rigidity and weld geometry/configuration of the plate mock-up in comparison to the nozzle model. The welded support beams in the case of the plate mock-up were required to limit the deformations during welding. In the case of the nozzle mock-up the structure itself is rigid enough.

A detailed comparison of computed and measured stresses would require experimentally determined through-thickness stress profiles.

7. Residual stress measurements of Alloy 52 narrow-gap weld mock-up

Residual stresses were measured from as-welded state Alloy 52 NG-DMW root using two techniques: X-ray diffraction and centre hole drilling. X-ray measurements were done as a line across the weld using 4 mm collimator. Hole drilling was performed at the following weld locations:

- 2 measurements at the weld center line,
- 2 measurements at the piping steel: one at 5.5 mm and another at 12 mm from the weld center line,
- 2 measurements at the SS cladding: one at 6 mm and another at 11.5 mm from the weld center line.

X-ray diffraction method gives the residual stresses from the depth of around 10 µm from the weld root and hole drilling covers the depths between 0.1–1.0 mm from the weld root, respectively. Large grain size of the AISI 308 cladding hampers the X-ray residual stress measurement. Figure 258 presents the residual stress measurement locations on the root of the weld.

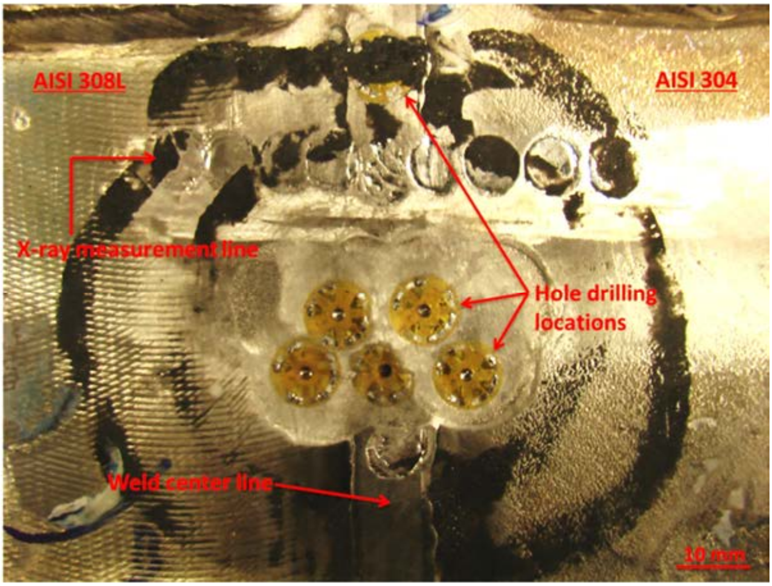

Figure 258. Residual stress measurement locations on the root of the weld.

Figures 259–262 present the results from the X-ray diffraction and centre hole drilling residual stress measurements both perpendicularly and parallel to the weld.

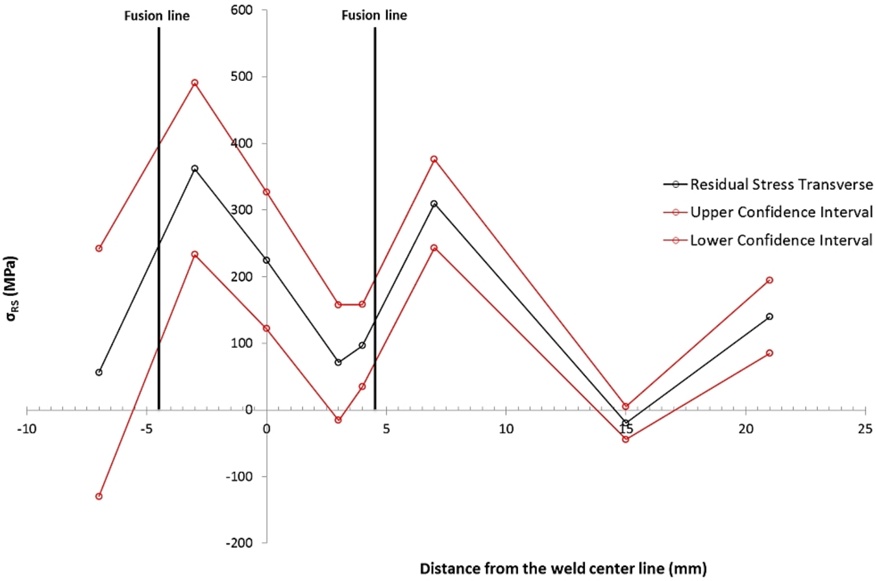

Figure 259. X-ray residual stress measurements perpendicular to the welding direction.

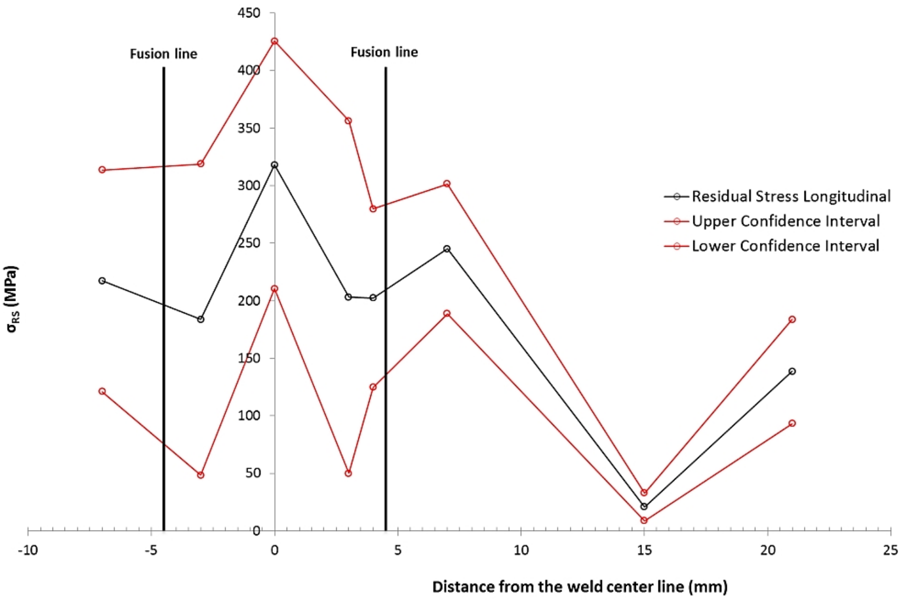

Figure 260. X-ray residual stress measurements parallel to the welding direction.

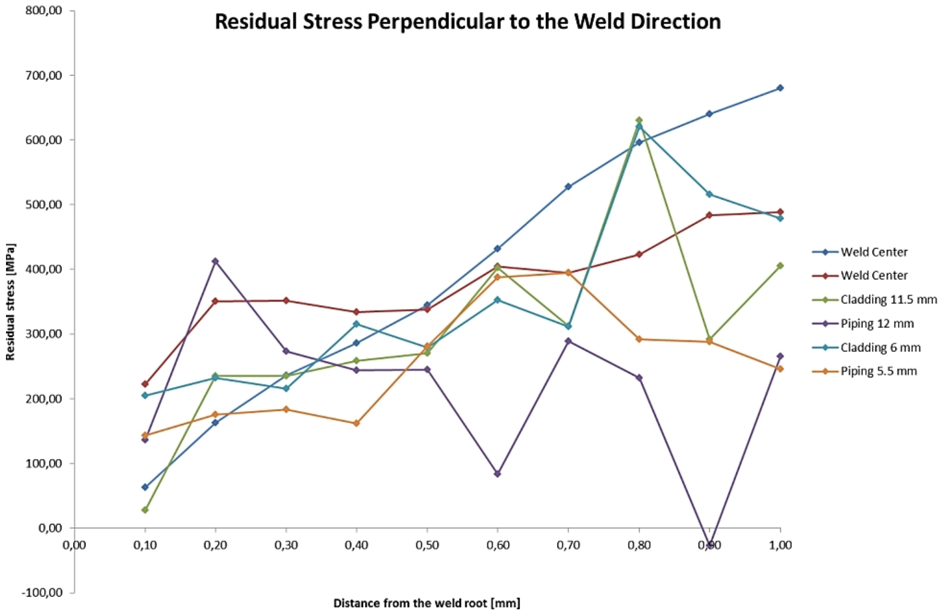

Figure 261. Hole drilling residual stress measurements perpendicular to the welding direction.

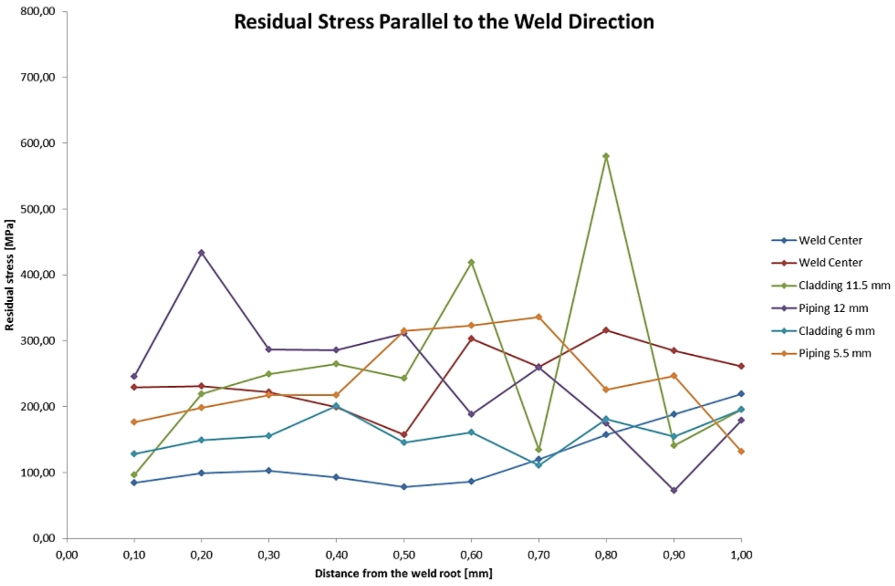

Figure 262. Hole drilling residual stress measurements parallel to the welding direction.

In conclusion, both residual stress measurement techniques showed only tensile residual stresses at the measured weld locations. This corresponds quite well with the simulation results from the plate mock-up after the first half of the boundary conditions were removed (shown in Figure 252). However, the measured residual stresses differ somewhat from the simulated residual stresses after the second half of the boundary conditions and 5 mm of the surface were removed (shown in Figure 253).

The differences in measured and simulated residual stress distributions may result from a number of reasons. As mentioned in the last chapter, the computed residual stresses of the plate mock-up include the effect of support beams and surface removal and the way of modelling those phases may affect the results, e.g. the order in which the boundary conditions are released. Also, the accuracy of these boundary conditions with respect to the actual weld mock-up may have an effect on the results. Furthermore, as mentioned, the utilised von Mises mixed hardening material model does not include effect of microstructural behaviour, e.g. phase changes except in the values of the certain material parameters and the use of three-dimensional models, although being much more time consuming, would give more detailed results as the utilised plane or axisymmetric models are simplifications of the real structure. In addition, the base materials may have had initial residual stress distributions which may have an effect on the residual stress distribution of the weld and the residual stress measurement techniques have some uncertainty in themselves as well.

As mentioned above, more detailed comparison of computed and measured residual stress distributions would require experimentally determined through-thickness stress profiles.

8. PARENT – Program to Assess Reliability of Emerging Nondestructive Techniques for Dissimilar Metal Welds

Susceptibility of dissimilar metal welds (DMWs) containing Alloys 600, 182 and 82 to primary water stress corrosion cracking (PWSCC) and interdendritic stress corrosion cracking (IDSCC) is a well-known problem in the nuclear power plants (NPPs) worldwide. Thus, reliable detection and sizing of PWSCC cracks using non-destructive examination (NDE) has a significant role in the safe operation of the NPPs. The application of NDE techniques to DMWs is challenging due to the complex branching and the tightness of the cracks combined with complex geometry and material of the DMW components.

The international cooperative research program PINC (Program for the Inspection of Nickel Alloy Components) was established by U.S. Nuclear Regulatory Commission (NRC) in 2004. The main objectives of the program were [Cumblidge et al. 2010]:

1) To compile knowledge base on PWSCC in nickel-based alloys in NPPs including the crack morphology and NDE responses.
2) To perform international blind round robin NDE tests on small bore pipe DMW (SBDMW) and BMI nozzle (BMI) specimens containing simulated PWSCC to make quantitative assessments of the detection, characterisation and sizing capabilities of NDE techniques.

The final report for PINC is available online (www.nrc.gov) as NUREG/CR-7019 [Cumblidge et al. 2010]. In February 2012, the NRC executed agreements with organizations in Finland, Japan, the Republic of Korea, Sweden, Switzerland, and the United States to establish a follow-on program to PINC called PARENT (Program to Assess the Reliability of Emerging Nondestructive Techniques) [Braatz et al. 2012]. PARENT members provide specimens, inspection teams, or both as an in-kind contribution.

A series of open and blind round robin tests are conducted on a set of piping components with realistically simulated PWSCC in components that have realistic geometries. The organizations participating PARENT conduct the tests on small-bore pipe DMWs (SBDMWs), bottom-mounted instrumentation penetrations (BMIs), and large bore pipe DMWs (LBDMWs). The test program is divided into blind round robin testing (RRT) and open RRT. Inspectors and procedures in blind testing are qualified by the standards for the nuclear industry in the respective countries. The NDE inspection teams taking part in the blind testing have no prior knowledge of the flaw locations or sizes. Open testing is conducted by teams with experimental and emerging NDE techniques. Teams participating in the open tests obtain the locations, sizes and types of the flaws in the test blocks [Braatz et al. 2012].

8.1 The goal of PARENT

The goal of PARENT is to continue the work begun in PINC. The objectives of PARENT are to pool international resources to cooperatively conduct research on emerging non-destructive evaluation (NDE) technologies to address detection, characterization and sizing for PWSCC in DMWs and apply the lessons learned from PINC [Braatz et al. 2012].

The goal of the open round robin testing is to engage universities, industry and research organizations to investigate the reliability of emerging NDE techniques to detect and size flaws of different lengths, depths, orientations, and locations. The objective of the blind testing is to evaluate the latest commercial and qualified NDE techniques and procedures to determine their detection reliability and sizing accuracy for PWSCC in DMWs. The probability of detection (POD) and false call rates together with sizing statistics for qualified NDE techniques is measured. The goal is also to identify and quantify the differences between qualified and non-qualified inspection techniques [Braatz et al. 2012].

8.2 Development of PARENT program

The PINC program gave a good amount of information about the capabilities of NDE techniques and procedures to detect and size (length and depth) PWSCC in SBDMWs and BMIs. After finalizing the program, there was an international consensus for continuing the work in a follow-on program, PARENT.

Before the start of the PARENT program, a questionnaire was sent to PINC members. The aim was to find out which of the various reactor components were the most desired for the continuation of research work. The top three components in order were: 1) BMI’s J-groove weld, 2) LBDMWs, and 3) SBDMWs. Also, ideas were asked how to apply lessons learned in PINC to enhance the PARENT research work. While PINC had only blind tests, the key idea of PARENT was to have both blind and open testing. The demonstrating of experimental techniques is restricted in blind testing, thus open testing gives more valuable information of non-qualified techniques [Braatz et al. 2012]. Some important lessons learned from PINC like the test block standardisation, the need of clear test block drawings as well as team and procedure qualifications were adopted to PARENT [Braatz & Heasler 2013].

A test block proposal was made at the PARENT-1 meeting held in June 2010. The foundation for PARENT round robin tests was made during 2010 (PARENT-2 meeting) and 2011 (PARENT-3 and PARENT-4 meetings). During these meetings, the proposed test blocks and their flaws were analysed and the optimal open and blind test block sets of the three categories were selected. PARENT participants established contracts to engage testing teams in open and blind round robin tests. A testing protocol and international testing and shipping schedules were developed [Braatz et al. 2012]. Blind testing began with Quick-Blind Test in 2011 and open testing began in early 2012 by testing teams from Europe.

8.3 PARENT round robin testing

The SBDMWs and LBDMWs contain pipe-to-nozzle welds and pipe-to-safe-end welds, PWR inlet and outlet nozzle welds and are similar to many piping welds, such as pressurizer surge line welds. Bottom-mounted instrumentation penetrations consist of an Alloy 600 penetration tube and an Alloy 182/82 J-groove weld [PARENT 2013]. The PARENT open round robin test blocks and the details about the flaws are shown in Table 20.

Table 20. The PARENT open test blocks [Braatz et al. 2012].

Test block	Test block type	Number of flaws	Flaw types	Flaw length range (mm)	Flaw depth range (mm)
P5	BMI	3	TFC	4–8	2–3
P7	BMI	4	WSC	3–4	1–7
P21	BMI	4	EDM	4–20	0.5–10
P22	BMI	4	EDM	4–20	0.5–10
BMI total flaws		15			
P1	SBDMW	4	TFC	21–46	7–23
P4	SBDMW	4	TF, hipped EDM	51–70	7–14
P28	SBDMW	1	SCC	35	12
P29	SBDMW	1	SCC	35	10
P30	SBDMW	1	TFC	35	18
P31	SBDMW	1	SCC	35	4
P32	SBDMW	1	SCC	35	15
P38	SBDMW	1	SCC	35	5
P41	SBDMW	12	EDM, WSC	6–50	2–26
P42	SBDMW	1	EDM	35	10
SBDMW total flaws		27			
P12	LBDMW	2	SCC, EDM	20–34	3–23
P23	LBDMW	3	EDM	26–43	8–43
P24	LBDMW	3	EDM	26–131	4–44
P37	LBDMW	11	WSC, SI, LOB	6–50	1–28
LBDMW total flaws		19			

EDM = electric discharge machined notch
LOB = lack of bond
SCC = stress corrosion crack
SI = slag inclusion
TFC = thermal fatigue crack
WSC = weld solidification crack

The diameter of open SBDMW testing blocks is about 300–400 mm and the wall thickness about 30–40 mm. The diameter of open LBDMW test blocks is about 900 mm and the wall thickness about 85–90 mm.

A wide range of advanced ultrasonic, electromagnetic and X-ray techniques were planned to be used by the testing teams in the open testing. Commercial techniques for blind testing contain sophisticated commercial ultrasonic, phased array ultrasonic and eddy current testing techniques. The NDE techniques that are applied to open test blocks and the number of teams planning to examine each test block are listed in Table 21.

Table 21. The open test blocks, the techniques applied and the number of teams planning to examine the block with at least one of the techniques listed.

Test block	NDE techniques for open blocks	Number of teams
P1	PA, SAFT, ECT, NUT, MM, TOFD, LUV	12
P4	PA, GW, ECT, MM, NUT, LUV	9
P5	GW, ECT, LUV	6
P7	PA, ECT, LUV	6
P12	PA, UIR, SAFT, ECT, NUT, MM, TOFD	12
P21	MM, ECT	2
P22	ECT	1
P23, P24	SAFT, MM, TOFD	3
P28, P29	PA, UIR, NUT, ECT, UT, X-Ray, SAFT, MM, TOFD	18
P30	PA, UIR, NUT, ECT, UT, X-Ray, SAFT, MM, TOFD	17
P31	PA, UIR, SAFT, ECT, NUT, MM, TOFD	13
P32	PA, UIR, UT, X-Ray, SAFT, ECT, NUT, MM, TOFD	15
P37	SAFT, ECT, TOFD, PA	5
P38	PA, UIR, UT, SAFT, ECT, TOFD	10
P41	UIR, PA, UT, X-Ray, SAFT, ECT, NUT, MM, TOFD	11
P42	PA, UT, SAFT, ECT	7

ECT = eddy current
GW = guided wave UT
LUV = laser ultrasound visualisation
MM = microwave microscopy
NUT = nonlinear UT
PA = phased array UT
SAFT = synthetic aperture focusing technique
SHUT = sub-harmonic UT
TOFD = time-of-flight diffraction
UIR = ultrasonic infrared
UT = conventional UT
X-Ray = X-Ray

The blind round robin test blocks are listed in Table 22. Not listed are the reference blocks containing reference reflectors for each of the three categories of test blocks. Data taken on reference reflectors provide for the possibility during data analysis to compare results between different test teams that have used the same NDE technique [Braatz et al. 2012].

Table 22. The PARENT blind test blocks [Braatz et al. 2012].

Test block	Test block type
P6, P8, P9, P25, P26	BMI
P35, P40	SBDMW
P13, P15, P16, P17, P33, P45	LBDMW
P27	weld overlay

The diameter of blind SBDMWs is about 300 mm and the wall thickness about 30–40 mm. The diameter of blind LBDMWs is about 900 mm and the wall thickness about 68–80 mm. Flaw types contained in these test blocks include EDM, LOB, SCC, and WSC, and mechanical fatigue (see Table 20 for definitions) [Braatz et al. 2012].

The NDE techniques that will be applied to blind test blocks and the number of teams planning to examine each test block are listed in Table 23. Only qualified inspectors and qualified procedures are employed in the blind testing.

Table 23. The blind test blocks, the techniques applied and the number of teams planning to examine the blocks with at least one of the techniques listed.

Test block	NDE techniques for blind blocks	Number of teams
P6, P8, P9, P25, P26	UT, ECT, TOFD	3
P13	UT, PA, ECT, UT+TOFD	5
P15, P16, P17	UT, PA, ECT	6
P27	PA	2
P33	PA, UT, ECT	8
P35	UT, PA, UT+TOFD	7
P40	UT, PA, UT+TOFD	6
P45	UT, PA, UT+PA, ECT	5

ECT = eddy current
PA = phased array UT
TOFD = time-of-flight diffraction
UT = conventional UT

The protocol for conducting open and blind round robin testing was developed cooperatively by the test invigilators in Europe, Japan, the Republic of Korea, and the United States. The protocol is a document including all necessary information for conducting the round robin testing. The document includes among others goals, scope, test teams and authorized personnel, compliance requirements, definitions of coordinate systems and points of reference on test blocks and scoring criteria for blind tests. The protocol sets the requirements for secrecy about blind test block flaws, the requirements for written inspection procedures for open and blind tests and reporting requirements and forms for test data and test results.

Round robin tests started in 2011 with quick blind testing and are scheduled to be completed during 2014.

The results of the PARENT program are documented in two NRC NUREG reports during 2015, one for open testing and another for blind testing. Blind round robin testing is being conducted in two segments, Quick Blind and Blind. Four LBDMW test blocks were examined by six test teams in the Quick Blind testing. The Quick Blind testing and destructive analysis were completed in 2013 and the report will be published in 2014 [Braatz & Heasler 2013].

8.4 Finland's participation in PARENT

As VTT and Helsinki University of Technology from Finland were participating in PINC program the continuation of the work within PARENT was clear. VTT participated in PARENT kick-off meeting in June 2010. The PARENT-2 meeting was hosted by VTT in Espoo in October 2010. Since then, VTT has been participating in PARENT meetings and work in the Steering Group and NDE Task Group. Aalto University is participating in PARENT Atlas development.

In 2011, VTT established two NDE teams for conducting open round robin testing and one team for blind round robin testing. A revised and extended version of the qualified procedure for conducting phased array ultrasonic testing of SBDMWs used during PINC RRT was purchased. The final implementation of the procedure and education of the testing personnel was done during open testing and the same procedure was used in the blind testing. VTT also developed some experimental ultrasonic testing techniques which were tested in the open testing.

The procedure, equipment and former experience set the limits for the test block selection. To maintain the extent of the round robin testing reasonable and ensuring the completion on schedule, the sets of open and blind SBDMWs were chosen to be examined by ultrasonic techniques.

The test blocks chosen for open testing with the teams and the techniques used are shown in Table 24. Examples of open SBDMW test blocks are seen in Figure 263.

Table 24. The open RRT test blocks, planned techniques and teams at VTT.

Test block	NDE techniques for open blocks	Teams
P1, P4, P41	PA1	VTT1
P28, P29, P30, P31, P32, P38, P42	PA1, PA2, PA3, PA4, FMC, SAM	VTT1, VTT3

PA1 = phased array UT, commercial procedure
PA2 = phased array UT, linear scan
PA3 = phased array UT, sectorial scan
PA4 = matrix phased array UT
FMC = full matrix capture
SAM = scanning acoustic microscopy

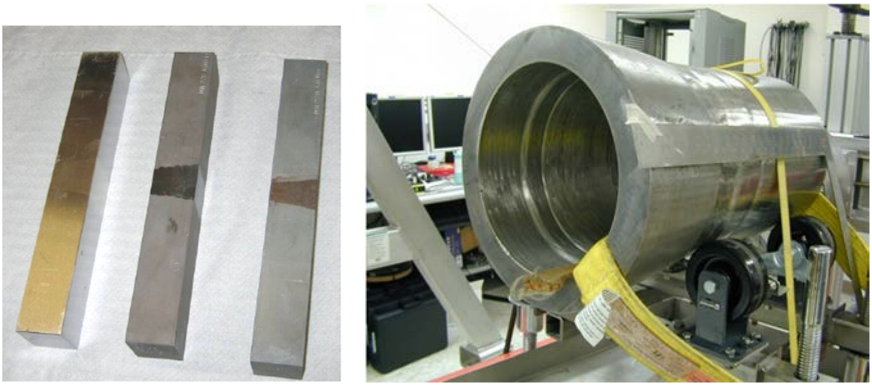

Figure 263. Examples of open SBDMW test blocks.

The commercial phased array ultrasonic testing procedure was used for all SBDMW test blocks. Several ultrasonic techniques were planned for the examination of test blocks P28, P29, P30, P31, P32, P38 and P42. These small test blocks each containing one flaw, were considered easy for testing by some experimental techniques. Finally, the results obtained from techniques PA1, PA2 and PA3 were reported. The main parameters of the three techniques are shown in Table 25.

There were two SBDMW test blocks, P35 and P40, available for blind testing. The testing was conducted by one team with qualified phased array ultrasonic testing procedure.

VTT did the open testing in February 2012. The data acquisition was conducted in two weeks without an invigilator’s presence. When the data acquisition was completed, a two day’s session was held with the invigilator to complete the technical descriptions of the techniques and to ensure the data collection was done according to the procedure and technical descriptions. The final data analysis and reporting was conducted during March 2012 and the final data sheets were given to the invigilator.

There were 27 flaws altogether in the open SBDMW test blocks. The data obtained with each beam angle of techniques PA1 and PA2 was analysed and reported separately, so the data analysis took a considerable amount of time and effort. The experimental techniques were developed before the open testing but they could be finally tested only with the real test blocks. It turned out that the flaws in the test blocks were challenging for some of the techniques and due to that, they were omitted from the final reporting. The commercial procedure showed its effectiveness in the challenging flaws which was a good starting point for the blind testing.

The blind testing was carried out at VTT in October 2012. The blind testing was found somewhat easier to carry out due to the use of qualified procedure together with smaller amount of test blocks. The data acquisition was completed during the first week and another week was left for the data analysis and reporting. After the process, all blind data was given to the invigilator to maintain the secrecy of the test blocks.

Table 25. VTT's open test technique parameters.

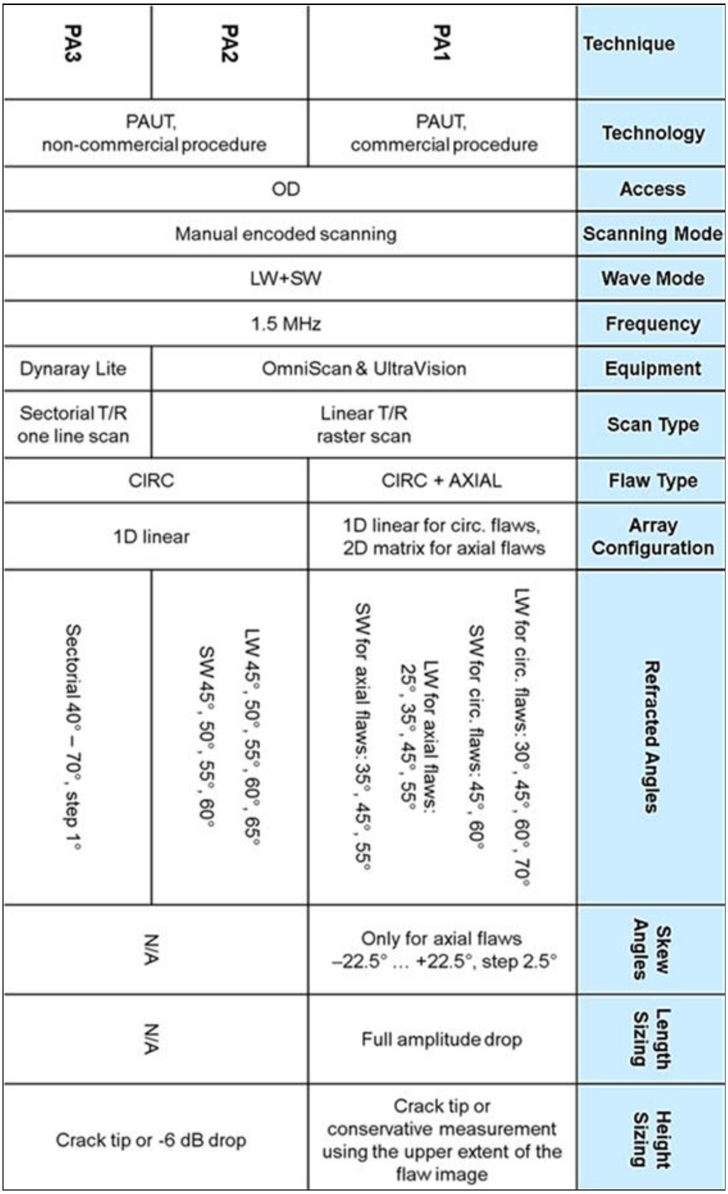

Technique	PA1	PA2	PA3
Technology	PAUT, commercial procedure	PAUT, non-commercial procedure	
Access	OD		
Scanning Mode	Manual encoded scanning		
Wave Mode	LW+SW		
Frequency	1.5 MHz		
Equipment	OmniScan & UltraVision		Dynaray Lite
Scan Type	Linear T/R raster scan		Sectorial T/R one line scan
Flaw Type	CIRC + AXIAL	CIRC	
Array Configuration	1D linear for circ. flaws, 2D matrix for axial flaws	1D linear	
Refracted Angles	LW for circ. flaws: 30°, 45°, 60°, 70° SW for circ. flaws: 45°, 60° LW for axial flaws: 25°, 35°, 45°, 55° SW for axial flaws: 35°, 45°, 55°	LW 45°, 50°, 55°, 60°, 65° SW 45°, 50°, 55°, 60°	Sectorial 40° – 70°, step 1°
Skew Angles	Only for axial flaws –22.5° … +22.5°, step 2.5°	N/A	
Length Sizing	Full amplitude drop	N/A	
Height Sizing	Crack tip or conservative measurement using the upper extent of the flaw image	Crack tip or -6 dB drop	

OD = outer diameter
SW = shear wave

LW = longitudinal wave
T/R = transmitter/receiver

8.5 Conclusions

The experience from the PINC project had already proven the benefits of international round robin testing as a way to bring together international resources to address a global problem. Some development was made with the idea of both open and blind round robin testing together with lessons learned from PINC which were adopted by PARENT. The use of open testing for the evaluation and testing of emerging and experimental techniques is a good way to get more information and experience of them and to find out the limits of the techniques as well. The most effective and reasonable way to conduct the blind testing is the use of established procedures by qualified personnel. In that way comparable results of good quality for making statistical conclusions are obtained and the amount of data is kept reasonable. Producing realistic test blocks with realistic flaws for the assessment and development of NDE techniques is expensive. Therefore an international project is a good way to multiple the possibilities of getting new data and experience.

9. Summary

The following conclusions can be drawn based on the results of this study:

- Characterization of the microstructures of dissimilar metal weld joints of Ni-base alloy weld metals, typical in boiling water reactor (BWR, Alloy 182) and pressurized water reactor (PWR, Alloy 52), was carried out. Special emphasis was put on the heterogeneous microstructures in the fusion line area and narrow-gap welds (Alloy 52) of the modern PWR plant.
- Determination of the mechanical properties was made by hardness testing, mechanical tensile testing using standard specimens and miniature-size flat-bar specimens as well as with fracture mechanical testing using full-size and miniature SE(B) specimens.
- A hardness peak was observed in the BWR weld in the low-alloy steel (SA 508) HAZ in the as-welded state and in the Alloy 52 weld metal side of the fusion line in the PWR NG-DMW after PWHT. Tempering decreased the hardness peak of the BWR weld markedly and in the NG-PWR weld tempering resulted in the hardness peak in the weld metal.
- A carbon-depleted zone was observed in the SA 508 steel side of the fusion line in PWR NG-DMW and PWHT increased the width of the CDZ from about 30 to 80 µm. In the BWR DMW no carbon-depleted zone was observed.
- The miniature flat-bar tensile specimens provided valid test results for specimens extracted from different zones of the weld and the results were in compliance with the hardness profiles. When the local strength properties were compared high mismatch was found at the fusion line between the HAZ and the buttering layer (Alloy 182) in the as-welded BWR DMW samples. PWHT lowered the mismatch markedly. In Alloy 52 PWR NG-DMW after PWHT high mismatch was also observed at the fusion line between the HAZ and the weld metal.
- Fracture mechanical testing showed always ductile fracture in the studied weld zones and the fracture resistance was always high but some variability was present in the fracture resistance depending on the location of the

initial pre-crack tip. The distribution of MnS inclusions in the microstructure was also affecting the fracture resistance values. In Alloy 52 PWR NG-DMW the PWHT decreased the fracture resistance of the fusion zone. The crack propagation took place along the fusion line in the CDZ in the SA 508 steel HAZ as ductile fracture.

- The EAC susceptibility of different weld metals in pure and doped steam at 400 °C as well as in PWR primary water at 360 °C was studied. In PWR water no EAC initiated in 4500 h in any studied material. In pure and doped steam cracking took place in Alloy 600, Alloy 182 and Alloy 82. Alloy 52 did not show EAC initiation in any testing conditions.
- The accelerated doped steam test for Ni-base alloys results in a high acceleration factor and it was not possible to determine reliably based on the limited test time.
- The oxidation of Ni-base alloys in different test environments was studied carefully with FE-SEM, XPS and AES. A clear difference in the oxide thickness of Alloy 182 was observed between doped and pure steam as well as with PWR primary water environments. In doped steam the thick oxide layer consisted of lamellar layers of Cr-rich oxide and metallic Ni deposits. In Alloy 52 almost no difference in oxide structure was observed between different testing conditions. The film consisted of Cr-rich oxide with small metallic Ni deposits inside the oxide layer.
- Specimens containing weld defects did not show any EAC crack extension from the weld defects.
- Alloy 52 narrow-gap weld plate mock-up showed extensive hot cracking during welding the root passes. A rigidity comparison to tubular safe-end mock-up was made and the weld strain development was compared to the critical strain curves of hot cracking susceptibility of the weld metals. The comparison showed that the nozzle mock-up is much more rigid than the plate mock-up. The calculated residual stresses were also verified with the residual stress measurements on the root side of the plate NG-DMW.
- Participation to the international PARENT (Program to Assess Reliability of Emerging Non-destructive Techniques for Dissimilar Metal Welds) round-robin program was completed. New non-destructive testing methods were developed to enhance the reliability of detection and accuracy of sizing of flaws in Ni-base alloy dissimilar metal welds.

Acknowledgements

The project Structural integrity of Ni-base alloy welds (SINI), launched in 2010, deals with dissimilar metal weld issues in nuclear power industry. The three-year project was funded by Tekes, Teollisuuden Voima Oyj (TVO), Fortum Power and Heat Oy, Vattenfall Aktiebolag, OKG Aktiebolag, Fennovoima Oy, VTT Technical Research Centre of Finland and Aalto University School of Engineering, which is gratefully acknowledged. Additional acknowledgements belong to Department of Physics and Astronomy, University of Turku for conducting ESCA and Auger measurements and to STUK – Radiation and Nuclear Safety Authority for participating to the project as a monitoring party.

References

Abaqus Theory Manual (2011), version 6.11-1. Dassault Systemes.

Alexandrov, B.T., Lippold, J.C., Sowards, J.W., Hope A.T. and Saltzmann D.R. (2013), Fusion boundary microstructure evolution associated with embrittlement of Ni-base alloy overlays applied to carbon steel. Weld World, Vol. 57, 39–53.

Armstrong, P.J. and Frederick, C.O. (1966), A Mathematical representation of the multiaxial Bauschinger effect. C.E.G.B. Report RD/B/ N731, Berkeley Nuclear Laboratories, Berkeley, UK, Reprint in: Frederick, CO, and Armstrong, P.J., “A mathematical representation of the multiaxial Bauschinger effect”, Mater. High Temp, Vol. 24 (1) 1–26, (2007).

Bauschke, H.-M. and Koçak, M. (1997), Strength mis-match effect in R-curve behavior of austenitic steel welds. Mis-matching of interfaces and welds, Editors: Schwalbe, K.-H. and Koçak, M. Geesthacht, Germany: GKSS Research Center Publications, pp. 385–397.

Braatz, B.G. and Heasler, P.G. (2013), PARENT Quick Blind Round-Robin Test Report. Draft version, PNNL-22677-DRAFT. Pacific Northwest National Laboratory, Richland, Washington, USA, 56 p. + app. 142 p.

Braatz, B.G., Cumblidge, S.E., Doctor, S.R. and Prokofiev, I.G. (2012), Primary water stress corrosion cracks in nickel alloy dissimilar metal welds: Detection and sizing using established and emerging non-destructive examination techniques. IAEA-CN-194-025. International Atomic Energy Agency. 3. International Conference on Nuclear Power Plant Life Management (PLiM) for Long Term Operations (LTO), Salt Lake City, Utah, USA, 14–18 May 2012, 8 p.

Chaboche, J.L. (1989), Constitutive equations for cyclic plasticity and cyclic viscoplasticity. Int. J. of Plasticity, 5, 247–302.

Chen, J. and Hao, L. (2010), Investigation on ductility dip cracking susceptibility of filler metal 82 in welding. Transactions of JWRI, Vol. 39 (2), 91–93.

Combrade, P., Scott, P., Foucault, M., Andrieu, E. and Marcus, P. (2005), Oxidation of Ni base alloys in PWR water: oxide layers and associated damage to the base metal. Proceedings of the 12th International Conference on Environmental Degradation of Materials in Nuclear Power Systems-

Water Reactors. Editos: Allen, T., King, P. and Nelson, L. The Minerals, Metals & Materials Society, pp. 883–890.

Computational Weld Mechanics Simulation of Hot Crack Nucleation. (2012), Ahmed Nasser under the supervision of Prof. John Goldak. Carleton University. http://www.weck.ca/MSS/ppts/16March2012.pdf, 24 p.

Crooker, P. and Rathbun, H. (2011), Weld Residual Stress Finite Element Analysis Validation. Introduction and Overview. June 14–15, 2011, Rockville, MD, USA, 298 p.

Cumblidge, S.E., Doctor, S.R., Heasler, P.G. and Taylor, T.T. (2010), Results of the Program for the Inspection of Nickel Alloy Components, NUREG/CR-7019; PNNL-18713. U.S. Nuclear Regulatory Commission, Washington, D.C., USA, 174 p. + app. 377 p.

Delabrouille, F., Legras, L., Vaillant, F., Scott, P., Viguier, B. and Andrieu, E. (2005), Effect of the chromium content and strain on the corrosion of nickel based alloys in primary water of pressurized water reactors. Proceedings of the 12th International Conference on Environmental Degradation of Materials in Nuclear Power Systems-Water Reactors. Editors: Allen, T., King, P. and Nelson, L. The Minerals, Metals & Materials Society, pp. 903–911.

Engelhard, G., Habip, L.M., Pellkofer, D., Schmidt, J. and Weber, J. (2000), Optimization of residual welding stresses in austenitic steel piping: prooftesting and numerical simulation of welding and postwelding processes. Nuclear Engineering and Design, Vol. 198 (1–2), 141–151

Faidy, C., Martin, G., Taylor, N., Youtsos, A., Katsareas, D., Keinänen, H., Laukkanen, A., Wintle, J., Sherry, A., Lidbury, D., Safa, N., Cipiere, M.F., Gilles, P., Chapuliot, S., Kaiser, Y. and Lenkey, G. (2004), Assessment of aged piping dissimilar metal weld integrity. ADIMEW Synthesis report, Contract FIKS-CT-2000-00047, European Commission, January 2004, 45 p.

Gaško, M. and Rosenberg, G. (2011), Correlation between hardness and tensile properties in ultra-high strength dual phase steels – short communication. Materials Engineering, Vol. 18, 155–159.

Guinebretiere, R. (2007), X-ray diffraction by polycrystalline materials, ISTE Ltd, London, UK, 351 p.

Hänninen, H., Aaltonen, P., Brederholm, A., Ehrnstén, U., Gripenberg, H., Toivonen, A., Pitkänen, J. and Virkkunen, I. (2006), Dissimilar metal weld joints and their performance in nuclear power plant and oil refinery conditions. VTT Research Notes 2347, VTT Technical Research Centre of Finland, Espoo, Finland, 209 p. http://www.vtt.fi/inf/pdf/tiedotteet/2006/T2347.pdf.

Hänninen, H., Toivonen, A., Brederholm, A., Saukkonen, T., Ehrnstén, U. and Aaltonen, P. (2007a), Environment-assisted cracking and hot cracking of Ni-base alloy dissimilar metal welds. Proceedings of the 13th Int. Conf. on Environmental Degradation of Materials in Nuclear Systems – Water Reactors. Whistler, British Columbia, Canada, 19–23 August, 2007, (CD-ROM), 19 p.

Hänninen, H., Brederholm, A., Saukkonen, S., Gripenberg, H., Toivonen, A., Ehrnstén, U. and Aaltonen, P. (2007b), Hot cracking and environment-assisted cracking susceptibility of dissimilar metal welds. VTT Research Notes 2399, VTT Technical Research Centre of Finland, Espoo, Finland, 177 p. http://www.vtt.fi/inf/pdf/tiedotteet/2007/T2399.pdf.

Hänninen, H., Toivonen, A., Saukkonen, T., Brederholm, A., Aaltonen, P. and Ehrnstén, U. (2009), EAC crack initiation in nickel-based dissimilar metal welds using doped steam test. Proceedings of the 14th Int. Conf. on Environmental Degradation of Materials in Nuclear Systems – Water Reactors. Hilton Virginia Beach, Virginia Beach, VA, USA, 23–27 August 2009. (CD-ROM), pp. 333–343.

Hänninen, H., Brederholm, A., Saukkonen, T., Ivanchenko, M., Toivonen, A., Karlsen, W., Ehrnstén, U. and Aaltonen, P. (2011), Environment-assisted cracking and hot cracking susceptibility of nickel-base alloy weld metal. VTT Research Notes 2582, VTT Technical Research Centre of Finland, Espoo, Finland, 152 p. http://www.vtt.fi/inf/pdf/tiedotteet/2011/T2582.pdf.

Holmström, P., Sarikka, T., Brederholm, A., Karjalainen-Roikonen, P., Saukkonen, T., Nevasmaa, P. and Hänninen, H. (2013), Effect of strength mismatch and microstructure on mechanical properties of BWR dissimilar metal safe-end welds. Proceedings of the 16th Int. Conf. on Environmental Degradation of Materials in Nuclear Systems – Water Reactors. Asheville, NC, USA, August 2013, 13 p.

Hou, J., Peng, Q.J., Takeda, Y., Kuniya, J., Shoji, T., Wang, J.Q., Han, E.-H., and Ke, W. (2010), Microstructure and Mechanical Properties of the Fusion Boundary Region in an Alloy 182 – Low Alloy Steel Dissimilar Weld Joint. Journal of Material Science, Vol. 45, 5332–5338.

International Weld Residual Stress Round Robin Problem Statement. (2009), Version 1.0, December 14, 2009. US Nuclear Regulatory Commission, Office of Nuclear Regulatory Research, Division of Engineering, Component Integrity Branch, 95 p.

Jacko, R.J., Gold, R.E. and Kroes, A. (2003), Accelerated corrosion testing of alloy 52M and alloy 182 weldments, Proceedings of the 11th International Conference on Environmental Degradation of Materials in Nuclear Systems – Water Reactors, Stevenson, WA, USA, 10–14 August 2003, CD-ROM.

Jang, C., Lee, J., Kim, J.S. and Jin, T.E. (2008), Mechanical property variation within Inconel 82/182 dissimilar metal weld between low alloy steel and 316 stainless steel. International Journal of Pressure Vessels and Piping, Vol. 85, 635–646.

Jang, C., Cho, P.Y., Kim, M., Oh, S.J. and Yang, S.J. (2010), Effects of microstructure and residual stress on fatigue crack growth of stainless steel narrow gap welds. Materials and Design, Vol. 31, 1862–1870.

Karlsen, W. and Pakarinen, J. (2009), TEM investigation of cracks in dissimilar metal weld Inconel 182 following doped steam testing. Research Report VTT-R-05722-09, VTT Technical Research Centre of Finland, Espoo, Finland, 29 p. http://www.vtt.fi/inf/julkaisut/muut/2009/VTT-R-05722-09.pdf.

Karlsson, L. (1995), Welding of dissimilar metals. Welding in the World, Vol. 36, 125–132.

Keinänen, H., Laukkanen, A. and Nevasmaa, P. (2003), Fracture and tensile testing of the ‘AD01’ mock-up’ (ADIMEW – Work Package 2: Material Characterization). Research Report TUO72-033337, VTT Industrial Systems, Espoo, Finland, 41 p.

Kim, J.W., Lee, K., Kim, J.S. and Byun, T.S. (2009), Local mechanical properties of Alloy 82/182 dissimilar weld joint between SA508 Gr.1a and F316 SS at RT and 320 °C. Journal of Nuclear Materials, Vol. 384, 212–221.

Kim, Y.-J., Koçak, M., Ainsworth, R.A., and Zerbst, U. (2000), SINTAP defect assessment procedure for strength mismatched structures. Engineering Fracture Mechanics, Vol. 67, 529–546.

Kuo, T. and Lee, H. (2002), Effects of filler metal composition on joining properties of alloy 690 weldments. Materials Science and Engineering, Vol. 338, 202–212.

Laukkanen, A., Nevasmaa, P., Ehrnstén, U. and Rintamaa, R. (2001), Mapping of characteristic features of bimetallic welds from the standpoint of engineering critical analysis. Proceedings of the 16th Int. Conf. on Structural Mechanics in Reactor Technology (SMiRT-16); Div. G, Fracture Mech. Washington DC, 12–17 August 2001. Editos: Vernon C. Matzen and C.C. David Tung. International Association for Structural Mechanics in Reactor Technology (IASMiRT), USA. Paper #1566 (CD-ROM), 8 p.

Lee, H.T. and Jeng, S.L (2001), Characteristics of dissimilar welding of alloy 690 to 304L stainless steel. Science and Technology of Welding & Joining, Vol. 6 (4), 225–234.

Lippold, J.C. and Kotecki, D.J. (2005), Welding metallurgy and weldability of stainless steels. John Wiley and Sons, Inc., New Jersey, USA. ISBN: 978-0471-47379-4.

Moran, P.M. and Shih, C.F. (1998), Crack growth and cleavage in mismatched welds: a micromechanics study using cell model. International Journal of Fracture, Vol. 92, 153–174.

Morra, M., Othon, M., Willis, E. and McCracken, S. (2011), Characterization of structures and strains in 52-type and 152 welds. Alloy 690/52/152 PWSCC research collaboration meeting, November 29 – December 2, Tampa, Florida, USA, pp. 1–183.

Naffakh, H., Shamanian, M. and Ashrafizadeh, F. (2009), Dissimilar welding of AISI 310 austenitic stainless steel to nickel-based alloy Inconel 657. Journal of Materials Processing Technology, Vol. 209, 3628–3639.

Nelson, T.W., Lippold, J.C. and Mills, M.J. (1999), Nature and evolution of the fusion boundary in ferritic-austenitic dissimilar weld metals, Part 1 – nucleation and growth. Welding Journal, Vol. 78 (10), 329–337.

Nevasmaa, P. and Laukkanen, A. (2005), VTT tuotteet ja tuotanto tutkimusraportti. Hitsausliitosten yli- ja alilujien vyöhykkeiden (nk. lujuuden mis-match) vaikutukset rakenteelliseen eheyteen ja kuormankantokykyyn – SHI:n materiaalifoorumin esiselvitys, VTT Research Report No. BTUO72-051350, VTT Technical Research Centre of Finland, Espoo, Finland, 39 p.

Nevasmaa, P., Laukkanen, A. and Ehrnstén, U. (1999a), Structural Integrity of Bi-Metallic Components (BIMET) – TG2: Material characterisation of dissimilar ferrite-austenite welds. VTT Research Report VAL C 517, VTT Manufacturing Technology, Espoo, Finland, 73 p.

Nevasmaa, P., Laukkanen, A., and Ehrnstén, U. (1999b), Structural integrity of bimetallic components (BIMET). TG2 – Material characterization report, VTT Report VALC517, 73 p.

Nevasmaa, P., Laukkanen, A. and Ehrnstén, U. (2000), Fracture resistance and failure characteristics of AISI 304/SA508 bimetallic weld in ductile regime. Proceedings of the 13th Eur. Conf. on Fracture – Fracture Mech.: Applications and Challenges (ECF 13), San Sebastian, Spain, 6–9 September 2000, ESIS / Eng. Mat. Advisory Services Ltd., Paper No. 1N.49 (CD-ROM), 8 p.

Nevasmaa, P., Holmström, P., Karjalainen-Roikonen, P., Sarikka, T., Ahonen, M., Mouginot, R., Ehrnstén, U., Brederholm, A., Aaltonen, P. and Hänninen, H. (2013), Fracture mechanical characterization of ferrite-austenite dissimilar metal welds (DMWs) for elevated temperature service in view of metallurgical mis-match. In: Baltica IX. International Conference on Life Management and Maintenance for Power Plants. Editors: Pertti Auerkari and Juha Veivo. VTT Technology 106, VTT Technical Research Centre of Finland, Espoo, Finland, pp. 152–173. http://www.vtt.fi/inf/pdf/technology/2013/T106.pdf.

PARENT – An International Collaboration to Explore the NDE Responses of Cracks in Nickel Alloy Components (2013), http://www.nrc.gov/public-involve/conference-symposia/ric/past/2011/docs/posters/11-parent-ric-poster-final.pdf (accessed 17 December 2013).

Pavlina, E.J. and Van Tyne, C.J. (2008), Correlation of yield strength and tensile strength with hardness for steels. Journal of Materials Engineering and Performance, Vol. 17 (6), 888–893.

Rao, G.V., Jacko, R.J. and McIlree, A.R. (2002), An assesment of the CRDM Alloy 600 reactor vessel head penetration PWSCC remedial techniques. Proceedings of Fontevraud 5, Contribution of Materials Investigation to the Resolution of Problems Encountered in Pressurized Water Reactors, SFEN, Fontevraud, France, 23–27 September 2002, CD-ROM.

Sennour, M., Marchetti, L., Martin, F., Perrin, S., Molins, R. and Pijolat, M. (2010), A detailed TEM and SEM study of Ni-base alloys oxide scales formed in primary conditions of pressurized water reactor. Journal of Nuclear Materials, Vol. 402, 147–156.

Sireesha, M., Shankar, V., Albert, S.K. and Sundaresan, S. (2000), Microstructural features of dissimilar welds between 316LN austenitic stainless steel and Alloy 800. Materials Science and Engineering, Vol. A292, 74–82.

Sireesha, M., Albert, S.K. and Sundaresan, S. (2001), Microstructure and mechanical properties of weld fusion zones in modified 9Cr-1Mo steel. Journal of Materials Engineering and Performance, Vol. 10, 320–330.

Soares, B., De Abreu Mendonça Schvartzman, M.M. and Reis da Costa Campos, W. (2007), Characterization of the dissimilar welding – austenitic stainless steel with nickel alloy filler metal. International Nuclear Atlantic Conference, ISBN 978-85-99141-02-1, 6 p.

Staehle, R.W. and Gorman, J.A. (2004), Quantitative assessment of submodes of stress corrosion cracking on the secondary side of steam generator tubing in pressurized water reactors: Part 2. Corrosion, Vol. 60 (1), 5–63.

Thaulow, C., Hauge, M., Zhang, Z.L., Ranestad, Ø. and Fattorini, F. (1999a), On the interrelationship between fracture toughness and material mismatch for cracks located at the fusion line of weldments. Engineering Fracture Mechanics, Vol. 64, 367–382.

Thaulow, C., Zhang, Z.L., Hauge, M., Burget, W. and Memhard, D. (1999b), Constraint effects on crack tip stress fields for cracks located at the fusion line of weldments. Computational Material Science, Vol. 15, 275–284.

Valo, M. (2014), Principal scientist, VTT, Espoo. Personal conversation 15.2.2014.

Wang, H.T., Wang, G.Z., Xuan, F.Z. and Tu, S.T. (2013), An experimental investigation of local fracture resistance and crack growth paths in a dissimilar metal welded joint. Materials and Design, Vol. 44, 179–189.

Zang, W., Gunnars, J., Dong, P. and Hong, J.K. (2009), Improvement and validation of weld residual stress modelling procedure. SSM Research 2009:15. ISSN: 2000-0456, 48 p.

Ziemniak, S. and Hanson, M. (2003), Corrosion Behavior of NiCrMo, Alloy 625 in High Temperature, Hydrogenated Water. Corrosion Science, Vol. 45, 1595–1618.

Ziemniak, S. and Hanson, M. (2006), Corrosion Behavior of NiCrMo, Alloy 600 in High Temperature, Hydrogenated Water. Corrosion Science, Vol. 48, 498–521.

Series title and number
VTT Technology 175

Title	**Structural integrity of Ni-base alloy welds**
Author(s)	Hannu Hänninen, Anssi Brederholm, Teemu Sarikka, Roman Mouginot, Petra Holmström, Tapio Saukkonen, Aki Toivonen, Päivi Karjalainen-Roikonen, Pekka Nevasmaa, Heikki Keinänen, Esa Leskelä, Matias Ahonen, Ulla Ehrnstén & Pertti Aaltonen
Abstract	The Tekes project Structural integrity of Ni-base alloy welds (SINI) was carried out at Aalto University and VTT during the period from 2010 to 2014. In nuclear industry applications, the degradation of Ni-base alloy dissimilar metal welds (DMWs), both in pressurised water reactor (PWR) and in boiling water reactor (BWR) plants, is an extensive international problem. The project participates with ongoing international cooperation in USA (Electric Power Research Institute EPRI, Alloy 690/52/152 PWSCC Research Collaboration) and in Japan (Tohoku University) for the conduction of new Ni-base alloy research. The research need is actual, especially because indications have been found in the DMWs in the reactor pressure vessel nozzle of BWRs similar to Finnish BWR designs and European pressurised water reactor (EPR PWR) -plant under construction contains a large number of varying and new types of dissimilar metal welds of which no previous experience is available. The main focus of the project was to investigate the weldability of Alloy 690 base metal corresponding filler metal Alloy 52 and the properties of the welded joint. Comparable reactor pressure vessel (RPV) safe-end weld joint was made by narrow-gap tungsten inert gas (TIG) welding with Alloy 52 filler metal for research purposes. Also prototypical BWR reactor pressure vessel (RPV) safe-end weld joint was made with Alloy 82/182 filler metals. Determination of the mechanical properties and characterization of the microstructures of the welded joints were conducted. Crack initiation tests in autoclave were made in different environments. After PINC (Program for the Inspection of Nickel Alloy Components) round-robin program new PARENT (Program to Assess Reliability of Emerging Non-destructive Techniques for Dissimilar Metal Welds) round-robin program was started where VTT participated. Based on the PINC results, new non-destructive testing methods were developed to enhance the reliability of detection and accuracy of sizing of flaws in nickel-based alloy dissimilar metal welds. Separate reports: 1. Holmström, P. (2012), The effect of mismatch on the mechanical properties of a dissimilar metal weld. M.Sc. Thesis, Aalto University, Espoo, Finland, 162 p. + app. 4 p. 2. Mouginot, R. and Hänninen, H. (2013), Microstructures of nickel-base alloy dissimilar metal welds. Aalto University publication series SCIENCE + TECHNOLOGY, 5/2013, https://aaltodoc.aalto.fi/handle/123456789/9006, Aalto University, Espoo, Finland, 178 p. 3. Keinänen, H. (2013), Computational estimation of the risk of hot cracking in narrow gap welding. Research report VTT-R-08369-13, VTT Technical Research Centre of Finland, Espoo, Finland, 27 p. + app. 10 p.
ISBN, ISSN	ISBN 978-951-38-8259-4 (soft back ed.) ISSN 2242-1211 (soft back ed.) ISSN-L 2242-1211 ISBN 978-951-38-8260-0 (URL: http://www.vtt.fi/publications/index.jsp) ISSN 2242-122X (URL: http://www.vtt.fi/publications/index.jsp)
Date	June 2014
Language	English, Finnish abstract
Pages	257 p.
Keywords	Nickel-base alloys, welding, weld metal, dissimilar metal welds, nuclear power plant, environment-assisted cracking, fracture toughness, scanning electron microscopy, NDT
Publisher	VTT Technical Research Centre of Finland P.O. Box 1000, FI-02044 VTT, Finland, Tel. 020 722 111

Julkaisun sarja ja numero

VTT Technology 175

Nimeke	**Ni-seosten hitsausliitosten rakenteellinen turvallisuus**
Tekijä(t)	Hannu Hänninen, Anssi Brederholm, Teemu Sarikka, Roman Mouginot, Petra Holmström, Tapio Saukkonen, Aki Toivonen, Päivi Karjalainen-Roikonen, Pekka Nevasmaa, Heikki Keinänen, Esa Leskelä, Matias Ahonen, Ulla Ehrnstén & Pertti Aaltonen
Tiivistelmä	Tekes-projektissa Structural Integrity of Ni-base Alloy Welds (SINI) vuosina 2010–2014 Aalto-yliopistossa ja VTT:llä suoritettu tutkimus kohdistui ydinvoimalaitoksissa käytettäviin uusiin materiaaleihin ja hitsausmenetelmiin. Ydinvoimalaitosten Ni-seosten ja niiden hitsausliitosten vaurioituminen sekä painevesireaktori (PWR)- että kiehutusvesireaktori (BWR) -olosuhteissa on laaja kansainvälinen käytettävyys- ja tutkimusongelma. SINI-projekti osallistui useaan kansainväliseen yhteishankkeeseen USA:ssa (Electric Power Research Institute EPRI, Alloy 690/52/152 PWSCC Research Collaboration) ja Japanissa (Tohokun yliopisto). Myös Suomessa tutkimustarve on suuri: BWR-laitosten kriittisissä paineastian/putkiston eriparihitsausliitoksissa on havaittu indikaatioita, ja eurooppalainen painevesireaktorilaitos (EPR-PWR) sisältää kaikissa tärkeimmissä komponenteissa runsaasti uusia Ni-seoksia ja niiden eriparihitsausliitoksia, joista ei ole aiempaa käyttökokemusta. Projekti keskittyi erityisesti Alloy 690 -seosta vastaavan hitsauslisäaineen Alloy 52 hitsattavuuden ja hitsausliitoksen ominaisuuksien tutkimiseen. Tutkimuksia varten hitsattiin kapearailo-TIG-menetelmällä reaktoripaineastian safe-end-hitsausliitosta vastaavat koehitsit Alloy 52 -lisäaineella. Lisäksi hitsattiin perinteisen BWR-reaktoripaineastian safe-end-hitsausliitosta vastaava koehitsi Alloy 82/182 -lisäaineella. Hitsausliitoksista määritettiin niiden mekaaniset ominaisuudet sekä karakterisoitiin syntyvät mikrorakenteet. Autoklaavikokeilla tutkittiin särön ydintymistä eri ympäristöissä. PINC (Program for the Inspection of Nickel Alloy Components) -monilaboratoriotestauksen jatkona käynnistyi PARENT-ohjelma (Program to Assess Reliability of Emerging Non-destructive Techniques for Dissimilar Metal Welds), johon VTT osallistui. Ohjelmassa jatkettiin PINCin tulosten pohjalta uusien rikkomattomien tarkastusmenetelmien kehittämistä sekä parannettiin vikojen havaitsemistarkkuutta ja koon määrittämistä nikkelipohjaisissa eriparihitsausliitoksissa. Erilliset raportit: 1. Holmström, P. (2012), The effect of mismatch on the mechanical properties of a dissimilar metal weld. M.Sc. Thesis, Aalto University, Espoo, Finland, 162 p. + app. 4 p. 2. Mouginot, R. and Hänninen, H. (2013), Microstructures of nickel-base alloy dissimilar metal welds. Aalto University publication series SCIENCE + TECHNOLOGY, 5/2013, https://aaltodoc.aalto.fi/handle/123456789/9006, Aalto University, Espoo, Finland, 178 p. 3. Keinänen, H. (2013), Computational estimation of the risk of hot cracking in narrow gap welding. Research report VTT-R-08369-13, VTT Technical Research Centre of Finland, Espoo, Finland, 27 p. + app. 10 p.
ISBN, ISSN	ISBN 978-951-38-8259-4 (nid.) ISSN 2242-1211 (nid.) ISSN-L 2242-1211 ISBN 978-951-38-8260-0 (URL: http://www.vtt.fi/publications/index.jsp) ISSN 2242-122X (URL: http://www.vtt.fi/publications/index.jsp)
Julkaisuaika	Kesäkuu 2014
Kieli	Englanti, suomenkielinen tiivistelmä
Sivumäärä	257 s.
Avainsanat	Nikkelipohjaiset hitsauslisäaineet, hitsaus, eriparihitsi, ydinvoimalaitos, ympäristön aiheuttama murtuminen, murtumissitkeys, pyyhkäisyelektronimikroskopia, NDT
Julkaisija	VTT PL 1000, 02044 VTT, Puh. 020 722 111

Structural integrity of Ni-base alloy welds

The degradation of dissimilar metal welds (DMW) in both boiling water (BWR) and pressurized water reactor (PWR) plants is currently an area of widespread international interest. This is because indications have been found in the reactor pressure vessel nozzle DMWs of BWRs and PWRs. In nuclear power industry DMWs are also used in many other constructions and systems. Alloy 690 and associated weld metals (Alloy 52) are widely used in repair and replacement of the affected thick-section components. In the new reactors they are the main construction materials. Prototypical DMWs of BWR and PWR plants were welded and the welding process was modelled to evaluate stresses, strains and susceptibility to hot cracking. The DMWs were characterized metallographically and by mechanical testing using hardness, tensile and fracture mechanical testing. Crack initiation testing was made in different environments: simulated PWR water and high-temperature steam. New non-destructive testing methods were developed to enhance the reliability of detection and accurate sizing of flaws in Ni-base alloy DMWs.

ISBN 978-951-38-8259-4 (Soft back ed.)
ISBN 978-951-38-8260-0 (URL: http://www.vtt.fi/publications/index.jsp)
ISSN-L 2242-1211
ISSN 2242-1211 (Print)
ISSN 2242-122X (Online)